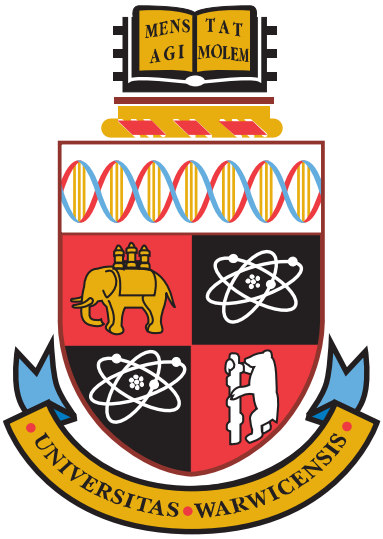

Estimating the space density of ultracompact binary stars

by

Philip J. Carter

Thesis

Submitted to the University of Warwick

for the degree of

Doctor of Philosophy

Department of Physics

April 2014

THE UNIVERSITY OF WARWICK

Contents

List of Tables

List of Figures

Acknowledgments

I am extremely grateful to Tom Marsh and Danny Steeghs for their guidance and support throughout the last three and a half years. Their insight has been invaluable. I would also like to thank Paul Groot, for giving me my first experience of observing on La Palma; Chris Copperwheat, for getting me started with data reduction; Elmé Breedt and Boris Gänsicke. I am indebted to all my collaborators, for their hard work, and provision of spectra, code, and comments that have helped to improve my work.

My thanks go to all the members of the Astronomy and Astrophysics group at Warwick, both past and present, for their advice, probing questions, and friendship. You have made this a wonderful place in which to study, and provided a constant source of support and entertainment. I must particularly thank: Rachel, for making me feel welcome from day one, Penélope, John, João, Nicola, Sandra, Madelon, Simon, Steve, Tom and Greg, your company has been an integral part of my PhD experience.

I am incredibly fortunate to have a supportive family who have always encouraged me. I will be forever grateful to my parents, this work would not have been possible without them.

I also want to acknowledge the brilliant people I have lived with during the last few years, especially those that lived in Minty. Sophie, Helen, Oli, Lolu, Nichola, Alex, Sarah Jane and Claire, I could not have wished for better people to spend my time with.

Finally, I would like to thank Chris Brady, without whom my life would have suffered from a terrible lack of curry.

Declarations

This thesis is submitted to the University of Warwick in support of my application for the degree of Doctor of Philosophy. It has been composed by myself and has not been submitted in any previous application for any degree. This thesis represents my own work except where stated otherwise. Parts of this thesis have been published during my period of study, as outlined below:

Chapters 3 and 6 are based on: Carter, P. J.; Marsh, T. R.; Steeghs, D.; Groot, P. J.; Nelemans, G.; Levitan, D.; Rau, A.; Copperwheat, C. M.; Kupfer, T. and Roelofs, G. H. A., "A search for the hidden population of AM CVn binaries in the Sloan Digital Sky Survey", MNRAS, 429, 2143 (2013).

Chapter 4 is based on: Carter, P. J.; Steeghs, D.; Marsh, T. R.; Kupfer, T.; Copperwheat, C. M.; Groot, P. J. and Nelemans, G., "The AM Canum Venaticorum binary SDSS J173047.59+554518.5", MNRAS, 437, 2894 (2014).

Chapter 5 is based on: Carter, P. J.; Steeghs, D.; de Miguel, E.; Goff, W.; Koff, R. A.; Krajci, T.; Marsh, T. R.; Gänsicke, B. T.; Breedt, E.; Groot, P. J.; Nelemans, G.; Roelofs, G. H. A.; Rau, A.; Koester, D. and Kupfer, T., "The helium-rich cataclysmic variable SBSS 1108+574", MNRAS, 431, 372 (2013).

Chapter 7 is based on: Carter, P. J.; Gänsicke, B. T.; Steeghs, D.; Marsh, T. R.; Breedt, E.; Kupfer, T.; Gentile Fusillo, N. P.; Groot, P. J. and Nelemans, G., "Two new AM Canum Venaticorum binaries from the Sloan Digital Sky Survey III", MNRAS, 439, 2848.

Figs. 3.2 and 8.3 were prepared for the proceedings of the workshop *The Golden Age of Cataclysmic Variables and Related Objects II*, to be published in Acta Poly.

The spectrum of SDSS J1043+5632 shown in Fig. 3.9 was obtained and reduced by D. Levitan. Calculations of the number of AM CVns expected in the SDSS footprint based on Nelemans et al. (2001)'s population synthesis (section 3.7) used data and code provided by G. Nelemans and G. H. A. Roelofs.

The photometry of SBSS 1108+574 presented in chapter 5 was carried out and reduced by observers from the Centre for Backyard Astrophysics (CBA). Analysis of this photometry (section 5.3.2) was originally conducted by E. de Miguel, and was repeated by myself during preparation of the paper. Sections 5.2.2 and 5.3.2 are partly based on material written by E. de Miguel. The white dwarf model fitting shown in Fig. 5.2 was performed by B. T. Gänsicke, who also wrote the description of this given in section 5.3.1.

B. T. Gänsicke carried out the period analysis presented in chapter 7, and produced Figs. 7.4, 7.5, 7.6 and 7.7.

Abstract

The AM Canum Venaticorum (AM CVn) binaries are a rare group of hydrogen-deficient, ultrashort period, mass-transferring white dwarf binaries, some of which may be Type Ia supernova progenitors. These systems represent the end product of several finely-tuned evolutionary pathways, and as such are of great interest for binary stellar evolution theory. They are also some of the strongest known sources of low-frequency gravitational waves. Establishing their space density is important for constraining evolutionary models, and the signals we expect to detect from the Galactic population. This has been difficult as much of the known population has been discovered in a heterogeneous manner.

In this thesis I present the latest results from a spectroscopic survey designed to uncover the hidden population of AM CVn binaries in the photometric database of the Sloan Digital Sky Survey (SDSS). This small, colour-selected sample of ∼2000 candidates, is expected to contain the majority of all AM CVn binaries in the SDSS. The survey is now approximately 70 per cent complete, and the discovery of only seven new AM CVn binaries indicates a lower space density than previously predicted.

Characterisation of the sample requires detailed follow-up observations after the initial discovery, in order to determine the orbital period. I present time-resolved spectroscopy of the recently-discovered AM CVn binary SDSS J173047.59+554518.5, and the dwarf nova SBSS 1108+574. The orbital period I measure for SDSS J1730 confirms its ultracompact binary nature. The quiescent spectrum of SBSS 1108+574 is unusually rich in helium compared to typical cataclysmic variables (CVs). I find that its orbital period is significantly below the normal CV period minimum. This indicates that the donor in SBSS 1108+574 is highly evolved, making it a candidate for the often-dismissed 'evolved CV' channel for AM CVn binary formation.

I discuss a wider search for new AM CVns in the SDSS spectroscopic database, and present two new systems discovered in SDSS-III spectroscopy. Since this search has revealed only these two new systems, it is unlikely that we have missed a large population of AM CVn binaries, and their discovery should have little effect on our previous calculations of the AM CVn space density.

Chapter One

Introduction

Of all the 'stars' we see when we gaze into the night sky, only about half of these are actually single stars, the rest are multiple systems consisting of two or more stars orbiting each other due to their mutual gravitational attraction. The stars in many of these systems are sufficiently detached that they have almost no effect on one another, evolving in the same manner as isolated stars (Carroll & Ostlie, 2006). Stars in *close* binary systems, however, live much more interesting lives, their evolution governed by their companion.

The stars in close binary systems will interact at some point during their evolution. As stars enter the later stages of their lives they expand, and the surface of one or both of the stars will be distorted by its companion, causing material to flow from one star to the other. This can lead to a wide variety of phenomena including Algols and W UMa contact systems. If the stellar envelope expands rapidly, it can grow to encompass both stars in a common envelope (CE). The CE phase rapidly reduces the orbital separation of the two components (Paczyński, 1976), leading to the very close binary systems that are some of the most interesting objects in the Galaxy, including X-ray binaries, double white dwarf binaries, cataclysmic variables (CVs), and the progenitors of gamma-ray bursts (Ivanova et al., 2013).

The binary star system with the shortest known orbital period consists of two interacting white dwarfs that complete one orbit every 5 minutes (HM Cnc; Roelofs et al., 2010). It belongs to the rare class of objects known as the AM Canum Venaticorum (AM CVn) binaries. This thesis is concerned with the population of these ultracompact, helium accreting systems.

1.1 Close binary stars

1.1.1 Roche geometry

In order to gain an understanding of close binary star systems and their many interesting properties, it is useful to examine a basic concept in the theory of binaries, the Roche geometry. Consider the gravitational potential, Φ, a test particle would experience in the co-rotating coordinate frame of the binary; this is comprised of the separate gravitational potentials of the two stars, considered to be point masses, and a third term originating from the centrifugal force (e.g. Frank, King & Raine, 2002). With the primary star at the origin and the secondary a distance a along the x-axis, this can be expressed as,

$$\Phi = -\frac{GM_1}{(x^2+y^2+z^2)^{\frac{1}{2}}} - \frac{GM_2}{((x-a)^2+y^2+z^2)^{\frac{1}{2}}} - \frac{\omega^2}{2}\left[\left(x - \frac{aM_2}{M_1+M_2}\right)^2 + y^2\right], \tag{1.1}$$

where G is the gravitational constant, M_1 and M_2 are the masses of the primary and secondary stars, and ω is the angular velocity of their orbit.

The largest closed equipotential surface (Φ = constant) of each star is known as its Roche lobe. The Roche lobes of the two stars touch, along the line joining their centres, at the inner Lagrangian point, L_1. The Roche equipotentials depend solely upon the mass ratio of the binary, with the scale set by the binary separation, a. Fig. 1.1 shows equipotential surfaces in the xy-plane for a binary system with a mass ratio ($q = \frac{M_2}{M_1}$) of 0.2.

The Lagrange points are stationary points in the potential, at which a test particle would experience zero resultant force. The primary Lagrange point, L_1, is found at the point where the Roche lobes of the two objects meet. Material inside the critical surface defined by the Roche lobe is gravitationally bound to the star, but at the L_1 point the material is not bound to either star.

Thus if a star's atmosphere filled its Roche lobe, matter would be able to escape the stellar surface via the primary Lagrange point. If the surface of a star expands beyond the extent of its Roche lobe, this material is no longer bound to the parent star; when this material enters the Roche lobe of its companion it will be bound to the companion instead. Thus if a star expands slowly, material at its surface will flow into the Roche lobe of its companion via the L_1 point. This process is known as Roche lobe overflow, and is key to the evolution of close binaries.

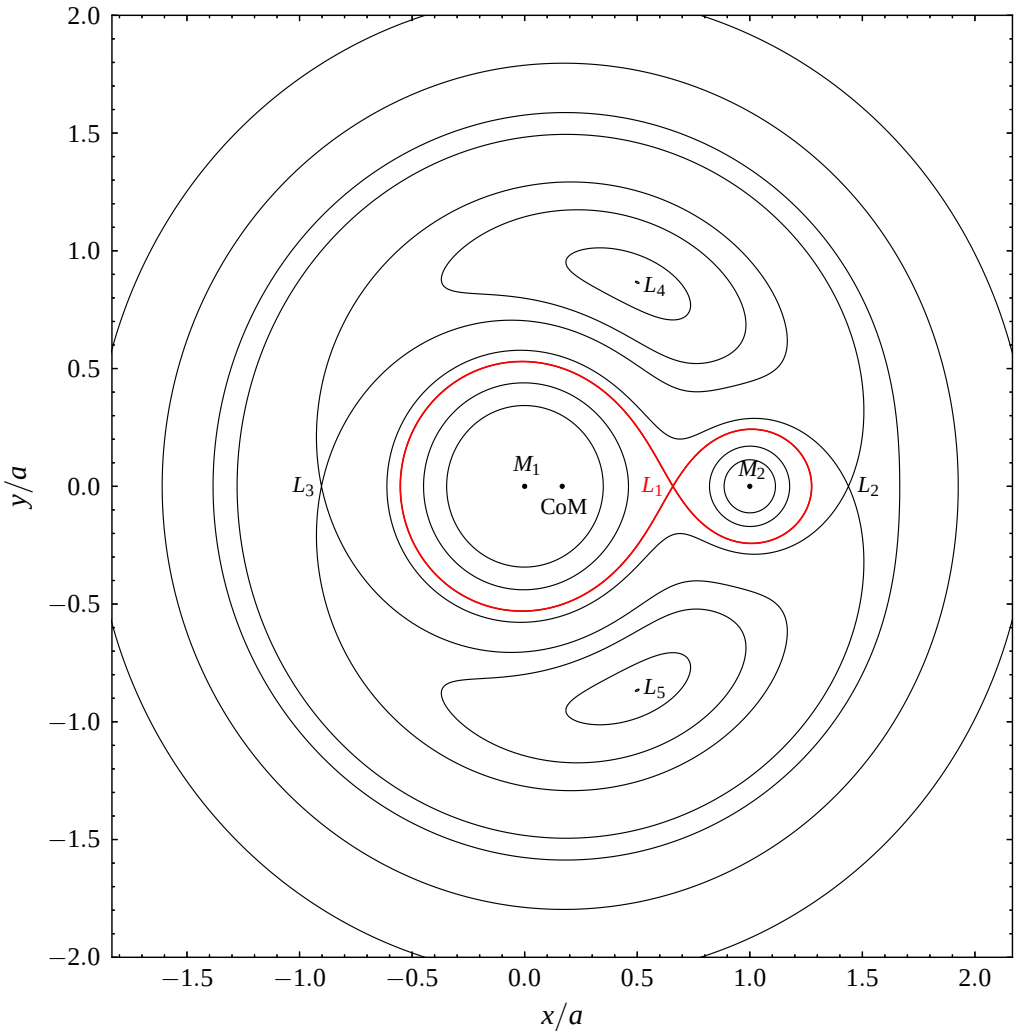

Figure 1.1: Equipotential surfaces of the Roche geometry for a binary with a mass ratio, q=0.2. The positions of the primary (M_1) and secondary (M_2) stars, the centre of mass (CoM) of the system and the Lagrange points are labelled. The Roche lobes of the stars, which meet at the primary Lagrange point, L_1, are coloured red. The axes are scaled in units of the binary separation, a.

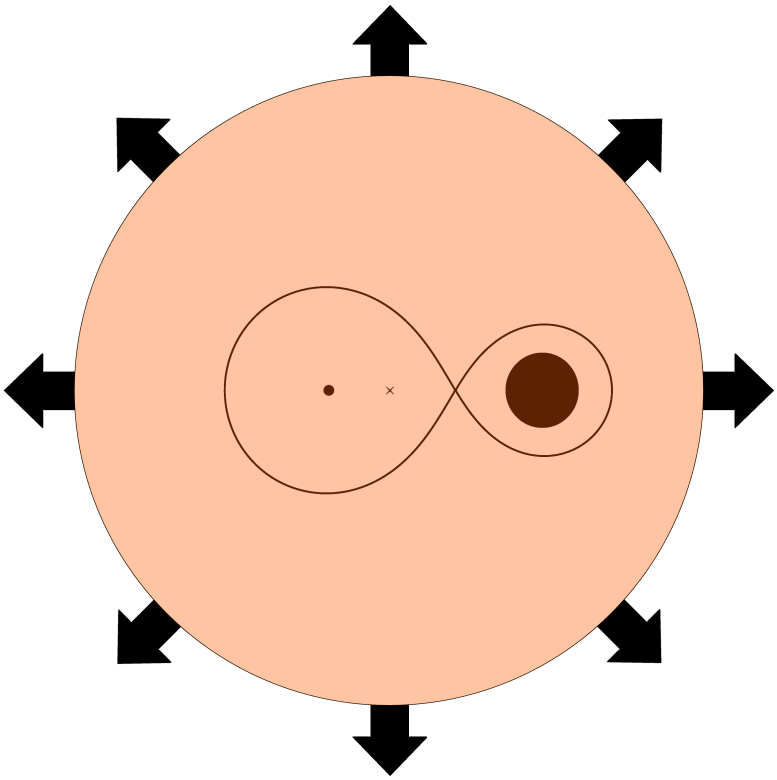

Figure 1.2: Schematic representation of the common envelope phase. The core of the evolved star (black dot in the larger Roche lobe) and the less massive main sequence star (large filled circle in the smaller lobe) orbit around the centre of mass of the system (cross) inside a common envelope. The envelope extracts angular momentum from the binary orbit and is ejected from the system. Based on fig. 11 from Iben (1991).

1.1.2 Binary evolution

Binaries can be divided into one of three subgroups based on whether the stars fill their Roche lobes. Detached systems are those in which neither star fills its Roche lobe, both stars are approximately spherical, as represented by the small circles in Fig. 1.1. Binaries in which one component fills its Roche lobe are known as semi-detached systems; those systems in which both stars fill their Roche lobes are known as contact binaries.

Most binary star systems are detached, the orbital separation is so great that neither component ever fills its Roche lobe, and the two stars evolve almost exactly as isolated stars of the same mass. In some binaries, however, the stars are close enough together when the more massive component evolves off the main sequence (more massive stars evolve faster), that its surface expands beyond its Roche lobe.

Material from the envelope of the red giant flows into the Roche lobe of its

companion much faster than the companion can readjust to the accreted mass, so the material builds up on the surface of the second star until it too fills its Roche lobe (Iben, 1991). The envelope of the red giant now engulfs both the core of the giant and the companion star (as depicted in Fig. 1.2), this is called the common envelope (CE) phase. The core of the giant and its companion experience drag forces from the CE, which extract angular momentum from the binary orbit, causing the stars to decrease their separation, and deposit energy in the envelope (e.g. Paczyński, 1976). The physics of the CE phase are not fully understood (e.g. Nelemans et al., 2000; Toonen & Nelemans, 2013), but the result is expulsion of the common envelope, leaving the newly formed compact object in a tighter orbit with its companion.

The exact nature of the remnant that emerges from the CE phase depends upon the mass and evolutionary state of the progenitor. Main-sequence progenitors with masses in the range ~ 1 to $\sim 7\,\mathrm{M}_{\odot}$ will produce either a He white dwarf or a CO white dwarf (Iben, 1991).

The unstable mass transfer that initiates the common envelope phase occurs because the loss of mass causes the Roche lobe of the primary to shrink more rapidly than its radius, leading to a runaway transfer of mass that the secondary is unable to accommodate. Stable Roche lobe overflow is possible if the mass loss would cause the Roche lobe to expand. For the case of conservative mass transfer (no angular momentum is lost from the binary), stable mass transfer occurs for $q < \frac{5}{6}$ (e.g. King, 1988). In order for stable Roche lobe overflow to be sustained, some mechanism must act to bring the stellar surface back into contact with its Roche lobe, for example, via shrinking of the Roche lobe due to loss of angular momentum from the system.

There are many possibilities for the further evolution of a close binary system, depending on the initial masses of the stars, and the orbital separation and relative masses of the objects that emerge from the CE phase. Binary evolution is described in more detail by Iben (1991). Two classes of binaries that form after passing through a CE phase, cataclysmic variables (CVs) and AM Canum Venaticorum (AM CVn) binaries, are discussed further in sections 1.2 and 1.3. Before we come to these I first discuss three further subjects that are of great importance to both CVs and AM CVns, and to close binaries in general.

1.1.3 White dwarfs

White dwarfs are compact, roughly Earth-sized objects that are the most common end-point of stellar evolution. They are extremely dense objects consisting of an electron degenerate core surrounded by a thin atmosphere of hydrogen or helium.

As they are supported against gravitational collapse by degeneracy pressure, they have a so-called *inverse* mass-radius relation – as the mass increases the radius decreases. Whilst a relativistic treatment is required to fully understand the white dwarf mass-radius relation, its inverse nature naturally implies a maximum mass limit, known as the Chandrasekhar mass (Chandrasekhar, 1939), $M_{\rm Ch} \simeq 1.4\,{\rm M}_{\odot}$ (e.g Koester & Weidemann, 1980). Above this mass the gravitational forces would cause the electrons to combine with the nuclei, and the object would collapse into a neutron star. It is generally thought that white dwarfs with CO cores approaching this mass limit via accretion will instead undergo a runaway thermonuclear explosion known as a Type Ia supernova (SN Ia; e.g. Hillebrandt & Niemeyer, 2000), though collapse into a neutron star may occur at high accretion rates (e.g. Saio & Nomoto, 1985).

We observe only the thin atmosphere on the surface of a white dwarf, and it is this atmosphere that largely controls the evolution and appearance of the white dwarf. White dwarfs are usually classified according to the scheme defined by Sion et al. (1983), based on the strongest elements observed in their spectra. The most common type are the hydrogen atmosphere, DA, white dwarfs.

As the end point in the evolution of ∼95 per cent of all main sequence stars (Koester & Weidemann, 1980), close binaries often contain one or two white dwarfs. The typical mass of field white dwarfs is $\sim 0.6\,{\rm M}_{\odot}$ (Liebert, Bergeron & Holberg, 2005), and it is only through close binary evolution that white dwarfs are able to accrete sufficient material to explode as Type Ia supernovae.

1.1.4 Angular momentum loss

As I have discussed, the CE extracts angular momentum from the orbit, shrinking the separation of the two stars and expelling the envelope. There are two further mechanisms for angular momentum loss that are important to our understanding of the accreting systems that are the subject of this work.

Magnetic braking

The spin rates and magnetic activity of late-type stars, including our own Sun, are correlated, and decrease with age (e.g. Skumanich, 1972). Stars are expected to 'spin down' at a rate correlated with their spin rate, due to the outward flow of ionised particles (e.g. Weber & Davis, 1967; Iben, 1991). The magnetic field forces electrically charged particles to flow along the field lines, and thus co-rotate with the star. These particles are accelerated to high velocities and then released, carrying

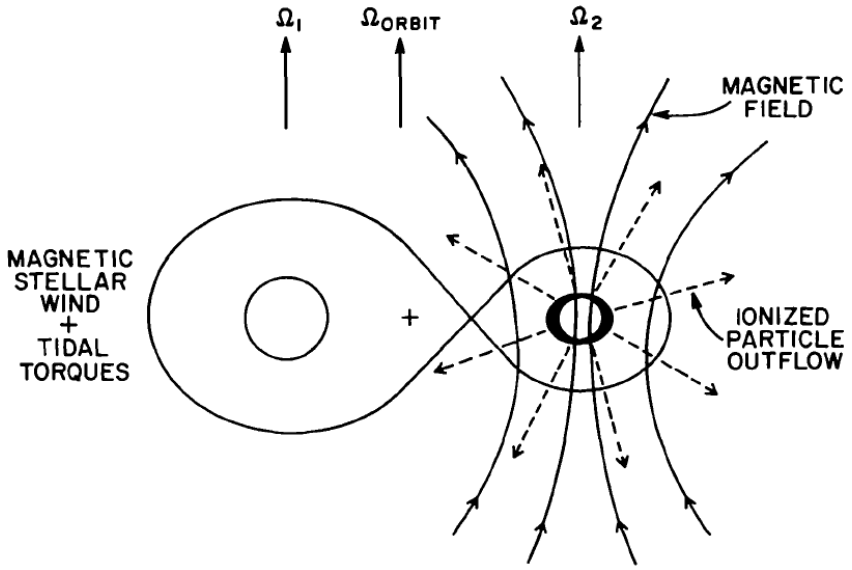

Figure 1.3: Schematic view of magnetic braking in close binary systems. Ionised particles are forced to flow along the magnetic field lines, before being released at large distances from the star, carrying away angular momentum. The angular momentum is extracted from the orbit due to synchronisation caused by tidal torques. From Iben (1991).

away angular momentum. The outflow of particles along the magnetic field, called a *magnetic stellar wind* thus extracts spin angular momentum from the star – this process is known as *magnetic braking*.

It is expected that low-mass main sequence stars in close binaries will also produce a magnetic stellar wind, and since such stars will have spin periods very close to the orbital period, due to tidal locking, they are expected to have strong magnetic fields. Such stars should also, therefore, lose spin angular momentum via magnetic braking. The tidal torques on the star return this lost spin, and hence the magnetic stellar wind extracts angular momentum from the orbit, causing the separation to decrease (Verbunt & Zwaan, 1981). Magnetic braking in a close binary system is illustrated in Fig. 1.3.

As the orbital separation decreases so does the period, and hence the spin rate increases, increasing the magnetic stellar wind, and the rate at which angular momentum is lost (Iben, 1991).

Gravitational wave radiation

In accordance with the general theory of relativity, binary stars radiate energy in the form of gravitational waves (GWs; Landau & Lifshitz, 1971). The energy required

to generate these waves is provided by the binary orbit, causing a loss of angular momentum. The rate at which angular momentum (J) is lost via gravitational radiation is given by (e.g. King, 1988),

$$\frac{\dot{J}_{\rm GR}}{J} = -\frac{32\,G^3}{5\,c^5}\frac{M_1 M_2 (M_1 + M_2)}{a^4}, \tag{1.2}$$

where c is the speed of light. This is a strong function of the orbital separation, a, and so angular momentum losses due to gravitational radiation are only significant at very small separations, or equivalently, very short orbital periods (Paczyński, 1967).

1.1.5 Accretion disc formation

Consider once again a semidetached binary, in which the less massive star fills its Roche lobe, causing material to flow out via the L_1 point.

From the perspective of the primary, a stream of matter with high angular momentum is 'squirted' into its Roche lobe. This angular momentum prevents the material from falling straight onto the star (which would violate conservation of angular momentum); it instead follows a ballistic trajectory, deflected around the star by the Coriolis force. There are several possibilities for the further behaviour of the matter stream, depending on the nature of the system. Provided the magnetic field of the primary is weak, and that the orbital period is not too short (Warner, 1995), direct impact of the stream onto the accretor will not occur. The stream will then come back around the primary to collide with itself. The collisions cause the gas to lose energy, however, particles retain their angular momentum, and the matter stream settles into a ring around the primary (Frank, King & Raine, 2002).

Material in this ring orbits with Keplerian angular velocities; particles closer to the primary move faster than particles farther away. This differential rotation causes friction in the ring, which heats the gas, causing energy to be radiated away. There is only one source for the lost energy, the potential in which the gas is orbiting; radiating away this gravitational energy will cause the gas to sink towards the primary star (Pringle, 1981). This requires the loss of angular momentum; which, since it is always conserved, requires that some material move to larger radii. As this continues, the ring of gas spreads out into a thin disc, as shown in Fig. 1.4. Material continually flows through the disc, spiralling inwards to be accreted onto the primary; angular momentum flows outwards, enabling the continued accretion and release of energy, and is soaked up by tidal interactions with the secondary.

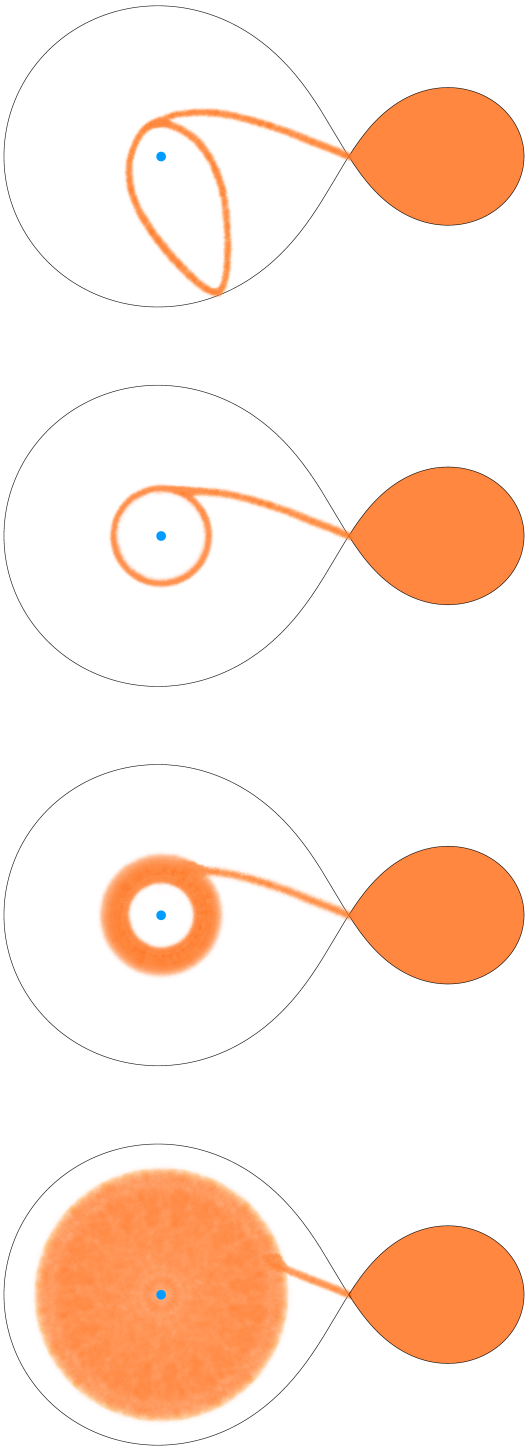

Figure 1.4: Illustration showing the formation of an accretion disc via Roche lobe overflow. Based on fig. 1 from Verbunt (1982).

This is an *accretion disc*, and is responsible for many of the observed properties of CVs and their ultracompact counterparts.

It should be noted that the viscosity that allows material and angular momentum to flow through the disc is not well understood. Accretion discs are far too diffuse for molecular viscosity to be significant (e.g. Lynden-Bell, 1969), the standard theory suggests that turbulence causes exchange of angular momentum and acts as viscosity (Shakura & Sunyaev, 1973). The viscosity, ν, is parametrized in terms of the sound speed, $c_{\rm s}$, and the height of the disc, H,

$$\nu = \alpha\, c_{\rm s}\, H, \tag{1.3}$$

where the parameter α represents the size of the viscosity as a fraction of the maximum case, where the turbulent eddies have the same height as the disc (Pringle, 1981). This turbulence is generally thought to be driven by magnetic instabilities (e.g. Hawley & Balbus, 1998).

1.2 Cataclysmic variables

Cataclysmic variable stars (CVs) are semi-detached systems in which a white dwarf accretes matter from a Roche lobe filling donor star. Their name derives from the characteristic large changes in brightness which many of them exhibit.

1.2.1 Types of CV

CVs can be divided into two broad categories depending on the strength of the accreting white dwarf's magnetic field.

In *magnetic systems* the magnetic field of the white dwarf disrupts the accretion disc, and the gas stream flows along the field lines to accrete onto the magnetic poles. These are further subdivided into *polars*, in which the magnetic field is strong enough to prevent a disc from forming, and *intermediate polars*, which have weaker fields, allowing a truncated disc.

The *non-magnetic* systems have white dwarfs with very weak magnetic fields, the accretion disc is not disrupted by the weak field, and accretion occurs where the disc meets the surface of the white dwarf.

The non-magnetic CVs are usually classified either as *nova-like* systems, which are 'non-eruptive' and show no large changes in brightness, or *dwarf novae*.

Dwarf novae are the class of CVs that undergo recurrent outbursts, with typical timescales of 2-20 days, and intervals between outbursts ranging from ten

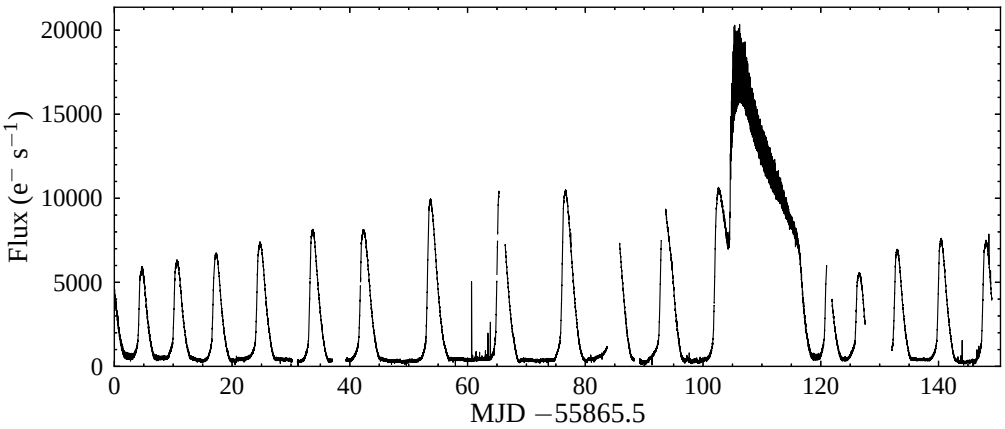

Figure 1.5: Part of the *Kepler* light curve of the dwarf nova V344 Lyrae, showing a series of normal outbursts and one superoutburst. The increase in the amplitude of the normal outbursts as the system builds towards the superoutburst, and the precursor outburst thought to trigger the superoutburst can be seen. Also noticeable is the significant modulation during the superoutburst caused by superhumps.

days to tens of years (Warner, 1995). These outbursts are thought to be due to an instability in the accretion disc, as will be discussed in the next section.

1.2.2 Dwarf nova outbursts

The presence of large amplitude dwarf nova outbursts implies an increase in the luminosity of the accretion disc (see Fig. 1.5). Osaki (1974) and Hōshi (1979) proposed a disc instability model to explain these outbursts.

Material is transferred from the secondary at a rate higher than it can be transported through the disc by viscous processes, causing material to build up in the disc, increasing the surface density. This gradually increases the viscosity, which leads to an increase in temperature. When the temperature reaches the point at which hydrogen begins to ionise, any further increase in temperature causes a huge increase in opacity, and hence a rapid rise in temperature, fully ionising the hydrogen, and the disc reaches a new equilibrium state (e.g. Hellier, 2001).

In the hot, bright, ionised state the viscosity of the disc is much higher, and so material flows through the disc much faster, and increases the accretion rate onto the white dwarf. The luminosity of the system increases, and the excess matter is drained from the disc.

The surface density and temperature decrease until the temperature is no longer high enough to keep all of the hydrogen ionised. At this point the high opacity returns, and a small drop in temperature results in the ions recombining, and the disc drops rapidly back to a low temperature, low viscosity, quiescent state. This

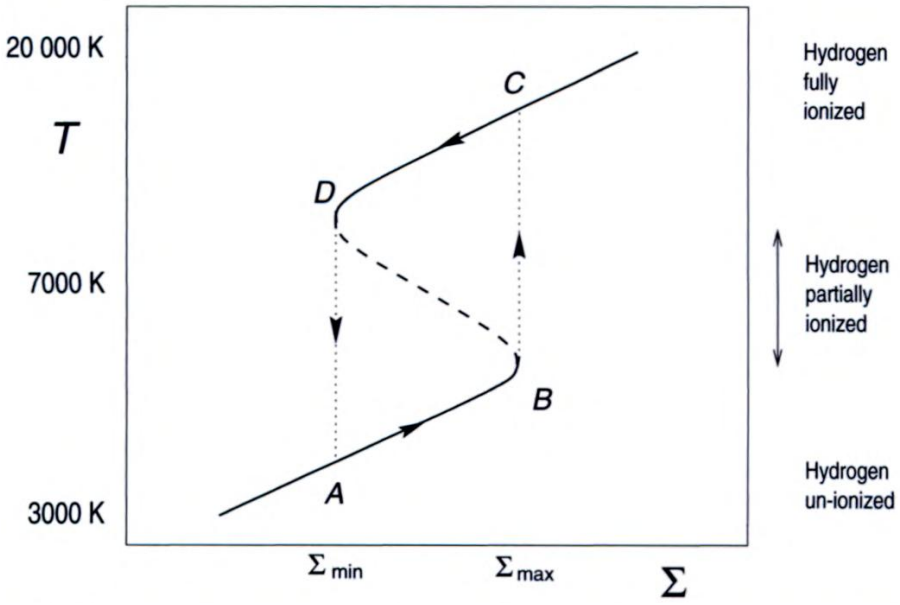

Figure 1.6: Schematic representation of the dwarf nova cycle. The S-curve relationship between surface density, Σ, and temperature, T, is the cause of the dwarf nova outburst. From Hellier (2001).

cycle is represented by the well known 'S-curve' in a plot of the disc's temperature against its surface density, as shown in Fig. 1.6.

Material then begins to build up again towards a new outburst. This is discussed in more detail by Smak (1984).

1.2.3 Superoutbursts and superhumps

As well as these 'normal outbursts', a subclass of dwarf novae known as the SU UMa stars also show *superoutbursts*, which are brighter than normal outbursts, and last longer. An example of a dwarf nova light curve is shown in Fig. 1.5, both a series of normal outbursts and a brighter superoutburst can be seen.

During a superoutburst, tidal interactions between the disc and the donor star cause the disc to become asymmetric. The increased viscous dissipation caused by this resonant interaction between the donor and the distorted disc, leads to periodic brightness variations known as *superhumps* (e.g. Whitehurst, 1988). The observed superhump period ($P_{\rm sh}$), which is typically a few percent longer than the orbital period, is the beat period between the orbital period of the system and the precession period of the deformed disc (Whitehurst, 1988). The origin of superhumps is discussed in detail by Wood et al. (2011).

As the superhump phenomenon is due to resonance, and the precession rate for resonant orbits depends upon the mass ratio of the system, there is a strong link between the superhump period and the mass ratio (e.g. Patterson et al., 2005). The superhump period-excess,

$$\epsilon = \frac{(P_{\rm sh} - P_{\rm orb})}{P_{\rm orb}}, \tag{1.4}$$

is found to increase with increasing mass ratio, q. An empirical $\epsilon - q$ relation can be derived from eclipsing dwarf novae, in which the mass ratio and superhump excess can be measured independently (Patterson et al., 2005; Knigge, 2006; Kato et al., 2009).

1.2.4 CV evolution

CV formation

CVs form from a binary containing two main sequence stars of different mass, initially separated by a few hundred solar radii, with an orbital period of about 10 years (Warner, 1995). The process of CV formation is depicted in Fig. 1.7. As has been discussed, the more massive star evolves fastest, and expands to become a red giant. A common envelope phase then begins and the orbit shrinks dramatically.

At the end of the CE phase, in order for a CV to form, the emerging stars must be a white dwarf and a low mass main sequence star, with a mass smaller than or similar to that of the white dwarf (Warner, 1995). The orbit continues to shrink due to magnetic braking, eventually driving the secondary star to fill its Roche lobe. The system then begins its new life as a CV.

Period distribution

The orbital period of a CV is often one of its most precisely known parameters (Warner, 1995), and immediately reveals something about the scale of the binary (via Kepler's third law). The orbital period distribution of CVs, Fig. 1.8, shows several interesting features (Gänsicke et al., 2009; Knigge, Baraffe & Patterson, 2011):

- There is an apparent *period minimum* at $\sim$1.3 hours, below which only a special subclass, the AM CVn stars (discussed later), are found;
- a *period gap* where there is a relative deficiency in the number of CVs, at about 2.2 to 2.8 hours;
- and a long period cut-off at about 12 hours.

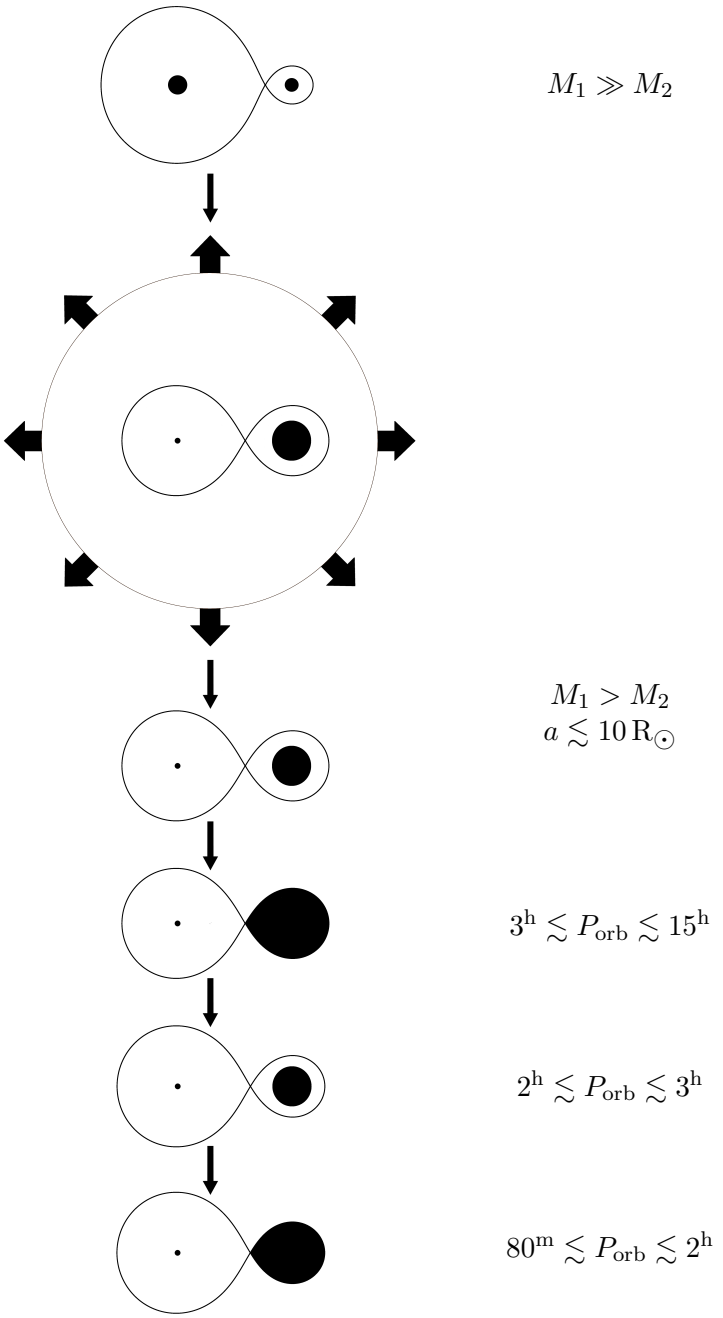

Figure 1.7: The formation and evolution of CVs. Shown are the Roche lobes and the two stellar components. A white dwarf is represented by a black dot, main sequence stars are indicated by larger filled circles. Solid black Roche lobes indicate that the star is Roche lobe filling. Starting from a detached binary with one massive and one considerably lighter star, the more massive star evolves quicker, becoming a red giant and initiating a CE phase. Once the outer layers are expelled, angular momentum loss will eventually bring the secondary into Roche lobe contact, forming a CV. As the system continues to lose angular momentum it will evolve through the period gap towards the CV period minimum. Based on fig. 14 from Iben (1991).

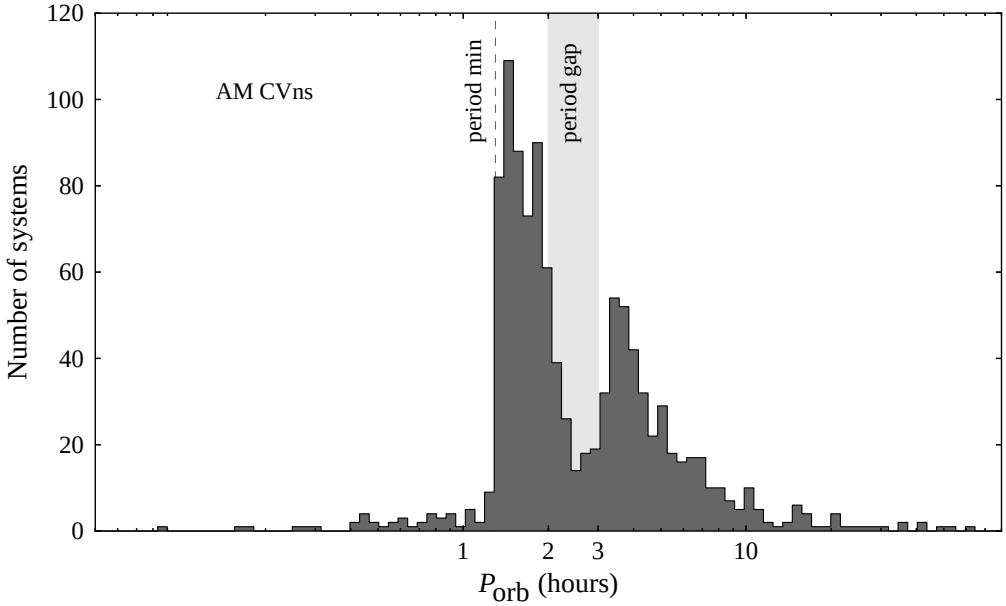

Figure 1.8: The distribution in orbital period of known CVs, data from Ritter & Kolb (2003). The normal period minimum at ∼80 minutes and the period gap at about 2–3 hours are labelled. The objects with periods below this minimum are the AM CVn binaries. The long-period cut-off at about 12 hours is also visible.

This distribution can be understood as the signature of CV evolution.

Stable mass transfer generally requires that the secondary have a lower mass than the white dwarf. Since white dwarfs have a maximum mass limit (the Chandrasekhar mass, $1.4\,\mathrm{M}_\odot$), the secondary must also have a mass below this limit. Since the size of a binary increases with orbital period, and filling a larger Roche lobe requires a more massive star, the mass of the secondary must increase with orbital period (Hellier, 2001). The upper mass limit thus imposes an upper period limit of about 13 hours (King, 1988). The systems detected above this limit are explained as having secondaries that are evolving towards being a giant, these will be much larger for a given mass than for normal red dwarfs (Hellier, 2001).

It has been noted that the mass-transfer rates below the period gap are characteristic of gravitational radiation, whereas the rates observed for systems above the gap are characteristic of accretion driven by magnetic braking (e.g. Knigge, Baraffe & Patterson, 2011). This leads to the suggestion that the period gap is caused by the switching off of magnetic braking at ∼3 hours. The preceding mass loss has driven the secondary out of equilibrium and once magnetic braking shuts off, the secondary contracts to its correct radius, turning off mass transfer, making the system much fainter, and hence much more difficult to detect. Gravitational wave radiation reduces the orbital period of the system, which eventually resumes

contact at about 2 hours; mass transfer resumes and evolution continues at the lower rate driven by GW radiation (Faulkner, 1971). Exceptions include systems which begin mass transfer in the gap and have thus not been driven out of equilibrium, and magnetic systems in which accretion is affected by the primary's strong magnetic field. Possible reasons for the turn-off of magnetic braking are discussed by King (1988).

As the decreasing orbital period reaches ∼80 minutes (Gänsicke et al., 2009) the mass of the red dwarf donor becomes too low to sustain hydrogen burning, and it is driven out of thermal equilibrium, becoming partially degenerate. It is no longer supported by the pressure of the gas, but instead is supported by the quantum-mechanical requirement that electrons not occupy the same state. The secondary no longer shrinks in response to mass loss (Rappaport, Joss & Webbink, 1982). As it continues to lose mass the orbital period increases, giving rise to the period minimum. The binary then continues to evolve towards longer periods with decreasing mass transfer rates. The period minimum for normal hydrogen-rich CVs is predicted theoretically to occur at ∼65–70 minutes (Rappaport, Joss & Webbink, 1982; Kolb & Baraffe, 1999), and is observed at ∼80 minutes (Gänsicke et al., 2009).

1.2.5 Spectroscopic features

The observed spectra of CVs are a combination of the spectra of the accretor, donor and accretion flow. This gives rise to distinctive spectra.

The white dwarf

The spectrum of a white dwarf is close to that of a blackbody of the same temperature. The thin atmosphere gives rise to broad absorption lines, usually of hydrogen or helium. For the accreting white dwarfs in CVs the optical region of the electromagnetic spectrum will feature a blue continuum, dominated by Balmer absorption lines.

The donor star

In most CVs the cool red dwarf donor will only contribute significant flux in the red part of the optical spectrum. The spectra of cool main sequence stars are often dominated by strong molecular absorption bands.

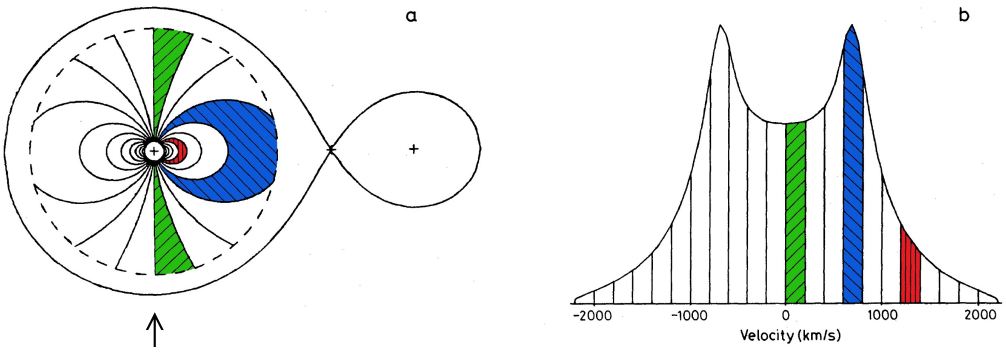

Figure 1.9: Formation of a double peaked emission line from an accretion disc. (a) An accretion disc in a binary of mass ratio $q = 0.15$ viewed from above. Loci of constant radial velocity form a dipole pattern on the disc surface. (The radial extent of the disc is shown by the dashed line, the solid line represents the stars' Roche lobes). (b) The emission line profile produced by the disc when viewed from below (as indicated by the arrow). Emission in the shaded velocity bins originates from the corresponding areas of the disc. From Horne & Marsh (1986)

The accretion disc

The continuum light from accretion discs is not well matched by a single blackbody. Unlike the surfaces of stars, an accretion disc has a strong temperature gradient across its surface, with the outer edge being relatively cool, and the inner regions, deep in the potential well of the accretor, being much hotter. Accretion discs are usually modelled as a series of blackbodies emitting from a series of annuli of the disc. This leads to a relatively flat continuum in the optical part of the spectrum (Hellier, 2001).

Optically thin regions of accretion discs also produce line emission. Doppler shifting of the light originating in the rotating disc leads to significant broadening of these emission lines when viewed at higher inclinations. The Keplerian rotation ensures that the inner regions of the disc will have higher orbital velocities than the outer parts. This leads to a dipole pattern of radial velocity across the accretion disc surface (Horne & Marsh, 1986), see Fig. 1.9a, causing the characteristic double peaked line profile shown in Fig. 1.9b.

An example of a three component model of the optical spectrum of a CV is shown in Fig. 1.10. In this system the absorption lines from the white dwarf are clearly visible in the spectrum. The combined contributions from the white dwarf, the disc and the donor provide a good match to the data.

We do not always see line emission from CVs, in some cases, particularly during dwarf nova outbursts, we instead see absorption lines from the optically thick disc. Again, these are broadened by the rotation of the disc. The more luminous

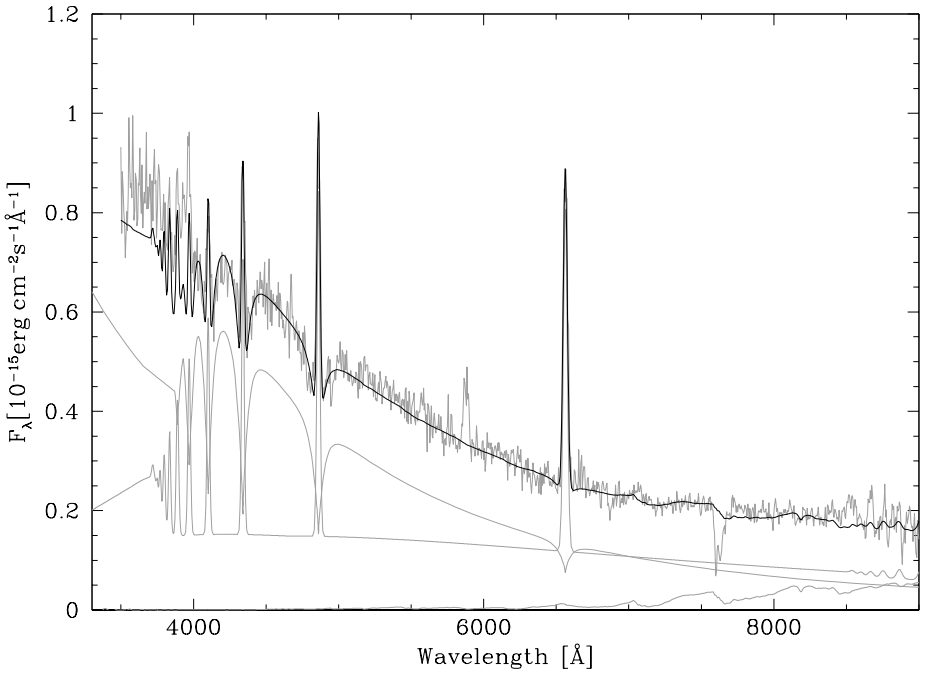

Figure 1.10: Three component model of the optical spectrum of the dwarf nova HS 2219+1824. The observed spectrum is the upper grey line, the grey lines below this are the model spectra of the white dwarf, the disc and the donor. The sum of the three components is plotted as a black line, providing a good fit to most of the continuum and the Balmer lines. From Rodríguez-Gil et al. (2005).

outbursting disc is usually sufficiently bright as to obscure the features displayed by the white dwarf and the donor.

1.3 AM Canum Venaticorum binaries

Whilst the number of CVs drops dramatically at the period minimum, it is not an absolute cut-off. There are several objects with periods less than ∼1 hour, most of these belong to the AM Canum Venaticorum (AM CVn) class: ultra-short period binaries consisting of a white dwarf accreting helium-rich material from a degenerate or semidegenerate donor. Their hydrogen deficient secondaries are much smaller for the same mass as compared to hydrogen rich stars, and therefore fill their Roche lobes at much smaller separations, giving orbital periods ranging from 5 (Israel et al., 2002) to 65 minutes (Ruiz et al., 2001). The AM CVn binaries appear as faint blue objects, and show variability on short-period timescales.

1.3.1 Properties

The gravitational wave emission thought to drive the evolution of the AM CVn binaries leads to a strong dependence of the mass accretion rate, and hence their observed properties, on the orbital period. The observational characteristics of an AM CVn binary are commonly separated into four distinct categories, based on a combination of empirical evidence and theoretical models.

1. Those with the shortest orbital periods (below $\sim$10 minutes) are expected to undergo direct impact accretion, with no accretion disc forming (Marsh & Steeghs, 2002; Ramsay et al., 2002; Roelofs et al., 2010).

2. At short orbital periods ($\sim$10 to $\sim$20 min), the mass transfer rate is sufficiently high to keep the disc in a stable hot, bright state (e.g. HP Lib, O'Donoghue et al. 1994; SDSS J1908+3940, Fontaine et al. 2011), similar to novalike CVs.

3. At intermediate orbital periods, the discs undergo quasi-periodic outbursts, cycling between a faint, quiescent state with a cool disc, observationally characterised by strong emission lines, and a hot, bright state, characterised by absorption lines from the optically thick disc (e.g. CR Boo, Wood et al. 1987; SDSS J0129+3842, Shears et al. 2012; PTF1 J0943+1029, Levitan et al. 2013).

4. At the longest orbital periods ($\gtrsim$45 min), corresponding to the lowest mass transfer rates, the disc is thought to be in a stable faint state, and the spectra of these systems are hence dominated by strong emission lines (e.g. GP Com, Nather, Robinson & Stover 1981; SDSS J1552+3201, Roelofs et al. 2007c).

Espaillat et al. (2005) argue that the lack of a detectable superhump period in ES Cet ($P_{\rm orb}$ =10.3 min) indicates that it is a direct impact accretion system, however, spectroscopic observations show disc-like emission (Steeghs et al., in preparation). There is also evidence to suggest HM Cnc ($P_{\rm orb}$ =5.4 min; Israel et al. 2002) is a direct impact system, also containing a small disc or ring around the white dwarf that produces double-peaked emission (Roelofs et al., 2010).

Spectra of AM CVn binaries

For the intermediate period systems, such as V803 Cen ($P_{\rm orb}$ = 26.6 min; Roelofs et al. 2007b), the spectra are seen to change from high states with absorption lines to low states with emission lines, the transition being caused by the same thermal instability that causes dwarf nova eruptions (Meyer & Meyer-Hofmeister, 1981;

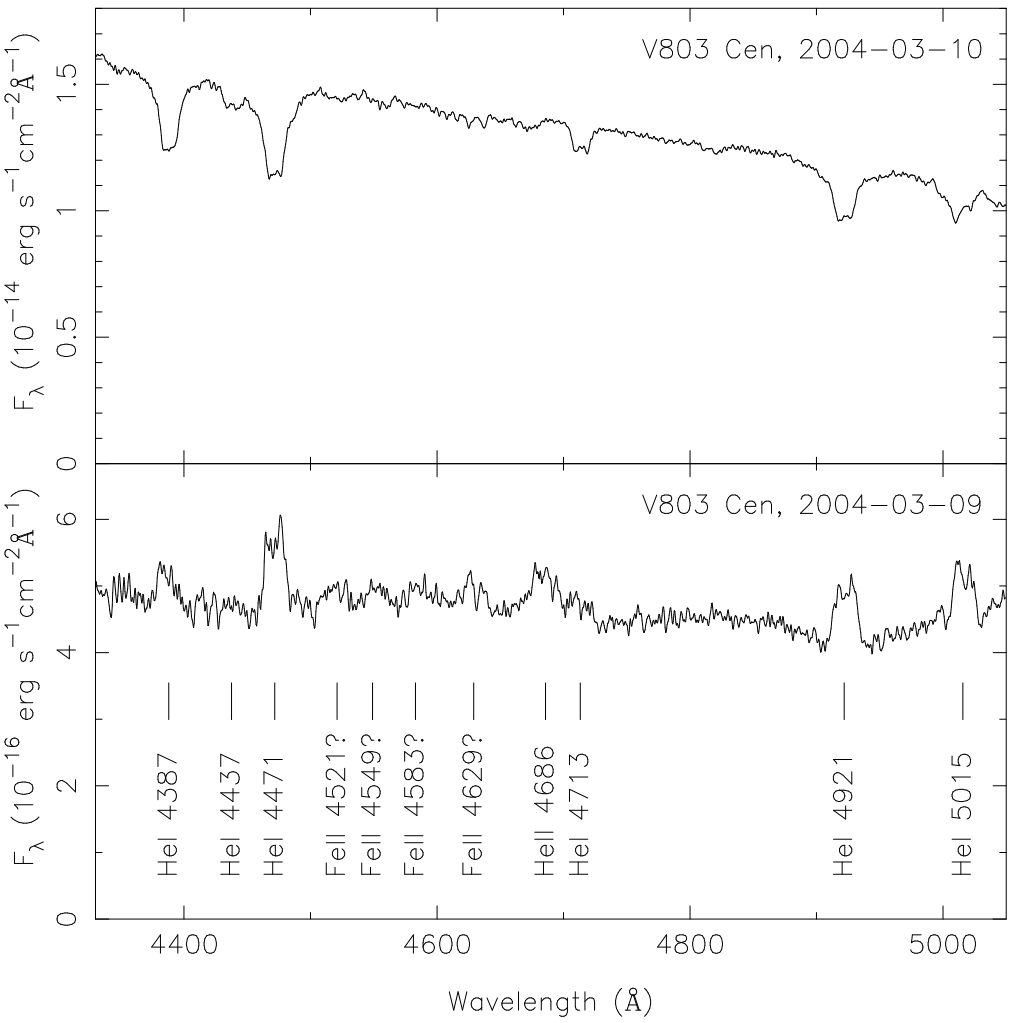

Figure 1.11: Spectra of V803 Cen taken one day apart with the New Technology Telescope. The upper panel shows the bright, outbursting state with absorption lines, the lower panel shows the quiescent state with emission lines. Note the change of vertical scale between the two panels. From Roelofs et al. (2007b).

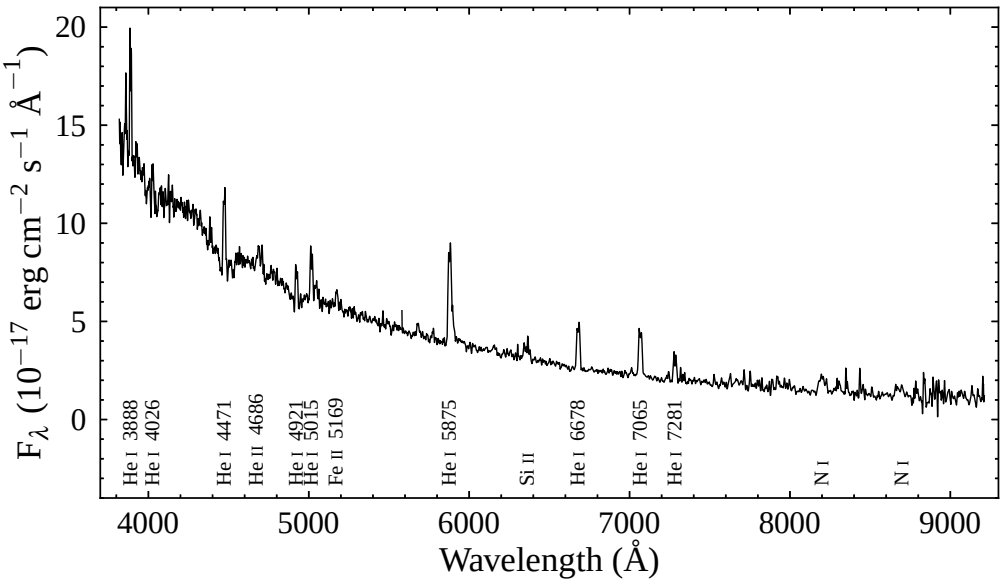

Figure 1.12: Sloan Digital Sky Survey spectrum of SDSS J1240−0159 in a quiescent state. The strongest emission features have been labelled. In contrast to ordinary CVs (e.g. Fig. 1.10), AM CVn spectra are dominated by helium features.

Tsugawa & Osaki, 1997; Kotko et al., 2012; Ramsay et al., 2012), with the exception that the disc is helium dominated not hydrogen dominated.

Spectra of V803 Cen in both outburst and quiescent states are shown in Fig. 1.11; the double peaked profile, characteristic of an accretion disc, is evident. The high state spectrum is similar to that of the shorter period absorption line systems, such as AM CVn itself, the low state spectrum is like to that of the long period systems, such as SDSS J0902+3819 (Rau et al., 2010).

The quiescent spectrum of the AM CVn binary SDSS J1240−0159 ($P_{\rm orb}$ = 37.4 min; Roelofs et al. 2005) is shown in Fig. 1.12. The blue continuum and strong helium emission lines are characteristic of the quiescent state in AM CVn binaries. The quiescent spectrum of SDSS J1240−0159 shows clear absorption wings around the He I 4471 and 4921 Å emission lines, thought to be due to the accreting white dwarf. Bildsten et al. (2006) show that the optical continuum is dominated by the accreting white dwarf in long period systems, however the absorption lines become weaker as the accretor cools, and so have only been seen in a small number of systems.

1.3.2 Formation and evolution

The AM CVn binaries are the result of several possible fine-tuned evolutionary pathways. Three possible channels have been identified for the formation of AM

CVn stars, each defined by the type of donor, two of which require the binary to undergo a second CE phase. The progenitor in all 3 channels is a binary consisting of two main sequence stars of mass low enough to produce white dwarf cores. The formation of AM CVns is summarised by Fig. 1.13.

The white dwarf channel

If the giant star develops a degenerate core during the second CE event, the result is a system with two degenerate stars (Paczyński, 1967; Faulkner, Flannery & Warner, 1972; Nather, Robinson & Stover, 1981). This is called the white dwarf channel. The double white dwarf binary evolves to very short periods, starting mass-transfer at periods of a few minutes. In order to support stable mass-transfer the donor white dwarf must be low mass, otherwise the stars will likely merge, possibly resulting in a Type Ia supernova (Nelemans et al., 2001; Marsh, Nelemans & Steeghs, 2004).

The helium star channel

More massive secondaries exit the second CE event as a star with a non-degenerate helium core, these systems form the helium star channel (Savonije, de Kool & van den Heuvel, 1986; Iben & Tutukov, 1987, 1991). In this channel the donor begins helium burning after the CE event. Helium burning may continue after mass transfer begins, which can lead to composition changes in the secondary. These systems evolve through a period minimum of about 10 minutes, when the helium star becomes semidegenerate. If the helium is exhausted before Roche lobe overflow occurs the helium star evolves into a white dwarf and the system belongs to the white dwarf channel.

The evolved CV channel

If the donor fills its Roche lobe when the hydrogen abundance in its core is low, it may evolve as a normal hydrogen CV, avoiding a second CE event. If the hydrogen abundance becomes sufficiently low, it may eventually evolve into a long-period AM CVn (Thorstensen et al., 2002; Podsiadlowski, Han & Rappaport, 2003). This is known as the hydrogen-star, or evolved CV channel. This formation channel has generally been considered to be unimportant in comparison to the double white dwarf and helium star channels. Podsiadlowski, Han & Rappaport (2003), however, argue that the evolved CV channel could contribute a significant fraction of the total AM CVn binary population.

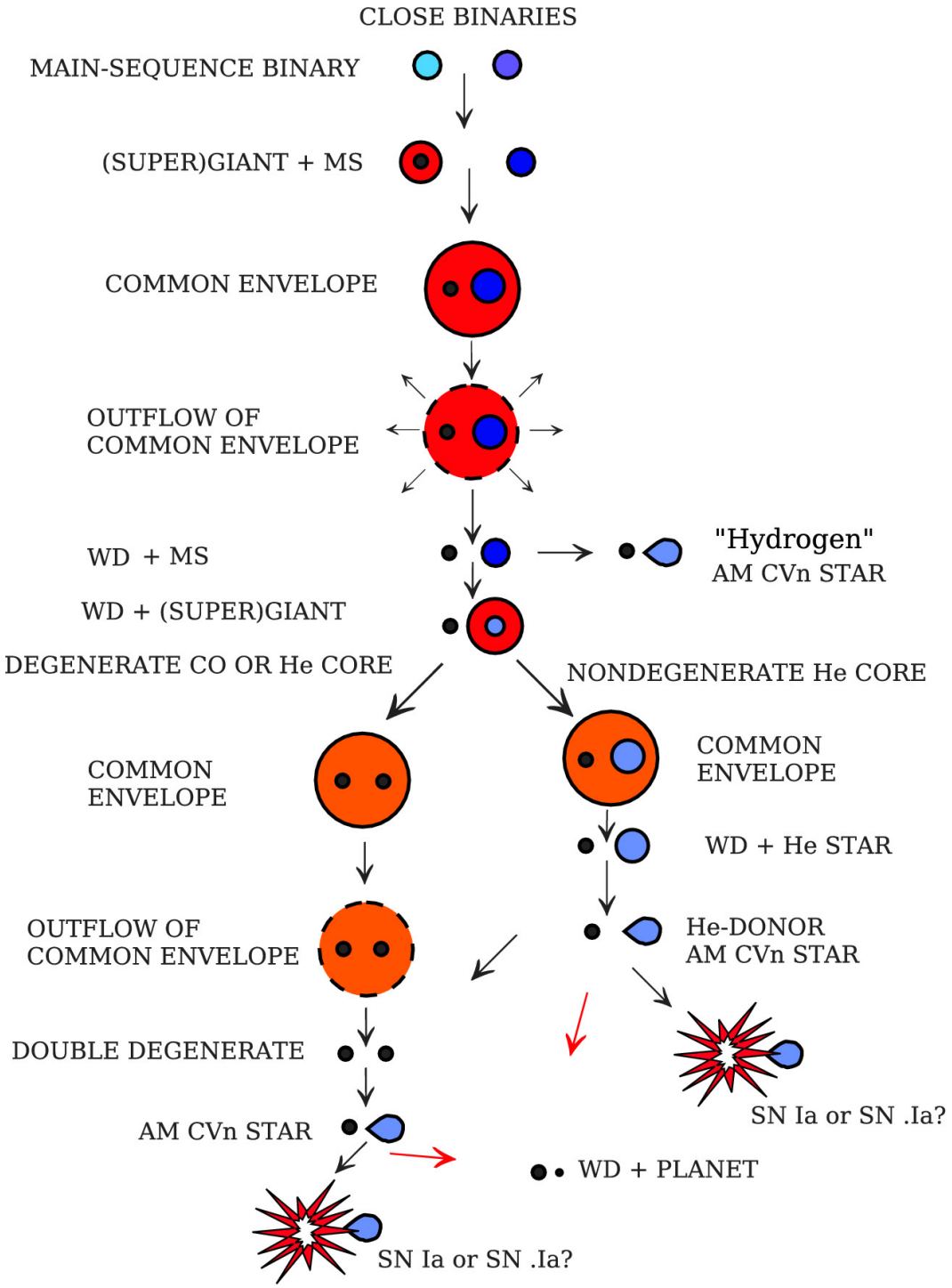

Figure 1.13: The basic steps of AM CVn formation and evolution for each of the three channels. From Solheim (2010), produced by L. Yungelson.

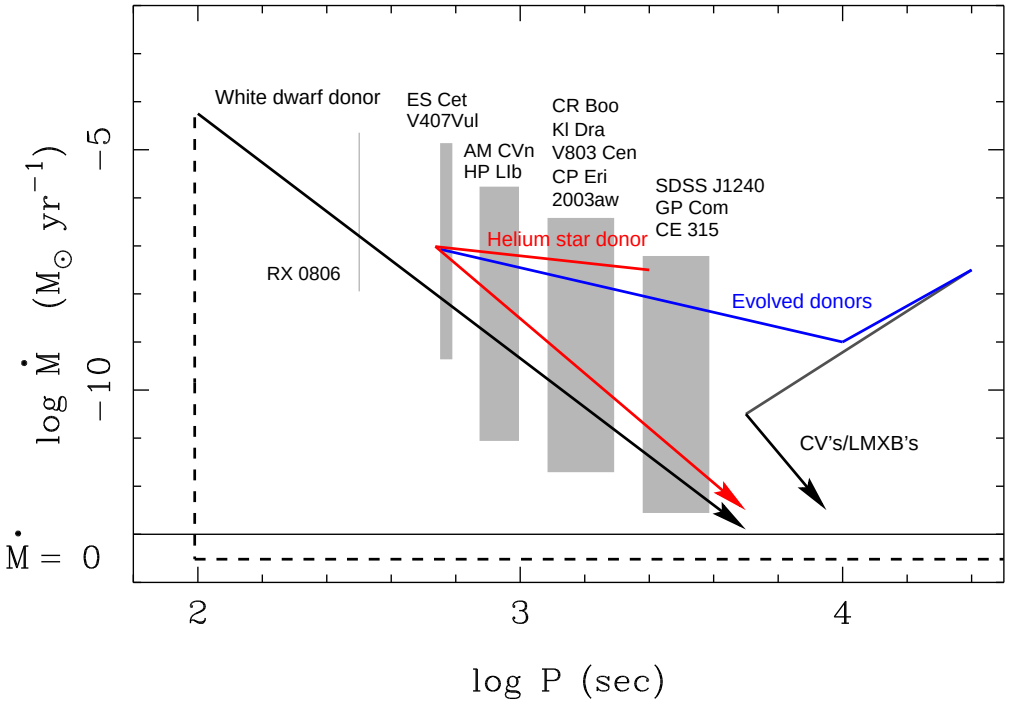

Figure 1.14: Evolutionary pathways for AM CVn stars in the period–$\dot{M}$ plane. The three formation channels are shown, along with the evolutionary path for normal CVs. Example known systems are shown at their orbital periods. From Nelemans (2005).

AM CVn evolution

Of critical importance to the formation is the evolution to shorter periods, which is thought to be governed by angular momentum loss due to GW radiation (Paczyński, 1967). This drives the system after the end of the second CE event, reducing the separation of the stars and shrinking their Roche lobe radii. Once the separation decreases to the point where the secondary fills its Roche lobe, mass transfer begins; the system passes through a period minimum, and then evolves towards longer orbital periods due to mass loss driven by GW radiation. This is depicted for each formation channel in Fig. 1.14.

As equation (1.2) shows, the rate of angular momentum loss thought to drive the evolution of AM CVn binaries is a strong function of the orbital separation. This means that as the period (or separation) increases after the evolution through the period minimum, the rate of the change in period (separation) decreases steeply. Thus the short period phase of AM CVn evolution is a small fraction of the lifetime of an AM CVn binary. As the system continues to evolve towards longer periods the mass-transfer rate, which depends upon the angular momentum loss rate (Paczyński, 1967), also decreases strongly, giving rise to the various observational categories

discussed in section 1.3.1.

Recently, a number of possible AM CVn progenitor systems have been identified via a survey searching for extremely low mass (ELM) white dwarfs (Brown et al., 2010, 2012). Several of the detached white dwarf binaries discovered by this survey have sufficiently low mass ratios that they are likely to survive the onset of mass transfer and form stable AM CVn systems, whilst the fates of other systems are less clear, with both mergers and AM CVns as possible scenarios (Brown et al., 2011). Brown et al. (2011) find that these ELM white dwarf binaries contribute at least 2 per cent to the total AM CVn population. Kilic et al. (2014) report observations of the ELM white dwarf binary SDSS J1741+6526 that indicate it has a mass ratio of $\sim$0.1, and will form an AM CVn system in the next $\sim$160 Myr.

AM CVn binaries may contribute to the Type Ia supernova population, the accreting white dwarf undergoing thermonuclear disruption if the mass approaches the Chandrasekhar mass via accretion (Solheim & Yungelson, 2005; Shen & Bildsten, 2009, 2014). They are also possible progenitors of rare sub-luminous SN Ia-like events ('SN.Ia'; Bildsten et al. 2007). The fate of most AM CVn systems, however, is expected to be much less dramatic, continuing to evolve to longer orbital periods with ever decreasing mass-transfer rates.

1.3.3 Population studies

The fact that AM CVn stars are the result of a fine-tuned evolution makes them especially interesting for the study of binary stars. The CE phase is difficult to model, due to its hydrodynamic nature, but is key to the formation of all close binaries (Iben, 1991). That many AM CVns must have undergone two such phases during their evolution makes them very useful for calibrating models of binary star evolution. A further property of the AM CVn stars that is of great interest, is their gravitational wave radiation. They will be among the strongest objects to be detected by the proposed *Evolved Laser Interferometer Space Antenna* (*eLISA*), which, according to Nelemans, Yungelson & Portegies Zwart (2004), will detect a large number of them. That many of these will also be detectable optically will allow independent measurements of the position and orbital period, leading to a better determination of other parameters that can be derived from the GW signal. The brightest short period AM CVns will serve as calibrators for the *eLISA* experiment (e.g. Amaro-Seoane et al., 2013; Nelemans, 2013). Also of great interest is the possibility that AM CVn stars could explode as Type Ia supernovae.

Population synthesis

A key property for these possibilities, and increasing our understanding of binary evolution, is the space density of AM CVn objects. In attempts to determine the numbers of AM CVn stars in the galaxy Nelemans et al. (2001) have carried out population synthesis based on the two main formation mechanisms.

They find that for the white dwarf channel no accretion disc forms at the onset of mass transfer, and that the final population from this channel depends heavily upon the effectiveness of the tidal coupling between the accretor and the orbital motion. Stable mass transfer requires angular momentum to be returned to the binary orbit; in the alternative case the spin of the accretor exceeds that of the binary and increases the GW radiation, decreasing the separation of the orbit. This could then lead to a runaway that results in the white dwarfs merging. Accretion discs easily fulfil the tidal coupling requirement, but the situation is less clear for the case of direct impact accretion. Efficient tidal coupling is therefore critical to the formation of AM CVns via this channel (Nelemans et al., 2001; Marsh, Nelemans & Steeghs, 2004).

In the helium star channel, formation of AM CVn systems can be prevented by thermonuclear runaway of accreted helium before period minimum. Accretion of material onto a carbon-oxygen white dwarf may trigger a detonation in the layer of accumulated matter. Further, this can cause detonation of the CO dwarf core (edge-lit detonation), which disrupts the system (Nelemans et al., 2001).

Nelemans et al. (2001) adopt two limiting cases for each formation channel: an efficient case, in which the factors discussed above favour formation of AM CVns; and an inefficient case, in which AM CVn formation is strongly suppressed. With slightly improved models (Roelofs, Nelemans & Groot, 2007) the population synthesis leads to local space densities of $6.1 \times 10^{-6}\,\mathrm{pc}^{-3}$ and $2.7 \times 10^{-5}\,\mathrm{pc}^{-3}$ respectively for the inefficient and efficient cases.

Observational calibration

Roelofs, Nelemans & Groot (2007) use the six emission line AM CVns discovered in a homogeneous manner in the Sloan Digital Sky Survey (SDSS) spectroscopic database (discussed below) to calibrate the model populations. Parametrizing the colours and absolute magnitudes of the emission line systems with their orbital periods and measuring the spectroscopic completeness as a function of colour, allows determination of the spectroscopic completeness of the SDSS as a function of orbital period. If an assumed orbital period distribution for AM CVn stars (based on

population synthesis studies) is convolved with this completeness, the result is the total number of emission-line AM CVn stars in the SDSS. Roelofs, Nelemans & Groot (2007) determine that there should be between 50 and 70 AM CVn stars in SDSS photometry based on the models of Nelemans et al. (2001) and Nelemans, Yungelson & Portegies Zwart (2004).

When calibrated with observations all the models give a local space density of $1\text{–}3 \times 10^{-6}\,\mathrm{pc}^{-3}$, which is lower than was expected. It is suggested that the white dwarf channel must be strongly suppressed, and that if the tidal coupling required to stabilise mass transfer between the two white dwarfs has a significant effect, the helium star channel must also be severely suppressed.

1.4 Discovering AM CVn binaries

The first AM CVn binaries were discovered serendipitously in a variety of different ways (e.g. Burbidge & Strittmatter, 1971; Israel et al., 1999). This made it impossible to study their population and to derive fundamental quantities required for calibration of predictions from binary evolution theory. In the past ten years dedicated surveys have tripled the number of known AM CVn binaries (Anderson et al., 2005, 2008; Roelofs et al., 2005, 2009; Rau et al., 2010; Levitan et al., 2011, 2013; Carter et al., 2013). These homogeneous samples have allowed the first detailed studies of the population, and estimation of the AM CVn space density.

1.4.1 The Sloan Digital Sky Survey

The Sloan Digital Sky Survey (SDSS) was originally designed to obtain CCD imaging in five broad band filters of one quarter of the sky, along with spectroscopy of the million brightest galaxies and 100,000 brightest quasars (York et al., 2000). The survey uses a 2.5 m telescope located at Apache Point Observatory, New Mexico.

The imaging camera contains 30 CCDs arranged in a grid; each of the five rows observing the sky through a different filter: u, g, r, i, z. The spectroscopy targets are selected from the imaging database and observed by a pair of fiber-fed double spectrographs (Abazajian et al., 2009). The telescope can record 640 spectra at a time, the fibers are held by an aluminium plate, each specially drilled for the selected galaxies in that region of the sky. Spare fibers are allocated to rare or peculiar targets – the serendipitous objects.

Abazajian et al. (2009) report that with the Seventh Data Release, the original goals of the SDSS were complete; the photometric database containing five-band

photometry for 357 million objects, and the spectroscopic database containing over 1.6 million spectra.

1.4.2 AM CVns in the SDSS

Many of the currently known AM CVn binaries have been discovered via systematic searches in the SDSS. Six of these were found in the SDSS spectroscopic database, identified from their distinctive helium emission dominated spectra (Anderson et al., 2005, 2008; Roelofs et al., 2005), one more was found in the course of follow-up of SDSS supernova candidates (Anderson et al., 2008), and a further 5 had been discovered by 2010, via a spectroscopic survey of colour-selected objects from the SDSS, again identified by their helium emission line spectra (Roelofs et al., 2009; Rau et al., 2010).

As has been mentioned, the AM CVn stars are all blue objects, and those identified or discovered in the SDSS occupy a small region in colour space (Anderson et al., 2008). The six helium emission line objects found in the SDSS Data Release 6 (DR6) spectroscopic database were largely serendipitous; the spectroscopic follow-up to the imaging is targeted mainly at finding quasars and galaxies. In order to obtain better estimates of the space density it is necessary to estimate the completeness of the SDSS spectroscopic follow-up. Anderson et al. (2008) estimate completeness between 10–20 per cent and 70 per cent, depending upon the magnitude, and thus adopted a lower limit of 24 per cent to the SDSS spectroscopic completeness in the colour box around the known AM CVns. These estimates are similar to the more detailed study by Roelofs, Nelemans & Groot (2007), who suggest that further follow-up spectroscopy of photometric candidates in the SDSS will further refine their space density estimate.

1.4.3 A search for new AM CVns in the SDSS

The first new AM CVn object discovered through such an independent survey was SDSS J080449.49+161624.8 (Roelofs et al., 2009). The sample for this survey was selected from the SDSS photometric database, guided by the colours of the known AM CVns. Roelofs et al. (2009) give their selection criteria:

1. Object is a point source.
2. Object is not saturated in any filter.
3. $g < 20.5$.
4. $u - g < \min[0.14, 1.35(g - r) + 0.32] - \sigma_{u-g}$

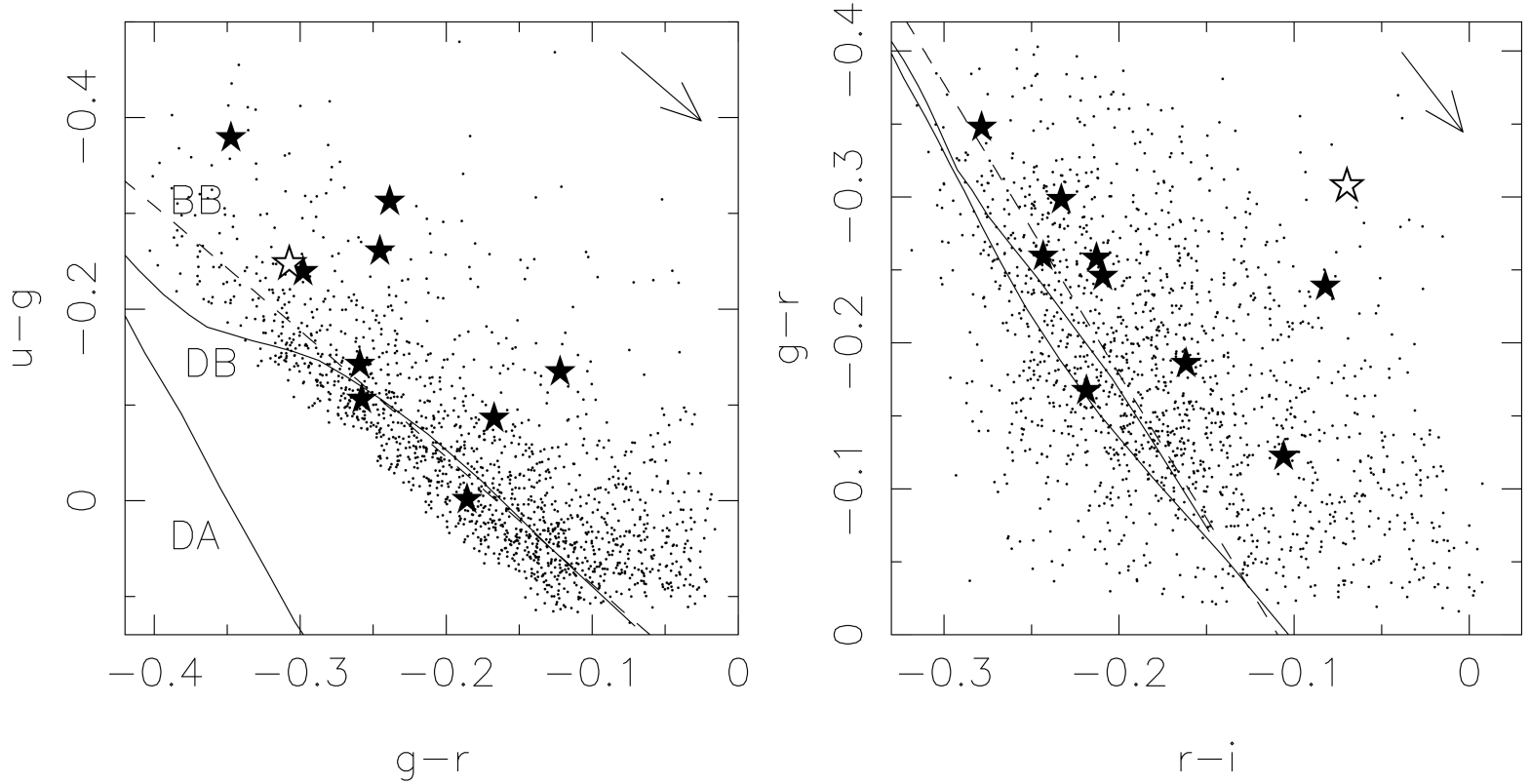

Figure 1.15: Colours (dereddened) of the known AM CVn stars in the SDSS DR6, together with the colour-selected sample. The open star symbol designates the first AM CVn object discovered in this survey, SDSS J0804+1616. The blackbody (BB) cooling track and model cooling tracks for hydrogen (DA) and helium (DB) atmosphere white dwarfs are shown. The arrow shows a reddening vector. From Roelofs et al. (2009).

5. $-0.42 + \sigma_{g-r} < g - r < 0.02 - \sigma_{g-r}$

6. $-0.33 + \sigma_{r-i} < r - i < 0.03 - \sigma_{r-i}$

where

$$\sigma_{u-g} = \sqrt{{\sigma_u}^2 + {\sigma_g}^2 + {\sigma_{E(u-g)}}^2}, \tag{1.5}$$

and similarly for the other colours. The assumed uncertainty in the reddening is

$${\sigma_{E(u-g)}}^2 = 0.5E(u-g), \tag{1.6}$$

and the uncertainties $\sigma_{u,g,r,i}$ are the photometric errors on the SDSS magnitudes u, g, r, i.

The resulting sample, based on the SDSS DR6, is shown in Fig. 1.15. The sample has been cut off parallel to the blackbody cooling track in order to minimise contamination from DA and DB white dwarfs. Whilst this risks neglecting several AM CVn stars, the spectroscopic completeness of the SDSS increases towards this cut-off, and as such it is unlikely that a large fraction of the AM CVn population fall outside the chosen sample (Roelofs et al., 2009). After removal of known sources and mistakes of the SDSS photometric data reduction pipeline, the final sample contained 1523 candidates. Roelofs et al. (2009) estimated that this sample should contain about 40 new AM CVn stars based on an assumed completeness of 90 per cent. Rau et al. (2010) reported discovery of a further four AM CVn objects discovered through this survey, lowering the expected total to 13 new AM CVns from the ∼1500 candidates; already suggesting a lower space density than previously predicted.

1.4.4 Using outbursts to find AM CVns

An alternative approach to the colour-selection method is to search for outbursts from AM CVn binaries. Both the Catalina Real-Time Transient Survey (CRTS; Drake et al. 2009) and the Palomar Transient Factory (PTF; Law et al., 2009) provide repeat observations of wide areas of the sky that are used to produce a large set of light curves. These light curves have been used to search for outbursts from AM CVn binaries and CVs, with targets that show outbursts identified by follow-up spectroscopy.

This method has lead to the discovery of nine new AM CVn systems over the past four years (Levitan et al., 2011, 2013, 2014; Woudt, Warner & Motsoaledi, 2013). As I have discussed, the outbursting AM CVn systems are generally found in a narrow period range, and we expect them to be significantly less numerous

than the longer period systems. This method can probe deeper as the objects need only be well detected during outburst (somewhat overcoming the problem of small numbers), but this does make follow-up observations much more challenging.

1.5 Thesis outline

In this chapter I have introduced cataclysmic variables and the related ultracompact systems known as the AM CVn binaries. I have discussed the evolution of close binaries, and how CVs and AM CVns relate to the larger unsolved problems in binary star physics. I have also discussed the observed properties of these systems, and the causes of their behaviour. I also introduced a spectroscopic survey designed to uncover new AM CVn systems in the photometric database of the SDSS.

This thesis focuses on the results of this survey, and using the findings to improve our understanding of AM CVn binaries. The next chapter will discuss the tools and techniques that have been used to collect and analyse the data required to achieve this goal. Chapter 3 presents a discussion of the survey as a whole, and details recent discoveries and results. Two interesting objects discovered as part of this survey are studied in detail in chapters 4 and 5. Finally, chapters 6 and 7 discuss ways to improve the efficiency of the AM CVn survey, and apply some of these techniques to new SDSS data.

Chapter Two

Methods and Techniques

2.1 Introduction

In this chapter I describe the processes involved in the collection, reduction and analysis of astronomical data used throughout this thesis. The first part of this chapter deals with making observations, and extracting data from the raw images. I then discuss the various techniques required for analysing the resulting data, and finish with a discussion of a tool used extensively in this thesis when considering large numbers of objects.

2.2 Observations and reduction

2.2.1 Detectors

Observational astronomy requires capturing the light from distant sources so that it can be analysed. In modern astronomy the charge-coupled device (CCD) has replaced the photographic plate, thanks to its much greater efficiency (Bradt, 2004). CCDs are sensitive over a large wavelength range, and are much better at recording incident photons than photographic plates. Unlike photographic film, which drops in sensitivity as the exposure length increases, CCDs have a highly linear response, and a large dynamic range. This allows CCDs to detect very faint objects at the same time as much brighter objects, and the signal produced will remain proportional to the number of photons hitting the CCD. With CCDs we can obtain much more precise, consistent measurements of astronomical objects than is possible with photographic film. Whilst some alternative detectors are used at very high or low energies, optical astronomy is now dominated by CCDs.

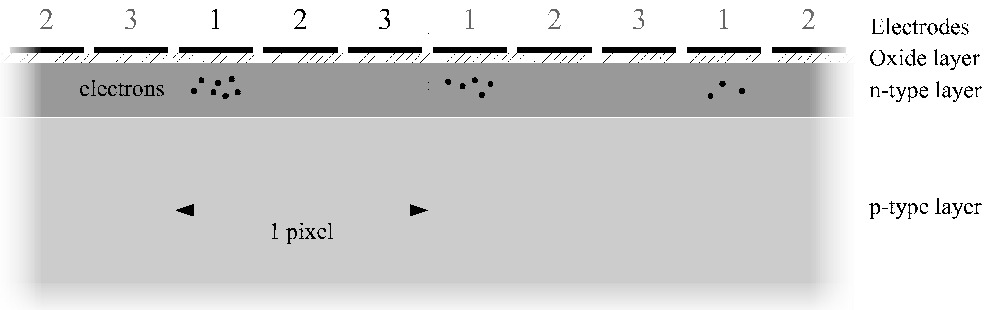

Figure 2.1: Cross-section of a CCD pixel. Each pixel has three electrodes above the layers of doped silicon to allow the electric fields within the pixel to be altered. Photons hitting the pixel during integration create photoelectrons that collect in the n-type layer in the area with lowest potential energy for that pixel – the region under electrode '1'. Based on Kitchin (1998), Howell (2000) and Bradt (2004)

A CCD consists of an array of metal-oxide-semiconductor capacitors, known as pixels. These generally consist of a thin layer of n-type doped silicon above a thicker layer of p-type doped silicon. On top of this there will be a very thin insulating layer and a set of electrodes that allow voltages to be applied to the pixel (Kitchin, 1998). The n-type silicon is dominated by free electron carriers, whereas the p-type silicon can be considered to be dominated by positive carriers known as 'holes'. When the two types are placed in contact, the free charges neutralise, leaving the n-type material with a net positive charge, and a region of the p-type material below it with net negative charge. These regions together are known as the depleted region, because they are depleted of free charges. Due to the electric field generated by the charged p and n-type regions, free electrons created in the depleted region move upwards into the n-type material.

During integration, when a photon hits a pixel on the CCD, it will generally be absorbed in the depleted region, ejecting an electron via the photoelectric effect. This electron is kept trapped within the pixel the photon struck by the application of different voltages to the pixel's electrodes. In this manner electrons collect in potential wells across the two dimensional array, in correspondence to the locations struck by photons (Bradt, 2004).

The CCD is then read out by adjusting the voltages applied to each pixel in order to shift the electrons across the array. In a three-phase CCD each pixel has three electrodes, as depicted in Fig. 2.1. The voltage applied to electrode '2' is increased to allow the electrons to migrate to the right, the voltage applied to electrode '1' is then decreased gradually, causing the electrons to move to the right and become trapped in the potential well under electrode '2'. In this state the voltage

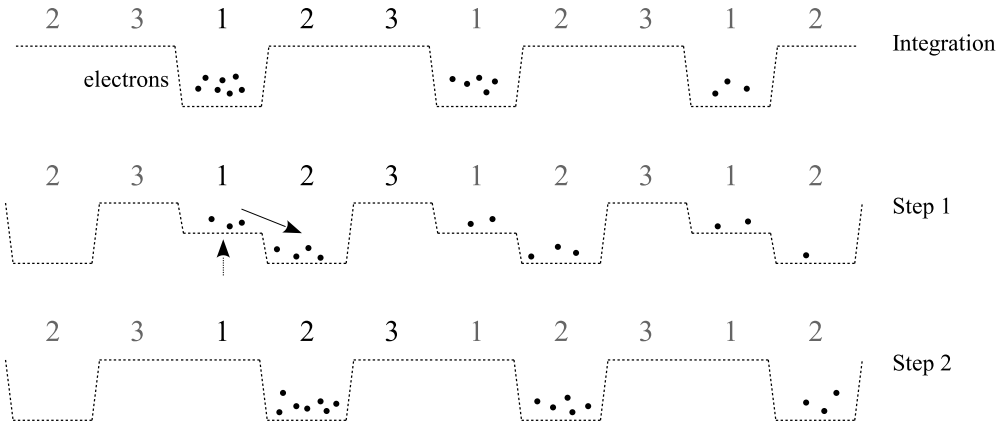

Figure 2.2: The readout process for a three-phase CCD. During integration the highest positive voltage, and lowest potential energy region for electrons is under electrode '1'. Readout commences by lowering the potential energy beneath electrode '2', then gradually raising the potential beneath electrode '1'. This causes the electrons to move to the new region of lowest potential energy, the area under electrode '2'. In 'step 2' the electrons have now moved one electrode to the right. Cycling of the voltages then continues in the same manner to move the electrons into the area beneath electrode '3', and then on into the next pixel, emptying the row pixel-by-pixel. Based on Kitchin (1998), Howell (2000) and Bradt (2004)

pattern and the electrons have now moved one electrode to the right, as depicted in Fig. 2.2. This process is repeated, cycling the voltages to transfer electrons from electrode '2' to electrode '3', and then on into the adjacent pixel, until the entire row is emptied (Kitchin, 1998). This process is known as charge-coupling, from which CCDs derive their name.

Every row is shifted across the CCD column-by-column, with the last column being shifted onto the transfer register, which has one pixel for each row of the main array, and is masked from illumination (Martinez & Klotz, 1998; Bradt, 2004). The charges are then moved perpendicularly along the transfer register to the output electronics; the transfer register must be emptied before each further shift of the rows in the main array. Thus each pixel's electrons are shifted through the array and off the transfer register to the analog-to-digital converter, where the charges are read out one pixel at a time. CCD readout thus produces a digital array representing the amount of light incident on each pixel for the duration of the exposure.

Whilst the charge transfer process is very quick, the final (and limiting) stage of readout is significantly slower. Readout of the entire array consisting of millions of pixels can therefore take a long time (more than 30 s). The electronics involved in the analog-to-digital conversion process add some small amount of noise to the signal. The precision of this process is also related to the speed at which the array is

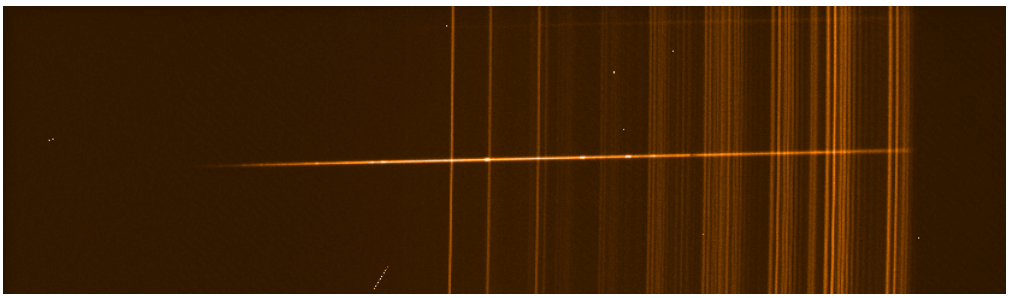

Figure 2.3: An example of a raw spectrum obtained using a CCD. The spatial direction runs vertically, whilst the dispersion direction runs horizontally across the page, with blue on the left and red on the right. The bright line running horizontally across the centre of the image is the spectrum of the target. The vertical lines are sky lines, and the white marks scattered across the image are due to cosmic ray hits. This is the optical spectrum of the AM CVn binary GP Com, obtained using ACAM on the WHT; note the bright spots along the spectrum caused by the emission lines.

read, faster readout would lead to lower precision and a reduction in the efficiency of the charge transfer process (Martinez & Klotz, 1998). This *read out noise* therefore increases if the CCD is read out at a faster rate; it is especially important to consider this when observing faint objects that will only produce a small signal during short exposures. Many CCDs allow windowing, in which only a specific subset of the pixels are actually read out, or binning, in which the charges collected in several pixels are combined before being read out, to provide faster readout. This is especially desirable when observing targets that vary in intensity rapidly.

2.2.2 Spectroscopy

Standard telescope optics focus an area of the sky onto the CCD, producing an image of the sky. This image contains spatial information in two directions, but any information about the energy of the incident photons is lost. With spectroscopy, we sacrifice one of the spatial directions in order to spread the incident light out into different wavelengths, allowing us to measure the amount of light an object emits over a range of energies – its spectrum.

Spectrographs contain a prism, diffraction grating or grism to disperse the incident light. Since the spectra of objects aligned in the dispersion direction would likely overlap, a slit is usually placed in the focal plane of the telescope to block light from sources other than the target. We thus obtain a series of monochromatic images of the slit, spread across the CCD according to wavelength. An example of a raw 2D spectrum is shown in Fig 2.3. This must be extracted and calibrated before it can be analysed.

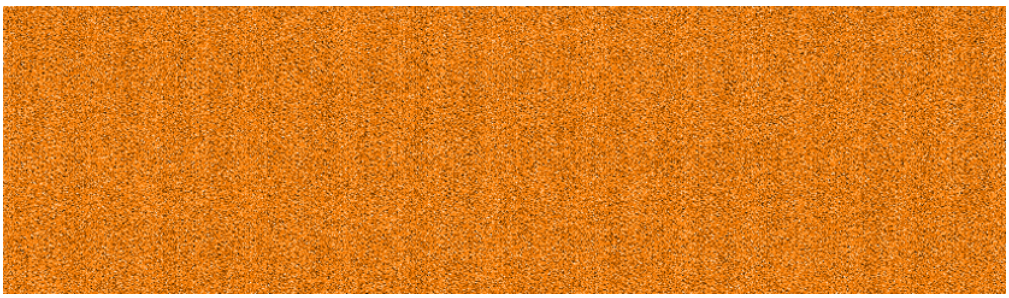

Figure 2.4: An example of a bias frame. The random noise usually has only a small standard deviation compared to the bias level.

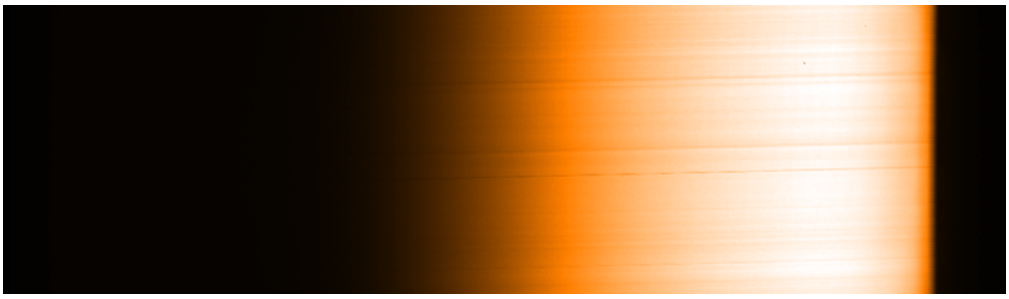

Figure 2.5: An example of a spectroscopic flat field. As well as the pixel-to-pixel variations in sensitivity, this frame includes the spectral distribution of the flat lamp.

2.2.3 Data reduction

This section outlines the procedures that must be followed in order to extract and properly calibrate spectroscopic observations.

Bias subtraction

The charge measurement process during CCD readout introduces statistical fluctuations to the data known as 'read out noise'. In order to prevent this from introducing negative values to pixels that received few photons (which would require an extra bit to store) a bias level is added to each pixel to offset the zero point of the CCD. This is typically about 1000 counts. There are two methods available for correcting this, bias frames and the overscan region (Martinez & Klotz, 1998).

Bias frames are images taken with zero exposure time, and allow estimation of the bias level. They also allow any structure in the bias to be removed by median-stacking a series of bias frames, and subtracting this average (Massey & Hanson, 2013). An example of a bias frame is shown in Fig. 2.4

Many CCDs will allow a few extra 'virtual' columns to be read out after the read out of the complete array. This *overscan* region provides a measure of the bias

level, which could fluctuate slightly over the course of a night, at the time the image was read out. The overscan region can be used to correct for the bias applied to the CCD, and can also be used to estimate the read out noise of each frame.

In the work presented in this thesis I generally subtract a median stacked bias frame, and correct for any remaining offset using the overscan region.

Flat-field correction

The pixels on a CCD are not all equally sensitive, there are small variations in their response to incident photons that must be corrected before any analysis can be carried out. Pixel-to-pixel sensitivity variations, or fixed pattern noise, are removed using *flat fields* (Bradt, 2004). These are uniform exposures of a featureless continuum illuminating the slit. This is usually obtained using a tungsten lamp built into the spectrograph.

Unlike photometric flat fields, spectroscopic flat fields contain the spectral distribution of the flat field lamp (see Fig. 2.5), which must be removed before we can correct for the sensitivity variations (Massey & Hanson, 2013). A series of flat field exposures are median-stacked, and then collapsed along the spatial direction to produce a 1D spectrum of the flat lamp. This is generally fitted with a low order polynomial; the 2D average flat field is then divided by this fit to remove the spectral distribution of the lamp. The resulting frame should then contain only the small variations in pixel sensitivity. This frame is normalised, and then inverted to produce the balance frame, which is multiplied into the science frames in order to correct them.

Additionally, one can further correct for variations along the slit, the slit illumination function, by using twilight flats. Exposures of the sky during twilight provide uniform illumination of the slit, and result in the spectrum of the Sun being recorded. These flats are median-stacked and collapsed this time along the dispersion direction (Massey & Hanson, 2013). If we choose to correct for variations along the slit, before producing the final balance frame as described above, the spatial profile of the flat field is divided out and the spatial profile of the twilight flat multiplied into the corrected flat frame. This frame is then normalised and inverted as described previously.

Extraction

After bias subtraction and production of the balance frame which will be multiplied into the data, we are now ready to extract the spectrum of our target. Consider

again Fig 2.3, showing the raw spectrum of GP Com, running approximately horizontally along the image. The slight tilt is introduced by the spectrograph and the atmosphere (Massey & Hanson, 2013), and the spectrum does not line up exactly with the columns of the CCD.

The first step is to trace the location of the tilted spectrum using a low order polynomial. A small region of sky is then selected on either side of the target spectrum in order to estimate the sky background in the region containing the target spectrum. This is achieved by fitting low order polynomials to the sky region along the rows, and interpolating into the region occupied by the target spectrum.

Optimal extraction requires weighting the contribution of each pixel, i, across the spectrum according to the spatial profile. For tilted or distorted spectra, this is achieved by fitting low order polynomials to the fraction of flux falling in each pixel parallel to the spectrum, as described by Marsh (1989). Finally the sky background is subtracted and the optimal weights, W_i, calculated previously are then used to extract the target spectrum, $S(\lambda)$, according to the equation given by Marsh (1989),

$$S(\lambda) \, = \, \sum_i W_i(\lambda) \, (C_i(\lambda) - B_i(\lambda)), \tag{2.1}$$

where C_i and B_i are the counts and sky background of the i-th pixel at wavelength λ. These weights are defined as,

$$W_i(\lambda) \, = \, \frac{P_i(\lambda)/V_i(\lambda)}{\sum_i P_i^2(\lambda)/V_i(\lambda)}, \tag{2.2}$$

according to the fraction of flux that falls in the i-th pixel, P_i, and the variance of that pixel, V_i. During this process outlying pixels caused by cosmic rays are removed (see Horne 1986).

We thus obtain a 1D spectrum giving the counts at each pixel; an example is shown in Fig. 2.6. The final stages of reduction involve calibrating these axes. The debiassing, flat-fielding and extraction performed in the work presented in this thesis have all been carried out using the PAMELA[1] spectral reduction package, and the STARLINK packages KAPPA, FIGARO and CONVERT. Errors are propagated throughout the extraction process; the variance of a pixel is given by,

$$V_i \, = \, R^2 + \left(\frac{F_i + B_i}{G} \right), \tag{2.3}$$

[1]PAMELA is included in the STARLINK distribution 'Hawaiki' and later releases. The STARLINK Software Group homepage can be found at `http://starlink.jach.hawaii.edu/starlink`.

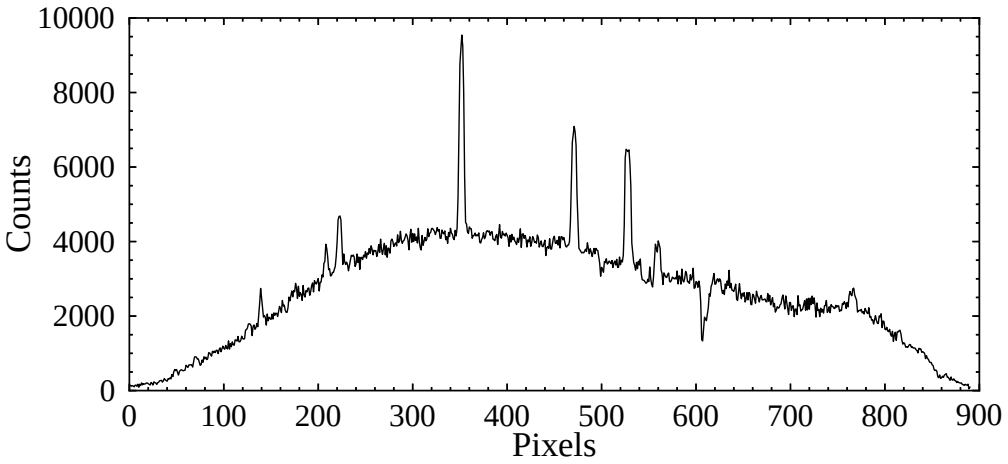

Figure 2.6: The 1D spectrum produced from the raw image shown in Fig. 2.3 using optimal extraction. The bright spots seen across the spectrum in Fig. 2.3 are revealed here as emission lines; note also that the sky background has been subtracted.

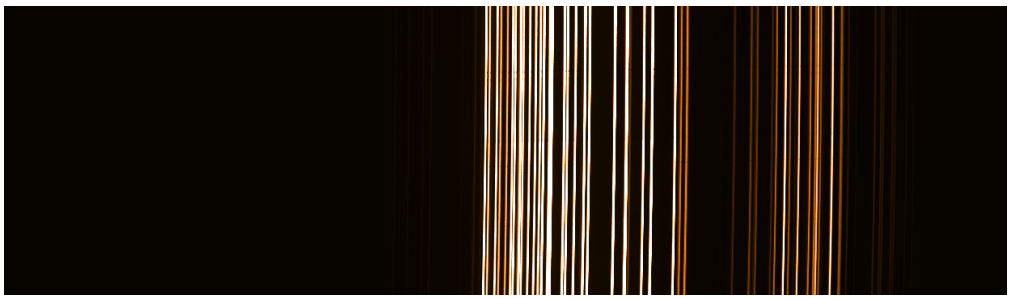

Figure 2.7: An example of an arc frame produced using a Cu-Ne arc lamp.

where G is the gain in electrons per analog-to-digital unit (ADU), and includes contributions from the read out noise, R, the photon noise due to the object, $\sqrt{F_i}$, and the photon noise due to the sky background, $\sqrt{B_i}$ (e.g. Massey & Hanson, 2013).

Wavelength calibration

To convert the x-axis from a pixel scale to a wavelength scale we use *arc spectra*. Using the same set up as for the science frames the slit is illuminated by lamps producing a number of emission features of known wavelengths (Martinez & Klotz, 1998). An example of the resulting arc frame is shown in Fig. 2.7. These frames are then extracted in the same manner as the target spectra to produce arc spectra.

The pixel position of each identified arc line is then compared to its known reference wavelength, and a polynomial is fitted to determine the conversion between pixels and wavelength. This transformation is then applied to the target spectra.

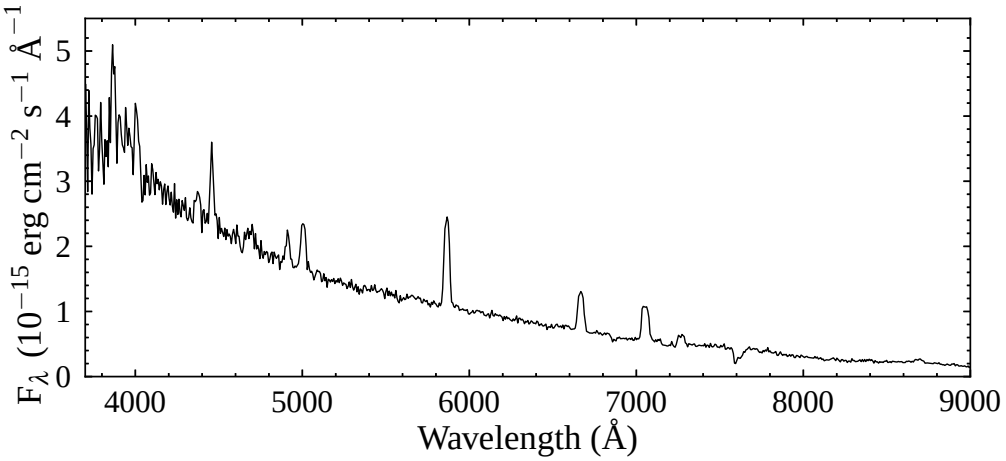

Figure 2.8: The spectrum of GP Com from Figs. 2.3 and 2.6 after wavelength and flux calibration. Now that the spectrum has a wavelength scale we can identify the emission as He I lines; the flux calibration reveals a blue continuum.

As the telescope moves during the night there can be some movement in the spectrograph, known as flexure, that may cause small drifts in the dispersion direction. In order to correct for this arc exposures can be taken at intervals throughout the night, and the arc scales interpolated in time before being applied to the science spectra.

Flux calibration

Flux calibrating the spectrum of the target is achieved via observation of a spectrophotometric standard star. During the night observations of an appropriate standard star are made using the same instrument configuration as used for the science spectra. Observations of flux standards are usually obtained using a wide slit, in order to maximise the flux collected. The standard observations are extracted in the same manner as the science spectra.

The observed spectrum of the standard star is then compared to the known tabulated flux data, and the ratio fitted with splines to determine the flux-to-counts ratio for each pixel. This conversion is then applied to the science spectra to flux calibrate them. This gives us a spectrum such as that shown in Fig. 2.8.

Note that science spectra are observed with a narrow slit in order to achieve a higher resolution, resulting in some of the flux from the target being lost on the slit. Due to these slit losses the flux calibration is not absolute. Variable seeing will also lead to varying slit losses through a night of observations. For accurate flux calibration of variable sources these variable slit losses can be corrected by

positioning a nearby constant source on the slit. The spectra of this source can then be used to correct the science spectra for variable slit losses.

In cases where we are interested in studying the spectral lines in detail, we may want to normalise the spectrum of the target rather than flux calibrating it (e.g. Massey & Hanson, 2013). A low order polynomial is fitted to the continuum and the spectrum is then divided by this fit.

For the data presented in this thesis wavelength and flux calibration are carried out using MOLLY[2].

2.3 Data analysis techniques

In this section we now turn our attention to the analysis of the processed data. The techniques described here are used throughout this thesis in the identification and analysis of accreting binaries.

2.3.1 Spectroscopic identification

The spectroscopic survey that is the subject of this thesis produces low-resolution, low signal-to-noise ratio spectra of objects selected as AM CVn candidates. Once extracted, these spectra must be examined for the spectral features expected for AM CVn binaries. In addition, it is desirable to classify all the objects which have been observed, in order to learn more about the composition of the colour box.

There are several approaches that one could use to achieve this, and whilst an automated system is desirable, the development of a reliable algorithm for classifying the diverse spectra in our sample would be challenging and time-consuming. Since the human brain is good at recognising patterns among noise, and our samples are small (a few thousand objects), I classify spectra by visual inspection.

Stellar objects will have very small Doppler shifts as they will be travelling at the low velocities of Galactic objects, and so only the strongest spectral lines in the optical region need be considered. AM CVn binaries are characterised by their lack of hydrogen, their spectra being instead dominated by helium features. I list the wavelengths of strong spectral lines that might be expected to be seen in Table 2.1. Since the strong helium and hydrogen lines fall between ∼4000 and ∼7000 Å, our spectroscopic observations have targeted this region of the optical band, enabling identification of AM CVn binaries.

[2]MOLLY is a spectral analysis program for 1D spectra written by T. R. Marsh, and is available at `http://www.warwick.ac.uk/go/trmarsh/software`.

Table 2.1: Strongest spectral features expected in our targeted spectral region for each element.

Element	Strongest lines (Å)
Hydrogen	Hα (6563), Hβ (4861), Hγ (4340), Hδ (4102)
Helium	He I 5875, 6678, 4471, 5015, 4921
	He II 4686
Carbon	C I 5041, 4775, 4932, 5380
	C II 5165, 4737, 4382
Calcium	Ca II H (3968) & K (3934)

Quasars and galaxies on the other hand will have significant redshifts. That their spectral lines fall in unexpected places, and the extremely broad (quasars) or narrow (galaxies) nature of these emission features, allows these objects to be easily distinguished.

The AM CVns and CVs should be very easy to identify, as they should exhibit strong broad emission lines at approximately the rest wavelengths of the helium and hydrogen lines listed in Table 2.1. Helium lines such as these can be seen in the spectrum of the AM CVn binary GP Com shown in Figs. 2.6 and 2.8. The defining characteristic of an AM CVn binary in this case is the lack of hydrogen, whilst CVs are expected to show clear hydrogen lines that are much stronger than the helium lines (if they are detected).

Hydrogen (DA) and helium (DB) atmosphere white dwarfs are expected to show broad absorption features. Objects which show narrow absorption lines of hydrogen and helium, are more likely to be subdwarf stars. Carbon or metal absorption lines on a blue continuum are shown by DQ and DZ white dwarfs respectively. Objects which show a smooth continuum are identified as DC white dwarfs. It is also possible to find white dwarfs which show features from more than one element in their spectra, in which case classifications such as DBZ, DAB will be assigned.

I show example spectra of the main classes of objects found in our sample in Fig. 2.9, with the features that identify them labelled.

2.3.2 The equivalent width

The equivalent width (EW) is used as a measure of the strength of a spectral line. It is defined as the width of the rectangle with a height set to that of the continuum, that has area equal to that of the spectral line (e.g. Carroll & Ostlie, 2006). See Fig. 2.10.

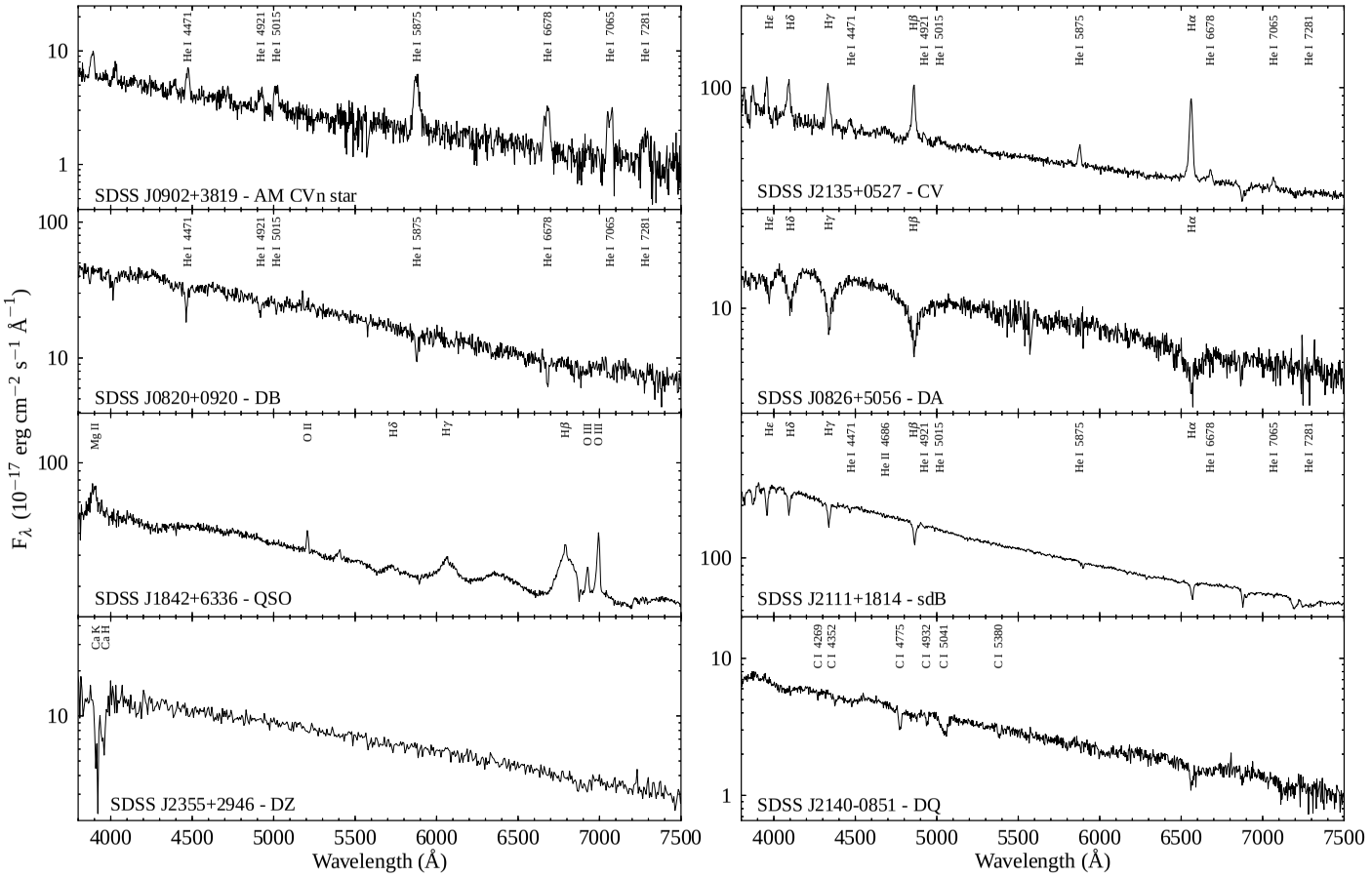

Figure 2.9: Identification spectra of select objects from our sample, demonstrating the appearance of the main object classes. The features that identify each object as a member of its class are labelled. The emission lines of helium and hydrogen present in the spectra of AM CVn binaries and CVs produce a strong contrast between them and the white dwarf contaminants, even at low signal-to-noise ratios. The extremely broad, redshifted emission lines seen in quasar spectra, distinguish them from the other object types.

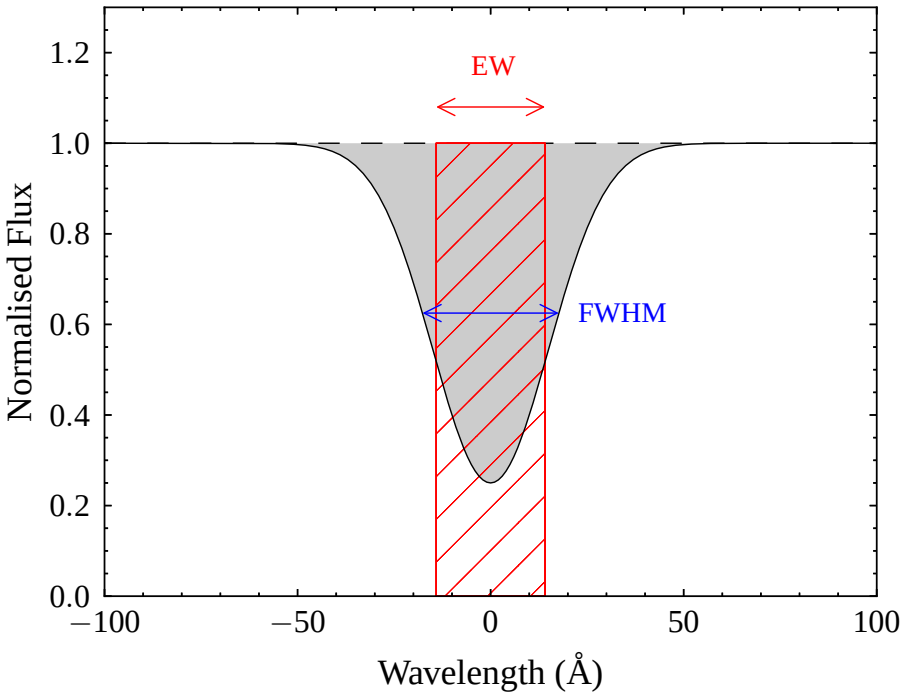

Figure 2.10: The equivalent width of a spectral line. The grey shaded area indicates the area enclosed by the spectral line, and the red box indicates a rectangle with the same area, and height equal to that of the continuum. The width of this rectangle is the EW of the line. The full width at half-maximum (FWHM) is also shown.

The EW is defined formally as:

$$\mathrm{EW} = \int \left(\frac{F_\mathrm{c} - F(\lambda)}{F_\mathrm{c}} \right) \mathrm{d}\lambda, \tag{2.4}$$

and gives the area enclosed between the continuum flux, F_c, and the line flux, $F(\lambda)$. This results in positive EWs for absorption lines, and negative EWs for emission lines.

In this work I approximate the EWs of lines as the area of a Gaussian fitted to the line profile in a continuum-normalised spectrum. The formal statistical error on the EW can then be defined simply from the variance of the fit parameters.

2.3.3 Radial velocity measurement

The spectral lines that help us to identify objects, also contain information about the object in which they originate, and spectra can be used to study interesting objects in more detail.

As the stars in a binary orbit the centre of mass of the system, their projected velocity along our line of sight (the radial velocity) will change. This causes varying Doppler shifts in the spectra of binary stars, that can be used to measure the velocity. To find the radial velocity of a spectral line, the wavelength of the feature, $\lambda_{\rm obs}$, must be measured and compared to the rest wavelength of the line, λ_0. At non-relativistic speeds, the radial velocity, V, is then calculated using the relation:

$$V = c\left(\frac{\lambda_{\rm obs} - \lambda_0}{\lambda_0}\right), \tag{2.5}$$

where c is the speed of light.

There are a number of techniques by which this can be achieved. In the simplest cases fitting a Gaussian to the line profile is sufficient to measure the central wavelength, but this may not be the best approach for the complex line profiles associated with accretion discs (see chapter 1), such as those found in CVs and AM CVn binaries.

Schneider & Young (1980) method

Schneider & Young (1980) described a technique for measuring the radial velocities of spectral lines in digital data. The wavelength, λ, of a spectral line can be found by solving the convolution:

$$\int_{-\infty}^{\infty} f(\Lambda)S(\Lambda - \lambda)\mathrm{d}\Lambda = 0, \tag{2.6}$$

where the function S is chosen by the user, considering both the data, $f(\Lambda)$, and the application (Schneider & Young, 1980).

S usually takes one of two forms, either a single Gaussian,

$$S(x) = x\,\exp\left(\frac{-x^2}{2\sigma^2}\right), \tag{2.7}$$

is used to measure the position of the core of the line, or two equal Gaussians,

$$S(x) = \exp\left[\frac{-(x - a/2)^2}{2\sigma^2}\right] - \exp\left[\frac{-(x + a/2)^2}{2\sigma^2}\right], \tag{2.8}$$

are used to measure the position of the line at various heights, by varying the separation a. The parameters σ and a, are chosen according to the data and the desired application.

For CVs, the double Gaussian method (equation 2.8) is commonly used to measure the radial velocities from the high velocity wings of the emission lines, as these are expected to originate close to the surface of the accretor, and should suffer less contamination from the bright spot (Smak, 1970; Rayne & Whelan, 1981; Shafter, 1983). By measuring the radial velocities at various separations, and comparing the resulting orbital fits, it is possible to determine the optimum separation for a particular set of data, see Shafter (1983) and Horne, Wade & Szkody (1986).

Combined Gaussian fitting

For lines with very low radial velocity amplitudes, or very low signal-to-noise ratios, the Schneider & Young (1980) methods may not produce good results, resulting in radial velocities that have very large uncertainties. Since the emission lines produced in an accretion disc should all follow approximately the same orbital motion, the radial velocities of each line ought to be consistent.

We can therefore fit a series of lines simultaneously with Gaussians, using a wavelength or velocity offset that is common to all the lines. I use the *mgfit* tool within MOLLY to fit the height, full width at half-maximum (FWHM) and offset for each Gaussian profile. To ensure the fit will converge for low signal-to-noise ratio spectra, the FWHM for each line is fixed to the value found from a fit to the average spectrum. The height of each line, and the common offset are then allowed to vary.

This procedure yields, for each spectrum, a single value for the radial velocity, along with a formal error, with a much greater precision than could be obtained for any single line.

2.3.4 Period finding

Once the radial velocities of the lines in a series of spectra have been measured, they can then be used to constrain the orbit of the binary. The emission lines in accreting binaries, formed in the disc, should approximately trace the motion of the accretor via the orbital motion of the accretion disc.

For measurement of the orbital period, all that is required is some signal that varies on the orbital period. If the brightness of the system varies with the orbital phase, the light curve can also be used to measure the period; however, the orbital period may not be the strongest signal in the light curve.

The power spectrum of the data is calculated, to identify the frequencies of periodic signals. With sufficient good data the strongest peak in the power spectrum

should correspond to the period. When this is not the case, the true period cannot be determined from the power spectrum alone.

The Lomb–Scargle periodogram

In this thesis I use the Lomb-Scargle periodogram (Lomb, 1976; Scargle, 1982) to find periodic signals. The Lomb-Scargle version of the periodogram, P_X, is defined as follows for data X_j observed at times t_j,

$$P_X(\omega) = \frac{1}{2}\left\{\frac{\left[\sum_j X_j \cos\omega(t_j-\tau)\right]^2}{\sum_j \cos^2\omega(t_j-\tau)} + \frac{\left[\sum_j X_j \sin\omega(t_j-\tau)\right]^2}{\sum_j \sin^2\omega(t_j-\tau)}\right\}, \tag{2.9}$$

where τ is defined by

$$\tan(2\omega\tau) = \frac{\left(\sum_j \sin 2\omega t_j\right)}{\left(\sum_j \cos 2\omega t_j\right)}, \tag{2.10}$$

(Scargle, 1982). This form works for unevenly sampled data, and is equivalent to minimising the sum of squares in least-squares fitting of sinusoids to the data (Lomb, 1976). I use the method shown by Press & Rybicki (1989) to evaluate equation (2.9) using the fast Fourier transform.

Peaks in the resulting periodogram correspond to periodic signals in the data, although noise and aliasing must be carefully considered. An example periodogram is shown in Fig. 2.11.

Fitting the orbit

Radial velocities are then fit with a circular orbit of the form,

$$V(t) = K \sin\left(\frac{2\pi(t-t_0)}{P_{\rm orb}}\right) + \gamma, \tag{2.11}$$

where $P_{\rm orb}$ is derived from the strongest peak in the periodogram. This gives the best fitting radial velocity amplitude, K, systemic velocity (the radial velocity of the system's centre of mass), γ, and zero phase, t_0.

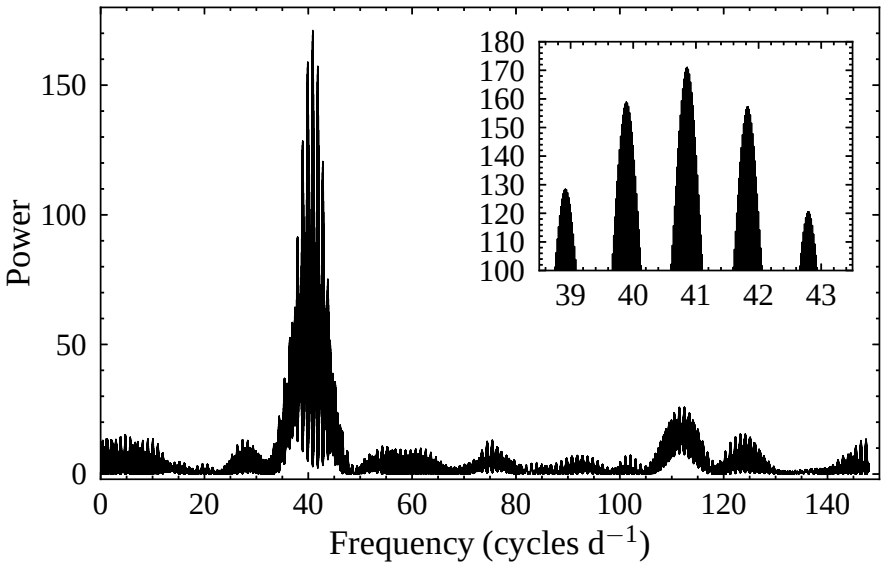

Figure 2.11: A Lomb-Scargle periodogram calculated from radial velocity measurements. There is a strong peak at $\sim$41 cycle d^{-1}, with both coarse ($\sim$1 day) and fine alias structure. The inset shows the detail around this peak.

Estimating the period uncertainty

I estimate uncertainties in the period by carrying out bootstrap selections (Efron, 1979) of the radial velocity curve. For each subset, I select the same number of radial velocities as were present in the original dataset from the full radial velocity curve, allowing for points to be selected more than once. The periodogram is then calculated from the new set of radial velocities, and the strongest peak is again taken as the period. The standard deviation of these computed periods is taken as a measure of the uncertainty in the derived orbital period.

Photometric periods in ultracompact binaries

Observations of long period AM CVn binaries have shown that they typically lack orbital signatures in their lightcurves (Warner, 1972; Woudt & Warner, 2001; Woudt, Warner & Pretorius, 2004), being instead dominated by flickering and quasi-periodic signals. For this reason, phase-resolved spectroscopy has generally been used to measure orbital periods in these objects.

Power spectra can be calculated from light curves, allowing the frequencies of any periodic signals to be extracted in the same way as for radial velocity curves. During outbursts some CVs and AM CVns develop superhumps, which have a strong photometric signal on a period slightly longer than the orbital period. It is some-

times possible in such cases, to see orbital modulations as well, but these may only become apparent after prewhitening the light curve to remove the stronger superhump signal. This is achieved by subtracting a sinusoidal fit to the light curve, with the frequency fixed to the strongest peak in the original periodogram.

2.3.5 Doppler tomography

Doppler tomography is an indirect imaging tool. It is commonly used when studying the time dependent spectral properties of CVs and AM CVns to produce two dimensional maps of the accretion disc. The disc cannot be reconstructed in position coordinates as there is likely emission from material that is not moving in a Keplerian orbit, but it is possible to construct an image in velocity coordinates. A spot of emission in the reference frame of the binary traces out a sinusoidal radial velocity curve, thus observations of an emission feature throughout the binary orbit provide the unique location of that feature in velocity space (Marsh & Horne, 1988).

The line profile at a certain phase is just the one dimensional projection of the velocity space image. With observations of the line profile at several phases, it is just a matter of inverting these projections to reconstruct the image (Marsh, 2001), a process known as tomography. In this thesis I use the maximum entropy inversion method for constructing Doppler maps (Marsh & Horne, 1988), using the DOPPLER[3] software package.

Fig. 2.12 shows the relation between the spatial coordinates in a binary system, and the velocity coordinates of a Doppler map. In the Doppler map the accreting white dwarf is located at $(0, -K_1)$, and the donor at $(0, K_2)$. The disc is centred on the velocity of the white dwarf, and is projected inside out because the Keplerian velocity increases towards the centre of the disc; the inner ring in velocity space is the outer edge of the disc. With the Doppler map correctly aligned in orbital phase, the bright spot caused by the impact of the stream and the disc is usually located in the upper left quadrant.

2.4 Colour-colour diagrams

Large astronomical surveys such as the SDSS (discussed in chapter 1) produce data for millions of objects. A commonly used tool that I exploit in this work is the 'colour-colour' diagram.

[3]DOPPLER was written by T. R. Marsh, and is available at `http://www.warwick.ac.uk/go/trmarsh/software`.

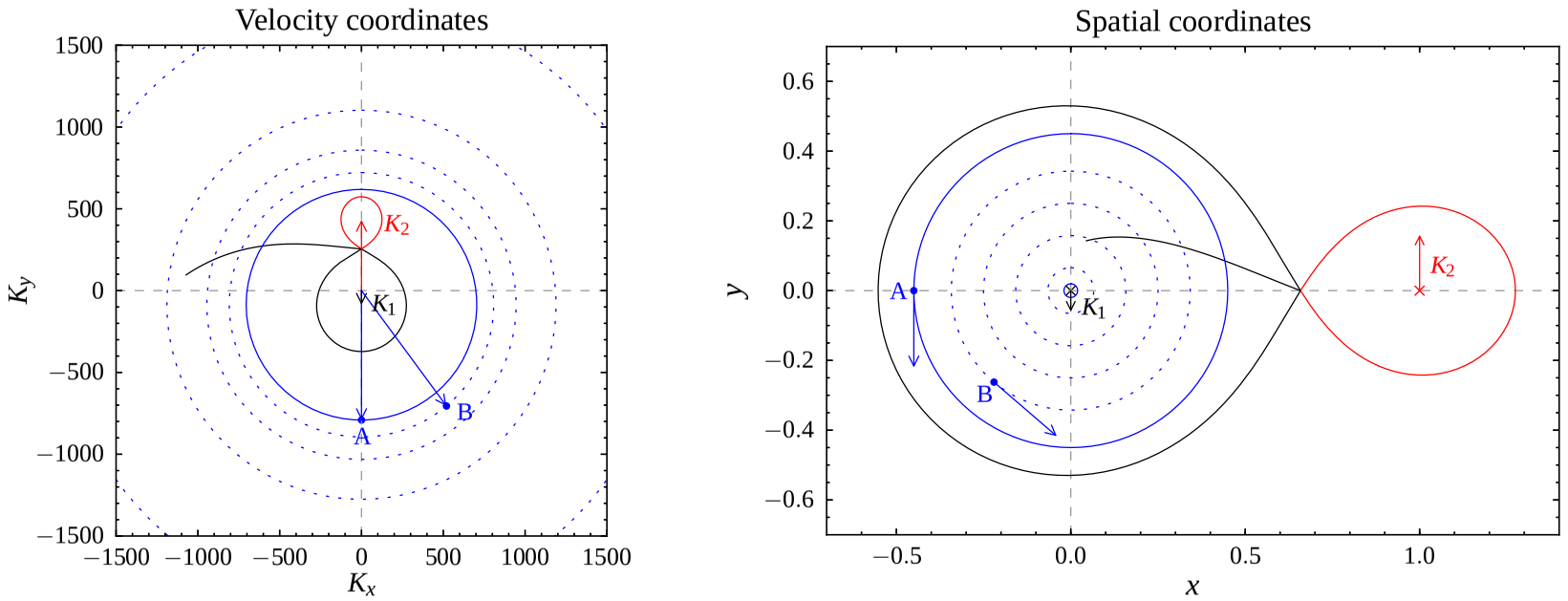

Figure 2.12: The relation between spatial (x, y) and velocity (K_x, K_y) coordinates in a Doppler map. The right-hand figure shows an example system at orbital phase 0.25, the Roche lobe of the donor is shown in red, and the Roche lobe of the primary and the gas stream are shown in black. The donor has velocity K_2, and the accreting white dwarf has velocity K_1. The solid blue line in both figures is the outer edge of the accretion disc, and the dotted blue lines represent Keplerian orbits within the disc. The points labelled A and B in each figure demonstrate how points in the disc map to locations in the Doppler tomogram. Based on Marsh & Horne (1988), Marsh (2001).

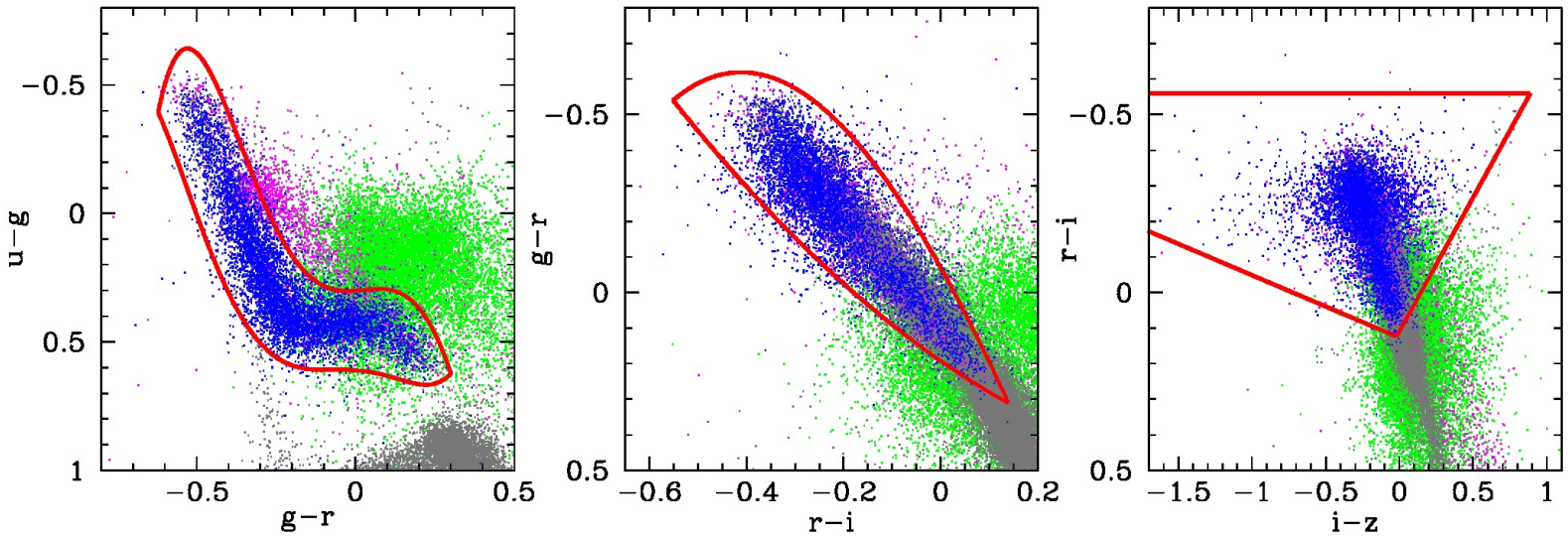

Figure 2.13: An example of a set of colour-colour diagrams using SDSS colours. The blue, magenta, green and grey dots represent DA white dwarfs, non-DA white dwarfs, quasars, and main sequence stars. The colour cuts used to select DA white dwarfs are shown in red. From Girven et al. (2011).

An object's colour index is defined as the difference between magnitudes in two different filters (or the ratio of the fluxes in those bands), and represents the slope of the spectral energy distribution (SED) over the wavelength range covered by those filters (Bradt, 2004). Colours are usually defined by subtracting the shorter wavelength magnitude from the longer wavelength magnitude, such that blue, hot objects have a negative colour, and red, cool objects have a positive colour (Carroll & Ostlie, 2006).

A plot of one colour against another is known as a colour-colour diagram, and is similar to the well known Hertzsprung-Russell colour-magnitude diagram (e.g. Kitchin, 1998). They are an incredibly useful tool for classification, as objects of different types form groups in certain colour-colour spaces due to their different SEDs. For example, using SDSS $u-g$ and $g-r$ colours, main sequence stars surround a track that deviates only slightly from the blackbody track, whilst quasars occupy a distinct area of colour-colour space due to their very different continua and redshifts (Stoughton et al., 2002).

Colour-colour diagrams are also very useful for selecting groups of objects that separate from other types of objects in a particular colour-colour space (e.g. Stoughton et al., 2002; Girven et al., 2011). Examples of a colour-colour diagrams, used by Girven et al. (2011) to select DA white dwarfs in the SDSS, are shown in Fig. 2.13. As was discussed in chapter 1, (Roelofs et al., 2009) used cuts in colour-colour diagrams to select the sample of candidates for the AM CVn survey that is the topic of this thesis. The colours of AM CVns and other objects are used extensively in this work to examine the sample, and test the methods employed in our survey.

2.5 Summary

In this chapter I have explored how astronomical spectra are observed and recorded using CCDs. I have outlined the procedures for reducing spectroscopic data that will be followed throughout this thesis to produce 1D spectra from raw data. I have also discussed the techniques that will be used in this work to analyse these spectra. In the chapters that follow I will show how these techniques allow us to identify new AM CVn binaries, and study individual systems in detail.

Chapter Three

A search for the hidden population of AM CVn binaries in the Sloan Digital Sky Survey

3.1 Introduction

Establishing the space density of AM CVn binaries is important for constraining binary evolution models, and understanding the gravitational wave signal we expect to detect from them. This has been difficult as much of the known population has been discovered in a heterogeneous manner. The six AM CVn binaries discovered in the first SDSS spectroscopic surveys provided the first relatively well defined sample for estimation of the local space density, but the accuracy is limited by the small sample size.

Since these AM CVns occupy a region of colour space that is both sparsely populated, and has a low spectroscopic completeness in the SDSS database, Roelofs et al. (2009) initiated a programme to uncover the 'hidden' population of AM CVns (see chapter 1).

I have extended the sample to include new targets from SDSS DR7 (Abazajian et al., 2009). This increase in the survey area should lead to a corresponding increase in the size of the resulting AM CVn sample (which is desirable given the still small number of systems found), however, it also increases the observation time required to complete the programme.

In this chapter I describe the observations carried out as part of this survey of colour-selected candidates from the SDSS. I present our sample of CVs, and compare them to those found in the SDSS spectroscopy. I detail the major results from the

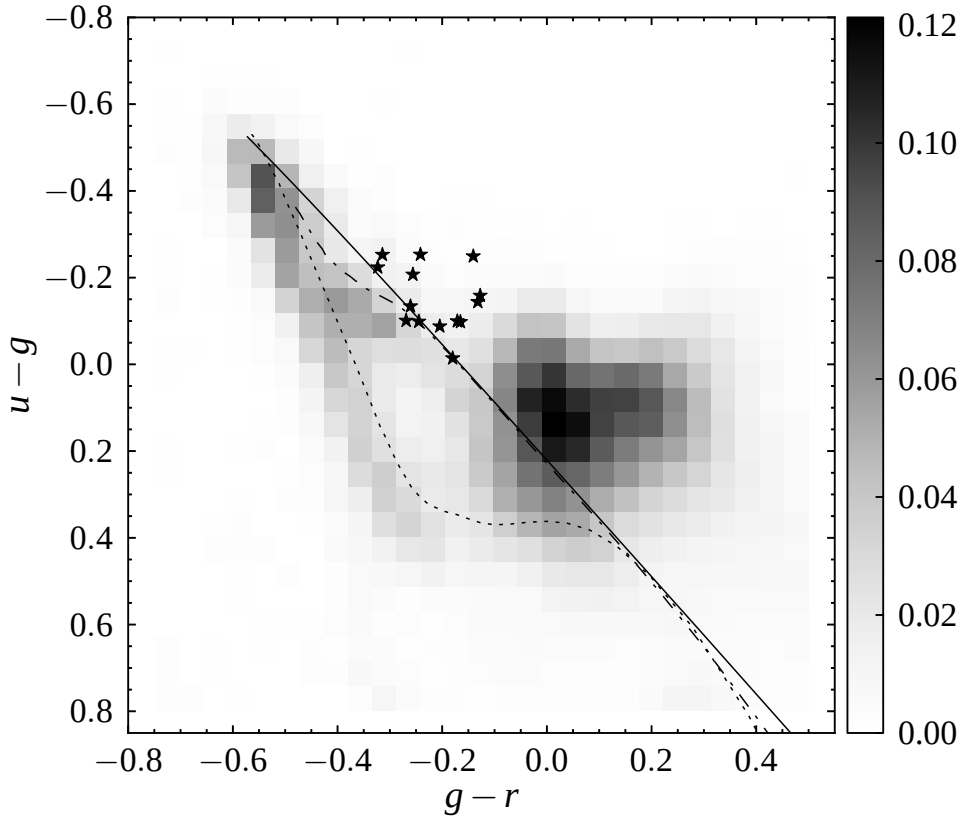

Figure 3.1: Completeness of SDSS DR9 spectroscopic follow-up as a function of colour, $u-g$ and $g-r$, to a limiting magnitude $g = 20.5$ (dereddened). The long period SDSS AM CVn binaries are indicated by star symbols. The solid line marks the blackbody cooling track, the dotted and dot-dashed lines indicate model cooling sequences for DA and DB white dwarfs.

survey, present the two candidate AM CVn binaries discovered in the most recent observations, and calculate a revised estimate of the AM CVn space density.

3.2 Survey observations

Fig. 3.1 shows the spectroscopic completeness of the SDSS Data Release 9 in the region occupied by the AM CVn binaries as a function of $u-g$ and $g-r$ colour, to a limiting g-band magnitude of 20.5. Also plotted is the blackbody cooling track, and Bergeron model colours[1] of the cooling sequences of hydrogen (DA) and helium (DB) atmosphere white dwarfs ($\log g = 8.0$; Holberg & Bergeron 2006; Kowalski & Saumon 2006; Bergeron et al. 2011; Tremblay, Bergeron & Gianninas 2011). The

[1]P. Bergeron's synthetic white dwarf colours were taken from `http://www.astro.umontreal.ca/~bergeron/CoolingModels`.

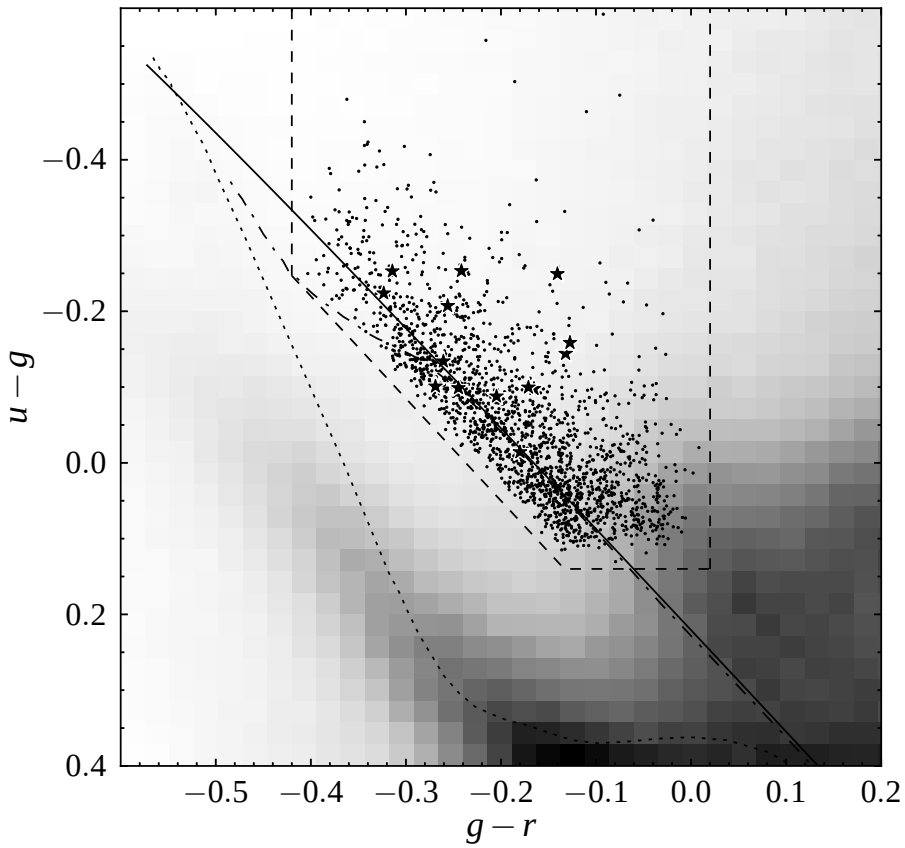

Figure 3.2: The greyscale represents the density of sources in the SDSS photometric database as a function of colour, $u-g$ and $g-r$, to a limiting magnitude $g=20.5$ (dereddened). The long period SDSS AM CVn binaries are indicated by star symbols. The solid line marks the blackbody cooling track, the dotted and dot-dashed lines indicate model cooling sequences for DA and DB white dwarfs. The dashed lines indicate the colour cuts given by Roelofs et al. (2009), and the dots indicate the candidates selected from the SDSS DR7 database.

known AM CVn binaries lie in an area of relatively low spectroscopic coverage, largely offset from the DB white dwarf track. The areas to the lower left and right are targeted for DA white dwarfs and quasars by the SDSS spectroscopic surveys.

I show the density of sources in the SDSS photometry as a function of colour in Fig. 3.2; also shown are the known long period AM CVn binaries, and the candidates selected by applying Roelofs et al. (2009)'s colour cuts to the SDSS DR7 photometric database. This shows that the known AM CVn binaries lie in a sparsely populated area of colour space, which is a key property in making a search for the hidden population of AM CVns possible (Roelofs et al., 2009; Rau et al., 2010).

As shown by Roelofs et al. (2009), AM CVn binaries with a He I 5875 EW $\geq$30 Å are easily detectable at a signal-to-noise ratio of 10, and resolutions as low

as $R = 300$. Even systems with weaker lines should still show some sign of helium emission that would be confirmed by a second, higher quality spectrum. The possibility that there exist some systems with much weaker lines was discussed by Roelofs et al. (2009). They concluded that the majority of the population should be detectable using this approach. This will be discussed further in section 3.5.

Low-resolution, low signal-to-noise ratio spectra of objects in our colour-selected sample have been obtained with several different instrument setups, using a variety of low and intermediate resolution spectrographs. To date, spectroscopic observations of 1418 of the 1948 candidates have been completed (see Fig. 3.3). These data were obtained using a number of telescopes: the Isaac Newton Telescope (INT), William Herschel Telescope (WHT), and Nordic Optical Telescope (NOT), on the island of La Palma; the 1.5-m Tillinghast telescope at the Fred Lawrence Whipple Observatory, Mt. Hopkins, Arizona; the Very Large Telescope (VLT), at Paranal; the 200-inch Hale telescope at the Palomar Observatory; both Gemini telescopes, South in Chile and North on Hawaii; and the New Technology Telescope (NTT), at La Silla. The largest telescopes, VLT and Gemini, have been used to observe the faintest part of the sample, g-band magnitude > 20. A log of our observations, listing the instrument setups used and the numbers of candidates observed, is given in Table 3.1.

Instrument setups were chosen such that all spectra cover the 4000–7000 Å wavelength range that includes the predominant lines of both helium and hydrogen, allowing identification of AM CVn binaries from their strong helium emission, and lack of hydrogen, as discussed in chapter 2.

The spectra obtained with the FAST spectrograph were reduced using the spectral extraction pipeline provided by the observatory. This pipeline is based on standard IRAF routines, see Tokarz & Roll (1997). All other data were reduced using optimal extraction as described in chapter 2. Wavelength calibration was obtained from various arc lamp exposures taken each night. Flux calibration was achieved with various standard stars observed at the beginning or end of each night. The flux calibration is not absolute, and approximately one third of the spectra do not have flux calibration due to lack of standard star observations.

Fig. 3.3 shows the current spectroscopic completeness of our sample. The target list at the bright end of the distribution has been effectively completed, allowing us to draw some preliminary conclusions. I estimate the number of systems in our sample, from the numbers we have found so far, by multiplying the numbers of AM CVn binaries found in each magnitude bin in Fig. 3.3 with the ratio of the total to observed number per bin. This suggests that there should be at least 5

Table 3.1: Summary of our observing campaign and the instrument setups used. The wavelength range and resolution achieved with each instrument are listed, as well as the number of candidates observed during each programme. Several of our candidates from SDSS DR7 have been observed by the SDSS as part of more recent data releases, those we have not observed previously ourselves are also listed here.

Dates	Telescope/Instrument	Candidates observed	Wavelength range (Å)	R at 5875Å
2008 Jan 09 – 2009 Apr 30	Tillinghast/FAST	225	3500 – 7400	810
2008 Feb 25 – 2008 Mar 02	INT/IDS	117	3500 – 8500	630
2008 Feb 27	Keck-I/LRIS	6	3400 – 5700, 6750 – 9000	730
2008 June 06 – 2008 Sep 20	VLT/FORS1	18	3600 – 8600	340
2008 June 03 – 2009 Apr 25	Hale/DBSP	143	3400 – 8000	540
2008 Dec 25 – 2008 Dec 28	WHT/ISIS	68	3200 – 8200	1160
2009 Feb 26 – 2009 Apr 22	Gemini-South/GMOS	14	3900 – 6700	640
2009 July 21 – 2009 Aug 24	Gemini-North/GMOS	15	3900 – 6700	640
2009 Mar 17 – 2009 Mar 23	INT/IDS	95	3500 – 8500	630
2009 May 24 – 2009 May 28	NOT/ALFOSC	131	3800 – 9000	180
2009 June 18 – 2009 June 24	WHT/ACAM	205	3800 – 9200	300
2009 Oct 09 – 2009 Oct 15	NTT/EFOSC	59	3800 – 8000	340
2009 Nov 08 – 2009 Nov 14	WHT/ACAM	130	3800 – 9200	300
2010 Aug 19 – 2010 Aug 23	WHT/ACAM	88	3800 – 9200	300
2010 Nov 01 – 2010 Nov 06	WHT/ACAM	5	3800 – 9200	300
2011 Feb 02 – 2011 Feb 06	NOT/ALFOSC	55	4000 – 9000	180
2012 May 22 – 2012 May 23	SOAR/Goodman	5	3800 – 7000	860
2012 June 13	Keck-I/LRIS	1	3100 – 10000	2100
2012 July 13	WHT/ISIS	4	3800 – 5200, 5600 – 7100	2200
2008 July – 2009 June	SDSS DR8	18	3800 – 9200	1800
2009 June – 2011 July	SDSS DR9	13	3650 – 10400	1800
2011 July – 2012 July	SDSS DR10	12	3650 – 10400	1800

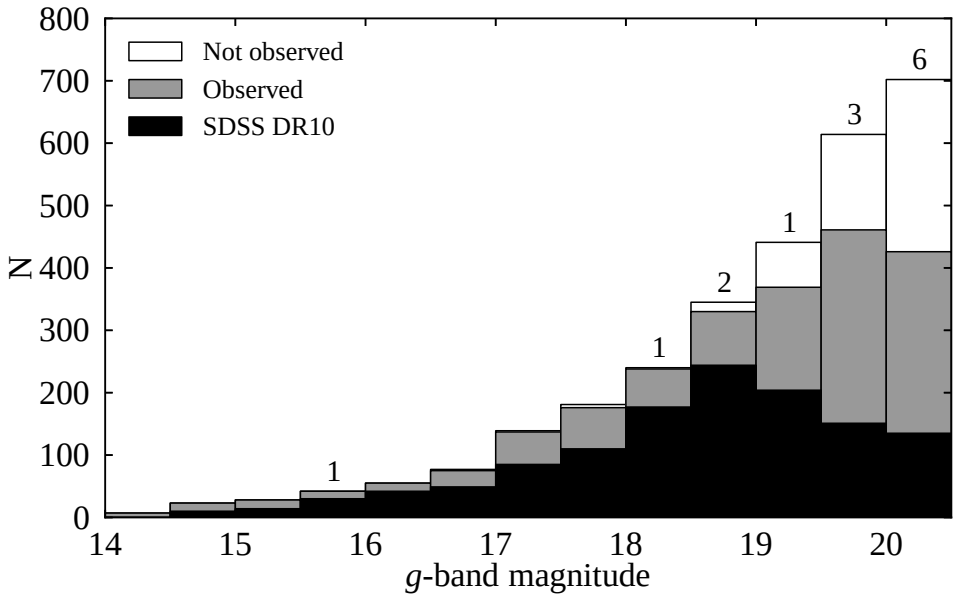

Figure 3.3: Spectroscopic completeness of our sample. I show objects meeting our selection criteria for which there are Sloan spectra (black), targets for which we have taken our own spectra (grey), and targets yet to be observed (empty). Numbers above bins indicate the number of currently known emission line AM CVn binaries in our spectroscopy or the SDSS DR10 spectroscopic database.

more systems yet to be discovered in our sample, however, it should be noted that with such small numbers there is a large uncertainty.

3.3 Spectroscopic identification

I assign a spectroscopic classification to each object based on visual inspection of its spectrum, as outlined in chapter 2. Table 3.2 gives the numbers of CVs, AM CVn binaries, white dwarfs, subdwarfs (see Heber 2009 for a recent review) and other objects identified in our sample. The white dwarfs are divided into several subclasses, DA white dwarfs are those with hydrogen atmospheres, DB those with helium atmospheres, DQ those with carbon dominated spectra, DZ those with spectra dominated by metal lines; and DC those with a continuum spectrum (see Wesemael et al. 1993 for an overview of white dwarf spectra). Fig. 2.9 shows example spectra of these main classes, with the features that identify them labelled. The AM CVn binaries, CVs and quasars are easily identified by their emission lines; the systems that show only absorption in their spectra often have less certain classifications. A full list of candidates with classifications, coordinates and u, g, r, i, z magnitudes is given in Carter et al. (2013).

Table 3.2: Numbers of main object types identified in our sample. Objects classified as DA, DB, DQ and DZ white dwarfs have spectra dominated by hydrogen, helium, carbon and metal lines respectively; DC white dwarfs are those that exhibit a continuum spectrum. The subdwarf classification includes objects identified as sdB, sdOB or sdO.

Class	Number
AM CVn	7
CV	30
quasar	109
galaxy	2
white dwarfs:	
DA	119
DB	433
DQ	27
DZ	23
DC	87
WD+dM	1
subdwarf	192
unknown	388
Total	1418

3.3.1 Testing the identifications

Fig. 3.4 shows the He I 5875 against Hα EW distribution of the spectra of our sample (here emission lines correctly have negative EWs, this is ignored for simplicity elsewhere in this chapter). These were calculated using a Gaussian fit to the normalised spectrum, with fit constraints chosen to be consistent with the line fitting algorithm used by the SDSS. If the fit failed, the offset from the expected central wavelength was larger than 20 Å or the Gaussian dispersion was measured to be less than 0.5 Å or greater than 100 Å the result was rejected and a value of zero taken. Objects appear in the expected regions of the diagram, with some scatter caused by noise.

The AM CVn binaries (stars) lie close to the line EW(Hα) = 0 Å, with negative He I 5875 EWs. SDSS J0804+1616 has significant He II 6559 emission that causes the apparent large EW for Hα. The CVs (orange inverted triangles) are all found below the line EW(Hα) = EW(5875), and (with the exception of SDSS J203311.78+134954.1, probably due to interstellar absorption) to the left of EW(5875) = 0 Å. As would be expected, the CVs identified all have hydrogen emission, which is always stronger than helium emission. SDSS J121534.77+025726.6, identified as a white dwarf + M dwarf binary, is also found in this part of the diagram due to the hydrogen emission in its spectrum (most likely due to irradiation or

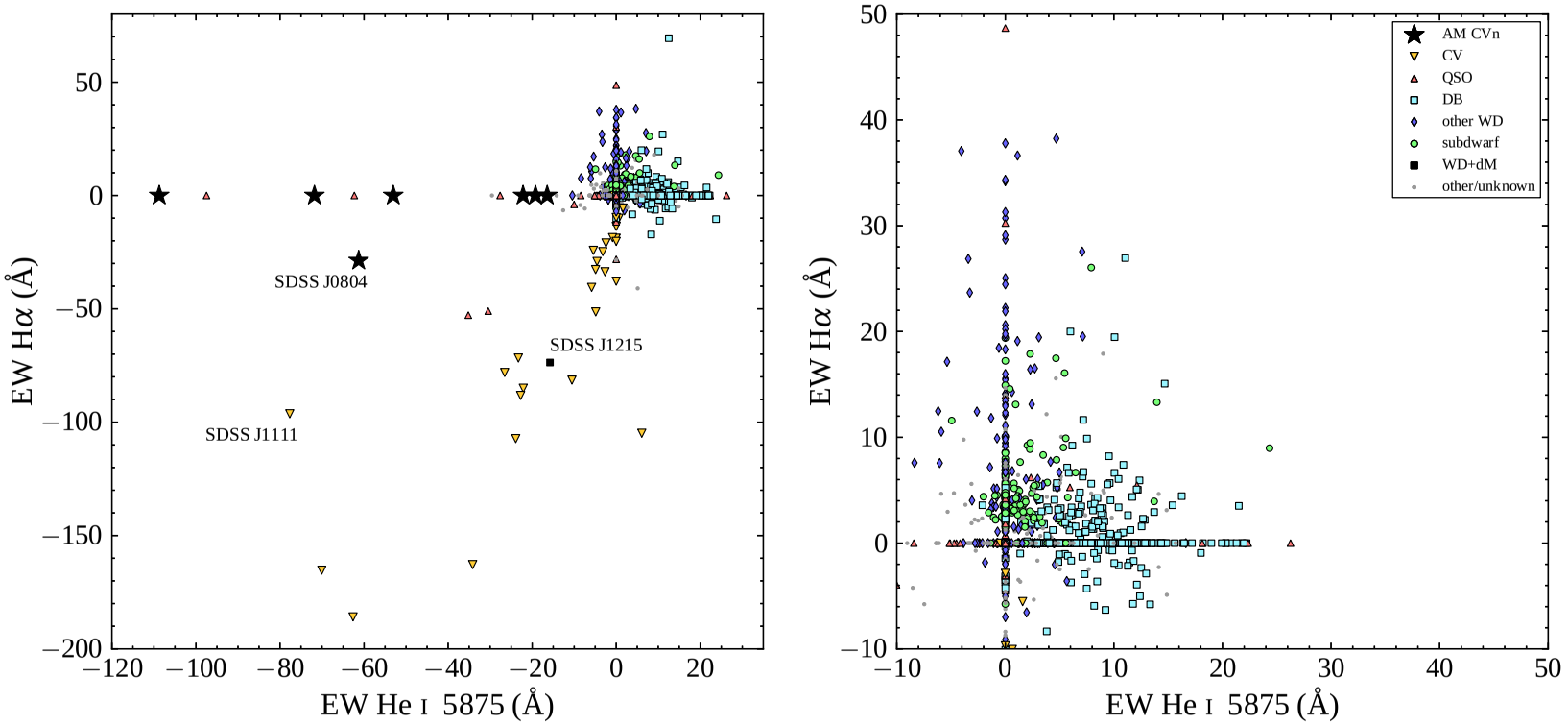

Figure 3.4: EW of He I 5875 vs Hα for our sample, the right hand panel shows the crowded area of the diagram, occupied mainly by white dwarfs, in more detail. The black stars and orange inverted triangles represent AM CVn binaries and CVs. Quasars, DB white dwarfs, other types of white dwarf, subdwarfs, and WD + M dwarf systems are represented by red triangles, cyan squares, blue diamonds, green circles and black squares respectively. Grey dots indicate those candidates that could not be classified. EWs have been calculated using a Gaussian plus sloped continuum fit; the large values for some unclassified objects are largely the result of noise. Objects appear in the expected regions with allowance for some scatter caused by noise. Note that He II 6559 emission would not be distinguished from Hα by the fitting algorithm. Several quasars have apparently valid EWs for some lines, and appear randomly distributed, but are distinguishable using other spectral features.

chromospheric activity). Several quasars have apparently valid EWs for some lines, and are scattered over the diagram; these are easily distinguished by visual inspection of their spectra, and also by their colour, which could be useful to distinguish those with low signal-to-noise ratio spectra falling in the AM CVn region of Fig. 3.4. That there are no significant large deviations from the expected position for any object type, suggests that our classification by visual inspection was successful.

There are 388 spectra which have no clear identifiable features, so no likely classification has been assigned. These objects are generally fainter, resulting in lower signal-to-noise ratio spectra, which makes weak features more difficult to discern. The majority of these objects are likely white dwarfs with weak lines or DC white dwarfs; I do not assign this classification as we do not want our assumptions as to their nature to affect our understanding of the colour space. With the exception of 18 candidates, none of these objects have helium emission with an EW greater than 3 Å as the dominant feature in their spectra, ruling them out as possible long period AM CVn binaries. The measured EWs for several of these exceptions that have possible helium emission, have very large errors, and the measurements are rejected on this basis. Fourteen of these unclassified objects are not consistent with having an He I EW of 0 Å; although the apparent emission would be classified as noise by visual inspection, they cannot be ruled out as AM CVn binaries and should be re-observed to obtain higher signal-to-noise ratio spectra.

3.3.2 AM CVn detection

The AM CVn binaries discovered in the SDSS spectroscopic database, and via this survey, all have EW > 13 Å for one of the 4686 or 5875 Å helium emission lines. This indicates our ability to identify candidate AM CVn binaries matches that of previous searches of the SDSS spectroscopic database (Anderson et al., 2005, 2008; Roelofs et al., 2005), and we can be confident that we would be able to detect the AM CVn binaries expected from predictions (Roelofs, Nelemans & Groot, 2007; Roelofs et al., 2009).

It must also be noted that high-state AM CVn binaries – those with short orbital periods and those in outburst – typically show absorption, rather than emission, in their spectra, due to the optically thick accretion disc. The spectra of these systems look very similar to those of DB white dwarfs, AM CVn itself was originally identified as such (Greenstein & Matthews, 1957), there are however, some differences in the line strengths that allow them to be distinguished with high-quality spectra (e.g. Robinson & Faulkner 1975; Fontaine et al. 2011). At the low spectral resolutions and signal-to-noise ratios employed in this survey, these high-state sys-

Table 3.3: He II 4686 and Hβ emission line EWs and line ratios for CVs with strong He II emission.

Name	EW He II 4686 (Å)	EW Hβ (Å)	Line ratio
SDSS J003719.29−215714.4	−3.3 ± 0.1	−3.8 ± 0.1	0.87 ± 0.03
SDSS J111126.83+571238.6	−19.0 ± 2.0	−34.0 ± 2.0	0.56 ± 0.07
SDSS J175320.59+251649.1	−6.0 ± 0.5	−6.9 ± 0.5	0.87 ± 0.10
SDSS J204643.30-000630.2	−3.8 ± 0.3	−5.9 ± 0.3	0.64 ± 0.06
SDSS J212617.62+192320.1	−18.0 ± 2.0	−33.0 ± 2.0	0.55 ± 0.07

tems are essentially indistinguishable from DB white dwarfs, or possibly DC white dwarfs (e.g. O'Donoghue, Menzies & Hill 1987).

The short period AM CVn binaries are expected to be far less numerous at the high Galactic latitudes of the SDSS, as the evolution from turn-on of mass transfer to $P_{\rm orb} > 30$ min is relatively rapid (Nelemans et al., 2001). Using a simple model for the evolution of a white dwarf channel system (Nelemans et al., 2001), I find that an AM CVn binary with typical values for the masses at period minimum (0.6 and 0.25 $M_{\odot}$ for the primary and secondary, following Levitan et al. 2011), has an orbital period below 30 minutes for 5.8 per cent of its life between period minimum and $P_{\rm orb}$ = 60 minutes. The high state accretion discs in the short period systems also make them much brighter, resulting in increased numbers in a magnitude limited sample. With an estimate of both the relative numbers and their absolute magnitude as a function of period, it is possible to calibrate the AM CVn space density based only on the emission line systems (Roelofs, Nelemans & Groot, 2007).

3.3.3 Cataclysmic variables

Fig. 3.5 shows the spectra of the CVs identified in our sample via their hydrogen emission. The range of line strengths and ratios seen in Fig. 3.4 are clear. The broad double-peaked line profile characteristic of an accretion disc is evident in several objects.

Wils et al. (2010) previously identified SDSS J074859.54+312512.7, SDSS J075107.51+300628.5 and SDSS J131432.11+444138.8 as dwarf nova candidates by based on their variability. The spectra presented here confirm these systems as CVs. SDSS J225417.54+074227.3 (USNO-A2.0 0975-21112378) was previously identified as a QSO candidate by Atlee & Gould (2007) based on its colour.

I compute the He II 4686/Hβ line ratios for the CVs with significant He II emission, in order to identify possible magnetic or nova-like systems. The five sys-

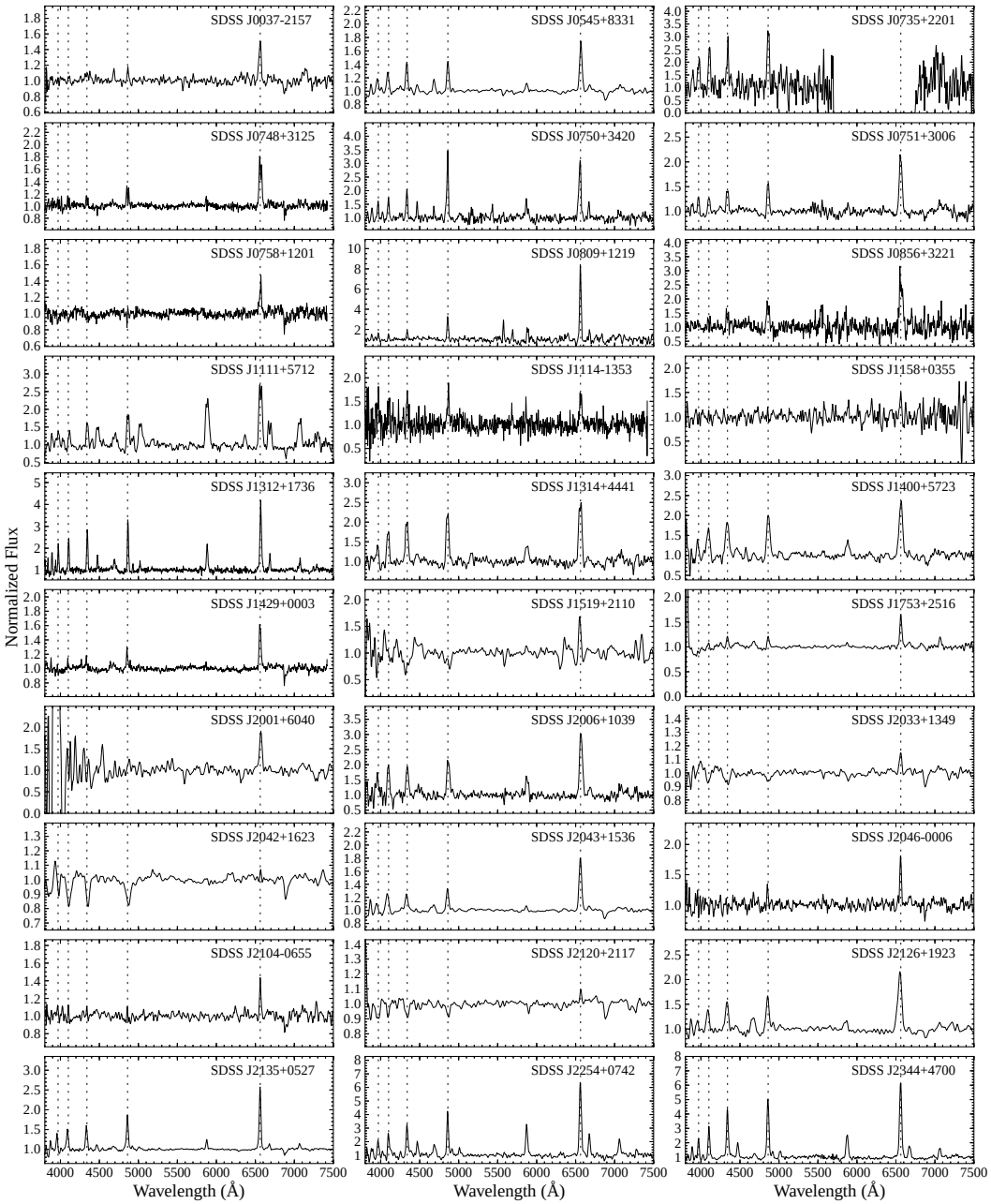

Figure 3.5: Identification spectra of the CVs discovered in our sample, displayed with 2 pixel Gaussian smoothing. Dotted lines indicate the wavelengths of the strongest hydrogen lines. SDSS J1312+1736 was observed as part of SDSS DR10, and has not been observed separately by us.

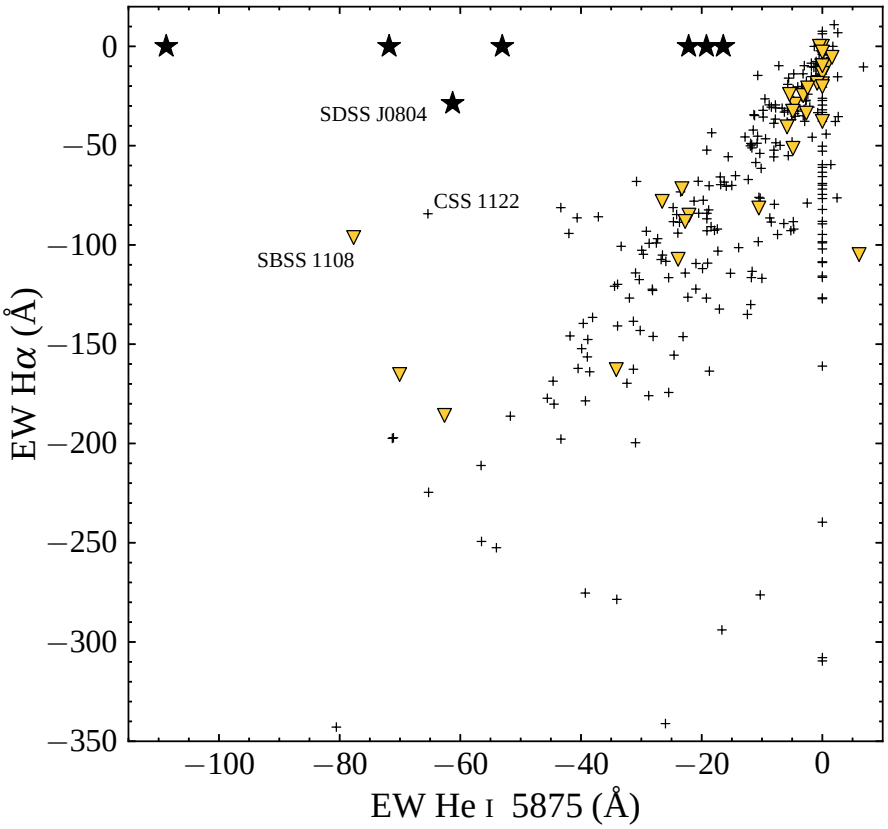

Figure 3.6: EW of He I 5875 vs Hα for our CV sample, and the Sloan CV population. Symbols have the same meanings as in Fig. 3.4, and the crosses represent the Sloan CVs. The two CVs with atypical He I line strengths, SBSS 1108+574 (SDSS J1111+5712) and CSS 1122 (SDSS J1122-1110), have been labelled.

tems with an EW ratio greater than 0.5 are listed in Table 3.3. The He II 4686 EWs measured for SDSS J175320.59 + 251649.1 and SDSS J212617.62 + 192320.1 may be affected by blending with nearby lines, but are still large compared with most CVs. The weak lines exhibited by SDSS J003719.29 − 215714.4 and SDSS J175320.59 + 251649.1, combined with the strong He II suggest they may be high accretion rate nova-like systems. SDSS J111126.83 + 571238.6 also shows unusually strong He I emission and is discussed further below.

Fig. 3.6 shows the EW distribution of our CV sample from Fig. 3.4, with the Sloan CV sample (Szkody et al., 2011) added for comparison. The distributions of the two CV populations look similar. The strongest Hα emitters fall outside our colour box, and none of the CVs in our sample have Hα emission as strong as the strongest Sloan CVs. There are two obvious outliers, SDSS J111126.83+571238.6 (SBSS 1108+574) from our sample and

SDSS J112253.3−111037.6 (CSS100603:112253−111037, Breedt et al. 2012) from the Sloan population, that have much stronger helium emission relative to hydrogen than the majority of CVs (this is also clear from the spectrum of SDSS J1111+5712 shown in Fig. 3.5). These may represent hybrid CV – AM CVn binaries, and may be AM CVn binaries forming via the evolved CV formation channel (Podsiadlowski, Han & Rappaport, 2003; Breedt et al., 2012). SDSS J1111+5712 will be studied further in chapter 5.

3.3.4 White dwarfs

DQ white dwarfs

Fig. 3.7 shows the spectra of the DQ white dwarfs identified in our sample. These objects have been identified as DQs due to the presence of either neutral carbon lines or molecular C_2 Swan bands in their spectra. A number of them also show weak Hα absorption and are classified as DQA.

The expected correlation of the transition from atomic to molecular carbon features with colour (or temperature), seen by Harris et al. (2003) in SDSS DQ white dwarfs, is also seen in our DQ sample.

DZ white dwarfs

Fig. 3.8 shows the spectra of the DZ white dwarfs identified in our sample. These objects have been identified as DZs due to the presence of the Ca II H & K lines in their spectra. A number also show weak Hα absorption and are classified as DZA.

SDSS J105338.16+285245.6 (USNO-A2.0 1125−06201629) was previously identified as a QSO candidate by Atlee & Gould (2007).

All the DZs in our sample show calcium absorption with no detection of other metals, similarly to the majority of SDSS DZ white dwarfs (Harris et al., 2003). They are all cool in ($u-g$, $g-r$), with the exception of SDSS J132430.43+055316.0, which also shows significant hydrogen in its spectrum.

3.4 New AM CVn binaries

The extracted spectra of SDSS J104325.08+563258.1 (hereafter SDSS J1043) and SDSS J173047.59+554518.5 (hereafter SDSS J1730) are shown in Fig. 3.9. Table 3.4 lists the EWs of the main lines seen in the spectra of SDSS J1043 and SDSS J1730. The helium emission lines at 4471, 5875, 6678 and 7065 Å are clearly detected, and no hydrogen is present. This suggests that SDSS J1043 and SDSS J1730 are likely

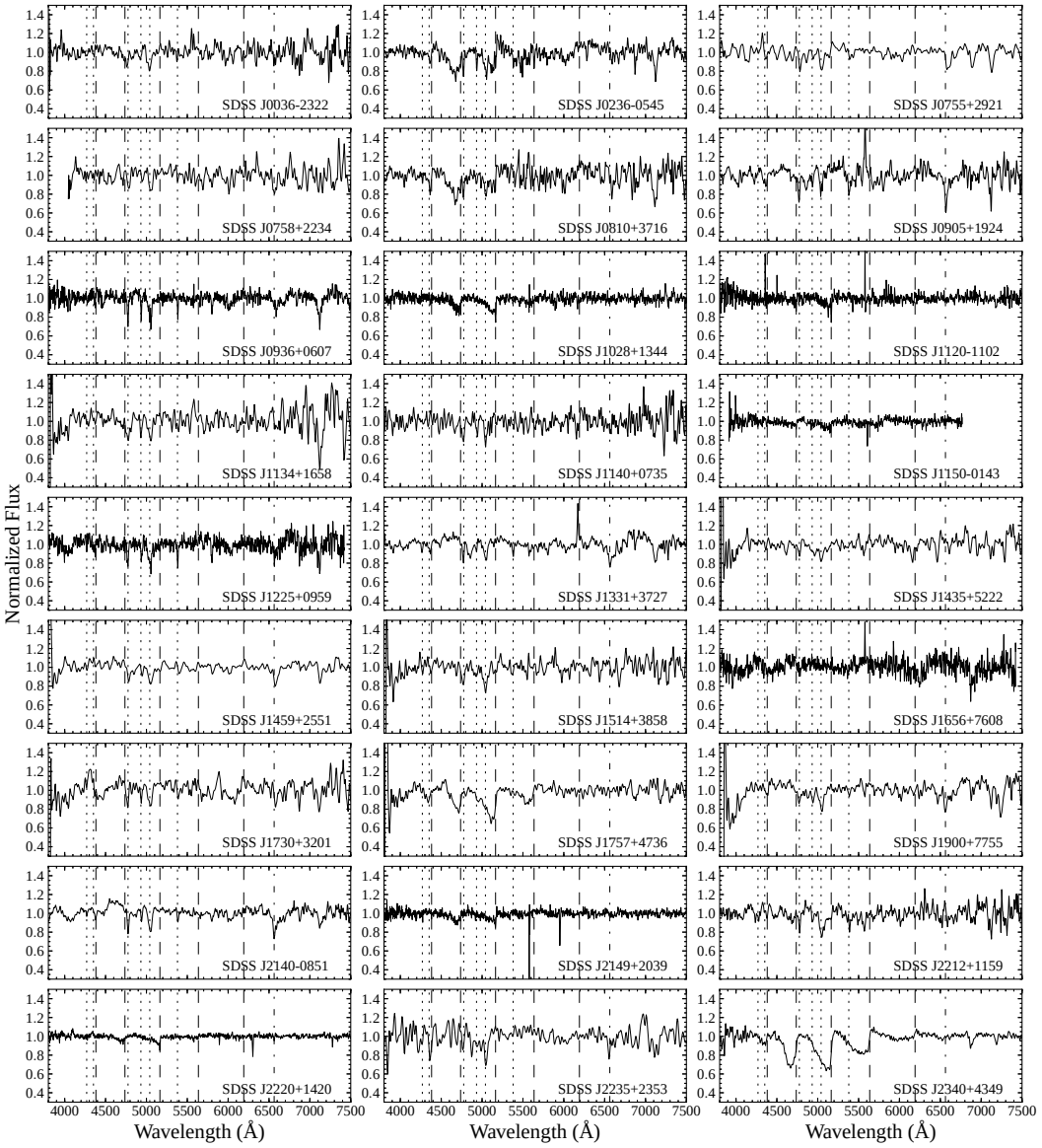

Figure 3.7: Identification spectra of the DQ white dwarfs discovered in our sample, displayed with 2 pixel Gaussian smoothing. Dotted lines indicate the wavelengths of the strongest lines of neutral carbon, dashed lines indicate the C_2 Swan band heads. The dot-dashed line indicates the wavelength of Hα, which is present in several objects. SDSS J1120−1102 was observed as part of SDSS-III, and has not been observed separately by us.

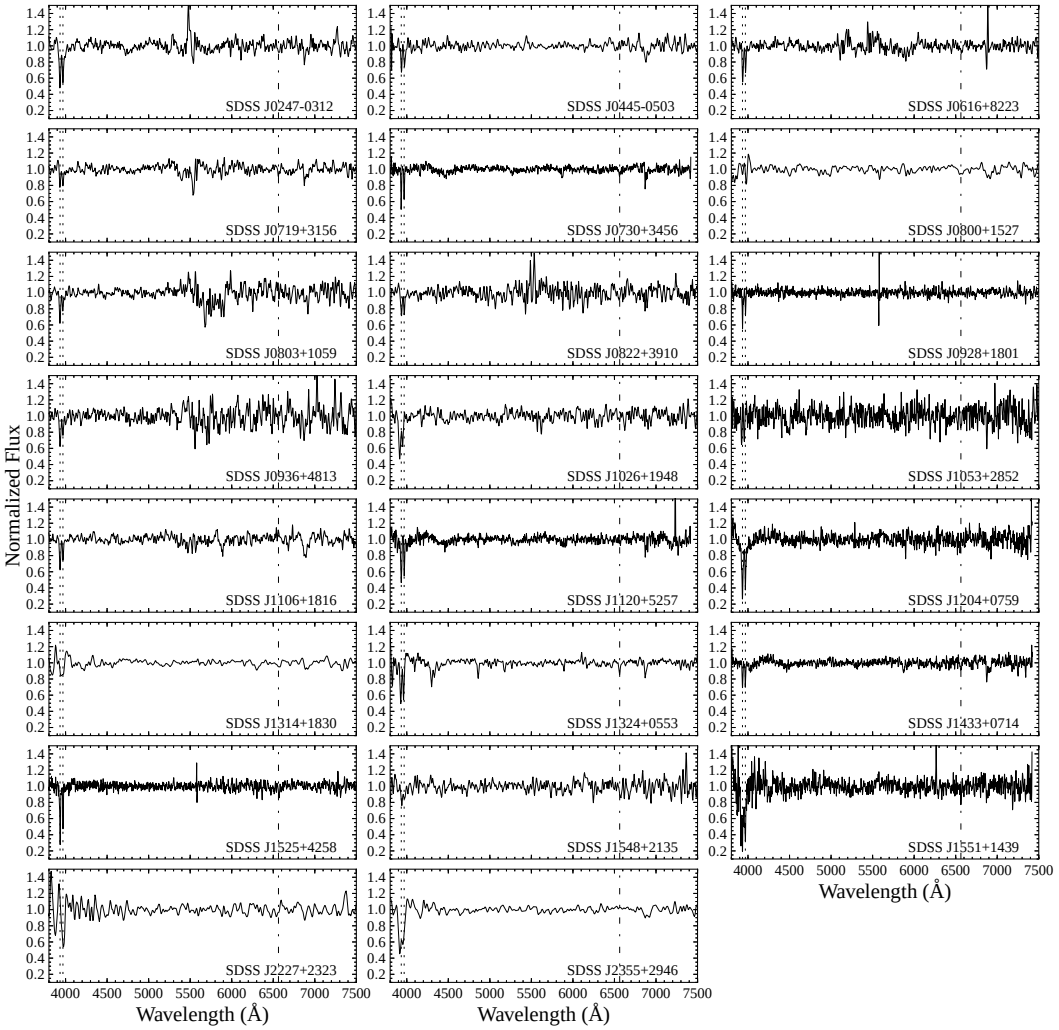

Figure 3.8: Identification spectra of the DZ white dwarfs discovered in our sample, displayed with 2 pixel Gaussian smoothing. Dotted lines indicate the wavelengths of the calcium H and K lines. The dot-dashed line indicates the wavelength of Hα, which is seen in several objects. SDSS J0928+1801 was observed as part of SDSS-III, and has not been observed separately by us.

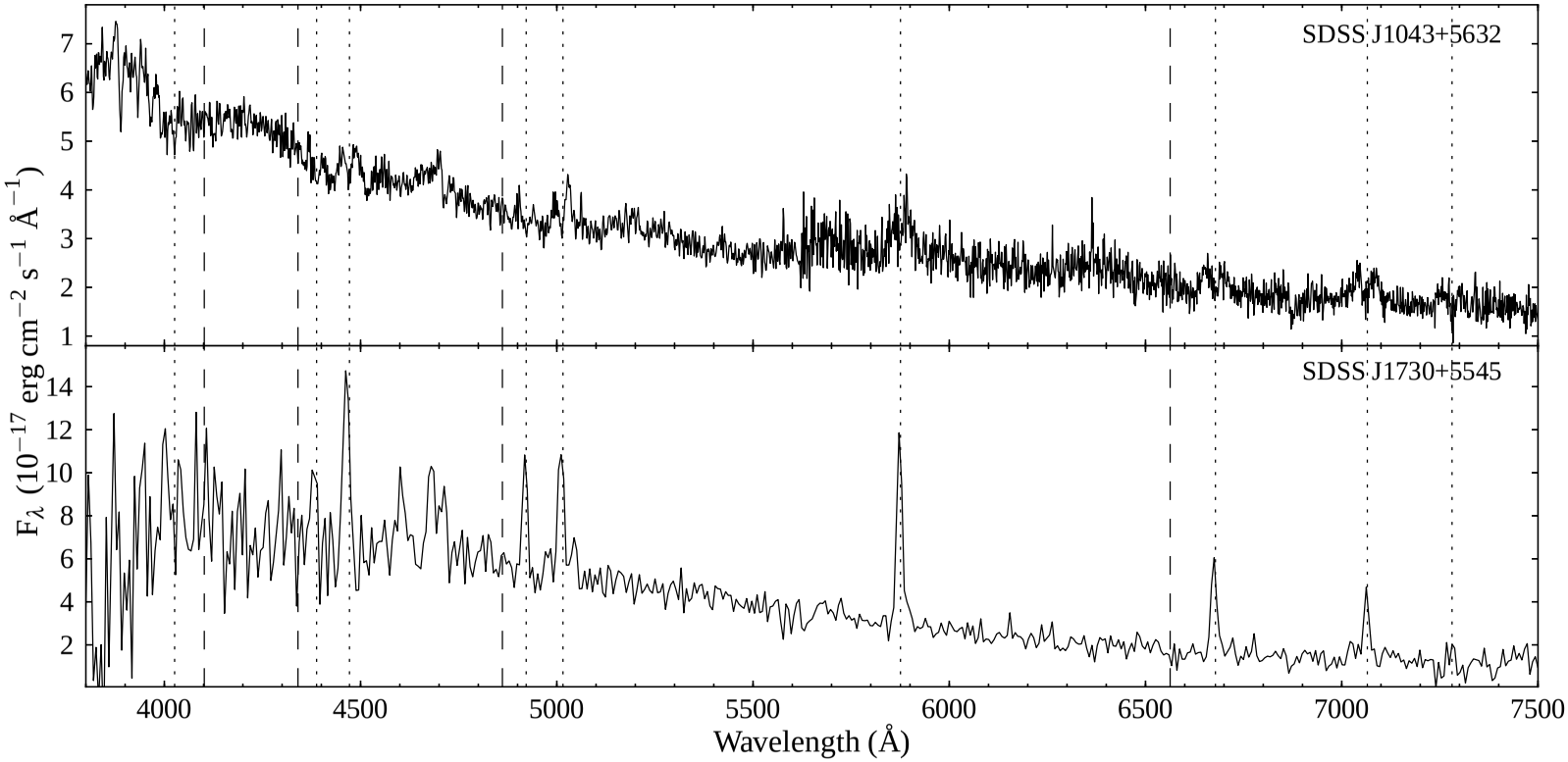

Figure 3.9: Identification spectra of SDSS J1043 (taken with LRIS on Keck I on 2012 June 13) and SDSS J1730 (taken with ACAM on the WHT on 2009 November 14). The wavelengths of the strongest He I and hydrogen lines are indicated by the dotted and dashed lines. The lack of hydrogen features in the spectra is clear. SDSS J1043 shows clear double-peaked line profiles, in contrast to the narrow lines displayed by SDSS J1730, this is likely due to a lower inclination of SDSS J1730. SDSS J1043 also shows absorption wings around the He I 4026 and 4471 Å lines, thought to be due to the accretor (e.g. Roelofs et al. 2004).

Table 3.4: EW and Gaussian FWHM for the prominent emission lines in SDSS J1043 and SDSS J1730. Estimated errors are largely due to uncertainty in the continuum.

Line	SDSS J1043		SDSS J1730	
	EW (Å)	FWHM (km s^{-1})	EW (Å)	FWHM (km s^{-1})
He I 4387	–	–	-9 ± 1	1100 ± 100
He I 4471	-4 ± 1	3300 ± 400	-20 ± 1	1100 ± 100
He II 4686 + He I 4713	-12 ± 2	5000 ± 500	-21 ± 1	2600 ± 200
He I 4921	–	–	-13 ± 1	820 ± 20
He I 5015	-10 ± 2	3200 ± 500	-19 ± 1	1010 ± 30
He I 5875	-16 ± 2	2900 ± 200	-53 ± 2	820 ± 10
He I 6678	-10 ± 2	3000 ± 300	-45 ± 2	730 ± 10
He I 7065	-20 ± 4	3500 ± 300	-40 ± 2	630 ± 40

Values marked '–' could not be measured reliably.

new members of the AM CVn class, although further observations are required to confirm their ultra-compact binary nature and determine their orbital periods.

3.4.1 SDSS J104325.08+563258.1

SDSS J1043 was identified as a candidate dwarf nova in the second *Galaxy Evolution Explorer* Ultraviolet Variability catalog (GUVV-2; Wheatley, Welsh & Browne 2008). This catalog consists of objects identified as varying by more than 0.6 mag in multiple near-ultraviolet observations of $\sim$161 deg^2 of the sky. The repeat observations of SDSS J1043 show two outbursts of >2 mag during the two year window. The Catalina Real-Time Transient Survey (CRTS; Drake et al. 2009) also shows three outbursts of > 2 mag during a $\sim$4.5 year time span.

The quiescent spectrum of SDSS J1043 shows the characteristic helium emission of AM CVn binaries, but is unusual in that it shows absorption wings around these lines. Similar spectra are shown by V406 Hya ($P_{\rm orb} = 33.8$ minutes; Roelofs et al. 2006) and SDSS J1240 ($P_{\rm orb} = 37.4$ minutes; Roelofs et al. 2005), in which the DB absorption features are assumed to be due to the accretor (Roelofs et al. 2004; which is still hot compared to the longer period AM CVn binaries that show no absorption features).

3.4.2 SDSS J173047.59+554518.5

The strong helium lines in SDSS J1730 are comparable to those shown by SDSS J1411 ($P_{\rm orb} = 46$ minutes; Roelofs 2007) and GP Com ($P_{\rm orb} = 46.5$ minutes;

Nather, Robinson & Stover 1981). Together with the absence of helium absorption at shorter wavelengths, this suggests that SDSS J1730 may be at the long period end of the AM CVn period distribution ($P_{\rm orb} \gtrsim 40$ minutes, Rau et al. 2010). Whilst the EWs of the lines are similar to those shown by other known AM CVn binaries, the lines are narrow compared with those shown by other systems in our sample. The small FWHM of the emission lines in SDSS J1730 may indicate a low inclination disc. The lack of obvious double peaked structure to the lines also suggests a low inclination for this system (Horne & Marsh, 1986). SDSS J1730 is the subject of chapter 4, in which it will be studied in more detail.

3.5 The AM CVn equivalent width – period relation

The orbital periods and He I 5875 EWs for AM CVn binaries with emission line spectra are collected in Table 3.5, objects for which no spectrum was available and no measured EW could be found are excluded. Fig. 3.10 shows the correlation of the EW of the He I 5875 emission line with orbital period for AM CVn binaries. There is a general trend for larger EWs with longer binary periods. This is probably due to the drop in continuum flux, against which the lines are measured, due to the cooling of the accreting white dwarf, and drop in accretion continuum as the mass transfer rate decreases towards longer periods. The expected increase in disc size at longer periods, as the orbit expands, may also contribute to the effect.

This trend would not be expected to hold below a period of ∼20 minutes, where the disc is expected to be in a stable high state. ES Cet is included as it shows helium in emission, although it might not be expected to follow the same trend due to its much shorter orbital period. ES Cet in fact shows very strong He II 4686 emission, but the weaker 5875 Å line appears to match the trend of the longer period systems reasonably well.

Whilst there is considerable scatter that prevents an accurate estimate of the orbital period based only on the EW, the relation does suggest a period range in which an object might be expected to be found. Based on Fig. 3.10, SDSS J1043 is expected to have an orbital period between 25 and 45 minutes; SDSS J1721 is expected to have an orbital period in the range 25–55 min; and SDSS J1730 is predicted to have an orbital period between 40 and 55 min.

This trend also demonstrates that AM CVn binaries with orbital periods in excess of 30 min should have emission lines sufficiently strong to be well above our detection threshold. Note that the drop in continuum flux at longer orbital periods is expected to make the longer period systems fainter, and less likely to be found

Table 3.5: Orbital period and EW of the He I 5875 line for the AM CVn binaries with quiescent spectroscopy.

Object	Orbital period (min)	EW (−Å)	References
ES Cet	10.3377 ± 0.0003	5	Warner & Woudt (2002); Espaillat et al. (2005)
CR Boo	24.5217 ± 0.0002	8	Provencal et al. (1997); Espaillat et al. (2005)
V803 Cen	26.61 ± 0.02	6	Roelofs et al. (2007b); Espaillat et al. (2005)
PTF1 J0719	26.77 ± 0.02	14.7 ± 0.3	Levitan et al. (2011)
SDSS J0926	28.31 ± 0.01	8 ± 1	Anderson et al. (2005); Carter et al. (2013)
CP Eri	28.7 ± 0.1	32 ± 2	Abbott et al. (1992); Groot et al. (2001)
PTF1 J0943	30.35 ± 0.06	21.8 ± 0.6	Levitan et al. (2013)
V406 Hya	33.80 ± 0.01	30.3 ± 0.5	Roelofs et al. (2006)
PTF1 J0435	34.31 ± 1.75	49.8 ± 2.0	Levitan et al. (2013)
SDSS J1240	37.355 ± 0.002	31.3 ± 0.5	Roelofs et al. (2005, 2006)
SDSS J0129	37.555 ± 0.003	24.4 ± 0.4	Kupfer et al. (2013)
SDSS J1525	44.32 ± 0.12	16.0 ± 0.3	Kupfer et al. (2013)
SDSS J0804	44.5 ± 0.1	60 ± 1	Roelofs et al. (2009)
SDSS J1411	46 ± 2	65	Roelofs (2007); Anderson et al. (2005)
GP Com	46.567 ± 0.003	77.7 ± 0.3	Marsh (1999); Marsh, Horne & Rosen (1991)
SDSS J0902	48.31 ± 0.08	79 ± 3	Rau et al. (2010)
SDSS J1208	52.56 ± 0.02	19.8 ± 0.4	Kupfer et al. (2013)
SDSS J1642	54.2 ± 0.4	56.8 ± 0.7	Kupfer et al. (2013)
SDSS J1552	56.272 ± 0.005	75	Roelofs et al. (2007c); Anderson et al. (2005)
V396 Hya	65.1 ± 0.7	90	Ruiz et al. (2001); Roelofs et al. (2009)
SDSS J1043	–	16 ± 2	Carter et al. (2013)
SDSS J1721	–	30 ± 6	Rau et al. (2010)
SDSS J1730	–	53 ± 2	Carter et al. (2013)

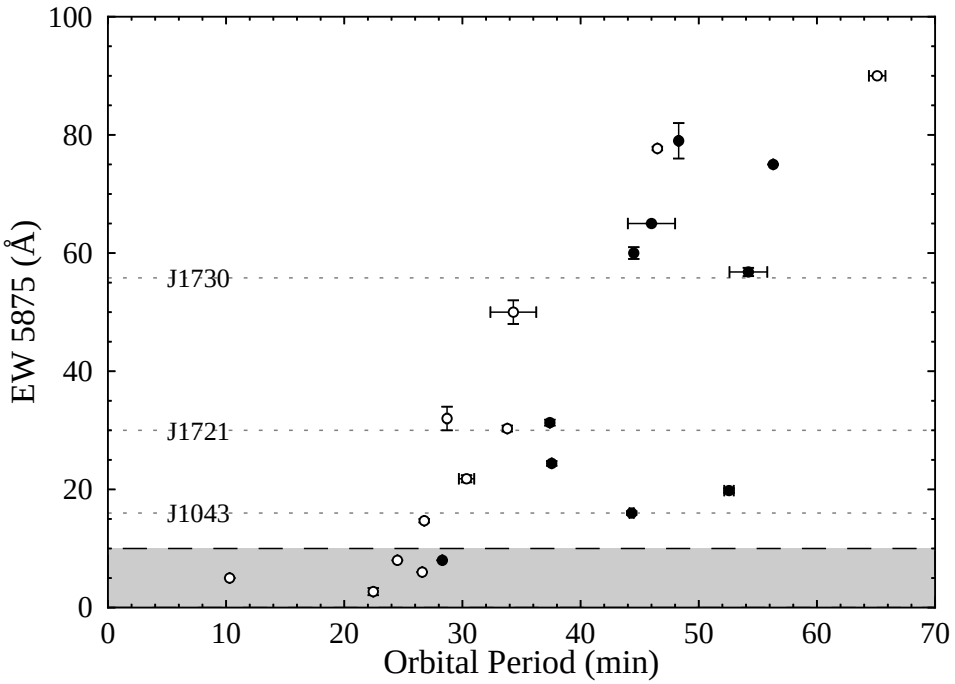

Figure 3.10: EW of the He I 5875 line versus orbital period for AM CVn binaries. The black circles represent those AM CVn binaries discovered from the SDSS. The dotted lines indicate He I 5875 EWs for the AM CVn binaries discovered via this survey whose periods are unknown. The dashed line and shaded area indicate our detection threshold.

within our g-band magnitude cut, or the SDSS spectroscopy. This may introduce a selection bias, only the systems with very strong emission appear sufficiently bright to have been observed, and hence there is the possibility of an undetected population of long period, low EW systems.

3.6 Colours of the sample

The $(u-g,\ g-r)$ and $(g-r,\ r-i)$ colour-colour diagrams of the sample and the colours of the known AM CVn binaries with *ugri* photometry (black stars) are shown in Fig. 3.11. The most significant of the classifications from Table 3.2 are indicated with different symbols. The colours of AM CVn itself may be affected by saturation due to its brightness, it has therefore been excluded. $u-g$ values calculated from the UBV photometry of CR Boo given in table 1 of Wood et al. (1987) (using conversions given by Jordi, Grebel & Ammon 2006), suggest that the colours can vary significantly over an outburst cycle. CR Boo was likely to have been in an intermediate state at the time of the SDSS photometry ($g = 15.6$ compared

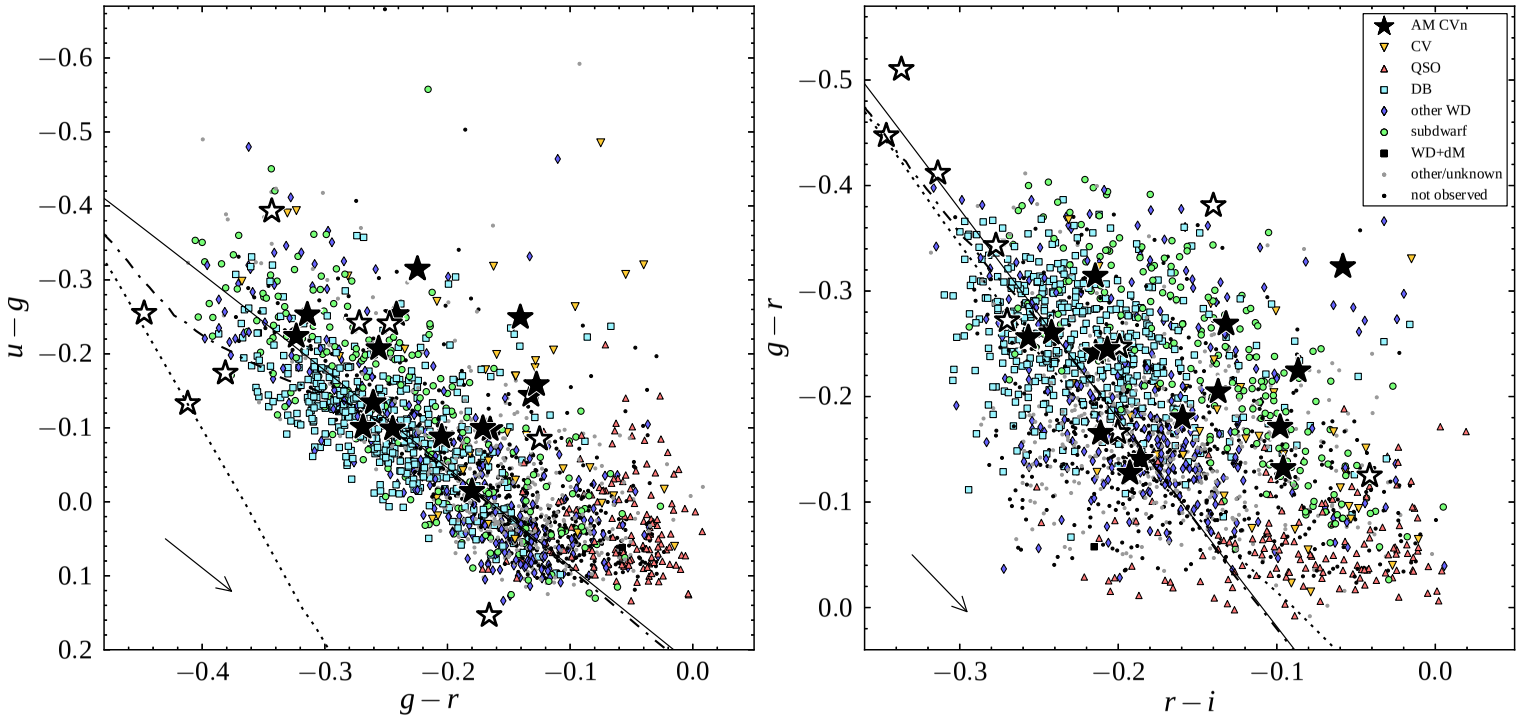

Figure 3.11: Colours of the known AM CVn binaries (black stars) together with our sample of candidates from SDSS DR7. The filled stars are the confirmed longer period systems, and the AM CVn binaries discovered via their emission line spectra in the SDSS or this survey. The open stars represent those systems to which we do not necessarily expect to be sensitive, from left to right (left hand panel) or from top to bottom (right hand panel), these are HM Cnc (right hand panel only), SDSS J1908, SDSS J2047, PTF1 J2219, ES Cet, PTF1 J0943, PTF1 J0435, CR Boo and PTF1 J0857. Colours of the faint systems discovered via the Palomar Transient Factory (PTF) are taken from Levitan et al. (2013). The orange inverted triangles represent CVs. Quasars, DB white dwarfs, other types of white dwarf, subdwarfs, and WD + M dwarf systems are represented by red triangles, cyan squares, blue diamonds, green circles and black squares respectively. Grey dots indicate those candidates that could not be classified, and black dots those that have not yet been observed. The solid line shows the blackbody cooling track, the dotted and dot-dashed lines represent the DA and DB white dwarf cooling tracks, and arrows represent reddening vectors for an extinction $A(g) = 0.2$.

to $g \simeq 17.1$ in quiescence, based on photometry from Wood et al. 1987), which may have caused the unusual $u-g$ colour. The seven systems discovered in the observed part of the sample further constrain the region of colour space occupied by AM CVn binaries.

It should be noted that the survey targets the specific area of colour–colour space in which the AM CVn binaries in the SDSS spectroscopic database are found. We are therefore only capable of finding systems that share these colours, and any long period AM CVn binaries that lie outside this colour box will remain undetected. The biases in the SDSS spectroscopic database are discussed by Roelofs, Nelemans & Groot (2007) and Roelofs et al. (2009), they conclude that it is unlikely that a large fraction of AM CVn binaries lie outside this region. This improved understanding of the colour box will be explored further in chapter 6.

3.7 Estimating the AM CVn binary space density

The discovery of only seven AM CVn binaries in the 73 per cent of the sample that has been observed, taking into account our spectroscopic completeness (Fig. 3.3), indicates the presence of significantly fewer AM CVn binaries in the SDSS photometric database than initially estimated by Roelofs, Nelemans & Groot (2007) and Roelofs et al. (2009). They estimated that there should be ∼40 new AM CVn binaries in the original sample of ∼1500 candidates from SDSS DR6 (there are ∼2000 objects in the DR7 sample). This suggests that the space density of AM CVn binaries is lower than previously predicted, or that there is some problem with our understanding of the biases in our sample, or the population models. Based on the analysis of the SDSS spectroscopic completeness presented in Roelofs, Nelemans & Groot (2007) and Roelofs et al. (2009), I consider the former to be likely.

Fig. 3.3 shows that our follow-up is almost complete to a depth of $g = 19$. I use this essentially complete sample of the brighter objects in the AM CVn colour box to adjust earlier space density estimates, although the large uncertainty resulting from such small samples must be noted. Following the prescription of Roelofs, Nelemans & Groot (2007), and taking the completeness to be unity, I calculate the expected magnitude distribution of the AM CVn binaries in the SDSS photometric database. The number of systems expected is then compared to the number found in the SDSS DR7 area.

Based on the optimistic model from Nelemans et al. (2001) and Nelemans, Yungelson & Portegies Zwart (2004), and the six AM CVn binaries discovered in the SDSS spectroscopy, Roelofs, Nelemans & Groot (2007) calculated an observed space

density of $1.5 \times 10^{-6}\,\mathrm{pc}^{-3}$. This corresponds to an expected 35 AM CVn binaries to a depth of $g = 20.5$ (see Table 3.6) in the DR5 photometric database (note that this number is essentially independent of the formation channel; see table 1 of Roelofs, Nelemans & Groot 2007). To find the distribution of systems the population synthesis predicts for our sample, I multiply the Roelofs, Nelemans & Groot (2007) distribution by the ratio of the photometric area of DR7 ($11\,663\,\mathrm{deg}^2$) to that of DR5 ($8000\,\mathrm{deg}^2$), $\sim$1.46. This gives expected numbers of 11 systems with $g \leq 19$, and 51 systems with $g \leq 20.5$.

I use the 4 long period emission line AM CVn binaries found in our essentially complete $g \leq 19$ sample to scale the expected numbers and observed space density (see Table 3.6). This gives the total number of AM CVn binaries expected in the DR7 photometry ($g \leq 20.5$) as 18, corresponding to a space density for AM CVn binaries of $5 \times 10^{-7}\,\mathrm{pc}^{-3}$.

The small sample of 4 known AM CVn binaries with $g \leq 19$ contributes an intrinsic uncertainty of 50 per cent to the derived space density. Roelofs, Nelemans & Groot (2007) estimate the uncertainties in the parametrization of temperature and absolute magnitude with orbital period as leading to $\sim$10 per cent and $\sim$32 per cent variations in the result. Combining these contributions leads to an estimated 60 per cent uncertainty in our value for the space density.

The space density calculations assume models for the intrinsic magnitude distribution of the AM CVn binaries (Roelofs, Nelemans & Groot, 2007). It is clear from Fig. 3.3 that we find an increasing number of these systems towards fainter magnitudes. This may reduce the discrepancy between the previously predicted space density and the numbers of systems found so far in our sample, but it may also indicate a significant deviation from the modelled magnitude distribution.

3.8 Discussion

3.8.1 Survey completeness

The results from our survey so far significantly improve our knowledge of the colours of AM CVn binaries, and the other objects found in the same region of colour space. The seven new AM CVn binaries lie in the central area of the selected colour region, implying that the initial selection should indeed have contained the majority of AM CVn binaries.

Fig. 3.12 shows the spectroscopic completeness of the survey colour box, combining both SDSS spectroscopy and our own. Our spectroscopic followup has been conducted without any specific colour bias beyond the initial selection criteria.

Table 3.6: Expected numbers of AM CVn binaries in the AM CVn colour box and corresponding space densities. Note that Roelofs, Nelemans & Groot 2007 use a depth of $g \simeq 21$, whereas our survey has a limit of $g \simeq 20.5$.

Distribution	Expected number of AM CVn binaries			Space density (pc^{-3})
	$g \leq 19$	$g \leq 20.5$	$g \leq 21$	
Roelofs, Nelemans & Groot (2007) DR5 area	8	35	53	1.5×10^{-6}
Roelofs, Nelemans & Groot (2007) DR7 area	11	51	77	1.5×10^{-6}
Scaled to $g \leq 19$ sample (DR7)	4	18	27	$(5 \pm 3) \times 10^{-7}$

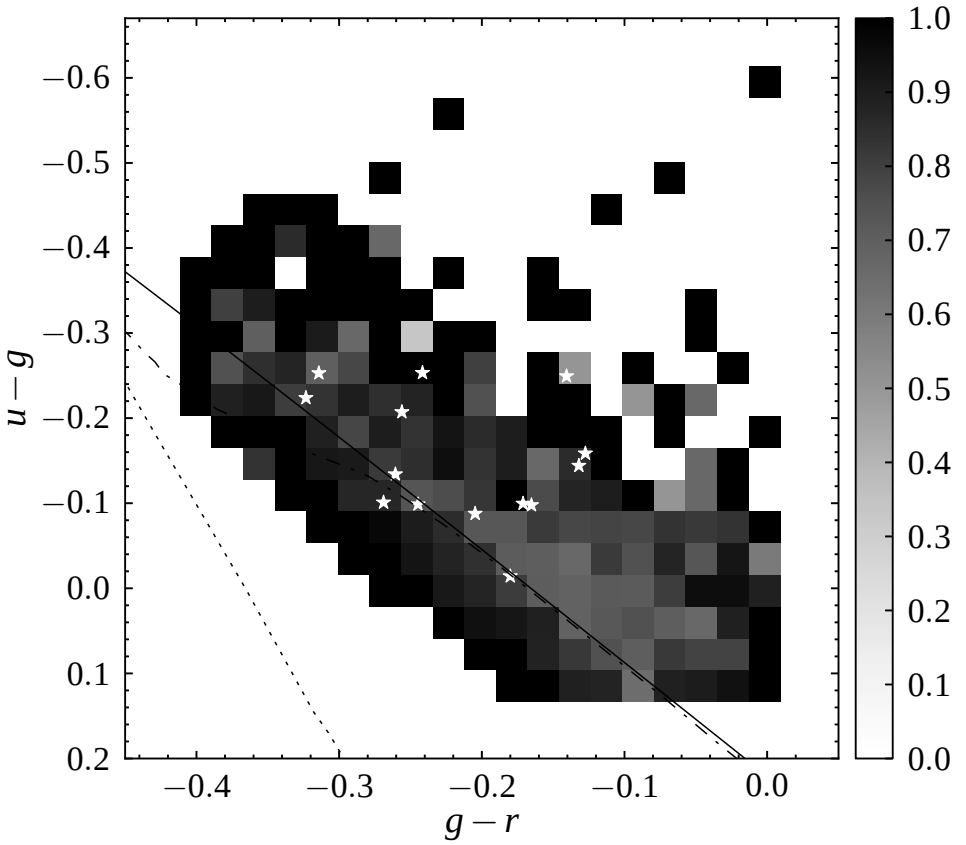

Figure 3.12: Completeness of the survey as a function of colour, $u-g$ and $g-r$, to a limiting magnitude $g = 20.5$ (dereddened), including both SDSS spectroscopy and our own. The AM CVn binaries with spectra taken as part of the SDSS or this survey, are indicated by star symbols. The solid line marks the blackbody cooling track, the dotted and dot-dashed lines indicate model cooling sequences for DA and DB white dwarfs.

However, the magnitude bias shown in Fig. 3.3 leads to a slight bias towards the bluer part of the $(u-g,\ g-r)$ distribution. The lower density of objects at the edges of our survey area leads to a significantly higher completeness. There is no clear bias that would affect the AM CVn distribution we observe.

The observed trend of increasing EW of emission lines with orbital period, coupled with the expectation that AM CVn binaries will evolve rapidly to longer periods, allows us to be confident that we are able to detect the majority of the population. This is important as I intend to use the number found to estimate the space density of the entire population. The EWs of the SDSS AM CVn binaries with unknown periods suggest that many of them are at the shorter period end of the expected distribution (see Roelofs, Nelemans & Groot 2007). This suggests that there should be more systems with $P_{\rm orb} > 50\,{\rm min}$ yet to be discovered in our sample, as this is where AM CVn binaries should accumulate due to their gravitational wave-driven evolution (Nelemans et al., 2001; Nissanke et al., 2012).

3.8.2 The space density

Using our essentially complete $g \leq 19$ sample, I calculate the expected number of AM CVn binaries in SDSS DR7 to be 18 ± 9 ($g \leq 20.5$). Since we know of 15 longer period systems with SDSS photometry[2], this suggests that there should be 3 undiscovered systems left in our sample, though the considerable uncertainty on this number leaves us unable to make firm predictions. From the spectroscopic completeness as a function of g-band magnitude (Fig. 3.3), we would expect to find $\sim$5 more systems in the remainder of our sample, giving a total of 19 AM CVns. Considering the different causes for the uncertainties in each case, it is reassuring that this number is consistent with the number derived from our revised space density estimate.

Roelofs, Nelemans & Groot (2007) calculated the AM CVn space density to be $1.5 \times 10^{-6}\,{\rm pc}^{-3}$, based on the six systems found in the SDSS spectroscopic database. Our revised value is 3 times lower than this, and 50 times lower than the optimistic model from Nelemans et al. (2001)'s population synthesis predicts.

Nissanke et al. (2012) suggest that the lower space density could be explained by a change to the Galactic disc model used by Nelemans et al. (2001). The distances of AM CVn binaries from our solar system, and hence the amplitude of their gravitational wave signal, depends upon the assumed scale height for AM CVn binaries

[2]This number includes the 6 systems discovered in the SDSS spectroscopy, the 7 systems discovered via our survey, GP Com, and SDSS J1427-0123 – which has not been observed spectroscopically by us or the SDSS.

in the Galaxy. In the proposed alteration (Nissanke et al., 2012), the old systems, that are the ones we would detect as emission line systems in the SDSS sample, have a larger scaleheight, and so are farther away. However, the young systems, that are the majority of those that would be detected via their gravitational wave emission, remain unchanged from the original distribution (Nelemans et al., 2001; Nelemans, Yungelson & Portegies Zwart, 2004). This results in the same total numbers of AM CVn binaries in the Galaxy, but the long period systems are at greater distances, and are hence fainter. This could explain why optical surveys find fewer systems than predicted by Nelemans et al. (2001) and Roelofs, Nelemans & Groot (2007), but has no significant effect on the numbers of AM CVn binaries detectable by space-based gravitational wave missions (compare cases 1 and 5 shown in table 2 and table 3 of Nissanke et al. 2012).

Alternatively, the lack of systems could be explained through problems with the binary population synthesis; if fewer systems than expected survive to become stable mass transferring AM CVn binaries, the predicted space density would fall. It should be noted that there is a large intrinsic uncertainty in the population synthesis numbers, this is why Nelemans et al. (2001) have optimistic and pessimistic models. It is also possible that the discrepancy is so large that it can only be explained by changes to both the population synthesis and the expected brightness distribution of the AM CVn binaries.

This survey is based on the colours of the known emission line AM CVn binaries, and hence targets the long period systems ($P_{\rm orb} > 30\,{\rm min}$). Whilst the majority of all systems fall within our colour box, we are only sensitive to intermediate period systems in their low state. In their high state these AM CVn binaries normally appear much like DB white dwarfs, and if they were also in their high state at the time the SDSS observed them, we would be unable to recognise them as AM CVn binaries. It should be noted that a small percentage of the total AM CVn population should be found as outbursting systems. I estimate that AM CVn binaries spend less than 6 per cent of their lifetime in this state. These frequent outbursting systems ($20 \gtrsim P_{\rm orb} \gtrsim 30\,{\rm min}$) can be detected more efficiently from their variability, using synoptic surveys, as in the case of PTF1 J0719+4858 (Levitan et al., 2011, 2013). Follow-up of these systems, however, may be more challenging as they are only expected to be found in significant numbers by increasing the depth of the search. SDSS J1043 is particularly interesting as it represents the overlap between these two methods, detected as a result of both its colours and its variability. These complimentary methods mostly sample different parts of the AM CVn orbital period distribution, and together, will lead to a better understanding of both this period

distribution, and the space density.

3.9 Summary

In this chapter I have described the status of our spectroscopic survey aimed at uncovering the expected hidden population of AM CVn binaries in the SDSS photometric database. The results currently indicate a lower space density than predictions suggest. Based on the brighter part of our sample, I have calculated an observed space density of $(5 \pm 3) \times 10^{-7}\,\mathrm{pc}^{-3}$.

I have presented two candidate AM CVn binaries recently found via this survey, SDSS J1043 and SDSS J1730. SDSS J1043 exhibits the helium absorption and low EW emission lines shown by the AM CVn binaries with orbital periods below ∼40 minutes. SDSS J1730 shows strong helium emission lines with no helium absorption at shorter wavelengths; together with the large He I 5875 EW, this suggests it has a longer orbital period. Follow-up observations of SDSS J1730 will be presented in the next chapter.

I also investigated the CVs discovered via this survey, and compared them to the CVs discovered via SDSS spectroscopy. We saw that these are largely similar, and also identified a CV with atypically strong helium emission.

The rest of this thesis focuses on further observations of objects identified in this chapter, and their implications for the AM CVn binary population. I will then discuss the methods I have developed to improve the efficiency of this survey.

Chapter Four

The AM Canum Venaticorum binary SDSS J1730+5545

4.1 Introduction

In this chapter I study the AM CVn binary SDSS J173047.59+554518.5 in more detail. This object, presented in the preceding chapter, was discovered via our survey due to its strong helium emission lines. Characterisation of the survey sample requires detailed follow-up observations after the initial discovery, in order to determine the orbital period, and confirm the ultra-compact binary nature of the candidate systems.

Here I present time-resolved spectroscopy of SDSS J1730, which I use to search for the periodic motion expected in a binary system. I then compare SDSS J1730 to other AM CVn systems, and discuss several interesting features of its spectrum.

4.2 Observations and data reduction

Optical spectroscopy of SDSS J1730 was obtained on 2012 May 21 with the Gemini Multi-Object Spectrograph (GMOS; Hook et al. 2004) at the Gemini-North telescope on Mauna Kea, Hawaii. The observations consist of 54 spectra, obtained using the B600+ grating with a 180 s exposure time. GMOS has three 2048×4608 e2v deep depletion CCDs, which were used in six amplifier mode. The resulting spectra cover the wavelength range 4120 – 6973 Å, with a resolution of ∼5.46 Å.

The GMOS observations were carried out with a 1.0 arcsec slit; 4×4 binning and 'slow' readout mode were used to minimise the read-out noise.

Table 4.1: Log of our observations of SDSS J1730.

Date	UT	Exposure time (s)	Exposures
Gemini/GMOS			
2012 May 21	10:45–13:34	180	54
WHT/ISIS			
2012 July 13	22:21–03:16	300	54
2012 July 14	21:14–03:24	300	67
2012 July 15	23:09–03:28	300	42

A second, longer set of phase-resolved spectra of SDSS J1730 were obtained on 2012 July 13, 14 and 15 on the William Herschel Telescope (WHT), situated on the island of La Palma, with the Intermediate dispersion Spectrograph and Imaging System (ISIS). These observations consist of 163 spectra obtained with 300 s exposures using the R600B grating in the blue arm and the R600R grating in the red arm. The resulting spectra cover the wavelength range 3750–5260 Å and 5540–7125 Å, with a spectral resolution of ∼2.43 Å in the blue arm, and ∼2.18 Å in the red arm.

All ISIS observations used 4×2 binning and a 1.2 arcsec slit. The detectors were used in 'slow' readout mode to minimise the read-out noise. The slit was kept at a fixed position angle of 145.3° in order to observe both SDSS J1730 and a nearby comparison star (SDSS J173050.53+554442.5, 44 arcsec southeast of SDSS J1730) simultaneously.

Bias subtraction was achieved using average bias frames constructed from bias frames taken each night. Normalized flatfield frames were constructed by averaging a series of tungsten lamp flatfield frames obtained during each night, additionally, for the ISIS observations, spatial profile correction was achieved using nightly averaged twilight flatfields.

Wavelength calibration was obtained from CuAr arc lamp exposures taken at the start, middle and end of the three hour GMOS observing block, and CuNeAr arc exposures obtained every ∼40 minutes for the duration of our ISIS observations of SDSS J1730. Fourth order polynomial fits to reference lines resulted in ∼0.15 and ∼0.05 Å rms residuals for the GMOS and ISIS spectra. Each exposure was wavelength calibrated by interpolating the solutions obtained from the two closest arcs, in order to correct for instrument flexure.

The comparison star spectra were used to correct the ISIS spectra of

SDSS J1730 for time and wavelength dependent slit-losses. The individual comparison star spectra were divided by the master comparison star spectrum obtained at lowest air mass. These ratio spectra were fitted with a second order polynomial, and the spectra of SDSS J1730 corrected by dividing by the corresponding polynomial fit. The ISIS spectra were flux-calibrated and corrected for instrumental response using the spectrophotometric standard star BD+28 4211.

All spectra were reduced using optimal extraction as described in chapter 2. Spectra were wavelength and flux calibrated using MOLLY. Our spectroscopic observations are summarised in Table 4.1.

4.3 Results

4.3.1 Average spectral features

The average GMOS spectrum of SDSS J1730 is shown in Fig. 4.1. It shows strong, narrow He I emission lines, as well as several He II lines.

Many of the He II lines in the optical region have wavelengths very close to those of lines in the hydrogen Balmer series, which could make identification of broad lines difficult. In order to ascertain whether the lines seen in the spectrum of SDSS J1730 are due to He II or H, we must consider the expected relative strengths of the lines (e.g. the relative strengths of the Balmer lines in the CVs shown in Fig. 3.5). Given that the weak He II 5411 Å line (for which there is no nearby H line) is detected, and the absence of a line close to Hγ (4340 Å), I associate the emission close to 6559 and 4859 Å with He II, and not with hydrogen. There is no clear sign of the accreting white dwarf in the spectrum.

Several lines of Fe, N, Si and Ne are also identified. Metal lines are often seen in quiescent AM CVn spectra (e.g. Roelofs et al., 2006, 2009; Kupfer et al., 2013; Levitan et al., 2013), however, neon has only previously been identified in the much brighter system GP Com (Marsh, Horne & Rosen, 1991; Nelemans et al., 2010).

The ISIS spectrum (Fig. 4.2) shows a blue continuum, and reveals the double-peaked line profiles expected from the accretion disc. The red wing of the He I 5875 line shows contamination from an emission feature around 5893 Å which is identified as being caused by the Na D doublet. Roelofs et al. (2006) reported similar blending in the spectra of SDSS J1240-0159 and V406 Hya. This feature is puzzling as any sodium in the disc should be largely ionized at the temperatures required to produce most of the emission lines observed (see Marsh, Horne & Rosen, 1991, for further discussion).

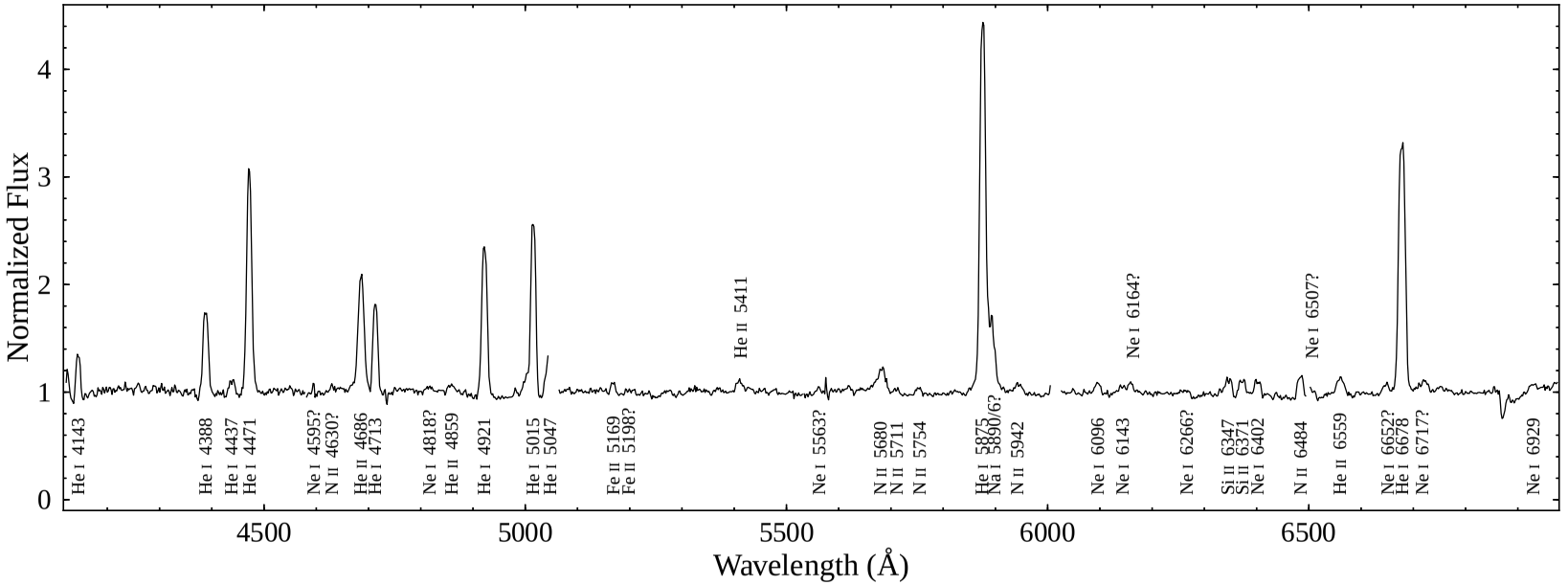

Figure 4.1: Normalized average spectrum of SDSS J1730 obtained with GMOS. The strong helium lines are prominent, in addition many weak metal lines are detected. The small gaps at 5055 and 6015 Å are due to gaps between the individual CCDs.

Figure 4.2: Average spectrum of SDSS J1730 obtained with ISIS. The prominent lines have been labelled.

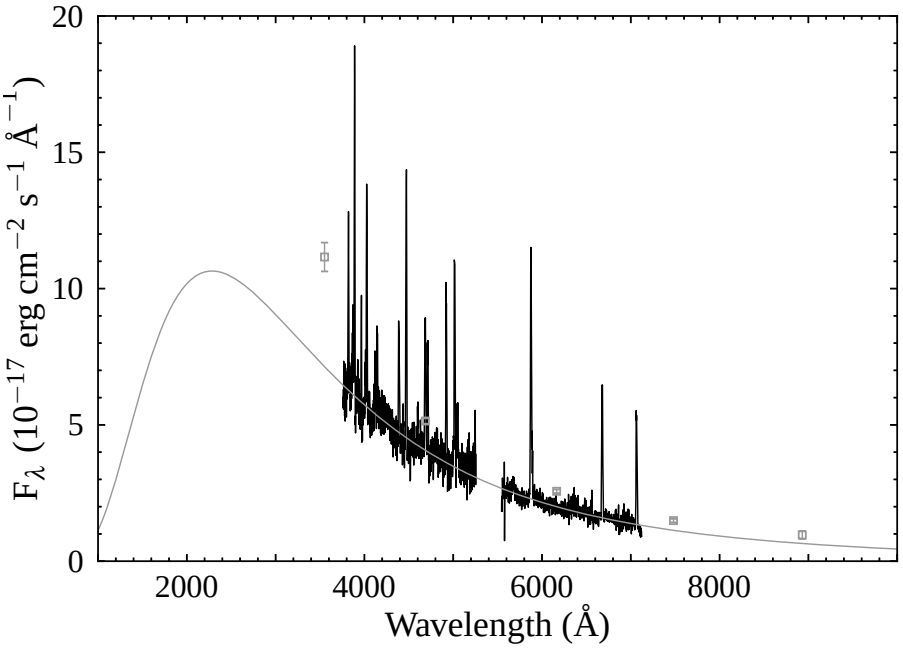

Figure 4.3: Flux calibrated ISIS average spectrum of SDSS J1730 together with SDSS photometric fluxes (grey squares). The grey line overplotted is a blackbody fit to the spectrum, $T = 12\,700 \pm 100$ K. Data have been corrected for Galactic extinction.

Table 4.2 shows the EW and FWHM of the prominent lines in the average spectra of SDSS J1730. The narrow emission lines, that reveal their double-peaked nature clearly in the higher resolution ISIS spectra, imply a low inclination (Horne & Marsh, 1986). This also results in a low radial velocity amplitude, which makes the periodic motion of the binary difficult to measure. In chapter 3 I used the EW of the He I 5875 line to predict an orbital period of 40–55 minutes based on the known population of AM CVn binaries (Carter et al., 2013).

I fit the average flux-calibrated spectrum with a blackbody, masking the obvious emission lines, obtaining a continuum temperature $T = 12\,700 \pm 100$ K. I give here the formal uncertainty in the fit, note that this does not reflect the considerable uncertainties in the contributions of the white dwarf and the disc to the continuum (see Bildsten et al., 2006). The data were corrected for Galactic extinction using the $R_V = 3.1$ prescription of Fitzpatrick (1999) and the full Galactic reddening according to Schlegel, Finkbeiner & Davis (1998), $E(B-V) = 0.047$. Without correction for extinction I obtain a temperature of 11 600 K.

Table 4.2: EW and FWHM of prominent lines in SDSS J1730.

Line	GMOS		ISIS	
	EW (Å)	FWHM (km s^{-1})	EW (Å)	FWHM (km s^{-1})
He I 3819	–	–	-9.2 ± 0.7	670 ± 40
He I 3867	–	–	-4.6 ± 0.7	970 ± 130
He I 3888	–	–	-16.3 ± 1.0	550 ± 30
He I 3964	–	–	-4.4 ± 0.7	480 ± 60
He I 4026	–	–	-14.3 ± 0.7	650 ± 30
He I 4120	–	–	-3.4 ± 1.0	630 ± 150
He I 4143	-3.1 ± 0.4	550 ± 50	-5.0 ± 0.8	670 ± 80
He I 4388	-8.3 ± 0.4	680 ± 20	-9.2 ± 0.7	620 ± 30
He I 4437	-1.2 ± 0.4	670 ± 170	-1.7 ± 0.6	600 ± 170
He I 4471	-23.7 ± 0.4	705 ± 10	-24.4 ± 0.7	660 ± 20
He II 4686	-15.1 ± 1.2	830 ± 50	-13.7 ± 1.3	730 ± 50
He I 4713	-9.0 ± 0.3	620 ± 20	-10.3 ± 0.7	610 ± 30
He I 4921	-16.6 ± 0.4	650 ± 10	-17.6 ± 0.8	620 ± 20
He I 5015	-18.4 ± 0.4	610 ± 10	-22.6 ± 0.9	590 ± 20
He I 5047	...	...	-8.0 ± 1.0	920 ± 90
Fe II 5169	-0.9 ± 0.2	470 ± 70	-3.0 ± 1.0	750 ± 190
He II 5411	-1.7 ± 0.3	860 ± 100	–	–
N II 5680	-4.4 ± 0.4	1050 ± 70	-4.4 ± 1.1	1200 ± 200
He I 5875	-47.1 ± 1.1	660 ± 10	-55.8 ± 1.3	640 ± 10
Ne I 6096	-1.1 ± 0.3	510 ± 90	-1.1 ± 0.6	500 ± 200
Si II 6347	-2.3 ± 0.3	670 ± 60	-3.3 ± 0.7	570 ± 100
Si II 6371	-2.3 ± 0.3	660 ± 60	-3.7 ± 1.0	820 ± 160
Ne I 6402	-2.0 ± 0.3	610 ± 60	-3.0 ± 0.9	630 ± 150
N II 6484	-2.3 ± 0.3	490 ± 50	-2.8 ± 0.7	470 ± 90
He II 6559	-2.8 ± 0.2	730 ± 50	-3.1 ± 1.0	610 ± 160
He I 6678	-34.8 ± 0.6	590 ± 10	-44.1 ± 1.1	560 ± 10
He I 7065	–	–	-48.9 ± 1.8	540 ± 10

Note: The values marked '...' could not be measured reliably. The values marked '–' indicate that the line falls outside the wavelength coverage.

4.3.2 The spectroscopic period

To find the spectroscopic period the radial velocity variation of the He I emission lines was measured using MOLLY. I tried several methods for measuring the radial velocities, finding that the methods described by Schneider & Young (1980) require averaging of the radial velocities from several lines in order to reveal periodic motion.

I therefore used an alternative approach, fitting each line with a single Gaussian and allowing the common velocity offset to vary, as described in chapter 2. The 6 strongest lines excluding He I 5875 (which causes a significant offset, probably due to contamination from the nearby Na feature) were used for the GMOS spectra, and the 11 strongest He I lines for the ISIS spectra. The fitting procedure thus yields, for each spectrum, a single value for the radial velocity, with a much greater precision than could be obtained for any single line. This allows us to detect the low amplitude velocity variations exhibited by SDSS J1730.

A radial velocity curve was constructed from these measurements, and the Lomb-Scargle periodogram (Scargle, 1982) calculated; assuming that the strongest peak corresponds to the orbital period. The radial velocities were then fit with a circular orbit as given by equation (2.11), where $P_{\rm orb}$ is fixed to the value derived from the strongest peak in the periodogram.

I show the Lomb-Scargle periodogram calculated from the He I radial velocities in Fig. 4.4. A clear signal is seen around 40.86 cycle d^{-1}, corresponding to a period of 35.2 minutes. As well as the obvious ± 1 cycle d^{-1} aliases, there is a fine alias structure caused by the $\sim$2 month offset between the Gemini and WHT observations. The He I radial velocity curve, folded on this period, is shown in Fig. 4.5. The parameters of the fits to equation (2.11), derived from the radial velocity measurements, are shown in Table 4.3. The zero phase, HJD$_0$, is defined by the blue to red crossing of the velocities.

Various sets of lines were tried, showing that the exact choice has no effect on the period, I therefore use the maximum possible number of (strong) lines. The Lomb-Scargle derived period was also compared to the value derived using the phase dispersion minimisation method (Stellingwerf, 1978), which gave consistent results. Some distortion of the systemic velocity due to the contamination of the He I 5875 line in the ISIS spectra cannot be ruled out, however, I find consistent values for γ when including or excluding this line, and so include it for the ISIS radial velocity measurements in order to increase the signal-to-noise ratio.

The uncertainty on the period was estimated by carrying out 1000 bootstrap selections of the radial velocity curve, as outlined in chapter 2. For each subset, 217 radial velocities were selected from the full radial velocity curve, allowing for points

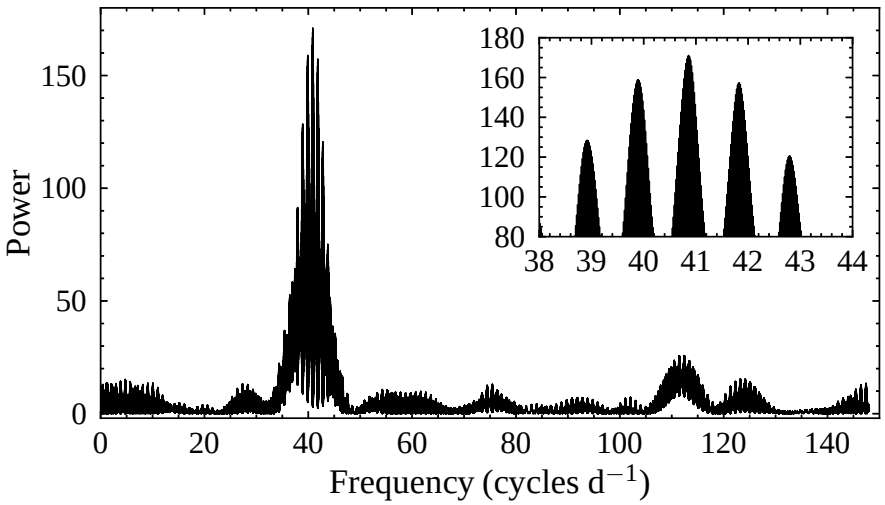

Figure 4.4: Lomb-Scargle periodogram calculated from the He I radial velocities of SDSS J1730. The inset shows the detail around the peak.

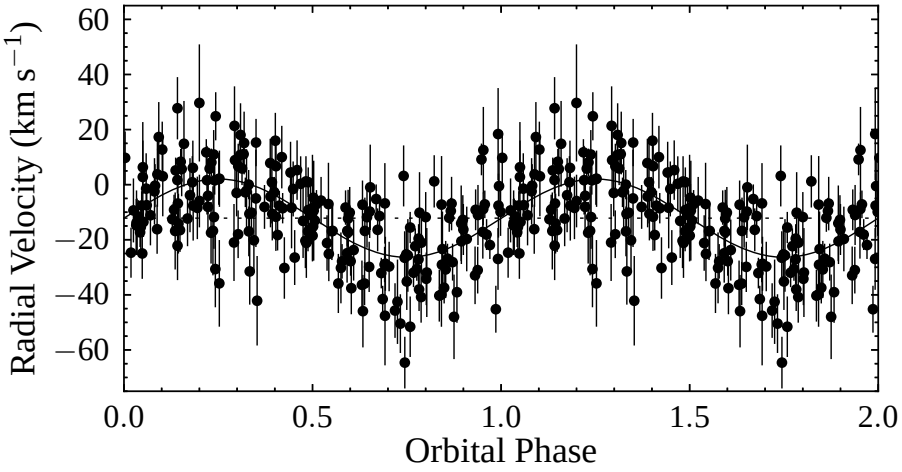

Figure 4.5: Measured He I radial velocities folded on a period of 35.2 minutes. The solid and dotted lines are the best fit radial velocity curve and systemic velocity, the parameters are shown in Table 4.3.

Table 4.3: Orbit parameters derived from radial velocity measurements. The orbital period is taken as the strongest peak in the periodogram, and its uncertainty derived using the bootstrap method. The zero phase, velocity amplitude and systemic velocity, and their corresponding uncertainties, result from the fit to equation (2.11).

$P_{\rm orb}$ (min)	$\rm HJD_0$	K (km s^{-1})	γ (km s^{-1})
35.2 ± 0.2	2456068.9549(3)	14.2 ± 1.1	-12.2 ± 0.8

to be selected more than once, and the periodogram calculated, taking the strongest peak as the period. The standard deviation of these computed periods, 0.2 min, is taken as a measure of the uncertainty in the derived orbital period.

Note that there is significant power in the $\pm 1\,\mathrm{cycle\,d^{-1}}$ aliases seen in Fig. 4.4, which correspond to periods of 34.4 and 36.1 minutes (see also the next section).

4.3.3 Dynamic spectrum

Trailed spectra for the strongest lines, folded on the measured orbital period, 35.2 minutes ($40.9\,\mathrm{cycles\,d^{-1}}$), are shown in Fig. 4.6. Some variability is evident in the trailed spectra, but the S-wave – commonly caused by the bright spot, formed by the impact of the accretion stream onto the outer disc – is clearly discernible only in the He I 6678, 7065 and combined He I line trails. The trailed spectra are also displayed with the average line profile subtracted in order to enhance the variability. The corresponding Doppler tomograms (Marsh & Horne, 1988) give a similar picture of emission in the disc. A bright region or spot is visible in most of the lines shown. Since these maps were calculated using the assumed zero phase, $\mathrm{HJD}_0 = 2456068.9549$, the maps may be rotated due to the unknown phase shift between our zero phase and the true zero phase of the white dwarf.

Doppler maps created at the frequency of the strongest peak in the periodogram and on the daily aliases show a weak preference for the central frequency, however, the $\pm 1\,\mathrm{cycle\,d^{-1}}$ aliases cannot be ruled out due to the lack of a strong bright spot.

4.4 Discussion

4.4.1 Current state

I have measured an orbital period $P_{\mathrm{orb}} = 35.2 \pm 0.2$ minutes, confirming SDSS J1730 as an ultracompact binary. This puts SDSS J1730 in the longer period region of the outbursting AM CVn binary period distribution, and we would expect that the system would spend the majority of its time in a low state (with appearance similar to that observed here), with infrequent, longer-duration outbursts, similar to those observed in V406 Hya ($P_{\mathrm{orb}} = 33.8$ min; Roelofs et al. 2006) and SDSS J0129 ($P_{\mathrm{orb}} = 37.6$ min; Kupfer et al. 2013) (Ramsay et al., 2012). Note that the CRTS (Drake et al., 2009) lightcurve appears to show the decline from a single outburst during its 7 year coverage. SDSS J1730 was detected in outburst by the CRTS on 2014 April 02, demonstrating the expected behaviour. The measured period is

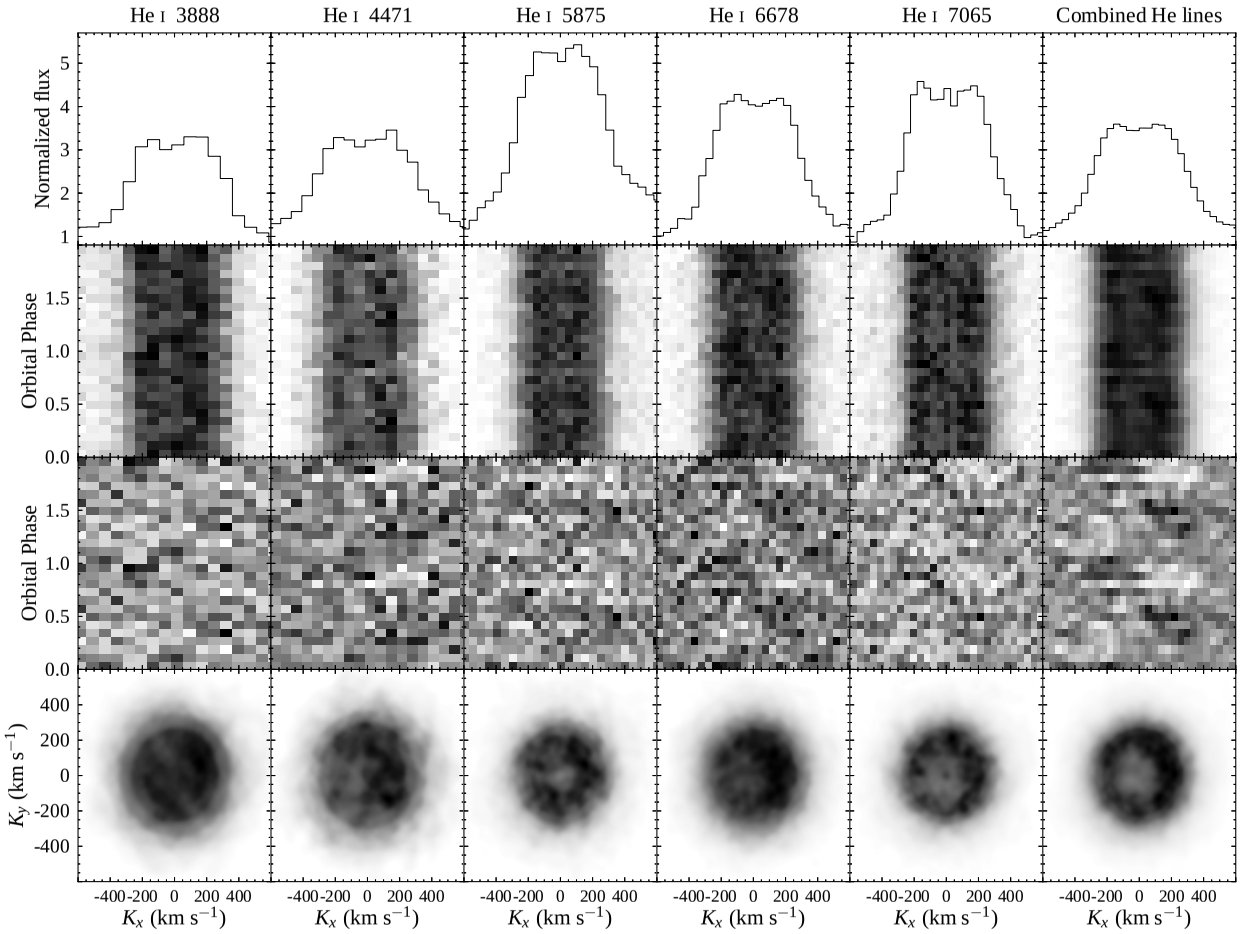

Figure 4.6: Average line profiles, phase-folded trailed spectra and Doppler maps for the strongest lines, and a combination of the 8 strongest He I lines. Here only the higher resolution ISIS spectra are used. The second row of trailed spectra have the average line profile subtracted in order to enhance the variability.

slightly shorter than I estimated in chapter 3 from the EW of the He I 5875 emission line (Carter et al., 2013), but does not indicate a significant deviation from the trend of EW increasing with orbital period.

Using double Gaussian fits to the emission lines I find an average peak separation of $320\,\mathrm{km\,s^{-1}}$. The velocities of the two peaks in the line profile produced by an accretion disc are related to the Keplerian velocity at the outer radius of the disc, and the inclination (Smak, 1981; Horne & Marsh, 1986). Thus the velocities estimated for the peaks, $\pm\,160\,\mathrm{km\,s^{-1}}$, can be used to constrain the inclination of the disc in SDSS J1730, with some assumptions about the masses of the two components, and the outer radius of the disc. In order to place a reasonable upper limit on the inclination I adopt a primary mass, $M_1 = 0.6\,\mathrm{M_\odot}$, and mass ratio, $q = 0.01$. Taking 80 percent of the volume radius of the Roche lobe of the primary (Eggleton, 1983) as an estimate of the maximum disc radius, gives an inclination, $i \leq 11^\circ$.

The measured separation of the peaks in the line profiles also places an upper limit on the velocity of the donor, $K_2 \leq 160\,\mathrm{km\,s^{-1}}$. Assuming that the measured radial velocity amplitude reflects the motion of the primary, K_1, this gives a mass ratio, $q \geq 0.09$. This is larger than typically found in AM CVn binaries with similar orbital periods (Roelofs et al. 2005, 2006; Armstrong, Patterson & Kemp 2012 and references therein; Kupfer et al. 2013), and it is expected that K_1 is in fact much smaller than this estimate. The radial velocity amplitude likely overestimates K_1 due to contamination by the higher velocity S-wave (Smak, 1970; Rayne & Whelan, 1981).

Bildsten et al. (2006) predict white dwarf surface temperatures in the range $\sim$13 000 – 27 000 K for an AM CVn binary with an orbital period of 35 minutes; the similar period systems V406 Hya and SDSS J1240−0159 both have estimated white dwarf temperatures of 17 000 K (Roelofs et al., 2004; Bildsten et al., 2006). Our estimate for SDSS J1730 is at the lower end of the expected range, however, at the orbital period of this system the disc may contribute significantly to the flux in quiescence (Bildsten et al., 2006), especially with the disc being so close to 'face-on'. The temperature of the accreting white dwarf may therefore be higher than this estimate from the continuum. The spectra of SDSS J1730 show no sign of helium absorption from the accretor, a feature that has been observed in several AM CVn binaries with orbital periods of 30–40 minutes (e.g. Roelofs et al., 2006). This would not be unexpected for a white dwarf with a temperature of 12 700 K, for which the disc would easily hide the weak absorption lines; however, a hotter accretor would require that the disc is still relatively bright in comparison.

4.4.2 Evolutionary history

Metals are often detected in the quiescent spectra of AM CVn binaries, and have been used to constrain the evolutionary history of some systems (Marsh, Horne & Rosen, 1991; Nelemans et al., 2010). In particular the presence of nitrogen lines without the detection of carbon/oxygen would suggest a helium white dwarf donor (Nelemans et al., 2010). With N II and Ne I lines detected in the spectrum, we would expect to see strong carbon and oxygen features (Marsh, Horne & Rosen, 1991, found that large N/C and N/O ratios were required to suppress these lines). The spectral range does not extend far enough into the red to cover the wavelengths of many of the strongest carbon, nitrogen and oxygen lines, so the N/C or N/O ratio cannot be strongly constrained with this data. That nitrogen lines are seen but the C II lines at 4267 and 6580 Å are missing, implies an overabundance of nitrogen that likely rules out all but the least-evolved helium star donors (Yungelson, 2008; Nelemans et al., 2010).

Models of helium accretion discs with solar metal abundances predict that Si II 6347 and 6371, Fe II 5169, and the Ca II H and K lines should be the strongest metal lines (Marsh, Horne & Rosen, 1991; Roelofs et al., 2005). Whilst the Si and Fe lines are clearly detected, there is no sign of Ca emission. This unexplained absence of calcium has been noted in several longer period AM CVn systems (e.g. Kupfer et al., 2013), including the similar period system SDSS J1240−0159 (Roelofs et al., 2005). However, Ca II emission has been detected in the slightly shorter period systems PTF1 J0943+1029, PTF1 J0435+0029 (Levitan et al., 2013) and V406 Hya (Roelofs et al., 2006), the latter of which has a spectrum that otherwise appears remarkably similar to SDSS J1240. Kupfer et al. (2013) discuss this anomaly in more detail, suggesting that sedimentation or settling could explain the under abundance of calcium. With the exception of the peculiar AM CVn system SDSS J0804+1616, there seems to be a sharp cut-off period for the appearance of calcium in AM CVn accretion discs.

The low inclination of SDSS J1730 causes the emission lines to be very narrow, making their identification much easier. In most systems the broad double-peaked lines blend together, making it difficult to determine which lines are present, and their relative strengths. This makes SDSS J1730 an excellent target for a detailed abundance analysis, which has proved difficult in other AM CVn binaries. *I*-band spectroscopic observations are encouraged in order to target the carbon, nitrogen and oxygen lines expected in this region that can reveal the prior evolution of the binary (Nelemans et al., 2010).

4.5 Summary

In this chapter I have presented time-resolved spectroscopy of the AM CVn binary SDSS J173047.59+554518.5, measuring an orbital period of 35.2 ± 0.2 minutes, confirming the ultra-compact binary nature of the system.

The average spectrum shows strong double-peaked helium emission lines, as well as a variety of metal lines, including neon, which has only been identified previously in GP Com. I detect no calcium in the accretion disc, this unexplained under-abundance of calcium has been noted in the majority of the longer-period AM CVn binaries.

I estimate the temperature of the continuum to be $12\,700 \pm 100$ K using a blackbody fit. The absence of obvious underlying absorption in the average spectrum is consistent with an accreting white dwarf at this temperature, however, the disc is expected to make a significant contribution to the continuum flux at the orbital period of SDSS J1730, which likely affects this estimate (Bildsten et al., 2006).

Using the measured peak velocities of the narrow double-peaked emission lines, I estimate an inclination, $i \leq 11°$. This low inclination makes SDSS J1730 an excellent system for the identification of emission lines, and a good target for abundance analysis. With I-band spectroscopy we would be able to investigate the N/C and N/O ratios that reveal much about the prior evolution of AM CVn binaries (Nelemans et al., 2010).

Chapter Five

The helium-rich cataclysmic variable SBSS 1108+574

5.1 Introduction

In this chapter I study SBSS 1108+574 (SDSS J111126.83+571238.6), one of the CVs identified in chapter 3. It was listed as a stellar source in the Second Byurakan Survey catalogue (Bicay et al., 2000), but was not identified as a CV until it was observed as part of our survey. As I have shown in Fig. 3.6, its spectrum shows unusually strong He I emission in addition to the Balmer emission lines, raising questions about its evolution, and a possible relation to the AM CVn binaries.

Our spectroscopic observations of this system were obtained in service mode just prior to its discovery in outburst by the CRTS. It was reported as a new SU UMa dwarf nova by Garnavich et al. (2012), and Kato et al. (2013) presented photometry of the outburst, identifying a possible orbital period of 55.367 minutes, in addition to superhumps.

In this chapter I present analysis of our observations of SBSS 1108+574, compare our results to Kato et al.'s, and discuss their implications for its evolutionary history.

5.2 Observations

5.2.1 Optical spectroscopy

Time-resolved spectroscopy of SBSS 1108+574 was obtained on 2012 February 28 and 2012 April 20 with GMOS at the Gemini-North telescope on Mauna Kea, Hawaii. The B600+ grating was used with a 1 arcsec slit. GMOS has three

Table 5.1: Summary of our spectroscopic observations of SBSS 1108+574.

Date	UT	Exposure time (s)	Exposures
2012 Feb 28	10:49–11:24	180	11
2012 Apr 20	06:06–08:55	173	54

2048×4608 e2v deep depletion CCDs, which were used in six amplifier mode. The resulting spectra cover the wavelength range 4120 – 6973 Å, with an average dispersion of 1.85 Å per pixel.

The observations consist of 65 spectra in total, most of which have an exposure time of 173 seconds. The observations in February were cut short after only about one half of the binary orbit, and so are insufficient to determine the orbital period of the system. A second attempt was made to complete a 3 hour observing block on 2012 April 20, when the system was caught in an unexpected outburst (it had not been identified as a dwarf nova prior to this outburst). These spectra cover approximately three binary orbits. The log of our spectroscopic observations is given in Table 5.1.

The spectra were reduced using optimal extraction as described in chapter 2. Wavelength calibration was obtained from copper-argon arc lamp exposures taken at the start of the first set of spectra, and at the start, middle and end of the observations during the second block. About 10 arc lines were identified for each of the six sections of the spectra, and fitted with fourth order polynomials, resulting in root mean square residuals of approximately 0.15 Å.

The spectra were corrected for instrumental response and flux-calibrated using the standard star Feige 34, observed as part of the Gemini baseline calibration programme. The spectra are not corrected for slit losses, so the flux calibration is not absolute, however, the relative flux calibration and continuum slope are reliable.

5.2.2 Photometry

SBSS 1108+574[1] was detected in outburst on 2012 April 22 by the CRTS, at a magnitude of 15.5. This is the only outburst of the system detected by CRTS during its six year coverage. It has also been observed on three occasions by the SDSS (see Table 5.2), indicating a previous outburst occurred on 2003 March 6, when it was detected at a g-magnitude of 15.6.

[1]SBSS 1108+574 was assigned the CRTS ID CSS120422:111127+571239 after the outburst.

Table 5.2: SDSS observations of SBSS 1108+574.

MJD	u	g	r	i	z
52233.50	18.92 ± 0.03	19.23 ± 0.02	19.27 ± 0.02	19.29 ± 0.02	19.39 ± 0.06
52704.27	15.91 ± 0.01	15.62 ± 0.01	15.82 ± 0.01	16.00 ± 0.01	16.17 ± 0.02
52708.37	15.82 ± 0.02	15.67 ± 0.02	15.85 ± 0.02	16.04 ± 0.02	16.23 ± 0.03

Table 5.3: Details of the observers, location, and telescope apertures used for the photometry.

Observer	Code	Location	Aperture (inch)
Goff	goff	California, USA	20
Koff	koff	Colorado, USA	10
Krajci	tomk	New Mexico, USA	14
de Miguel	edma	Huelva, Spain	16

Differential photometry was carried out by four observers of the Centre for Backyard Astrophysics (CBA), the observations spanning a total of ∼135 hours between 2012 April 23 and 2012 May 15. Details of the observers, locations and equipment are given in Table 5.3, and a log of our observations is given in Table 5.4. Unfiltered images were taken with exposure times in the range 50–120 seconds, while exposures using the V filter had integration times of 120 or 240 seconds. The comparison star was either GSC 3827-0886 or GSC 3827-0824, and all data were placed onto a common magnitude scale with uncertainties no larger than ∼0.05 mag. Magnitudes reported here are formed from adding the V magnitude of the comparison star to our differential magnitudes, and do not correspond to any standard system. Heliocentric corrections were applied to all observation times prior to analysis.

5.3 Results

5.3.1 Average spectral features

The average quiescent spectrum of SBSS 1108+574 is shown in Fig. 5.1. It shows a blue continuum with strong broad emission lines of both hydrogen and helium. As we saw in chapter 3, the helium lines are unusually strong, similarly to those seen in CSS 1122−1110 (Breedt et al., 2012), distinguishing SBSS 1108+574 from other dwarf novae. Fig. 3.6 shows the Hα and He I 5875 EWs of this system in relation to the normal CV population. It is also worth noting the similarity between the colour of SBSS 1108+574 and the AM CVn binaries, see Fig 3.11.

Table 5.4: Log of our photometric observations. C corresponds to unfiltered frames.

HJD start	HJD end	Observer	Exposures	Filter	mean magnitude
2456041.359	2456041.624	edma	356	C	16.05
2456041.627	2456041.853	koff	257	C	16.10
2456042.354	2456042.628	edma	368	C	16.21
2456042.622	2456042.911	koff	248	C	16.28
2456044.755	2456044.910	tomk	265	C	16.38
2456045.624	2456045.919	koff	298	C	16.44
2456046.660	2456046.938	goff	170	C	16.53
2456047.628	2456047.914	koff	227	C	16.60
2456047.660	2456047.958	goff	96	V	16.60
2456048.411	2456048.461	edma	48	C	16.59
2456052.698	2456052.932	goff	150	V	16.76
2456053.696	2456053.885	tomk	178	C	16.78
2456054.382	2456054.552	edma	156	C	16.74
2456054.670	2456054.921	goff	150	V	16.70
2456055.362	2456055.464	edma	90	C	16.65
2456056.399	2456056.598	edma	90	C	16.77
2456056.669	2456056.939	goff	164	V	16.75
2456057.365	2456057.549	edma	172	C	16.69
2456059.380	2456059.463	edma	78	C	16.88
2456059.669	2456059.928	goff	156	V	16.92
2456060.669	2456060.922	goff	151	V	16.87
2456061.702	2456061.916	goff	132	V	16.95
2456062.360	2456062.546	edma	173	C	17.07
2456062.677	2456062.809	goff	84	V	17.14
2456062.658	2456062.860	koff	155	C	17.17
2456063.371	2456063.480	edma	102	C	17.15

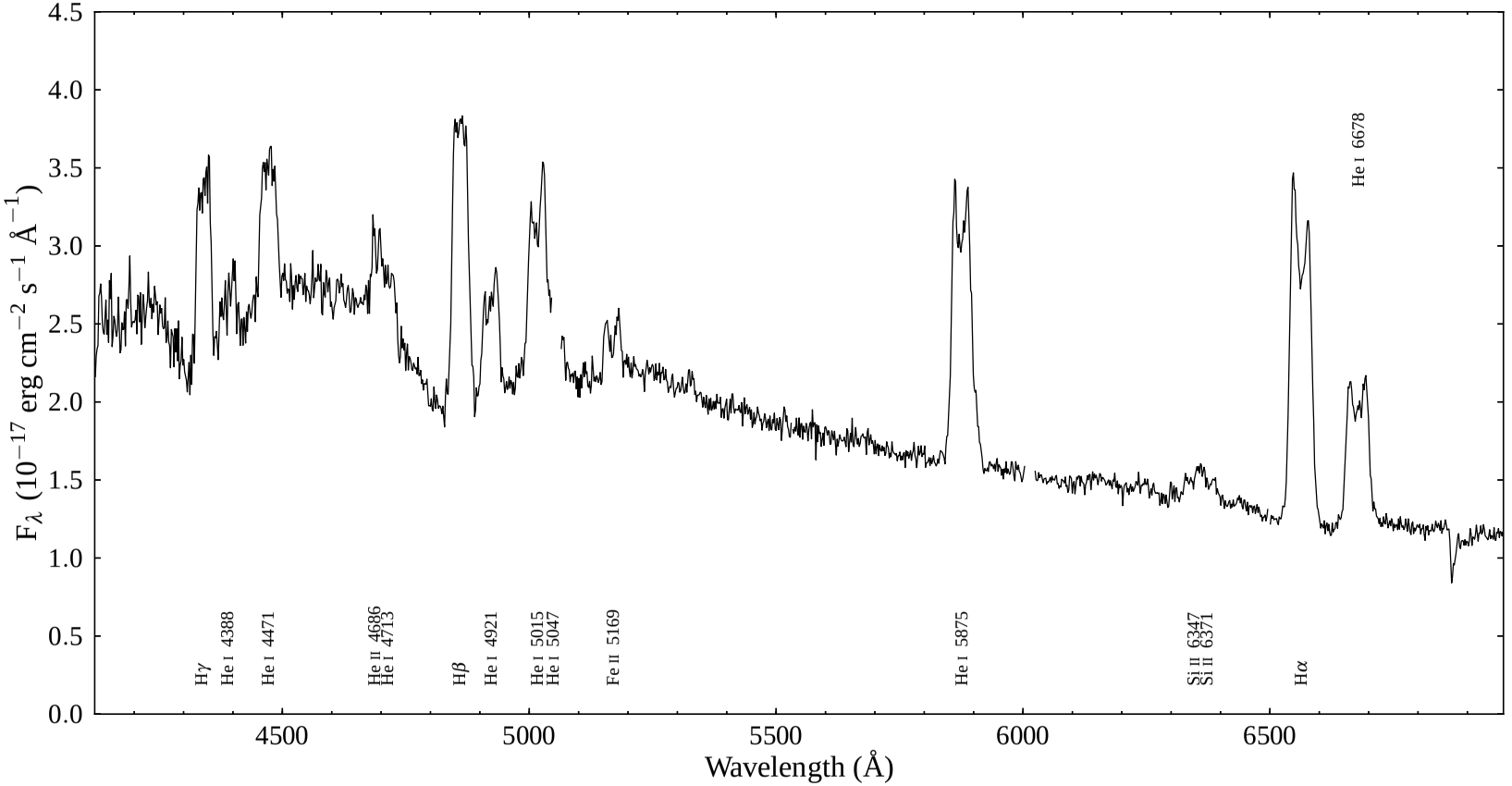

Figure 5.1: Average spectrum of SBSS 1108+574 in quiescence. The most prominent lines have been labelled.

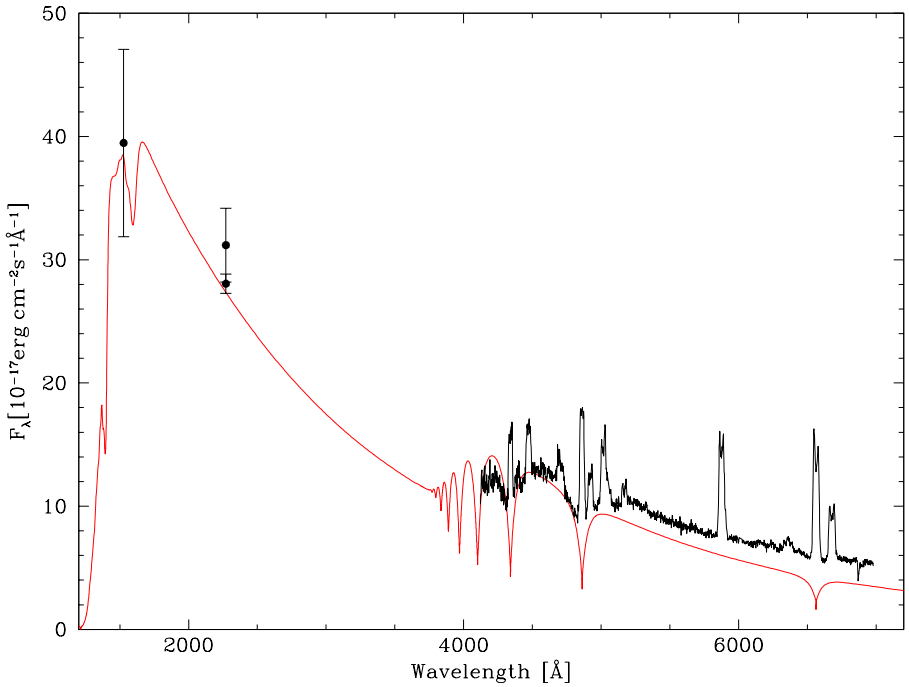

Figure 5.2: Shown in black are the Gemini spectrum, adjusted in flux to match the quiescent magnitude of SBSS 1108+574 ($g = 19.2$), and the UV fluxes measured by *GALEX*. A white dwarf with $M_{\rm wd} = 0.6\,{\rm M}_{\odot}$ and $T_{\rm eff} = 12\,000\,{\rm K}$ at a distance of 290 pc (shown in red) adequately matches the broad Balmer line profiles in the GMOS spectrum, and the UV fluxes. More accurate atmospheric parameters will require far-ultraviolet spectroscopy.

The He I lines and Hβ all show signs of being triple-peaked, exhibiting a central emission component in addition to the classic double-peaked emission from the accretion disc. A weak 'central spike' is a phenomenon almost never seen in CVs, but it is seen in the similar system CSS 1122−1110, and is a characteristic feature of the AM CVn binaries (e.g. Smak, 1975; Ruiz et al., 2001; Roelofs et al., 2005, 2007c; Carter et al., 2014b). This central emission component has a low radial velocity amplitude, and is identified as originating on or close to the surface of the accreting white dwarf (Marsh, 1999; Morales-Rueda et al., 2003). It is likely that the appearance of this feature in the average spectrum (Fig. 5.1) is due to the contribution of the bright spot, which does not completely average out due to incomplete coverage of the binary orbit.

The quiescent Gemini spectrum of SBSS 1108+574 shows broad depressions near 4340 Å and 4870 Å that are identified as Hγ and Hβ absorption lines from the white dwarf photosphere. These absorption profiles are substantially perturbed by the Balmer and He emission lines, preventing a meaningful estimate of the

Table 5.5: *GALEX* observations of SBSS 1108+574.

Date	Survey	FUV flux (μJy)	NUV flux (μJy)
2004 Jan 25	AIS	30.74 ± 5.92	53.64 ± 5.17
2005 Jan 25	MIS		48.25 ± 1.34

white dwarf atmospheric properties from the optical data alone. *GALEX* has detected SBSS 1108+574 during its All-Sky Imaging Survey (AIS) in the far-ultraviolet (FUV) and near-ultraviolet (NUV) channel, and again as part of the Medium Imaging Survey (MIS) using the NUV channel only, see Table 5.5. The Gemini spectrum (correcting the absolute flux to $g = 19.2$, measured in quiescence by SDSS) was modelled, along with the *GALEX* broad-band fluxes, using pure-hydrogen white dwarf atmosphere models from Koester (2010)[2]. For an adopted white dwarf mass of $M_{\rm wd} = 0.6\,{\rm M}_\odot$ we find a temperature of $T_{\rm eff} = 12\,000 \pm 1000\,{\rm K}$, and a distance of $d = 290 \pm 30\,{\rm pc}$ (Fig. 5.2). Allowing for $\pm 0.2\,{\rm M}_\odot$ in the white dwarf mass adds another $\simeq \pm 1000\,{\rm K}$ in the uncertainty of the temperature.

The vast majority of short-period CVs are relatively old systems with typical ages of several Gyr (e.g. Kolb, King & Ritter 1998; Schreiber & Gänsicke 2003; Knigge, Baraffe & Patterson 2011). The cooling ages implied by their white dwarf primaries are generally much shorter – in the case of SBSS 1108+574, the effective temperature corresponds to $\tau_{\rm cool} \simeq 4 \times 10^8\,{\rm yr}$ only. The solution to this conundrum is that the white dwarfs are (re-)heated by accretion. Short-term fluctuations of the mass transfer rate, such as dwarf nova outbursts, affect only their outer envelope of a white dwarf, and the effective temperature responds on time scales of weeks to years (e.g. Gänsicke & Beuermann 1996; Sion et al. 1998; Slevinsky et al. 1999). In contrast, the effective temperature determined sufficiently long after a dwarf nova outburst reflects the secular mean of the accretion rate over $\sim 10^5\,{\rm yr}$ (for low $\dot{M}$ systems, Townsley & Bildsten 2003; Townsley & Gänsicke 2009). Adopting a white dwarf mass of $M_{\rm wd} = 0.6\,{\rm M}_\odot$ ($M_{\rm wd} = 0.9\,{\rm M}_\odot$), we estimate $\dot{M} \sim 10^{-10}\,{\rm M}_\odot\,{\rm yr}^{-1}$($\dot{M} \sim 3 \times 10^{-11}\,{\rm M}_\odot\,{\rm yr}^{-1}$).

In addition to the hydrogen and helium lines, Fe II emission at 5169 Å, and Si emission at 6347 Å and 6371 Å are identified.

The average outburst spectrum is shown in Fig. 5.3. It shows a bluer continuum than the quiescent spectrum, and both helium and hydrogen in absorption, a common feature in outbursting dwarf novae due to the bright, optically thick disc. It

[2]Balmer/Lyman lines in the models were calculated with the modified Stark broadening profiles of Tremblay & Bergeron, ApJ 696, 1755, 2009, kindly made available by the authors.

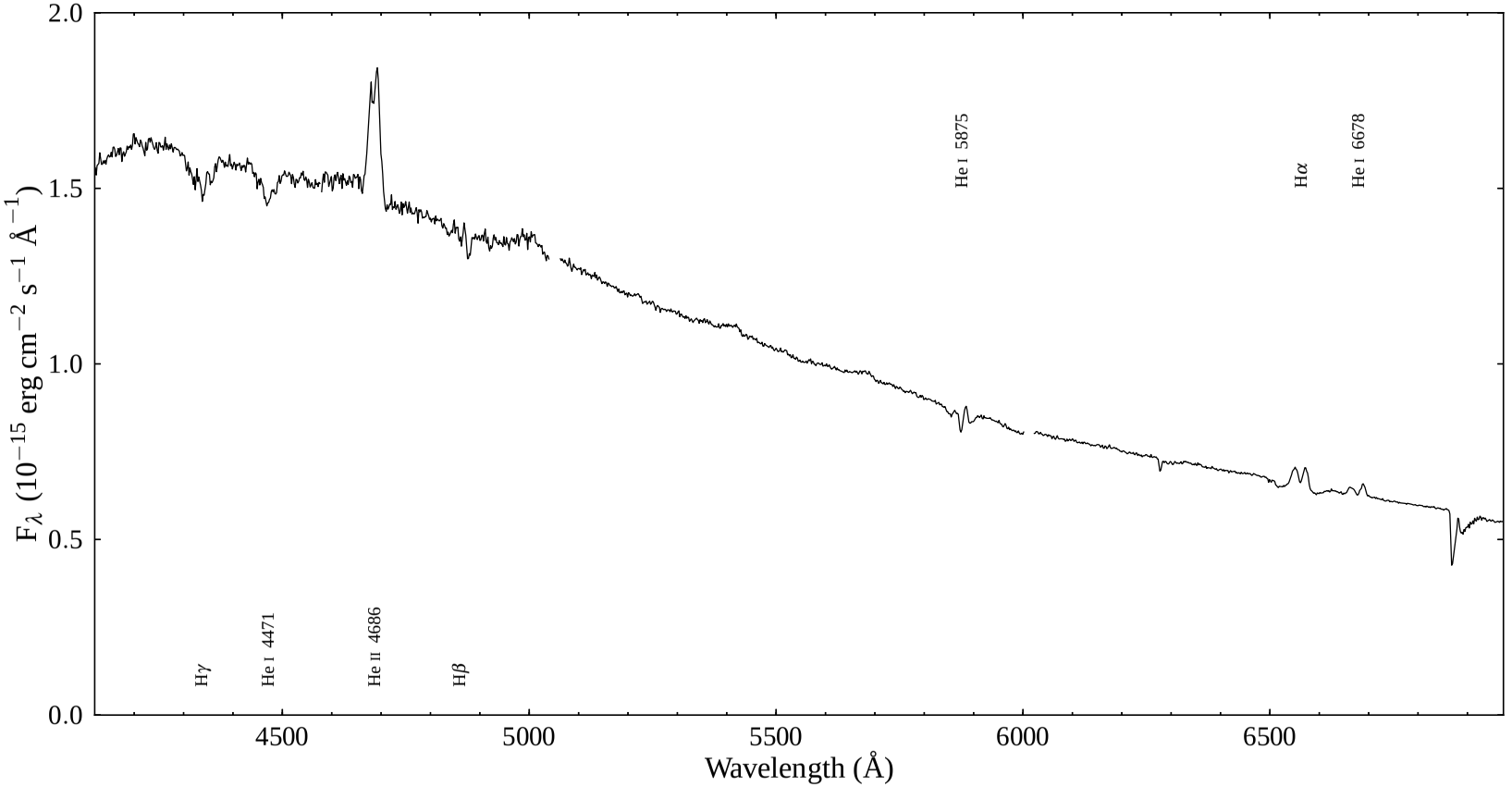

Figure 5.3: Average spectrum of SBSS 1108+574 during outburst. The most prominent lines have been labelled.

Table 5.6: Equivalent widths and FWHM of prominent lines. Estimated uncertainties are for a 1σ confidence level.

Line	Quiescent		Outburst	
	EW (Å)	FWHM ($\mathrm{km\,s^{-1}}$)	EW (Å)	FWHM ($\mathrm{km\,s^{-1}}$)
Hγ	-17.4 ± 2.0	2100 ± 50	3.7 ± 0.3	3500 ± 100
He I 4471	-12.9 ± 1.5	2200 ± 50	1.5 ± 0.2	2000 ± 100
He II 4686	-13.7 ± 1.5^a	3300 ± 200	-6.9 ± 0.1	1600 ± 50
Hβ	-32.0 ± 2.0	1900 ± 50	1.6 ± 0.3	4400 ± 300
He I 4921	-11.0 ± 1.5	1900 ± 100	...	...
He I 5015^b	-18.8 ± 0.5	2400 ± 100	...	...
He I 5875	-49.0 ± 1.0	2100 ± 50	1.3 ± 0.5	2300 ± 100
Hα	-84.0 ± 3.0	1950 ± 50	-5.0 ± 1.0	1700 ± 50
He I 6678	-35.5 ± 1.4	2000 ± 100	-1.3 ± 0.5	1800 ± 200

Values marked '...' could not be measured reliably.
[a]Blended with He I 4713.
[b]The red wing falls in the gap between the CCDs, and may be blended with He I 5047.

also shows He II 4686, Hα and He I 6678 in emission, with the classic double-peaked profile caused by the accretion disc.

Table 5.6 shows the reduction in EWs of the prominent lines between quiescence and outburst. The ratio of the EWs of Hα to He I 5875 is approximately 3 times smaller than typically found in CVs (Carter et al., 2013), see Fig. 3.6. From the quiescent spectrum I calculate a line flux ratio He I 5875/Hα $= 0.81 \pm 0.04$, a much higher ratio than normally observed in cataclysmic variables, where it is typically 0.2 – 0.4 (e.g. Williams & Ferguson 1982; Thorstensen & Taylor 2001; Breedt et al. 2012).

5.3.2 Photometric periods

Nightly lightcurves for April 23 and April 24 are shown in Fig. 5.4. A periodic signal of amplitude $\sim$80 mmag is clearly seen during the first two nights.

The full lightcurve of our observations is shown in Fig. 5.5. The system fades at a nearly constant rate of $\sim 0.10\,\mathrm{mag\,d^{-1}}$ over the first week. This is followed by a period of $\sim$6 – 10 days over which the mean magnitude remains essentially constant; afterwards, the system resumes its way to its low state. Oscillations were observed in all nightly light curves, although they tended to become less well-defined as the system turned fainter and the signal-to-noise ratio decreased. The amplitude was not seen to change appreciably.

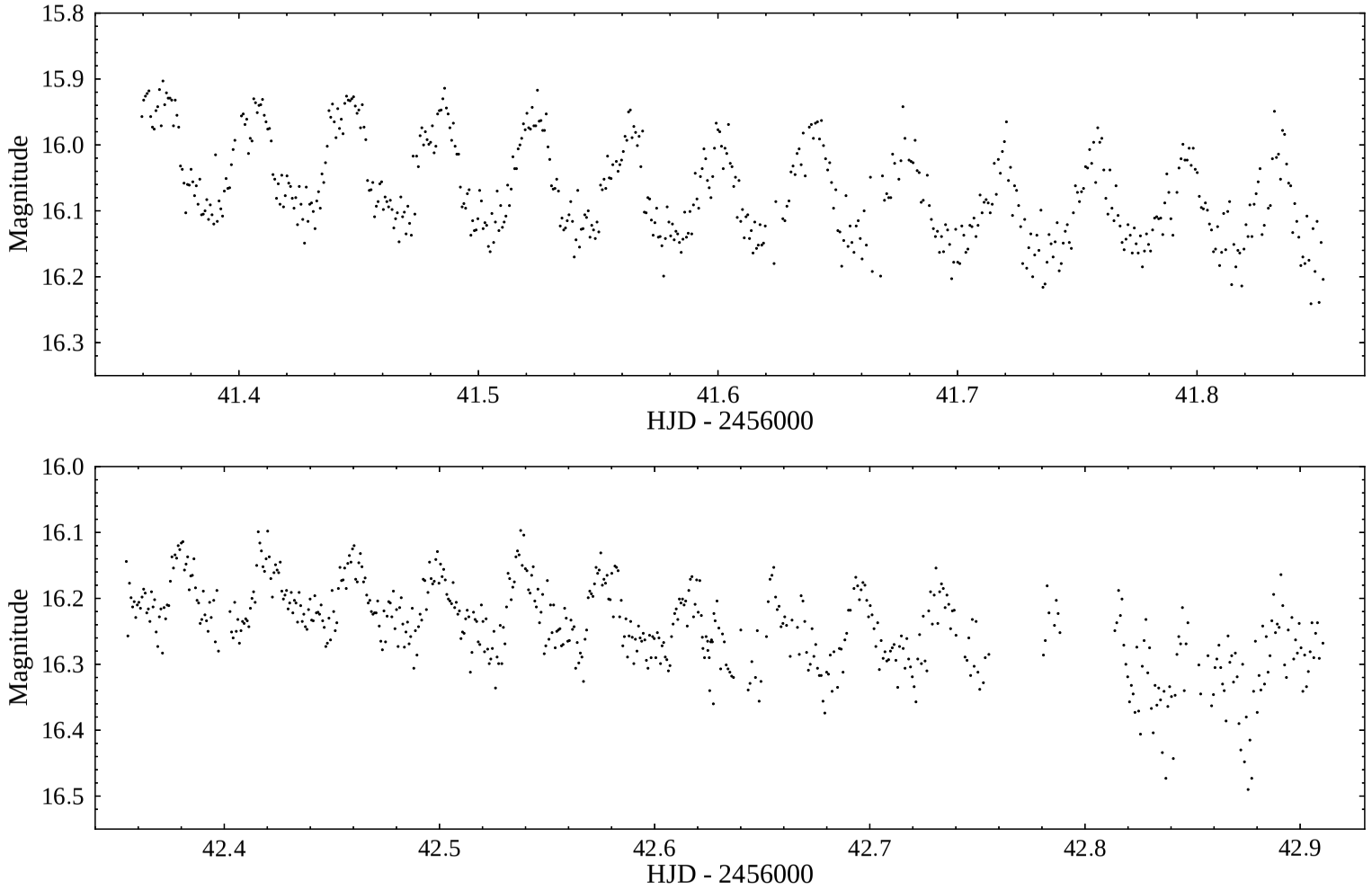

Figure 5.4: Lightcurves for April 23 and April 24. Each lightcurve spans ∼12 hours.

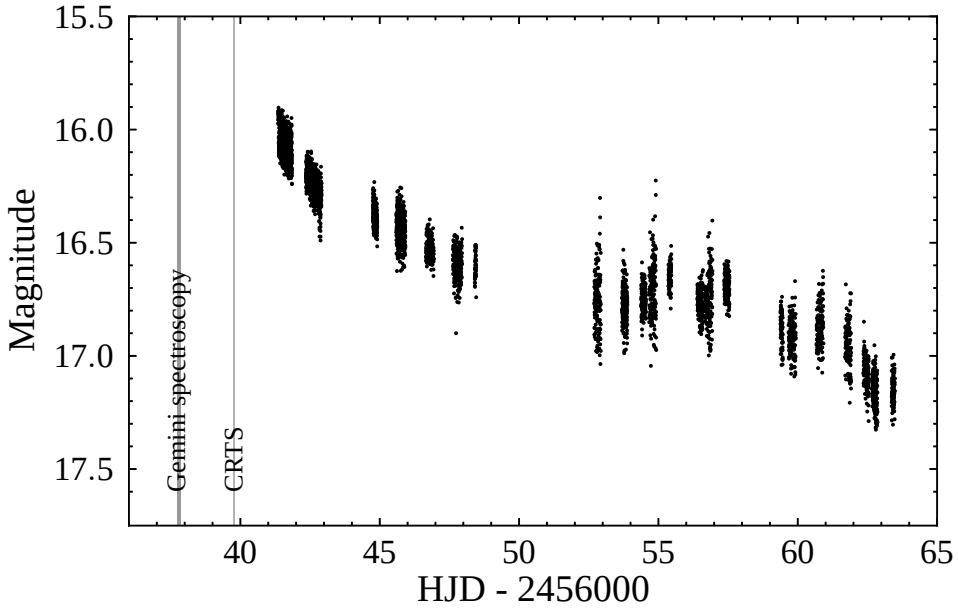

Figure 5.5: Full lightcurve of our photometric observations, showing the times of our spectroscopic observations and the detection by the CRTS.

The Lomb-Scargle periodogram (see chapter 2) of the whole data set is shown in Fig. 5.6. We first removed any obvious trend in the nightly light curves and subtracted the nightly mean magnitude. The frequency of the fundamental signal is found at 25.56 cycles d^{-1}, corresponding to a period of 56.34 minutes. The presence of a close peak at 25.64 cycles d^{-1} with nearly the same power is an indication of variations in the periodicity of the fundamental signal during the time spanned by our observations. As the superhump signal is not totally periodic, the power spreads out, resulting in the second peak. This period instability is typical of superhumps and rules out a possible orbital nature of the fundamental signal. The ± 1 cycle d^{-1} aliases are also clear in Fig. 5.6.

An $O - C$ analysis of our data confirms the variation in the period over the time spanned by our observations. This period instability has a significant impact on the accuracy with which we can determine the superhump period, we therefore take the strongest peak in the periodogram as our superhump period, and use the separation of the two strong peaks as an estimate of the uncertainty on this period, 56.34 ± 0.18 minutes. This estimated uncertainty is consistent with the variation revealed by the $O - C$ analysis. The phase-folded lightcurve constructed from the first two nights of observations is shown in Fig. 5.7.

There is an additional peak centred at 26.01 cycles d^{-1} which seems to bear no relation with the time windowing of our observations. This is identified as corre-

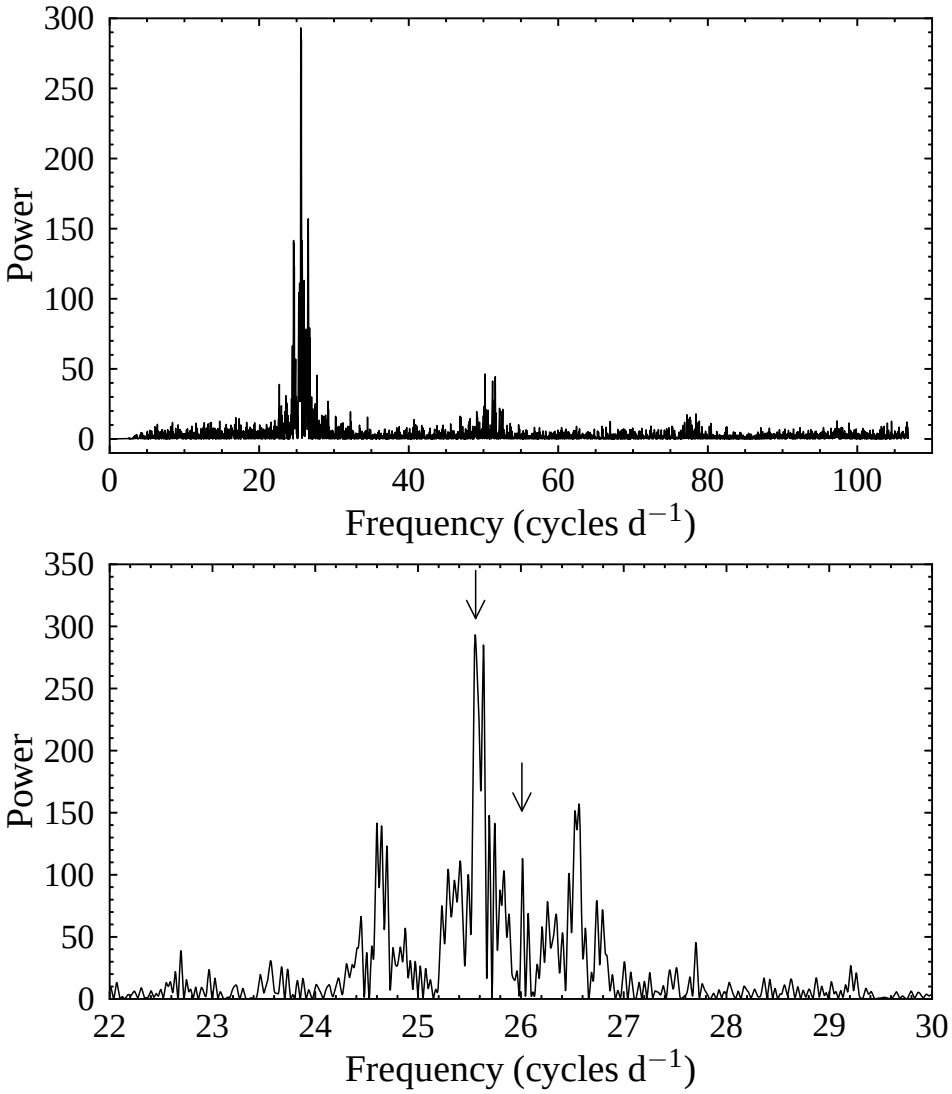

Figure 5.6: Lomb-Scargle periodogram of the photometric data set. The lower panel shows the detail around the strongest peak. The fundamental frequency and an additional peak that is not identified as due to aliasing, are indicated by arrows. These signals are interpreted as the superhump period and orbital period of the binary.

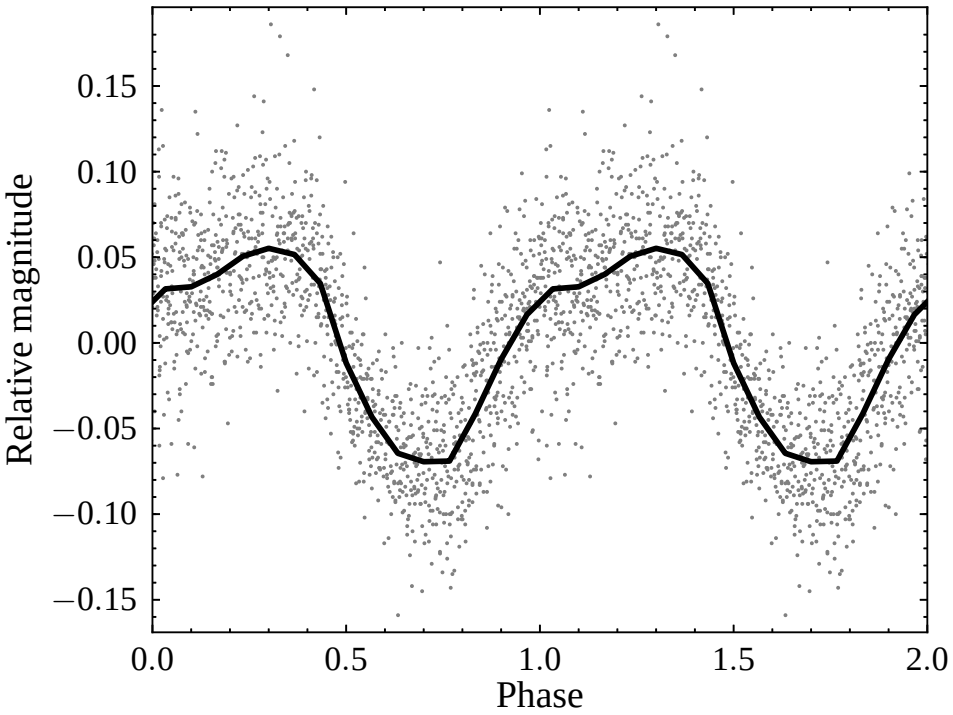

Figure 5.7: Lightcurve of the first two nights of observations, folded on the detected superhump period, 56.34 minutes. The solid line shows the mean, binned lightcurve. The zero phase is arbitrary.

sponding to the underlying orbital motion, giving a period of 55.36 ± 0.03 minutes, and confirming the findings of Kato et al. (2013). This signal remains after prewhitening the light curve with the main frequency at 25.56 cycles d^{-1}, and is the strongest signal remaining after sequentially prewhitening the residual light curve with two further strong frequencies (25.59 and 25.69 cycles d^{-1}) associated with the superhumps (see Fig. 5.8). We also find relatively strong signals corresponding to the third and fourth harmonics of this frequency. The strength of these peaks would not be unexpected given the sharp dip that would be caused by a possible eclipse of the disc (see section 5.3.6). This supports the identification of this frequency as corresponding to the orbital period.

5.3.3 The spectroscopic period

To find the spectroscopic period the radial velocity variation of the emission lines was measured using the single Gaussian technique of Schneider & Young (1980), as implemented in MOLLY (see section 2.3.3). The FWHM of this Gaussian was varied from 200 to 3000 km s^{-1}. For each resulting radial velocity curve the Lomb-Scargle periodogram (Scargle, 1982) was calculated, and the radial velocities were fitted

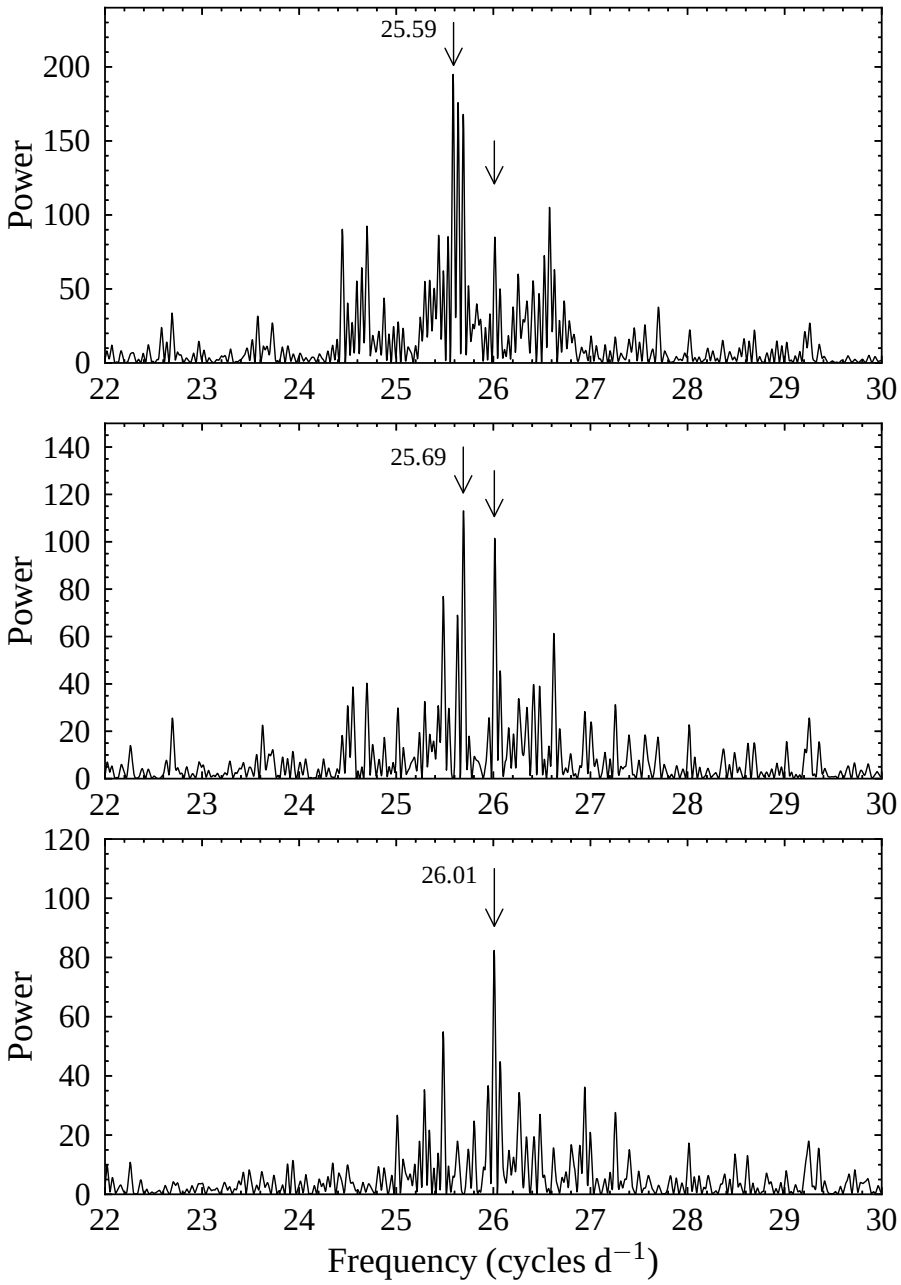

Figure 5.8: Periodograms of the photometric data set after prewhitening. The top panel shows the periodogram after prewhitening the data with the previously identified strongest frequency at 25.56 cycles d^{-1} (see Fig. 5.6). The strongest peak is at 25.59 cycles d^{-1}. The middle panel shows the periodogram after prewhitening the previous lightcurve with the 25.59 cycles d^{-1} signal. The strongest peak is now found at a frequency of 25.69 cycles d^{-1}. The lower panel shows the periodogram after prewhitening the previous lightcurve with the 25.69 cycles d^{-1} signal. The strongest peak is now found at 26.01 cycles d^{-1}, and is identified as corresponding to the orbital motion. The strongest peak and the 26.01 cycles d^{-1} signal are indicated by arrows in each panel.

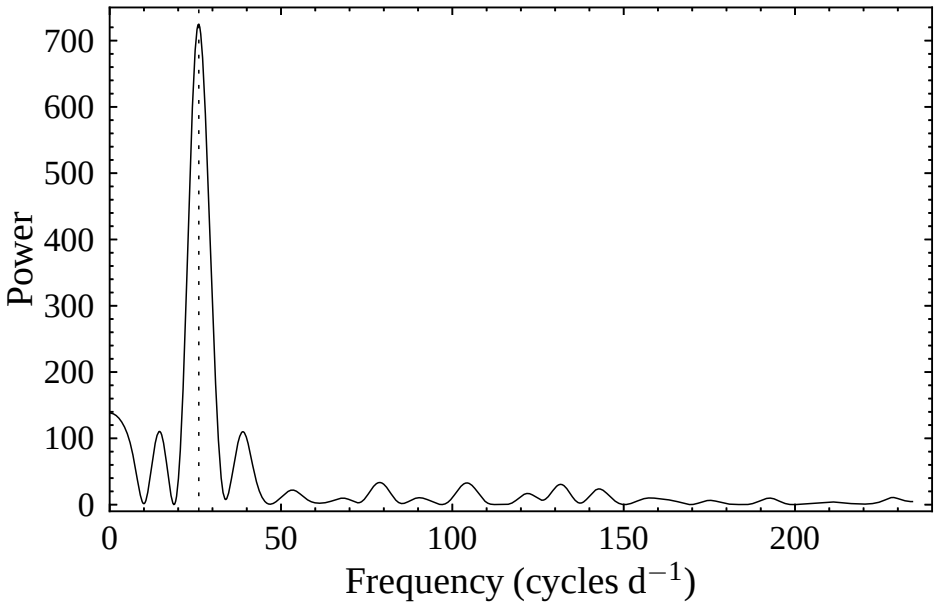

Figure 5.9: Lomb-Scargle periodogram calculated from the He II 4686 radial velocities of SBSS 1108+574. The location of the orbital period identified from the photometry is indicated by the dotted line for comparison.

Table 5.7: Orbit parameters for SBSS 1108+574 derived from radial velocity measurements

$P_{\rm orb}$ (min)	$\rm HJD_0$	K (km s^{-1})	γ (km s^{-1})
55.3 ± 0.8	2456037.7551(4)	111 ± 7	37.1 ± 5.0

with a circular orbit as given by equation (2.11), where $P_{\rm orb}$ is derived from the strongest peak in the periodogram.

Examining the results, I determined that the errors are smallest for a FWHM of $\sim$2200 km s^{-1} for the He II 4686 line. Such a wide Gaussian gives an average of the velocity over the entire line, minimising the errors introduced by the unusual structure of the lines from the outbursting disc. I show the Lomb-Scargle periodogram calculated from the He II radial velocities in Fig. 5.9. A clear signal is seen at 26.03 cycle d^{-1}, corresponding to a period of 55.3 minutes. The He II 4686 radial velocity curve, folded on this period, is shown in Fig. 5.10. The orbital parameters from the fit to equation (2.11), derived from the radial velocity measurements, are shown in Table 5.7. The zero phase, $\rm HJD_0$, is taken as the time of the blue to red crossing of the velocities.

There is considerable scatter around the radial velocity curve shown in Fig. 5.10, which is likely caused by the unusual line structure during the outburst

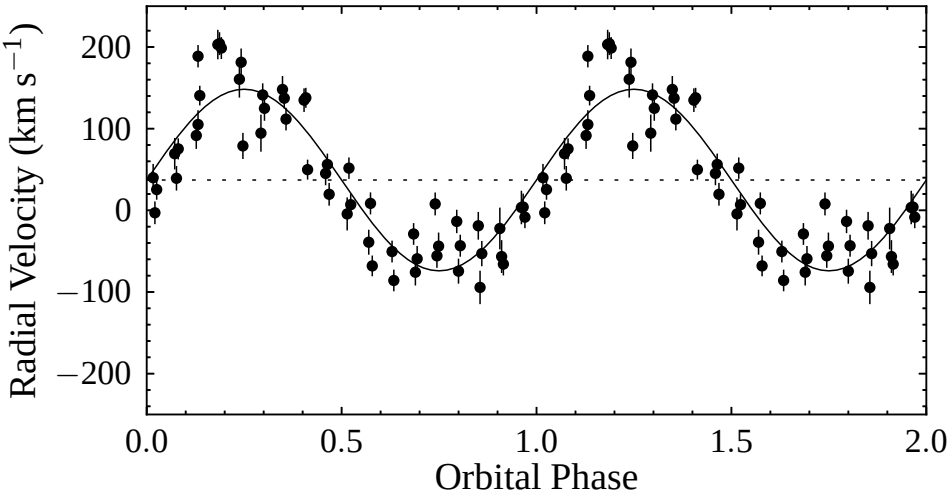

Figure 5.10: Measured He II radial velocities folded on a period of 55.3 minutes. The solid and dotted lines are the best fit radial velocity curve and γ velocity, the parameters are shown in Table 5.7.

(see Fig. 5.11). Calculating the radial velocities from the line wings using two narrower Gaussians gives similar results, but the effect of the unusual structure causes greater scatter in the radial velocities, and greater errors, and so the single Gaussian method is preferred.

The uncertainty on the period was estimated by carrying out 10 000 bootstrap selections of the radial velocity curve, as described in chapter 2. For each subset, 54 radial velocities were selected from the full radial velocity curve, allowing for points to be selected more than once, and the periodogram calculated, taking the strongest peak as the period. The standard deviation of these computed periods, ignoring those that correspond to higher harmonics, is taken as a measure of the uncertainty in the derived orbital period.

5.3.4 Mass ratio

As I discussed in chapter 1, superhumps are caused by a resonant interaction between the accretion disc and the donor star, that causes the disc to become asymmetric. The increased viscous dissipation caused by this interaction between the donor and the distorted disc, leads to the brightness variations observed during dwarf nova superoutbursts. The observed superhump period is the beat period between the orbital period of the system and the precession period of the deformed disc (Whitehurst, 1988).

As the superhump phenomenon is due to resonance, and the precession rate for resonant orbits depends upon the mass ratio of the system, there is a strong link

between the superhump period and the mass ratio. The superhump period-excess (equation 1.4) is found to increase with increasing mass ratio, q. An empirical relation is derived from eclipsing dwarf novae, in which the mass ratio and superhump excess can be measured independently (Patterson et al., 2005; Knigge, 2006; Kato et al., 2009).

Of the three alternative $\epsilon - q$ relations, the Patterson et al. (2005) form,

$$\epsilon = 0.18q + 0.29q^2, \tag{5.1}$$

and the Kato et al. (2009) form, both assume $\epsilon = 0$ when $q = 0$. This is a reasonable assumption as we would expect a secondary with negligible mass to have a negligible tidal interaction with the disc. The third version of the relation, given by Knigge (2006), does not use this assumption. The Patterson et al. (2005) formulation is usually favoured for AM CVn binaries (Breedt et al., 2012), as observations of the only known eclipsing system, SDSS J0926+3624, agree best with this form (Copperwheat et al., 2011), and so I use that version here.

The total time covered by our spectroscopic observations is not sufficiently long to reach the accuracy of the photometric periods, and so I take the weak additional signal in Fig. 5.6 as the orbital period. As the superhump period varies during the observations, we conservatively take the separation of the two strongest peaks in Fig. 5.6 as a measure of the uncertainty on the superhump period for calculation of the excess. This gives the superhump excess in SBSS 1108+574, $\epsilon = 0.0176 \pm 0.0032$, and the mass ratio, $q = 0.086 \pm 0.014$. Note that this is very large compared to the mass ratio found for CSS 1122−1110, $q = 0.017$ (Breedt et al., 2012), despite the similar orbital periods.

Our larger estimate for the superhump excess is consistent with the value found by Kato et al. (2013) for their stage B superhumps, $\epsilon = 0.0174 \pm 0.0002$. Using the smaller excess they measured for their stage C superhumps, and the Kato et al. (2009) form of the $\epsilon - q$ relation, they derive a mass ratio $q = 0.06$. The values I derive for q using the Patterson et al. (2005) form of the $\epsilon - q$ relation are consistent with the values calculated using the Knigge (2006) form. For our data the Kato et al. formulation gives a larger value of q, however, this relation is calibrated using the shorter superhump periods that occur late in the superoutburst, and so likely overestimates q for our longer periods from earlier in the superoutburst.

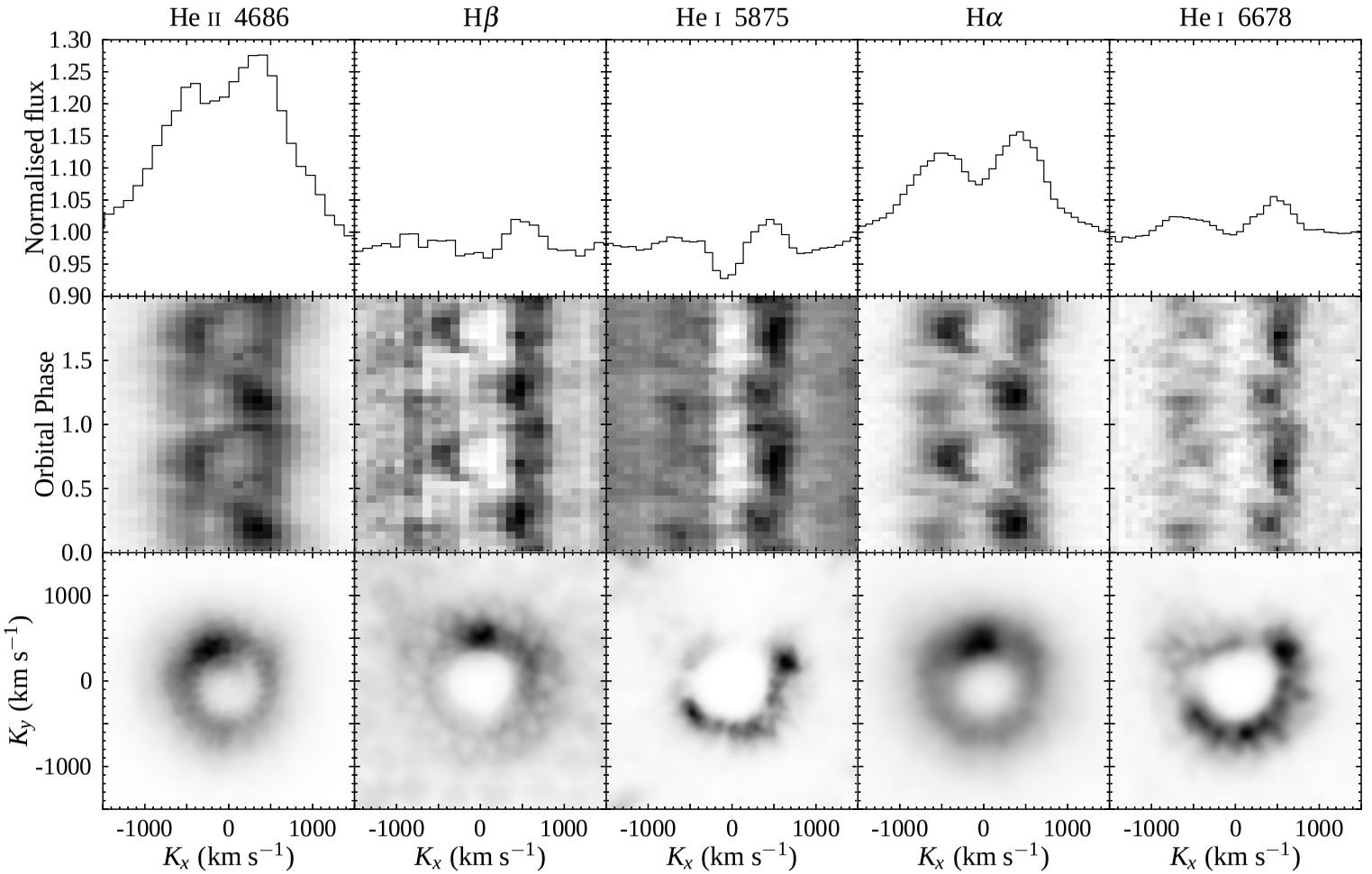

Figure 5.11: Average continuum-normalised line profiles, phase-folded trailed spectra, and Doppler maps of the strongest lines in the outburst spectra. The tomograms for Hβ and He I 5875 were created after subtracting a spline fit to the background.

5.3.5 Dynamic spectrum

The line profiles and trailed spectra for the strongest lines, folded on the orbital period, 55.3 minutes (26.03 cycles d^{-1}), are shown in Fig. 5.11. It is clear that there is greater flux in the redshifted line peak than the blueshifted peak; this unexplained asymmetry is often seen in the spectra of outbursting CVs. The presence of underlying absorption due to the optically thick outbursting disc is also noted, this is particularly noticeable in the He I 5875 line, and makes the S-wave difficult to discern when it crosses the line centres.

An S-wave is clear in the strongest line, He II 4686, but becomes weaker with decreasing line strength. The presence of this S-wave can be seen in the other lines shown in Fig. 5.11, however, the He I lines appear to show a brighter varying signal with higher velocities than the S-wave, that is almost in anti-phase. A second varying signal is also seen in the Hα trailed spectrum. This feature is likely responsible for the strength of the second harmonic in the periodograms of these lines. There is no coherent S-wave visible in the trailed spectra when folded on these second harmonic frequencies; thus we can be confident that I have identified the correct period of this system.

The corresponding Doppler tomograms (Marsh & Horne, 1988) give a similar picture of emission in the disc. A bright spot is clearly visible in the maps for He II 4686, Hα and Hβ. The bright spot is not usually seen in CVs during outburst, as the bright outbursting disc normally outshines it. Since these were calculated using the same zero phase for all lines, assumed from the He II 4686 radial velocities, $\mathrm{HJD}_0 = 2456037.7551$, the maps may be rotated due to the unknown phase shift between our zero phase and the true zero phase of the white dwarf. Note that the bright spot appears at slightly different phases in each line. The extended bright spot seen in Hα, overlaps in phase with the bright spots seen in both He II 4686 and Hβ. Some evidence of the bright spot may also be seen in the Doppler maps of the He I lines, however, they are dominated by the brighter varying signal causing the band of increased emission in the right-hand quadrants.

Note that spiral arms are not detected in our data. Spiral arms have been observed in a number of dwarf novae during outburst (e.g. Steeghs 2001; Baba et al. 2002), and are thought to be caused by the tidal affect of the donor on the large disc. As our observations may correspond to an early point in the evolution of the outburst, it is possible that the spiral arms reported by Littlefield et al. (2013) developed later in the outburst.

The Hβ line profile reveals a strong feature in the high velocity wing of the blueshifted peak, centred at about $-800\,\mathrm{km\,s^{-1}}$. The redshifted peak also extends

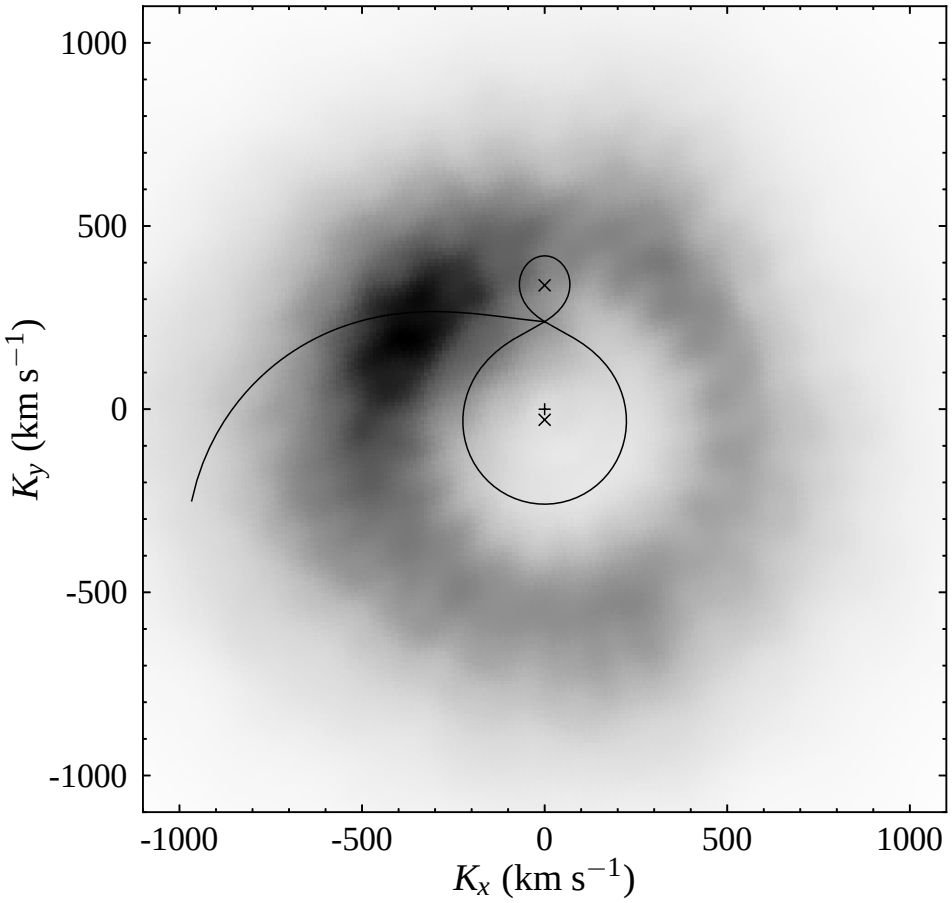

Figure 5.12: He II 4686 Doppler map overplotted with Roche lobes and stream velocities of a $q = 0.086$ binary. The map was rotated by applying a -0.08 phase shift compared to the maps in Fig. 5.11.

beyond the range of the bright spot visible in the trailed spectrum. The origin of this feature is unclear, and it appears in the Doppler map as a ring of emission at higher velocity than most of the disc emission.

No rotation is detected between Doppler maps created using only the first and only the third orbit, further verifying our identification of the orbital period.

I plot the Roche lobes and stream velocities for a $q = 0.086$ binary together with the He II 4686 Doppler map in Fig. 5.12. The velocity positions of the accretor, donor and centre of mass are also shown. Again, the map may be rotated about its origin due to the unknown phase shift between our assumed zero phase and the true zero phase.

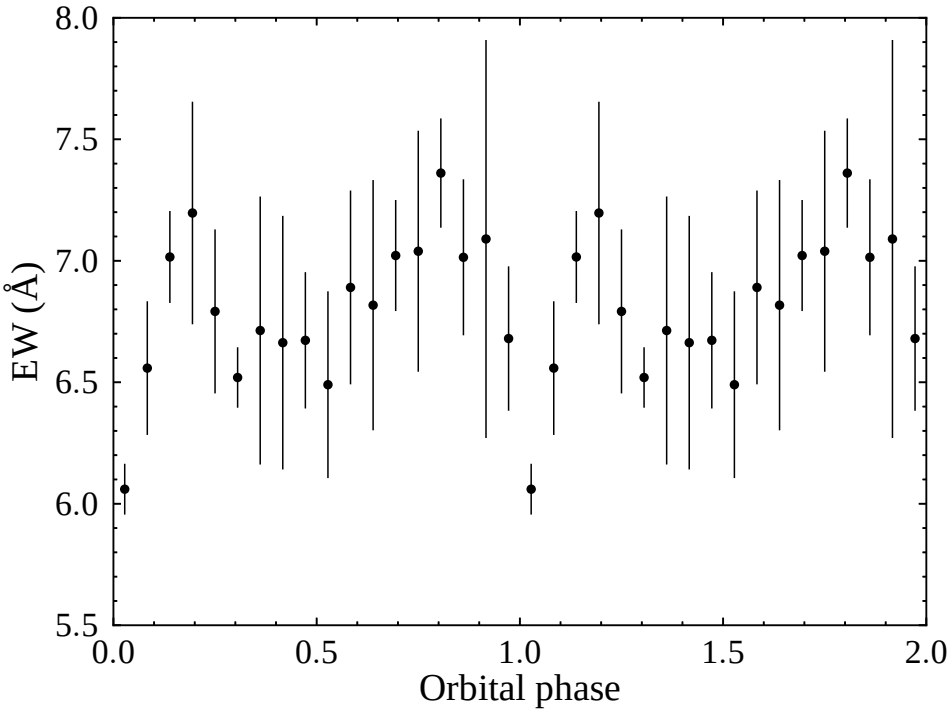

Figure 5.13: Binned, phase-folded He II 4686 EW against orbital phase. The dip at about phase zero is attributed to a grazing eclipse of the accretion disc. Note that the EW axis has a narrow range, the depth of the eclipse is approximately 11 per cent.

5.3.6 Grazing eclipse

The trailed spectra (Fig. 5.11) show a slight reduction in the line flux at a phase of ∼1. To examine this further I construct a lightcurve of the He II 4686 EW, shown in Fig. 5.13. This reveals a clear dip, which is attributed to an eclipse of the outer disc.

This allows us to constrain the inclination of the system, as it must be large enough that the outer edge of the disc can be eclipsed. Since there is no eclipse of the inner disc or the accretor, we can also place an upper limit on its value. Using our derived value for q, the Eggleton (1983) formula for the Roche lobe radius of the secondary, and the approximate tidal limit for the maximum radius of the accretion disc (e.g. Warner 1995), I find $63.8 \pm 1.0^\circ < i < 78.6 \pm 0.6^\circ$.

The outbursting disc is expected to be larger than the quiescent disc, significantly increasing the likelihood of a grazing eclipse during outburst. It is therefore likely that there will be no eclipse detectable in quiescence.

5.4 Discussion

The strength of the helium emission lines compared to the hydrogen lines in the average spectrum shown in this chapter (Fig. 5.1 and Table 5.6), again highlights the unusual nature of this system. Whilst a detailed abundance analysis cannot be carried out with our current data, as we lack the wavelength coverage and detailed models of helium dominated accretion discs, this is a strong indication of a much greater helium abundance than normally seen in CVs.

Models of accretion discs and donors in CVs and AM CVns indicate that very little hydrogen is required to excite strong Balmer lines (Williams & Ferguson, 1982; Marsh, Horne & Rosen, 1991; Nagel, Rauch & Werner, 2009; Nelemans et al., 2010), and the hydrogen abundance in SBSS 1108+574 may be significantly lower than 1 per cent. Littlefield et al. (2013) estimate that SBSS 1108+574 has a H abundance less than 10 per cent that of normal CVs, but still more than 10 times that seen in AM CVns. In order to determine accurate abundances we would require precise models of accretion discs for the full range of hydrogen abundances. These are not currently available, but we would be able to further constrain abundances with UV spectroscopy.

Our derived period, 55.3 ± 0.8 minutes (26.03 ± 0.38 cycles d^{-1}), is well below the CV period minimum, clearly indicating that the donor is significantly evolved, having been stripped of most of its hydrogen by mass-transfer or prior to the onset of mass-transfer. Our spectroscopic period favours the weak 55.36 minute (26.01 ± 0.01 cycles d^{-1}) signal detected from the photometry and identified as the orbital period, over the 56.34 minute (25.56 cycles d^{-1}) signal identified as the superhump period. We can therefore be confident that the candidate orbital period signal detected in our photometry and by Kato et al. (2013), is the correct orbital period. This confirms SBSS 1108+574 as one of the shortest period CVs known, and places it well within the AM CVn period range.

As was discussed in chapter 1, there are three proposed formation channels for the AM CVn binaries, defined by the type of donor. The donor can be (1) a second, lower mass white dwarf (Paczyński, 1967; Faulkner, Flannery & Warner, 1972), (2) a semi-degenerate helium star (Savonije, de Kool & van den Heuvel, 1986; Iben & Tutukov, 1987), or (3) an evolved main-sequence star that has lost most of its hydrogen envelope. The latter is thought to form via the 'evolved CV' channel (Thorstensen et al., 2002; Podsiadlowski, Han & Rappaport, 2003), but this formation channel has generally been considered to be unimportant in comparison to the double white dwarf and helium star channels. Podsiadlowski, Han &

Rappaport (2003), however, argue that the evolved CV channel could contribute a significant fraction of the total AM CVn binary population. SBSS 1108+574 has all the characteristics of an AM CVn progenitor in the evolved CV formation channel.

It must be noted that not all CVs with evolved donors reaching periods below the normal period minimum, will form AM CVn binaries as they are currently recognised (Yungelson et al., in preparation). Many systems will in fact reach their own period 'bounce', and evolve back towards longer orbital periods, without depleting their hydrogen sufficiently to appear as AM CVn binaries. Current models suggest that the fraction of evolved CV channel AM CVn binaries may be lower than previously predicted (Podsiadlowski, Han & Rappaport 2003; Yungelson et al., in preparation). It is clear, however, that systems like SBSS 1108+574 and CSS 1122−1110 (Breedt et al., 2012) fall between the standard definitions of AM CVn binaries and CVs.

The large mass ratio I derive, $q = 0.086 \pm 0.014$, indicates a different evolution to the standard AM CVn binary population; for GP Com ($P_{\rm orb} = 46.6$ minutes; Marsh 1999), $q = 0.018$ (Roelofs et al., 2007a), and for V396 Hya ($P_{\rm orb} = 65.1$ minutes; Ruiz et al. 2001), q=0.013 (Steeghs, 2010). The fact that the system shows outbursts indicates that the mass transfer rate is still relatively high, which is not expected for AM CVn binaries that have passed $P_{\rm min}$ and evolved back to long periods (e.g. Nelemans 2005; Kotko et al. 2012). Compare our estimated accretion rate, $\dot{M} \sim 10^{-10}\,{\rm M}_{\odot}\,{\rm yr}^{-1}$ (for a $0.6\,{\rm M}_{\odot}$ accretor), to the value Roelofs et al. (2007a) derived for GP Com, $\dot{M} < 3.6 \times 10^{-12}\,{\rm M}_{\odot}\,{\rm yr}^{-1}$, and the value Nagel, Rauch & Werner (2009) estimated for V396 Hya, $\dot{M} \sim 10^{-11}\,{\rm M}_{\odot}\,{\rm yr}^{-1}$, again presenting a strong contrast between SBSS 1108+574 and the long period AM CVn binaries. This indicates that SBSS 1108+574 is still evolving towards shorter orbital periods, becoming increasingly helium-rich.

5.5 Summary

In this chapter I have presented time-resolved spectroscopy of the helium-rich dwarf nova SBSS 1108+574 (SDSS J1111+5712), confirming the period detected photometrically during the 2012 April outburst. The system shows unusually strong helium emission in both outburst and quiescence, suggesting a high helium abundance.

I measure the superhump period from our photometry as 56.34 ± 0.18 minutes, consistent with the result of Kato et al. (2013). The spectroscopic period is found to be 55.3 ± 0.8 minutes, significantly below the normal period minimum (∼80 minutes), confirming the system as an ultracompact

CV containing a highly evolved donor. The relatively high accretion rate, together with the large mass ratio, suggests that SBSS 1108+574 is still evolving towards its period minimum.

The results presented in this chapter have reinforced our initial hypothesis that this system lies somewhere between normal CVs and normal AM CVn binaries. As more of these 'hybrid' systems are discovered, the question of their importance to compact binary evolution, and the AM CVn population, becomes increasingly apparent.

Chapter Six

Improving the efficiency of the survey

6.1 Introduction

In this chapter I return to the SDSS AM CVn survey, to discuss procedures for increasing the efficiency. As has been discussed, the majority of the brighter objects in the sample have been observed, and larger telescopes and longer exposures are now required in order to observe the fainter targets. It is therefore desirable to reduce the number of targets that would need to be observed to push the sample to fainter limits.

Firstly I describe cross-matching the SDSS sample with other surveys. I then investigate the new colours that this provides, and describe new colour cuts that could be applied to remove contaminants from the sample. Finally I discuss the possibilities of using lightcurves of the candidates to further optimise the search.

6.2 Cross-matching

Cross-matching our sample with other surveys that probe different wavelength bands provides extra information about the spectral energy distribution of objects that have detections in these other surveys. This also allows us to calculate new colours, that may be helpful in separating some groups of objects in colour-colour diagrams. Here I investigate two surveys that extend the coverage both to shorter and longer wavelengths than the SDSS.

6.2.1 *GALEX*

The *Galaxy Evolution Explorer* (*GALEX*) satellite has conducted a series of imaging and spectroscopic surveys, including the first UV all sky survey (Martin et al., 2005). This consists of imaging in two broad bands, near-ultraviolet (NUV, 1770–2730 Å) and far-ultraviolet (FUV, 1350–1780 Å), of ∼26,000 square degrees of sky, to a depth of 20.5 mag (*GALEX* uses the AB photometric system). This is complemented by medium and deep imaging surveys with greater depths, covering smaller areas.

All candidates from the SDSS DR7 colour selection were matched against the *GALEX* Data Release 6 catalogue, taking the closest neighbour within 2 arcsec. This matching radius was chosen to ensure good coverage of the expected distribution of offsets between *GALEX* and SDSS astrometry, without introducing a significant number of false or multiple matches (Morrissey et al., 2007).

I do not use the predefined *GALEX*–SDSS cross-match described by Budavári et al. (2009), preferring the smaller FUV–NUV match radius used for the standard catalogs, in order to minimize false matches (Morrissey et al., 2007). I also prefer to have greater freedom in the choice of *GALEX*–SDSS matching radius. The results are identical in most cases.

The false match probability is estimated by repeating the search of the *GALEX* database after applying a random 10 arcsec offset to the coordinates of each SDSS source for which a *GALEX* counterpart has been found. The number of matched coordinates divided by the total number of offset sources gives an estimate of the false match rate; I derive a value of approximately 3.5 per cent.

A total of 1622 of the 1947 SDSS DR7 objects have at least one measured UV magnitude, 1590 of these have a NUV detection, and 1138 are detected in both *GALEX* bands.

6.2.2 UKIDSS

The SDSS DR7 sample was also matched to the UKIRT (United Kingdom Infrared Telescope) Infrared Deep Sky Survey (UKIDSS) DR9 catalogue. When complete, the UKIDSS Large Area Survey will cover 4028 square degrees of sky, with imaging in four broad-band filters, Y, J, H and K, to a Y-band limiting magnitude of 20.3 (Dye et al., 2006). A matching radius of 1.0 arcsec was used for the UKIDSS catalogue (which has a greater astrometric accuracy than *GALEX*), this covers the majority of the offset distribution.

Again I estimate the false match rate by offsetting the coordinates of the matched sample and repeating the search. I find a false match probability of

$\sim$1 per cent for the UKIDSS. Of our 1947 SDSS targets, only 516 are in the area that has been covered by UKIDSS, and 398 have a detection in at least one filter.

6.3 Colour cuts

The initial selection of the sample by Roelofs et al. (2009) was based on the colours of the nine emission line AM CVn binaries with SDSS photometry known at the time. Fig. 6.1 shows the colours of 24 of the 37 currently known AM CVn binaries. Whilst many of the systems discovered since have been found through this survey, all long period systems, and most intermediate period systems with quiescent SDSS photometry, fall within our colour box (see also Levitan et al. 2013, for a discussion of the colours of outbursting systems found by the PTF). The survey colour bias was discussed in chapter 3, where I concluded that it is unlikely that a large population of AM CVns has been missed. This more robust knowledge of the location in colour space of AM CVn binaries, and other objects in this region, allows us to improve upon the initial selection criteria and reduce the sample size.

It is clear from Fig. 6.1 that the known AM CVn binaries with SDSS photometry occupy the region with

$$g - r < -0.1;$$

approximately 81 per cent of the quasars (red triangles) have $g - r$ above this limit, and many could be safely removed. It should be noted that the spectroscopic completeness of the SDSS increases with increasing $g - r$ over the densely populated area of this region, where objects have been targeted for quasars (see Fig. 3.1). The original sample of systems from the SDSS spectroscopic database is thus slightly biased towards the red cut-off. This makes it unlikely that a large fraction of AM CVn binaries lie beyond $g-r = -0.1$, and the risk to our completeness is considered to be small in comparison to the gain in efficiency.

The addition of UV photometry allows further examination of the sample in additional colour spaces. Fig. 6.2 shows colour diagrams of the part of the sample with *GALEX* NUV detections, these diagrams include 17 of the known AM CVn binaries. UV extinction was estimated using the $R_V = 3.1$ prescription of Cardelli, Clayton & Mathis (1989) and the full Galactic reddening according to Schlegel, Finkbeiner & Davis (1998), in order to match the procedure used for the SDSS. Note that CR Boo and SDSS J1043 were much closer to their maximum brightness states when observed by *GALEX*, compared with their SDSS photometry, causing the large negative NUV$-u$. There are also several other objects with NUV$-u < -1$,

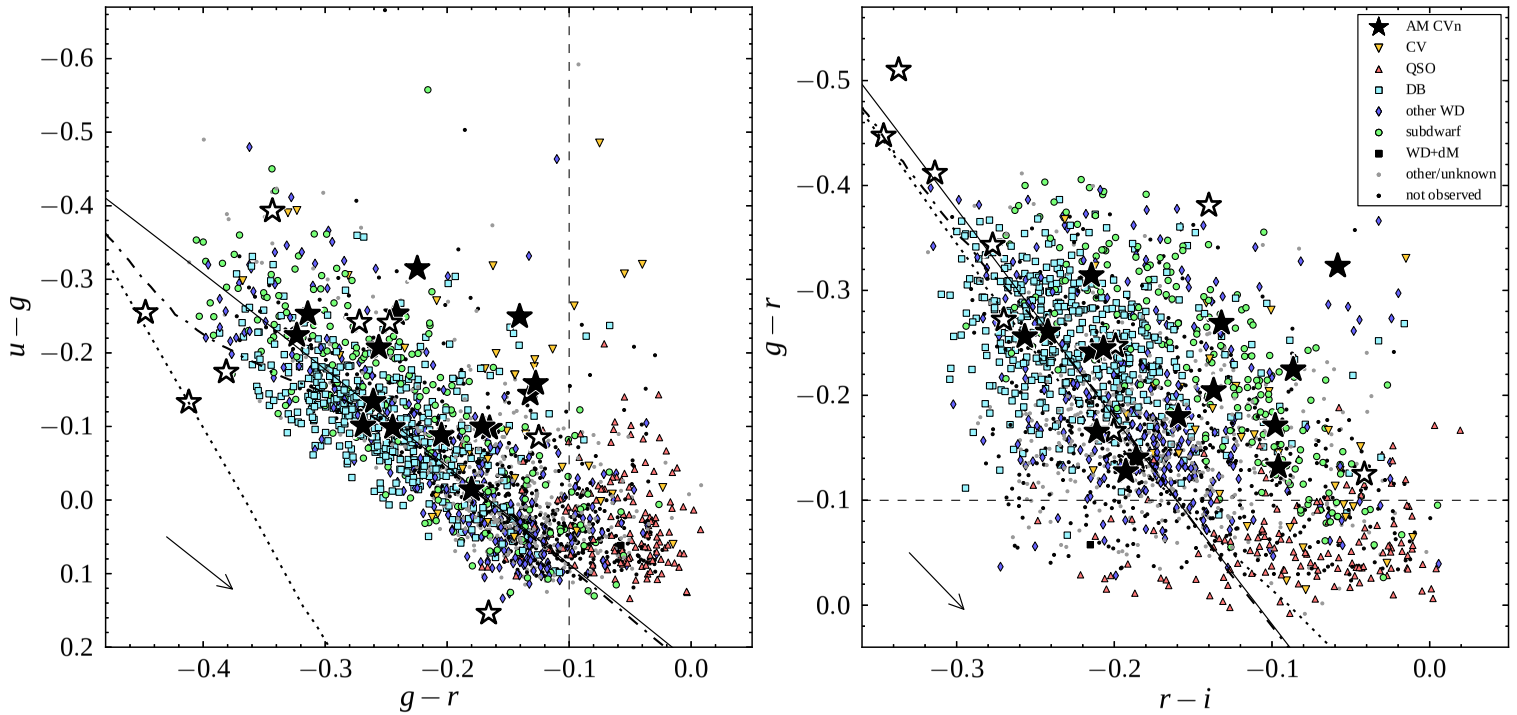

Figure 6.1: Colours of the known AM CVn binaries (black stars) together with our sample of candidates from SDSS DR7. The filled stars are the confirmed longer period systems, and the AM CVn binaries discovered via their emission line spectra in the SDSS or this survey. The open stars represent those systems to which we do not necessarily expect to be sensitive, from left to right (left hand panel) or from top to bottom (right hand panel), these are HM Cnc (right hand panel only), SDSS J1908, SDSS J2047, PTF1 J2219, ES Cet, PTF1 J0943, PTF1 J0435, CR Boo and PTF1 J0857. Colours of the faint PTF-discovered systems are taken from Levitan et al. (2013). The orange inverted triangles represent CVs. Quasars, DB white dwarfs, other types of white dwarf, subdwarfs, and WD + M dwarf systems are represented by red triangles, cyan squares, blue diamonds, green circles and black squares respectively. Grey dots indicate those candidates that could not be classified, and black dots those that have not yet been observed. The solid line shows the blackbody cooling track, the dotted and dot-dashed lines represent the DA and DB white dwarf cooling tracks, and arrows represent reddening vectors for an extinction $A(g) = 0.2$. This is identical to Fig. 3.11 with the addition of the dashed line to represent the new colour cut.

for which different brightness states are a possibility (NUV $- u \simeq -1$ is the limit for a hot blackbody).

The NUV $- u$ colour greatly increases the separation of some object types compared with only Sloan colours. The subdwarfs and white dwarfs occupy mostly separated areas of the diagrams in Fig. 6.2; NUV $- u$ also separates the subdwarfs and the quasars. Many of the subdwarfs (green circles) in the upper right corner of the left hand panel of Fig. 6.2 could also be discarded, as the AM CVn binaries do not spread into this region. By requiring

$$\mathrm{NUV} - u > 4.34(g - r) + 0.5,$$

46 per cent of the subdwarfs can be removed (this cut removes objects above the dashed line in the left-hand panel of Fig. 6.2.), and the sample size is reduced by 11 per cent.

The DB white dwarfs (cyan squares) lie around and close to the blackbody cooling track in (NUV $- u$, $r - i$) colour space, whereas the AM CVn binaries all lie above. With a cut close to this cooling track, and parallel to the reddening vector,

$$\mathrm{NUV} - u < 6.76(r - i) + 1.85,$$

approximately one fifth of the DB white dwarfs can be removed from the sample (this cut removes objects below the dashed line in the right-hand panel of Fig. 6.2.), significantly reducing the numbers of the main contaminant, and reducing the total size of the sample to $\sim$1500.

These additional cuts increase the risk of missing some AM CVn binaries that are present in the SDSS photometry, making it more difficult to judge the completeness, and the accuracy of the space density. However, the increase in efficiency offers a significant advantage in reducing the observing time required to complete such a survey.

The UKIDSS colours of the sample are shown in Fig. 6.3. The separation of quasars from the rest of the sample is clear even with the limited sky coverage (see also Richards et al. 2009; Wu & Jia 2010; for a discussion of quasar selection via infrared colours). As only four of the known AM CVn binaries have been covered by UKIDSS, and none with sufficient detections whilst in the same brightness state to appear in Fig. 6.3, any attempt to remove targets from the sample based on infrared colours would be unreliable. Greater coverage with infrared photometry could, however, allow further improvements to the sample size. The *WISE* mission (Wright et al., 2010) has recently conducted an all sky infrared survey, however,

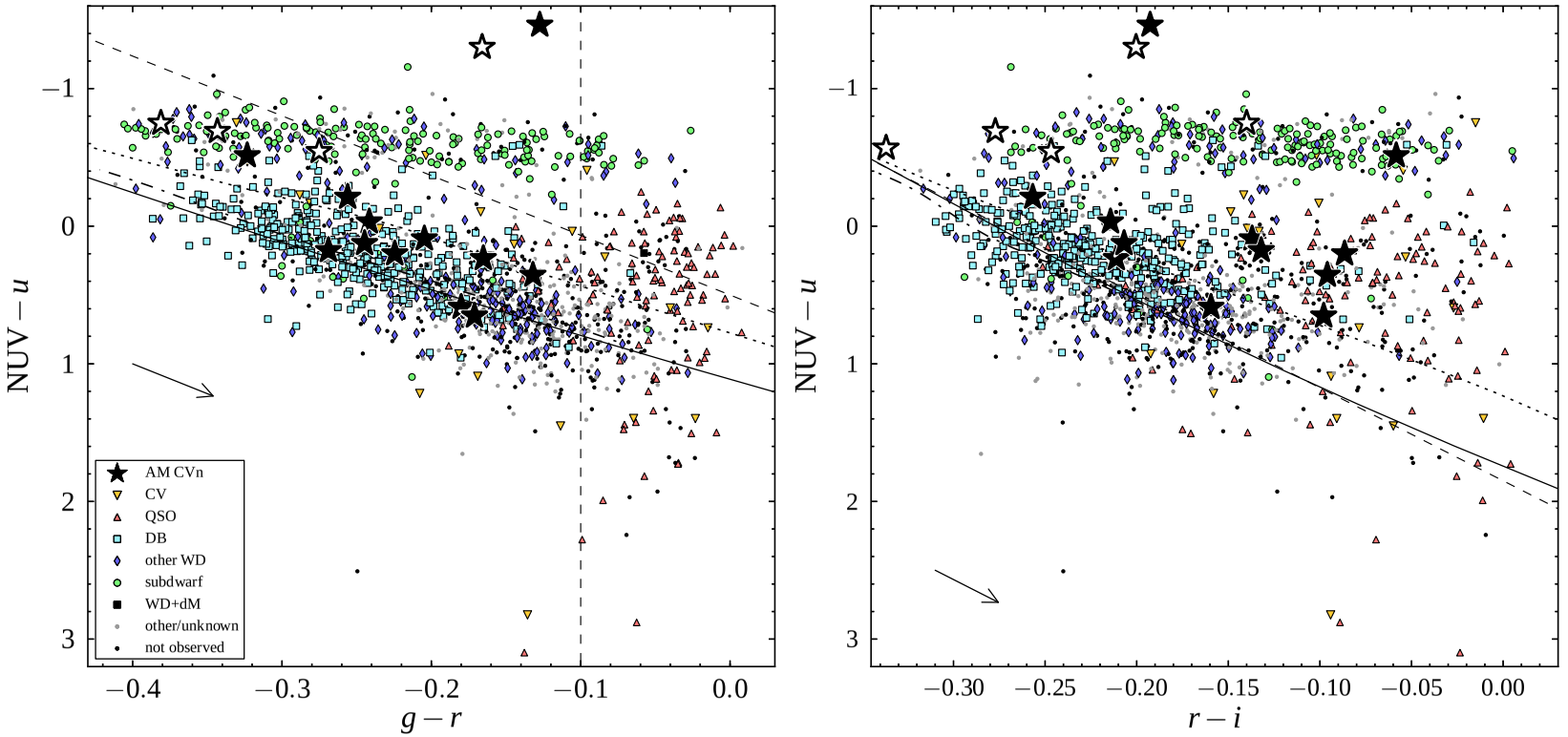

Figure 6.2: Colours of the known AM CVn binaries (black stars) together with our sample of candidates from SDSS DR7 combining *GALEX* NUV detections. The symbols have the same meanings as in Fig. 6.1. The open stars represent, from top to bottom, CR Boo, PTF1 J2219, ES Cet, HM Cnc (right hand panel only) and PTF1 J0857. The large negative NUV $-$ u colours of CR Boo and SDSS J1043 are caused by their varying brightness states between the epochs of *GALEX* and SDSS observations. The solid line shows the blackbody cooling track, the dotted and dot-dashed lines represent the DA and DB white dwarf cooling tracks, and arrows represent reddening vectors for an extinction $A(g) = 0.2$. A significant portion of DB white dwarfs lie below of slightly above the blackbody cooling track in (NUV $-$ u, $r - i$) colour space, whereas the AM CVn binaries all lie above this track. The dashed lines represent the new colour cuts. This figure makes use of white dwarf model spectra kindly provided by Detlev Koester.

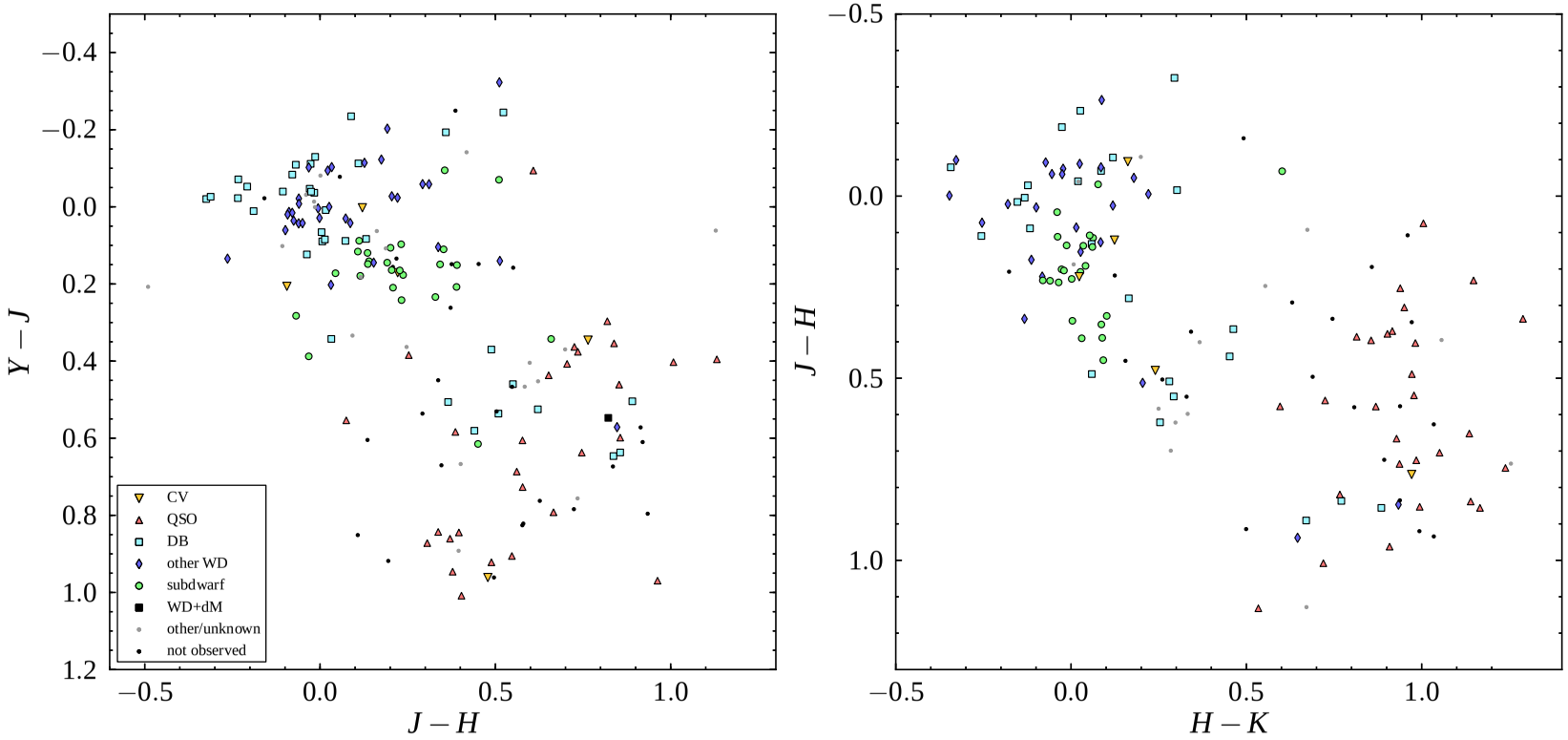

Figure 6.3: Infrared colours of our sample. The symbols have the same meanings as in Fig. 6.1. Both diagrams show the potential for removing quasars that infrared data provides, however, greater coverage is required to enable reliable cuts to be made.

the depth of the survey is insufficient for the majority of known AM CVn binaries. Ongoing and future deep infrared surveys, such as those carried out using the Visible and Infrared Survey Telescope for Astronomy, will be very useful for separating quasars from AM CVns.

6.4 Variability

As both the PTF (Law et al., 2009) and the CRTS (Drake et al., 2009, 2014) have proven, outbursts of AM CVn binaries and CVs can be incredibly useful for identifying new systems, as well as studying them (e.g. Levitan et al., 2011, 2013, 2014; Breedt et al., 2012; Woudt, Warner & Motsoaledi, 2013). Whilst many of the AM CVn binaries contained in our sample are not expected to undergo outbursts (existing in a stable quiescent state), there should still be a significant fraction that do show outbursts.

Even those systems that do not undergo outbursts may show some significant variability that does not appear like normal outbursts or superoutbursts, as has been observed in SDSS J0804+1616 (Ramsay et al., 2012), and will also likely exhibit some rapid low-level variability associated with accretion (e.g. Warner, 1972; Levitan et al., 2011). AM CVn binaries may also show intensity modulations on their orbital periods; this has been observed in the shorter period systems (e.g. Smak, 1967; Ramsay & Hakala, 2005; Fontaine et al., 2011), but is often not detected in the longer period AM CVns with quiescent discs (e.g. Warner, 1972; Woudt & Warner, 2001; Woudt, Warner & Pretorius, 2004). Detecting AM CVn binaries via their orbital brightness variations is the goal of the Rapid Temporal Survey (RATS; Ramsay & Hakala, 2005; Ramsay et al., 2006; Barclay et al., 2011). The RATS uses wide-field cameras to obtain deep, high-cadence observations that will reveal objects which vary on periods less than $\sim$1 hour.

Detecting the rapid flickering or possible low-amplitude orbital modulations amongst our colour-selected objects would require rapid, high-precision photometry, such as that produced by the RATS. However, this approach would be impractical for our candidates as they span thousands of square degrees of sky. Large-amplitude outbursts, however, are characteristic behaviour of CVs and AM CVns, which, once found, can be distinguished easily by a low resolution spectrum. We could thus heavily prioritise the spectroscopic observing campaign towards objects with this kind of large-amplitude variability.

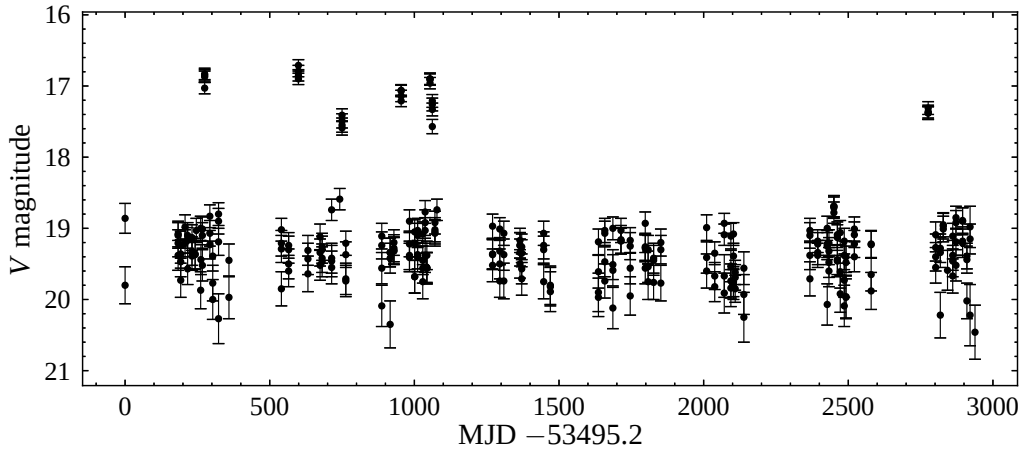

Figure 6.4: CRTS lightcurve for SDSS J0926. Several outbursts are seen during the first 3 years of coverage, the lack of outbursts detected in most of the period following this may be due to a change in state, though some outbursts may have been missed.

6.4.1 Detecting outbursts

There are a wide range of possible sources of multi-epoch photometric data, and as can be seen for SDSS J1043 in Fig. 6.2, two well-timed data points could be sufficient to detect an outburst. However, in order to be of practical use we require regular coverage of a large number of our candidates. The CRTS provides observations of a significant fraction of our targets, with reasonably regular coverage, and a long baseline.

The CRTS has its own transient detection pipeline, that detects objects with brightness variations greater than 2 mag (Drake et al., 2009). Objects with well detected outbursts will therefore likely have been identified already as CRTS transients, as is the case for the CV SBSS 1108+574 (albeit after our own identification, see chapter 5). However, objects with low-amplitude outbursts, or outbursts that were only caught during the decline, and not sufficiently close to maximum, will likely have been missed, as may be the case for SDSS J1730 (see chapter 4, and Fig. 6.5).

Combining data from both the Catalina Sky Survey (CSS) and Mt. Lemmon Survey (MLS) telescopes, 1780 of our 1948 candidates are covered. These lightcurves are visually inspected to look for outburst-like features that suggest the candidate may be an AM CVn or CV. I show some examples of CRTS outburst lightcurves in the following sections.

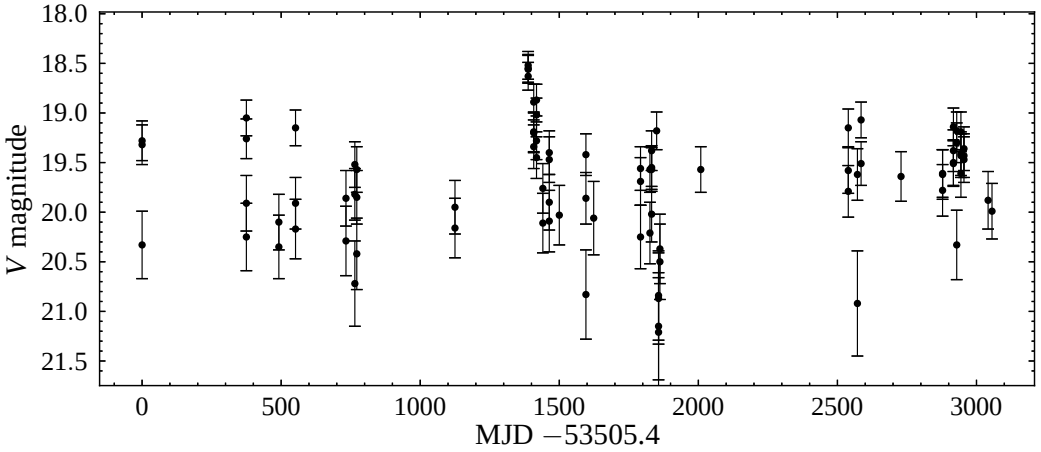

Figure 6.5: CRTS lightcurve for SDSS J1730. There is a possible decline from an outburst visible at about 1400 days, but any outburst maximum corresponding to this was not covered.

6.4.2 AM CVn lightcurves

Figs. 6.4 and 6.5 show the CRTS lightcurves of two AM CVn systems.

SDSS J0926 (Fig. 6.4) has an orbital period of 28.3 min (Anderson et al., 2005; Copperwheat et al., 2011), and shows regular outbursts for at least part of the ∼8 year coverage. The reason for the lack of detected outbursts between days 1100 and 2700 is unclear, it is possible that the system has changed state during this time and stopped undergoing frequent outbursts, however, it is known that at least one outburst was missed during this time (Copperwheat et al., 2011).

SDSS J1730 (Fig. 6.5) has a longer orbital period (35.2 min, see chapter 4), and would therefore be expected to undergo outbursts less frequently than SDSS J0926. There is no definite detection of an outburst in the CRTS data, but the feature at about day 1400 is suggestive of a decline from an outburst, the maximum of which would have been missed if this was indeed an outburst.

6.4.3 CV lightcurves

The CRTS lightcurves of two CVs identified via our survey are shown in Figs. 6.6 and 6.7.

The first object, SDSS J073559.96+220132.0 (Fig. 6.6), shows outburst behaviour similar to SDSS J0926 (Fig. 6.4), being in a quiescent state for the vast majority of detections, with just a few observations during outburst when the system is ∼2.5 mag brighter.

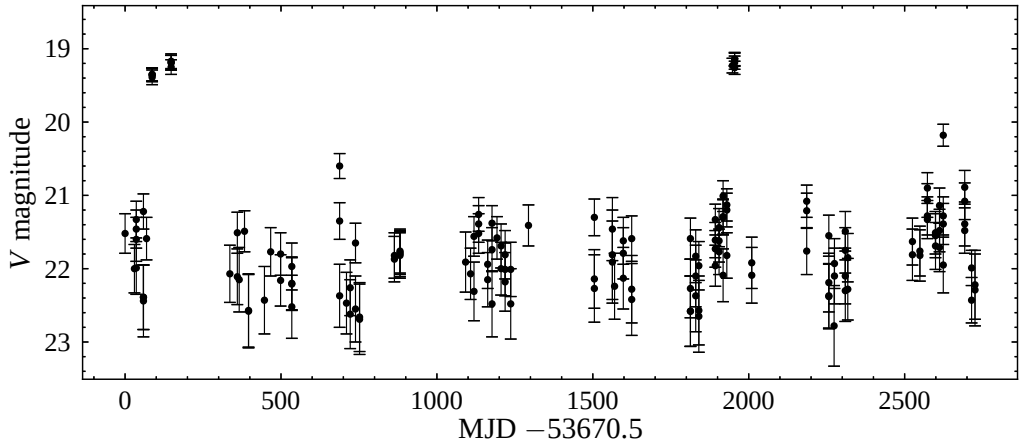

Figure 6.6: MLS lightcurve for SDSS J0735+2201, one of the CVs discovered in our survey (see chapter 3).

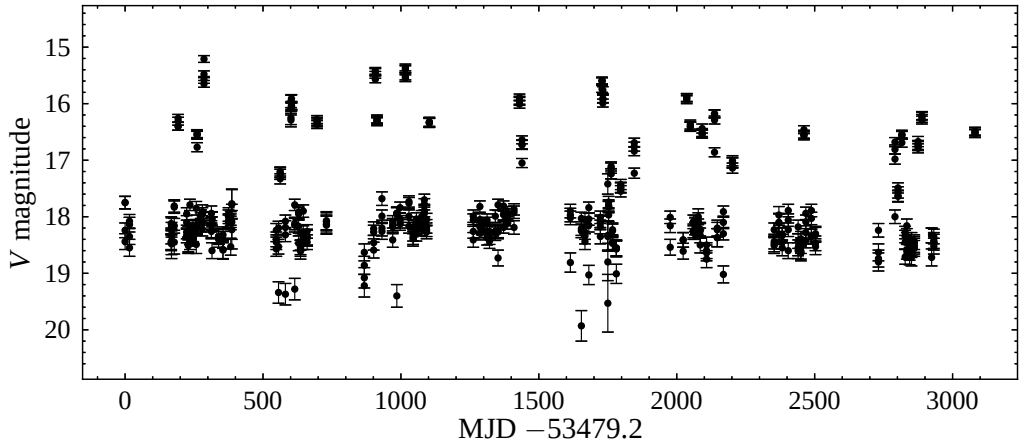

Figure 6.7: CRTS lightcurve for SDSS J0748+3125, one of the CVs discovered in our survey (see chapter 3). This object shows frequent outbursts.

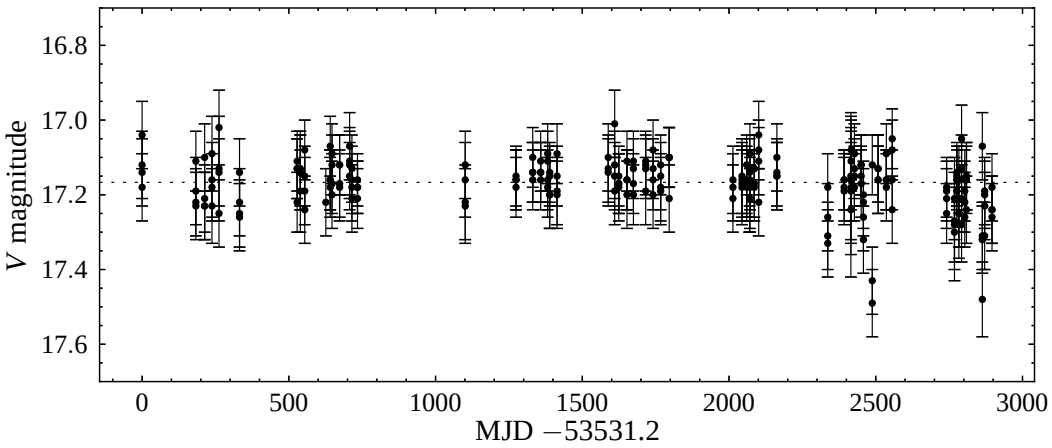

Figure 6.8: CRTS lightcurve for SDSS J0929+4936, a DB white dwarf identified in our survey. This object appears to have a constant brightness.

The second CV, SDSS J074859.54+312512.7 (Fig. 6.7), shows much more frequent outbursts, though it should be noted that this system has greater coverage.

Lightcurves similar to those shown in Figs. 6.4, 6.5, 6.6 and 6.7 would suggest outburst behaviour from the candidate, indicating that the object is very likely an AM CVn or a CV, and making it a high priority target for follow-up spectroscopy.

6.4.4 Searching for variability

As well as inspecting lightcurves for large changes in brightness associated with outbursts, it is possible to perform formal tests to search for variable sources, in an attempt to distinguish low amplitude variability objects from those that show no changes in brightness, and automatically identify those with large amplitude changes.

Fig. 6.8 shows the CRTS lightcurve for SDSS J092950.11+493614.8, an object identified as a DB white dwarf. Whilst there is some scatter, this lightcurve appears to be approximately flat, with almost no deviation from a straight horizontal line (note that the magnitude range in this plot is much smaller than in those shown in the previous sections).

In order to quantify how variable this object is, the value of the chi-squared statistic is calculated assuming that the intensity of the source is constant. The data are first fit with a single parameter (a straight horizontal line) to determine the constant magnitude that gives the lowest chi-squared, and the reduced chi-squared is then calculated. A value close to unity would imply that the data are

consistent with the source not varying, whereas a significantly larger value would suggest that it is variable.

The dashed line in Fig. 6.8 represents this constant brightness for SDSS J0929+4936, which gives $\chi^2_{\rm red} = 0.530$, suggesting that SDSS J0929+4936 does not vary significantly (and that the uncertainties on this data may have been overestimated). In contrast I obtain $\chi^2_{\rm red} = 4.80$ for SDSS J1730 (Fig. 6.5), and $\chi^2_{\rm red} = 43.5$ for SDSS J0926 (Fig. 6.4) both of which show clear variability. This procedure could be automated and applied to the entire sample, however, the CRTS data for our targets lack the precision required to detect low amplitude changes in brightness.

6.5 Discussion

To increase the efficiency of our AM CVn search it is necessary to remove contaminants from the sample, without significantly increasing the risks of missing hidden AM CVn binaries. Fig. 6.1 shows that the reddest part of the $g-r$ distribution of our sample is largely made up of quasars and unclassified objects, which can be removed from the sample.

Cross matching the sample with the *GALEX* catalogue provides a further colour space that proves to be very useful in separating different classes of object. The majority of the subdwarfs in our sample are brighter in NUV relative to u than the white dwarfs, causing the gap between the two populations that is not seen with only Sloan colours. That the AM CVn binaries are slightly redder than many of the DB white dwarfs in $r-i$, perhaps due to the contribution of the accretion disc, is very useful when combined with their distribution in NUV $- u$. This increased splitting of DB white dwarfs from the other objects in the sample in (NUV$-u$, $r-i$) colour space, allows about one fifth of this major contaminant to be safely discarded. Subdwarfs and AM CVn binaries become increasingly separated with increasing $g-r$ in (NUV$-u$, $g-r$) colour space, such that the majority of the redder subdwarfs can be cut. Making these cuts parallel to the reddening vectors ensures that objects are not removed unintentionally due to poorly estimated extinction. The small number of objects with NUV $- u < -1$ or NUV $- u > 1.5$ are kept, as the large values may be caused by varying brightness state between the epochs of *GALEX* and SDSS observations (which could be due to an outburst).

Combining the two new cuts involving NUV $- u$, and the more efficient $g-r$ cut-off, in addition to the original $u-g$, $g-r$ and $r-i$ colour cuts used to produce the sample, reduces the total size by 43 per cent. Removing 268 of the 544 remaining targets, brings the goal of detecting all of the hidden AM CVn population much

closer to completion. These extra cuts, whilst greatly increasing our efficiency, risk reducing our completeness. Although the new colour criteria avoid the regions in which AM CVn binaries have been found, it is possible that there exists some as yet undetected part of the population that deviates from the current distribution. Any such systems would not be expected to represent the majority of the population, and the risk in losing them is considered to be small. Increasing the efficiency of our survey becomes increasingly important as we move to fainter targets, where greater numbers of AM CVn binaries have been found (see Fig. 3.3), in order to keep the project feasible.

Near infrared photometry could be extremely useful for rejecting quasars from the sample, and whilst the currently available data that I have discussed in this chapter does not go deep enough to be of use, future surveys are likely to be able to make good use of infrared colours to optimise the search for AM CVns.

The addition of long baseline light curves for 90 per cent of our candidates could prove very useful for prioritising future follow-up spectroscopy. Candidates that show behaviour similar to outbursts in their lightcurves have a much higher chance of being either an AM CVn or a CV. Ideally we would be able to use the photometry of candidates to remove those that have lightcurves that could not be produced by an AM CVn binary, however, this is unfortunately not practical for the vast majority of sample with the data we have available. The CRTS coverage varies significantly between our candidates, and those with small numbers of observations can be very badly affected by one or two low signal-to-noise ratio measurements. Future deeper and more precise surveys, however, have great potential for further optimising colour-selected samples.

As we push towards fainter targets, removing candidates that are very unlikely to be AM CVn binaries, and prioritising our follow-up are important in order to ensure that observing the remainder of the sample remains practically achievable. Combining new constraints provided by *GALEX* fluxes with our increased knowledge of the region of colour space occupied by AM CVn binaries, cuts the number of objects still requiring observation by 49 per cent, to 275. This should result in a corresponding increase in our AM CVn hit-rate, and allow the remaining long period AM CVn binaries hidden in the SDSS photometric database to be uncovered.

6.6 Summary

In this chapter I have discussed using photometry from other surveys to improve our AM CVn discovery rate. Cross-matching our sample with the *GALEX* survey

provides us with a new colour that is very useful for discarding contaminants. The addition of CRTS lightcurves allows us to prioritise our spectroscopic follow-up to objects with a higher chance of being an AM CVn binary.

These improvements should allow us to significantly increase the efficiency of our survey, and similar surveys that will take place in the future. This will enable the estimates of the space density to be greatly refined, providing constraints for common envelope (CE) evolution models, allowing more accurate modelling of the gravitational wave signal and foreground, and leading to a better understanding of the stability of mass transfer in possible progenitor systems.

The new colour cuts I have developed here will be used again in the next chapter to increase the efficiency of a related search of the SDSS spectroscopic database.

Chapter Seven

New AM Canum Venaticorum binaries from the Sloan Digital Sky Survey III

7.1 Introduction

More than a third of the total known population of AM CVn binaries have been discovered via the SDSS, though recently they have also been found increasingly via synoptic surveys (Levitan et al., 2011, 2013, 2014; Woudt, Warner & Motsoaledi, 2013). In this chapter I present two new systems discovered amongst the SDSS-III spectroscopic data. Motivated by their discovery, I have applied the proposed colour-cuts based on *GALEX* (see chapter 6), whilst extending the original colour-selection in the SDSS bands, to search for any further AM CVns in the most recent SDSS spectroscopy.

7.2 A search of the SDSS spectroscopic database

The SDSS-III comprises four spectroscopic surveys, largely targeting quasars and galaxies (Eisenstein et al., 2011). Recent data releases have significantly increased the number of spectra available. The two new systems discussed in this chapter were discovered whilst examining spectra of objects targeted as white dwarfs by the SDSS-III. This motivated us to conduct a fuller search of the SDSS spectroscopic database, examining objects observed as part of the SDSS-III with colours similar to the known AM CVns (the spectroscopic observations from the SDSS and SDSS-II

Table 7.1: Colour selection used to search for AM CVns in the SDSS spectroscopic database. I select only objects classified as a point source, with spectra that were made available in SDSS Data Releases 8, 9 or 10.

Colour	Constraint
$u-g$	< 0.35
$u-g$	$< 2.83\,(g-r)+1.05$
$g-r$	< 0.02
$g-r$	> -0.48
$r-i$	< 0.03
$r-i$	> -0.35
NUV $-\,u$	$> 4.34\,(g-r)+0.5$ OR < -1
NUV $-\,u$	$< 6.76\,(r-i)+1.85$ OR > 1.5

have been well explored by previous studies, Anderson et al. 2005, 2008; Roelofs et al. 2005).

The similar colours of the known AM CVns have been exploited previously to conduct a dedicated survey of objects with only photometry in the SDSS database, to search for the 'hidden' population (see chapter 3). The two new AM CVns both have $u-g$ colours slightly outside the range occupied by the previously identified SDSS AM CVns, and so I have expanded Roelofs et al. (2009)'s original colour selection (see chapter 1) for our new search of the spectroscopic database, as shown in Fig. 7.1 and Table 7.1. I also apply the colour-cuts based on *GALEX* NUV photometry, to increase the efficiency of our search, as these remove many of the subdwarfs and quasars from the sample (see chapter 6). As I described in the previous chapter, objects that have extreme NUV $-\,u$ colours are retained (as they may be variable), as are those that do not have a match in the *GALEX* database. The constraints are summarised in Table 7.1. Colours are corrected for Galactic extinction as before (Roelofs et al., 2009; Carter et al., 2013).

Applying these constraints to SDSS Data Release 10 (DR10), cross-matched with *GALEX* Release 7, resulted in the selection of 5728 objects, for which the spectra were then visually inspected. The main contaminants in this colour-selection are hydrogen atmosphere (DA) white dwarfs, and quasars. I recovered five AM CVns with spectra taken as part of the SDSS-III surveys[1], including the two new systems, but found no additional new AM CVns.

[1]The previously known AM CVns with new spectra in the SDSS-III are SDSS J0129+3842, SDSS J0804+1616 and SDSS J1721+2733.

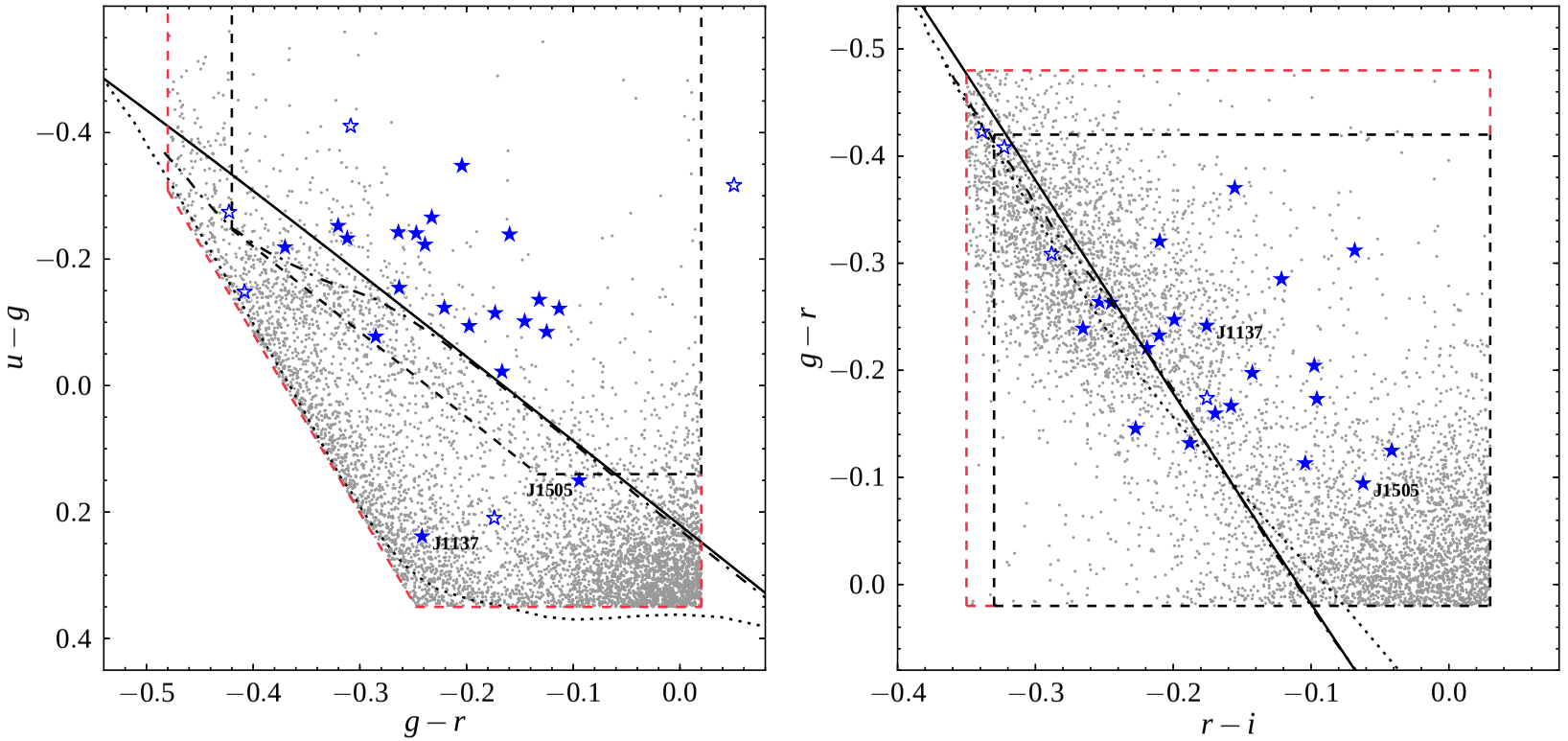

Figure 7.1: Dereddened colours of the known AM CVn binaries with *ugri* photometry (blue stars). Those systems that have short periods, or photometry that may not correspond to their quiescent state are marked with open stars. The new AM CVns are labelled. Colours of the faint PTF-discovered systems are taken from Levitan et al. (2013). The black dashed lines show the Roelofs et al. (2009) colour-cuts, the red dashed lines represent the extended cuts I use here. The objects selected are plotted as grey dots. The two AM CVns with $u-g$ outside the original cuts are the new systems discussed in this chapter. The solid line shows the blackbody cooling track, the dotted and dot-dashed lines represent the DA and DB white dwarf cooling tracks ($\log g = 8.0$; Holberg & Bergeron 2006; Kowalski & Saumon 2006; Bergeron et al. 2011; Tremblay, Bergeron & Gianninas 2011).

7.3 The new AM CVn binaries

7.3.1 Average spectra

I show the SDSS spectra of the two new AM CVn binaries, SDSS J113732.32+405458.3 (hereafter SDSS J1137) and SDSS J150551.58+065948.7 (hereafter SDSS J1505) in Fig. 7.2. These were identified via the strong helium emission lines they display. Their spectra are both remarkably similar to the spectrum of SDSS J1208 from Kupfer et al. (2013), which is reproduced in Fig. 7.2 for reference. Both SDSS J1137 and SDSS J1505 show triple-peaked emission lines, combining the standard double-peak associated with the accretion disc (Horne & Marsh, 1986, see chapter 1), and a 'central spike'. This feature has been seen in several AM CVn systems, and is thought to originate close to the surface of the accreting white dwarf (Marsh, 1999; Morales-Rueda et al., 2003).

There are signs of underlying absorption around the 5875 Å emission line in both spectra. Similar features have been seen in several AM CVns (e.g. SDSS J1240, V406 Hya Roelofs et al., 2006), where this is identified as being from the accretor, but it is usually clearest in the bluest lines. Both systems also show broad nitrogen emission lines in the red parts of their spectra (see Fig. 7.2).

Table 7.2 gives the SDSS and *GALEX* photometric magnitudes for the two systems. I fit a blackbody to both the spectrum (masking the emission lines) and the photometric fluxes for each object in order to estimate the continuum temperature. The data have been corrected for extinction using the full Galactic reddening according to Schlegel, Finkbeiner & Davis (1998), $E(B-V) = 0.018$ and 0.032 for SDSS J1137 and SDSS J1505 respectively. The fits are shown in Fig. 7.3. I give the formal uncertainties from the fits. Note that the contribution of the disc to the continuum is unknown, and is expected to vary significantly with orbital period (see e.g. Nelemans, Yungelson & Portegies Zwart, 2004; Bildsten et al., 2006).

7.3.2 Radial velocities

The SDSS spectra (Fig. 7.2) are the average of at least three exposures, known as sub-spectra, with typical exposure times of 15 min. There are six sub-spectra for SDSS J1137, and four for SDSS J1505. I searched for radial velocity variations between the SDSS subspectra in order to search for the orbital periods of these systems.

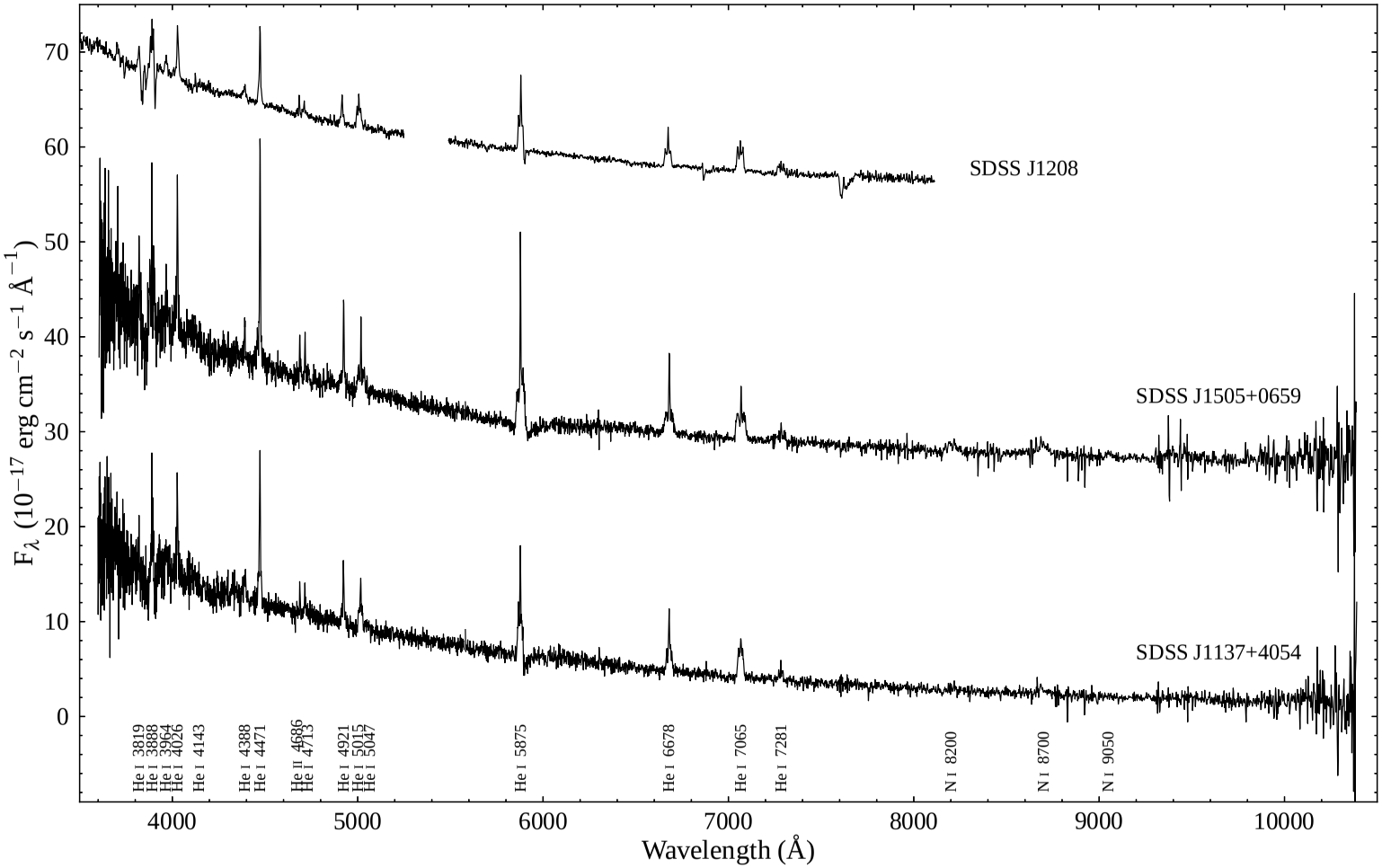

Figure 7.2: SDSS spectra of the two new AM CVn binaries and SDSS J1208 (Kupfer et al., 2013). The prominent emission lines have been labelled. The spectra of SDSS J1505 and SDSS J1208 have been offset by 25×10^{-17} and 54×10^{-17} erg cm^{-2} s^{-1} Å^{-1} respectively.

Table 7.2: Spectral energy distribution and EW of the He I 5875 Å emission line for the two AM CVn binaries. Numbers in parentheses indicate uncertainties in the corresponding number of last digits.

Object	FUV	NUV	u	g	r	i	z	$A(g)$	EW (Å)
SDSS J113732.32+405458.3	–	19.87(9)	19.26(3)	19.00(1)	19.23(1)	19.39(2)	19.45(6)	0.07	−30(3)
SDSS J150551.58+065948.7	22.69(23)	20.05(17)	19.30(3)	19.11(1)	19.17(1)	19.21(2)	19.35(5)	0.12	−50(3)

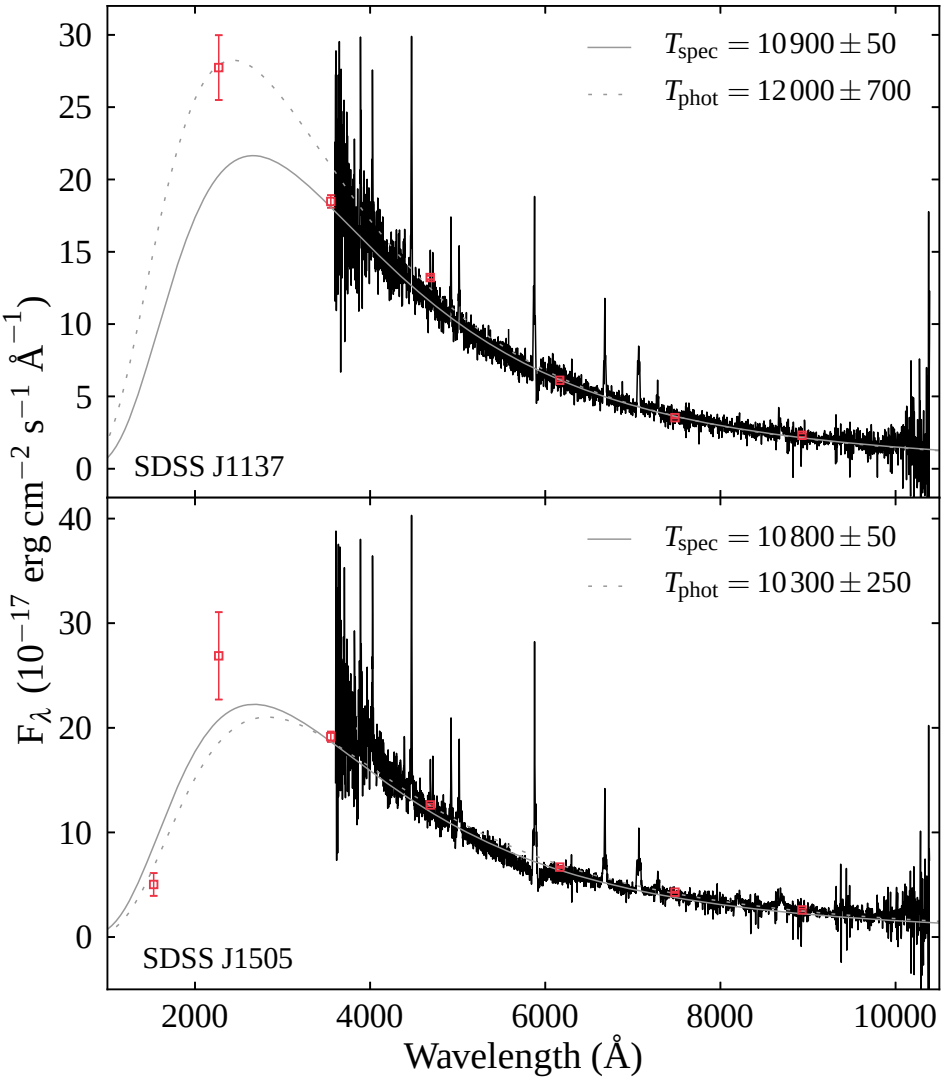

Figure 7.3: Spectra of the two new AM CVn binaries with photometric data from SDSS and *GALEX* overplotted (red squares). The solid and dashed lines are blackbody fits to the spectra and photometry respectively. The temperatures of these fits are given in Kelvin. Data have been corrected for Galactic extinction

Table 7.3: Radial velocities measured from the SDSS J1137 subspectra.

HJD	Radial velocity (km s^{-1})
2455620.8272816	38.20 ± 16.85
2455620.8386465	102.47 ± 19.84
2455620.8500112	-24.08 ± 18.58
2455620.8613760	-13.26 ± 19.39
2455620.8727523	95.37 ± 14.75
2455620.8841171	89.73 ± 14.71

Table 7.4: Radial velocities measured from the SDSS J1505 subspectra.

HJD	Radial velocity (km s^{-1})
2455712.6830284	76.53 ± 27.44
2455712.6944161	54.92 ± 28.41
2455712.7057808	87.89 ± 26.39
2455712.7171455	94.27 ± 24.99

The radial velocities of the nine strongest He I emission lines[2] were measured using MOLLY. Each line was fit by a single Gaussian, with the initial values of the fit parameters determined from a fit to the average spectrum. The FWHM for each line was fixed to this value, whilst the velocity offset common to all lines, and the height of each line were allowed to vary, as outlined in chapter 2. This gives a radial velocity for each subspectrum that is much more precise than achievable using any single line.

The measured radial velocities, given in Tables 7.3 and 7.4, were then used to construct power spectra for each object, to search for periodic signals. Both the Lomb-Scargle (Lomb, 1976; Scargle, 1982) and orthogonal polynomial (ORT; Schwarzenberg-Czerny, 1996) methods are used to calculate power spectra.

The power spectrum for SDSS J1137 (shown in Fig. 7.4) is dominated by two strong peaks, corresponding to periods of 22.56 ± 0.39 and 59.63 ± 2.74 min. The phase folded radial velocity curve for the longer period is shown in Fig. 7.5.

The power spectrum for SDSS J1505 shows a similar result (Fig. 7.6), with the stronger peak corresponding to a period of 50.6 min. The radial velocity curve folded on this period is shown in Fig. 7.7. However, with only four data points, the low radial velocity amplitude and the large uncertainties on the measurements, this is not considered to be a reliable measurement of the orbital period.

[2]The following He I emission lines were used to measure the radial velocities: 3888, 4026, 4471, 4921, 5015, 5875, 6678, 7065 and 7281 Å

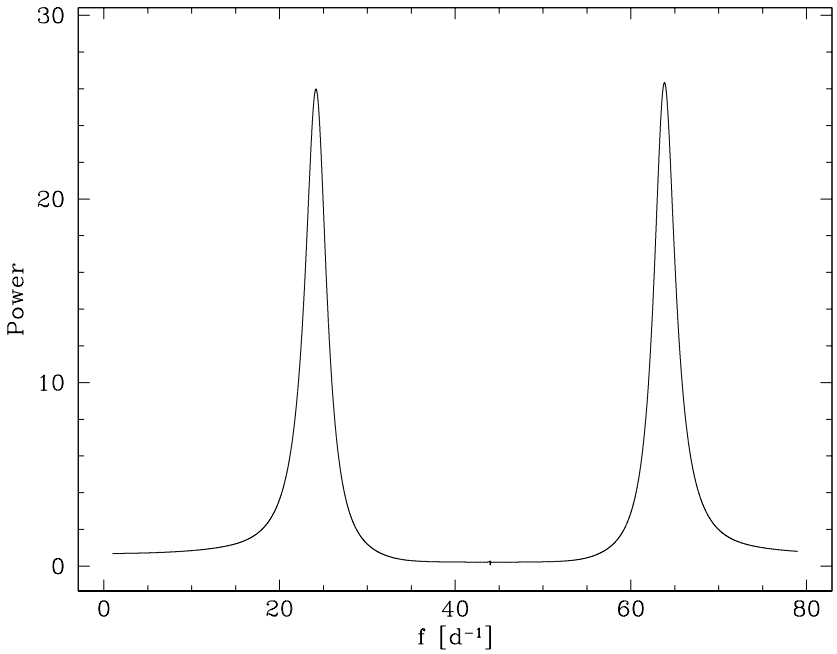

Figure 7.4: ORT power spectrum calculated from the He I radial velocities of SDSS J1137. Two strong peaks of almost equal power are seen at 24.1 and 63.8 cycles d^{-1}.

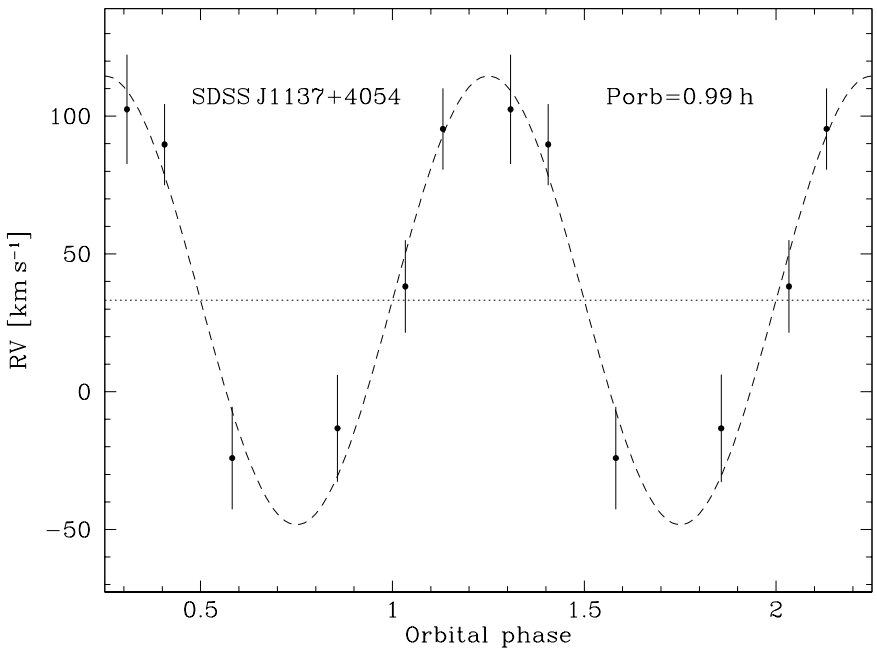

Figure 7.5: Measured He I radial velocities folded on a period of 59.6 minutes. The dashed and dotted lines are the best fit radial velocity curve and systemic velocity

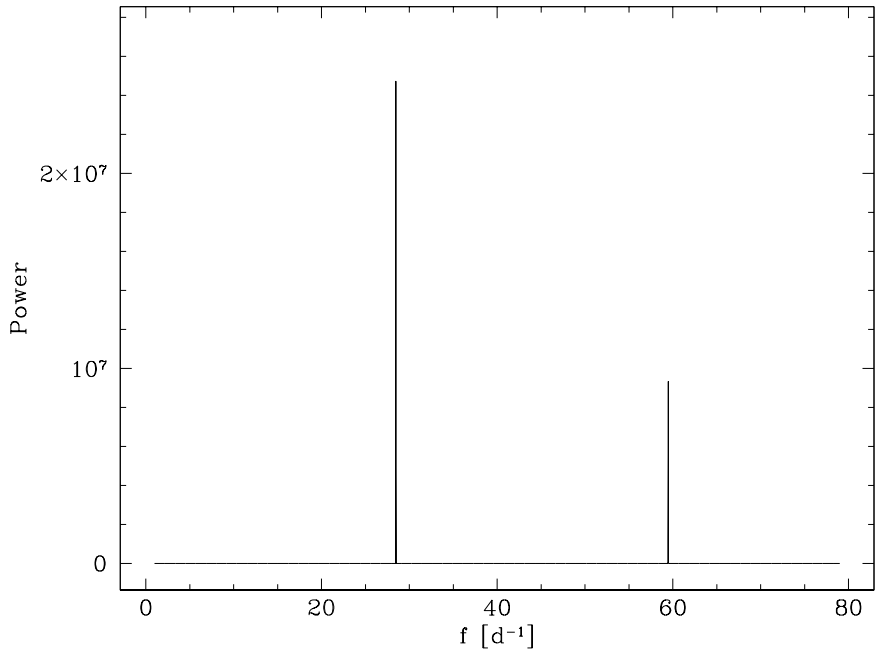

Figure 7.6: ORT power spectrum calculated from the He I radial velocities of SDSS J1505.

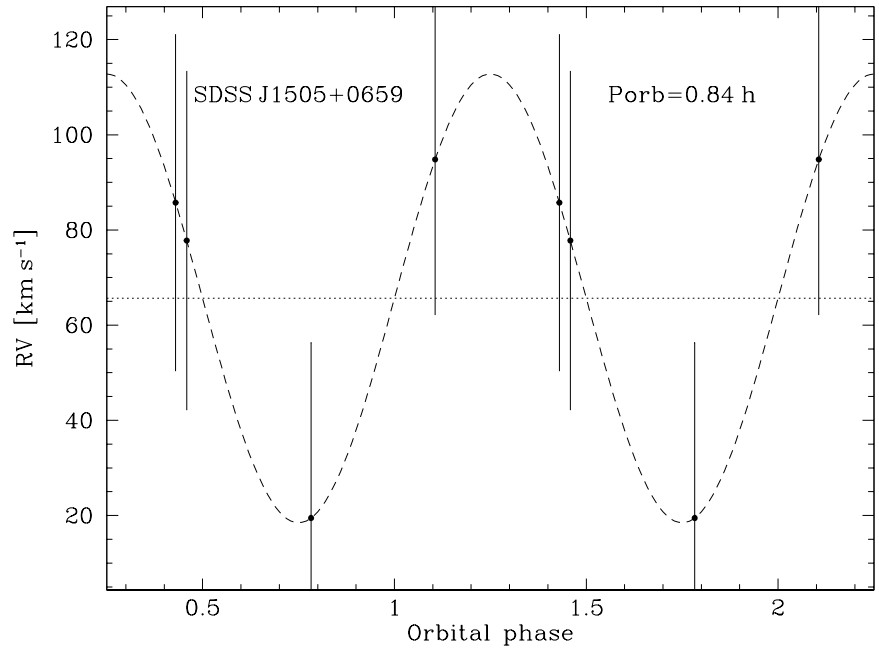

Figure 7.7: Measured He I radial velocities folded on a period of 50.6 minutes. The dashed and dotted lines are the best fit radial velocity curve and systemic velocity

7.4 Discussion

The spectra of the two new AM CVn binaries are very similar to that of the long period AM CVn system SDSS J1208+3550 ($P_{\rm orb}$ = 53 min; Anderson et al., 2008; Kupfer et al., 2013), showing broad double-peaked helium emission with strong central spikes. Due to the mass transfer rate being a steep function of the orbital period, the spectra of AM CVn binaries vary considerably with period. That these new systems have spectra that appear similar to SDSS J1208 suggests that they may also be long period AM CVn binaries ($\gtrsim$50 min).

The two possible periods determined from radial velocities of the subspectra for SDSS J1137 have almost equal power in the power spectra. At an orbital period of 22.5 min we would expect the system to spend much of its time in a high state, or to undergo frequent outbursts (similarly to KL Dra; Ramsay et al. 2012). On the other hand, at a period of 59.6 min we would not expect to see any outbursts, with the disc being in a stable quiescent state. As there is no evidence of outbursts (or other significant variability) in the 9 year coverage of the CRTS lightcurve (Drake et al., 2009), and the similarity of SDSS J1137's spectrum to that of the long period system SDSS J1208, gives support to the longer of the two possible periods.

The CRTS light curve for SDSS J1505 also shows no sign of any outbursts (though infrequent outbursts could have been missed), and the spectrum is also very similar to that of SDSS J1208 (Fig. 7.2), again suggesting a long period for this system. The periodic signal measured for SDSS J1505 is not considered a reliable measure of the orbital period due to the paucity of data, but it might lend further support to the suggestion that it is a another long period system.

The chemical abundances of material in the accretion discs of AM CVns can, in principle, be used to infer the formation channel of these systems (Nelemans et al. 2010; defined by the evolutionary state of the donor at the onset of Roche-lobe overflow, see e.g. Solheim 2010). The detection of nitrogen emission in the spectra of AM CVn binaries has been used to suggest that they are more likely to have white dwarf donors than helium star donors (e.g. Levitan et al., 2013; Carter et al., 2014a). The N/C ratio cannot be constrained as there are no strong carbon lines in the optical, but the detection of N I lines likely rules out significantly evolved He star donors (Nelemans et al., 2010).

Both spectra show signs of absorption wings around the He I 5875 emission line (especially SDSS J1505), that could be associated with the accreting white dwarf. However, this would require a white dwarf temperature of $\sim$15 000 K or higher, which does not seem to be compatible with the NUV flux detected for either

system. It is also worth noting that at a period longer than 50 min, such a temperature would be unexpectedly high, as the white dwarf should cool as the orbital period increases (Bildsten et al., 2006). Note that where DB absorption wings have been observed in other AM CVn binaries, it has been strongest around bluer lines, particularly He I 4471, and has not been noticeable around the 5875 Å line (e.g. Roelofs et al., 2006). This feature may be due to interstellar Na absorption, SDSS J1137 shows only a red wing, and the red wing appears stronger in SDSS J1505.

The continuum temperatures suggest cool accretors for both systems, this would be expected for long period systems, and helps to explain the redder than average $u - g$ colours that push these objects outside of our original colour box. Even considering the low temperature of the accretor, SDSS J1137 has an extremely red $u - g$ colour that puts it surprisingly close to the DA white dwarf track in $u - g$, $g - r$ colour space (see Fig. 7.1).

That no further new systems were found in this search of the SDSS spectroscopic database suggests that these two systems are outliers from the main colour distribution of AM CVn binaries. If they represent an additional population that is missed in our earlier systematic search (Carter et al., 2013), then this population is likely small, since there are only two such systems in the SDSS spectroscopic database (compared to the nine systems with SDSS spectra in Roelofs et al. 2009's original colour box). The discovery of these two new AM CVns should have very little effect upon previous estimates of the AM CVn space density.

7.5 Summary

In this chapter I have applied the colour cuts developed in chapter 6 to increase the efficiency of a new search for AM CVns amongst the SDSS-III spectroscopic data. These two new AM CVns remind us that there are still more systems to be found, and that they can still challenge our understanding. The detection of only two new systems in this sample suggests that there should be little effect on the estimate of the space density given in chapter 3.

I studied the radial velocity variations present in the SDSS subspectra of the two new AM CVns, measuring a likely orbital period of 59.6 min for SDSS J1137. The data also suggest a long period for SDSS J1505, but both systems require follow-up observations to confirm their orbital periods.

Chapter Eight

Conclusions

8.1 Summary

The aims of the work presented in this thesis were to develop our understanding of the colour-colour space occupied by the AM CVn binaries, in order to use this knowledge to better understand the AM CVn binary population, and their space density.

I have presented the observational status of a dedicated survey designed to uncover AM CVn binaries hidden in the photometric database of the SDSS, and studied the various contaminants that occupy this colour space. I have shown the small sample of hydrogen-rich CVs that have similar colours to the long period AM CVns, and presented the new AM CVn binaries discovered from a coherent examination of the entire dataset. With the complete bright part of the sample, I have derived a revised space density for the AM CVn binaries, based on Nelemans et al. (2001)'s population synthesis.

I then presented precise studies of two systems, one of the two new AM CVns and an unusually helium-rich CV found in our survey. SDSS J1730+5545 was found to have an orbital period of 35.2 ± 0.2 minutes, confirming it as an ultracompact binary. SBSS 1108+574 was found to have an orbital period of 55.3 ± 0.8 minutes, well below the expected period minimum for ordinary CVs, confirming its atypical nature.

Finally, I explored using variability to detect AM CVn systems, and developed new colour cuts using *GALEX* photometry to improve the AM CVn detection efficiency of the survey. I then applied these, whilst expanding the original SDSS cuts, to search for further AM CVn binaries in the latest spectroscopic data from

the SDSS. I also presented and discussed the implications of two further new AM CVns found in these recent SDSS data releases.

8.2 Discussion

8.2.1 The AM CVn binary space density

In chapter 3 I calculated the AM CVn binary space density to be $(5 \pm 3) \times 10^{-7}\,\mathrm{pc}^{-3}$, using the numbers of AM CVns expected from Nelemans et al. (2001)'s population synthesis, and taking the completeness of our sample above $g = 19$ as unity. Roelofs, Nelemans & Groot (2007) calculated the AM CVn space density to be $1.5 \times 10^{-6}\,\mathrm{pc}^{-3}$, based on the six systems found in the SDSS-I spectroscopic database. Our revised value is 3 times lower than this, and 50 times lower than the optimistic model from the Nelemans et al. (2001) population synthesis. Whilst the uncertainties are still large, the results from our survey, and the SDSS spectroscopic database, strongly suggest a space density lower than Roelofs, Nelemans & Groot (2007)'s estimate.

The much larger *complete* sample that Roelofs et al. (2009) set out to obtain still eludes us. The much lower than expected AM CVn hit rate has resulted in the sample size remaining very small, and therefore contributing a large uncertainty to space density calculations. The small number of AM CVns found, whilst still contributing significantly to the total known population, inhibits testing of the orbital period and luminosity distributions for the AM CVn binaries that would allow us to test our understanding of their evolution.

It was suggested by Nissanke et al. (2012) that the lower space density found using the long period AM CVn systems could be explained by a change to the Galactic disc model used by Nelemans et al. (2001). The distances of AM CVn binaries from our solar system, and hence their brightness, depends upon the assumed scale height for the distribution of AM CVn binaries in the Galaxy. If the period of star formation that formed the older AM CVns (the ones we would detect as emission line systems today) occurred in a thick disc, whilst the younger systems formed in a thin disc, the total numbers of AM CVn binaries formed is unchanged, but the long period systems are at greater distances, and are hence fainter (Nelemans et al., 2001; Nelemans, Yungelson & Portegies Zwart, 2004).

This may solve the discrepancy, but will be difficult to verify. Detecting a significant population of shorter period AM CVn systems is difficult using electromagnetic observations, as their lifetimes are expected to be extremely short, and hence their numbers in a magnitude limited sample are small. Space-based gravi-

tational wave detectors such as the upcoming *Evolved Laser Interferometer Space Antenna* (*eLISA*), should be able to detect large numbers of short period AM CVns if they are there, and help resolve this question.

In the meantime, continued observations, and searches for more AM CVn systems, will help to reduce the uncertainties on the various models that contribute to the space density calculations.

8.2.2 The AM CVn orbital period distribution

The AM CVn binary SDSS J1730 appears to be a fairly typical long period AM CVn system from its identification spectrum shown in Fig. 3.9. The measured orbital period, 35.2 ± 0.2 minutes, reveals the system to be in the longer period region of the outbursting AM CVn binary period distribution. The models on which our estimates of the space density depend, are critically linked to the orbital period distribution. It is therefore necessary to measure accurate orbital periods for the known systems, to compare the period distribution of the observed systems to the model period distribution. A significant deviation would have implications for our theories of binary evolution, and indicate some problem in the models used to calculate the space density, which may change our expectations for the numbers of systems we expect to detect.

Roelofs, Nelemans & Groot (2007) show the orbital period distribution expected for a magnitude limited sample of AM CVns in the SDSS based on their assumed magnitude distribution. This distribution peaks at $\sim$50 min, with approximately similar numbers above and below this peak (see Fig. 8.1). It should be noted that as the accreting white dwarf cools and the accretion rate drops as the orbital period increases, the longer orbital period AM CVns would be expected to be fainter. It is important to note that the given distribution includes the completeness of the SDSS-I spectroscopy, which is biased towards brighter objects (see Fig. 3.3), and so Fig. 8.1 likely under-represents the numbers of the longest period systems. Table 8.1 lists the orbital periods of the AM CVn binaries found in the SDSS with g-band magnitudes down to 21. It is noticeable that we have found many more AM CVns in the SDSS footprint with orbital periods below 50 min than above.

To consider the entire list of systems in Table 8.1 introduces several biases. Those systems discovered via the PTF are naturally outbursting systems, and therefore (likely) have orbital periods between 20 and 40 min; the shorter period group were not discovered in the same manner. If we consider only those systems discovered via our survey, and those that would have been included if they were not already known (the highlighted subset of systems in Table 8.1), we still draw the

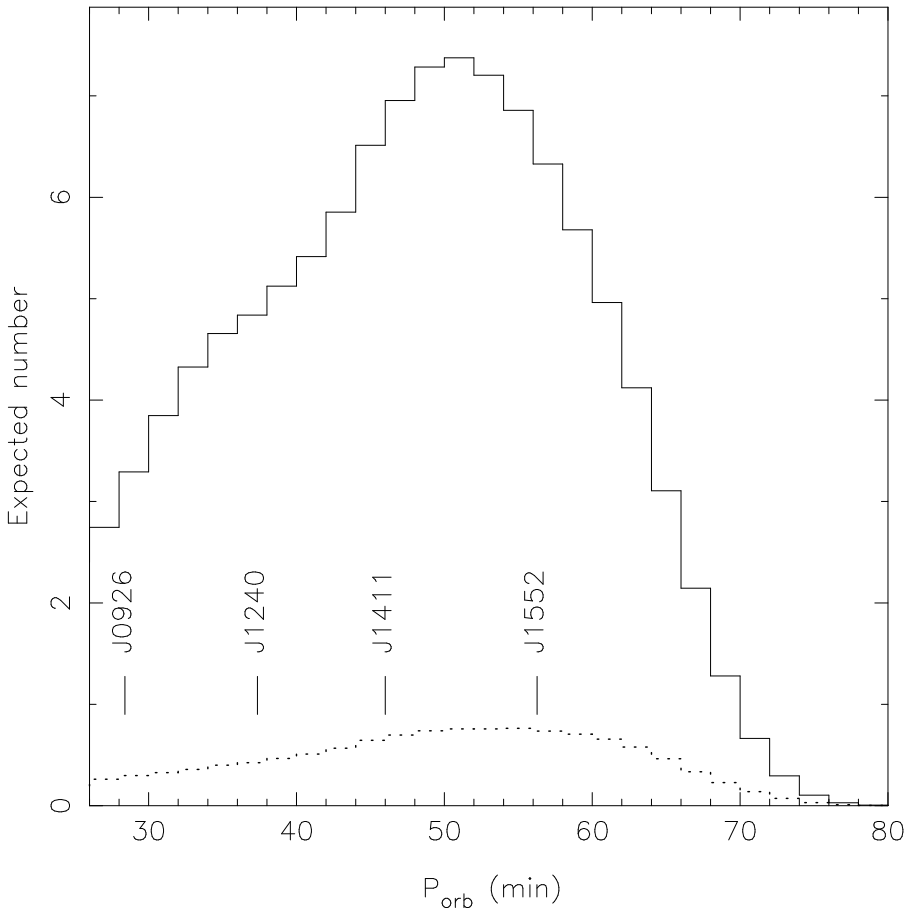

Figure 8.1: Modelled period distribution of AM CVn binaries in SDSS-I spectroscopy. The solid and dotted lines represent Nelemans et al. (2001)'s optimistic and pessimistic models respectively. From Roelofs, Nelemans & Groot (2007).

Table 8.1: Orbital periods for AM CVns in the SDSS with $g \leq 21$. Those systems that fall inside Roelofs et al. (2009)'s original colour box are indicated by a † symbol. The systems that meet the strict requirements for the space density calculations presented in chapter 3 are highlighted with bold text.

Object	Orbital period (min)	References
ES Cet†	10.3377 ± 0.0003	Warner & Woudt (2002)
SDSS J1908	15.89	Fontaine et al. (2011)
AM CVn	17.14554 ± 0.00001	Harvey et al. (1998)
HP Lib	18.380 ± 0.003	Roelofs et al. (2007b)
CR Boo	24.5217 ± 0.0002	Provencal et al. (1997)
V803 Cen	26.61 ± 0.02	Roelofs et al. (2007b)
SDSS J0926†	**28.31 ± 0.01**	Anderson et al. (2005)
PTF1 J0943†	30.35 ± 0.06	Levitan et al. (2013)
SDSS J1730†	**35.2± 0.2**	Carter et al. (2014a)
2QZ J1427†	**36.6**[a]	Woudt, Warner & Rykoff (2005)
SDSS J1240†	**37.355 ± 0.002**	Roelofs et al. (2005)
SDSS J0129†	**37.555 ± 0.003**	Kupfer et al. (2013)
SDSS J2047	outbursting	Anderson et al. (2008)
SDSS J1721†	**outbursting**	Rau et al. (2010)
SDSS J1043†	**outbursting**	Carter et al. (2013)
PTF1 J2219†	outbursting	Levitan et al. (2013)
SDSS J1525†	**44.32 ± 0.12**	Kupfer et al. (2013)
SDSS J0804†	**44.5 ± 0.1**	Roelofs et al. (2009)
SDSS J1411†	**46 ± 2**	Roelofs (2007)
GP Com†	**46.567 ± 0.003**	Marsh (1999)
SDSS J0902†	**48.31 ± 0.08**	Rau et al. (2010)
SDSS J1208†	**52.56 ± 0.02**	Kupfer et al. (2013)
SDSS J1642†	**54.2 ± 0.4**	Kupfer et al. (2013)
SDSS J1552†	**56.272 ± 0.005**	Roelofs et al. (2007c)
SDSS J1505	50.6[b] ?	Carter et al. (2014b)
SDSS J1137	59.6[c] ?	Carter et al. (2014b)

[a] superhump period
[b] unconfirmed period
[c] unconfirmed period

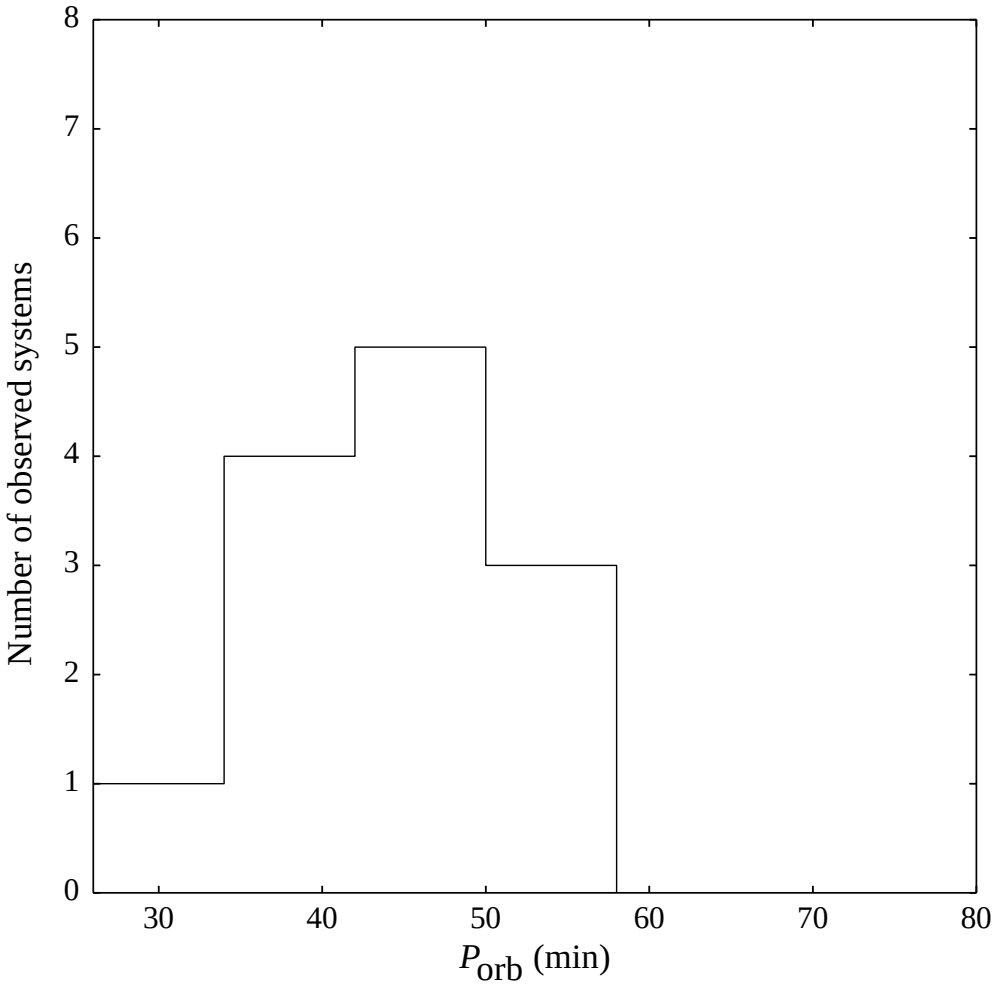

Figure 8.2: Period distribution of AM CVn binaries in the SDSS. Only the highlighted systems from Table 8.1 have been included. This shows the deficit of stems with orbital periods above 50 min compared with the model distribution shown in Fig. 8.1.

same conclusion. Fewer systems have been found with orbital periods above 50 min than below (see Fig. 8.2), regardless of whether the outbursting systems that have not yet had their periods measured are included.

As of yet the samples that can be used to test the period distribution are still small, and no strong conclusions can be drawn. Measuring precise orbital periods for the remainder of the known systems will improve the situation, and allow the distribution in period of the outbursting systems to be tested separately. This will give us further insight into the orbital period distribution of the AM CVn binaries, that will in turn help us to improve our wider understanding of binary evolution.

8.2.3 The evolved CV formation channel

The evolved CV channel for the formation of ultracompact binaries was suggested by Sienkiewicz (1984) and Tutukov et al. (1985). Since it was expected that this channel would not be a major channel for AM CVn formation, and none of the AM CVns known at the time showed any sign of hydrogen in their spectra, this channel has often been dismissed entirely.

Podsiadlowski, Han & Rappaport (2003) conclude that the evolved CV channel is a very important mechanism for the formation of AM CVn binaries, whilst Nelemans, Yungelson & Portegies Zwart (2004) find that this formation channel contributes less than 2 per cent to the total population. Yungelson et al. (in preparation)'s latest models suggest that many evolved CV systems reach their period minima before becoming sufficiently hydrogen depleted to appear as AM CVn systems, but we do not yet have a good observational constraint for comparison.

In the last few years a number of CVs have been identified with orbital periods below the standard period minimum. V485 Cen ($P_{\rm orb} = 59$ min; Augusteijn, van Kerkwijk & van Paradijs 1993; Augusteijn et al. 1996) and EI Psc ($P_{\rm orb} = 64.2$ min; Thorstensen et al. 2002) both show signs of a red secondary star in their spectra and, apart from their short orbital periods, appear much like ordinary hydrogen-rich CVs. The short orbital period of SDSS J150722.30+523039.8 ($P_{\rm orb} = 66.6$ min; Littlefair et al. 2007) was suggested to be due to a brown dwarf donor, but Uthas et al. (2011) showed the donor to be a low metallicity Galactic halo star, explaining its short period.

Breedt et al. (2012) showed CSS100603:112253−111037 ($P_{\rm orb} = 65.2$ min) must have a highly evolved donor star, having been stripped of most of its hydrogen by mass-transfer or prior to the onset of mass-transfer. Unlike the systems mentioned above, CSS 1122−1110 shows no sign of the donor in its optical spectrum, and has an extreme mass ratio similar to those found amongst the AM CVn

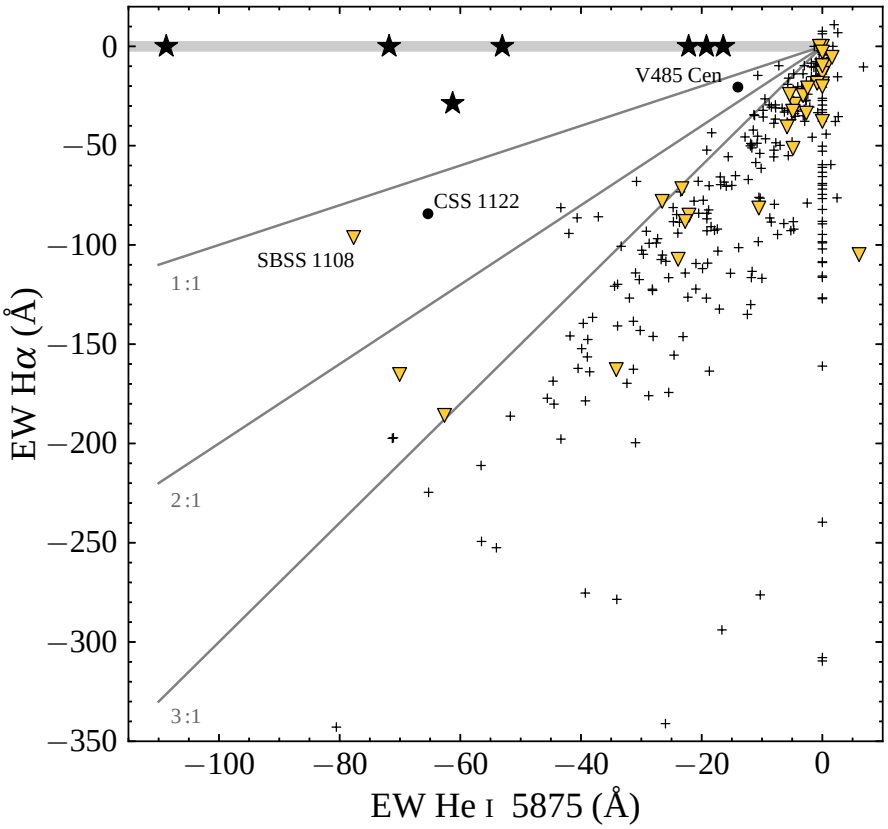

Figure 8.3: EW of He I 5875 versus Hα for our CV sample (triangles), the CV population from the SDSS (crosses) and the AM CVns from our survey (stars). Also plotted are lines showing Hα to He I 5875 EW ratios. The helium-rich CVs are labelled, and V485 Cen (Augusteijn, van Kerkwijk & van Paradijs, 1993) is also shown for comparison. In these systems the helium emission is almost as strong as the hydrogen emission, whereas hydrogen lines are at least three times stronger in the vast majority of CVs.

stars, prompting Breedt et al. (2012) to suggest the donor may be semidegenerate. CSS 1122−1110 also shows unusually strong helium lines compared to the hydrogen lines, and a central spike in these line profiles, a feature considered to be characteristic of the AM CVn binaries.

As I discussed in chapter 5, SBSS 1108+574 shows similarly strong helium emission, and has an even shorter orbital period, 55.3 ± 0.8 minutes. I show a modified version of Fig. 3.6 in Fig. 8.3. It is clear that the helium emission is almost as strong as the hydrogen emission in these ultracompact helium-rich CVs, whereas hydrogen lines are three or more times stronger in most CVs. The properties of these two systems are a strong suggestion that they are on the evolved CV pathway to becoming AM CVn stars, and that we may finally have evidence to support the existence of this channel.

It is clear from equation (1.2) that higher mass ratios will give greater angular momentum loss rates. Since the rate of angular momentum loss is closely related to the mass transfer rate in interacting binaries, systems with larger mass ratios will have higher mass transfer rates at a given orbital period. As shown in Fig. 1.14, CVs and AM CVns are expected to have higher mass transfer rates during their evolution towards period minimum than during their later evolution back towards longer periods. Since higher mass transfer rates are required to drive (more frequent) outbursts, and the long period AM CVns are expected to be in a stable quiescent state, the outbursts observed in these helium-rich CVs suggest that they are still evolving towards their respective period minima.

There are three further sub-period minimum dwarf novae that have been discovered via their outbursts in CRTS photometry, CSS 102843−081927 (P = 52.1 min; Woudt et al. 2012), CSS 233313−155744 (P = 61.7 min; Woudt & Warner 2011) and CSS 174033+414756 (P = 64.8 min; Kato 2013a; Chochol et al. 2014). So far there has been little follow-up data on these objects, but the fact that they show outbursts at these orbital periods has lead to their classification as CVs rather than AM CVns. Spectroscopic observations of CSS 1740+4147 show that it has Balmer emission lines with enhanced helium emission (Prieto et al., 2013), leading to the suggestion that it may also be a pre-AM CVn type object (Kato, 2013b).

Ramsay et al. (2014) discuss the discovery of a cataclysmic variable in the original field of view of the *Kepler* spacecraft that exhibits a stable photometric period of 56.6 min. Similarly to the helium-rich CVs I have already discussed, BOKS 45906 shows outbursts (albeit of a somewhat atypical nature), and the probable orbital period puts it well below the normal CV period minimum. The spectra Ramsay et al. obtained of this system show no signs of helium emission lines, but they have very low signal-to-noise ratios that could easily hide weaker helium emission such as seen in EI Psc.

These helium-rich CVs are still a very rare class of objects, but we seem to be discovering them at an increasing rate. Regardless of whether any of these systems will ever become sufficiently hydrogen depleted to appear as 'normal' AM CVn binaries, they are certainly of great interest for the subject of binary evolution. It seems that the distinction between AM CVns and CVs is becoming less clear, and we now know of several systems that lie between the classical definitions of the two classes. If a significant percentage of the AM CVn population does form via this evolved CV channel, it could have a profound effect upon the AM CVn orbital period distribution, and the expected space density. This makes it very important to continue studying these objects.

As I have discussed, AM CVn binaries with orbital periods greater than ∼40 minutes are expected to be in a stable quiescent state. Indeed the bright, 46.6 min period AM CVn binary GP Com has not been observed to undergo an outburst in the 40 years since its discovery. It was therefore a surprise when an AM CVn system discovered via an outburst in the CRTS (CSS121123:045020−093113; Drake et al., 2012) was later found to have a probable orbital period of 47.3 min (Woudt, Warner & Motsoaledi, 2013). Only a noisy spectrum of this system has been seen, but it shows helium emission similar to SDSS J1240, and no hydrogen lines (Drake et al., 2012). It is possible that the hydrogen lines are too weak to have been seen, and that this system descends from an evolved CV, thereby explaining the outburst at such a long period, but it is also possible that our understanding of the disc instability in AM CVn binaries is lacking. Further observations of this system are highly desired in order to answer this question.

8.3 Outlook

We have seen how the SDSS has resulted in a huge increase in the numbers of known AM CVn systems, helping us to develop a greater understanding of these interesting binaries. In recent years the PTF and the CRTS have also made a significant contribution to the known AM CVn population by detecting outbursting systems. Whilst the time when each new system revolutionised our understanding of AM CVns has passed, there is still much to be learned, and much to look forward to in the field of ultracompact binaries.

There are currently more than 10 recently discovered AM CVns for which we have not yet measured an orbital period. Determining the periods of these systems is key to developing our understanding of the orbital period distribution. We now have to question whether the longest period systems really are in a stable quiescent state. SDSS J0902+3819 ($P_{\rm orb}$ = 48.3 min; Rau et al. 2010) has recently been observed in an unexpected outburst (Denisenko, 2014; Kato, 2014), and we may now be forced to reconsider the mechanism driving these outbursts. The question of the importance of the evolved CV channel has never been more relevant, continued observations and new discoveries will undoubtedly shed light on the formation of these rare binaries.

As I have discussed, precise determinations of element abundances from AM CVn spectra has been impeded by the lack of detailed models for helium accretion discs. We are now beginning to see results from recent modelling efforts that show great promise for unlocking the evolutionary history of AM CVn sys-

tems (Nagel, Rauch & Werner, 2009; Gehron et al., 2014). The spectral analysis of PTF1 J0719+4858 conducted by Gehron et al. (2014) reveals strong subsolar abundances of metals, and favours the white dwarf formation channel. As I have already discussed the low inclination of SDSS J1730 makes it an excellent system for studying abundances, and the uncertain nature of the helium-rich CVs such as SBSS 1108+574 make them very interesting targets for similar studies.

Looking further ahead, there are a number of upcoming projects with exciting prospects for the study of ultracompact binaries.

The *Gaia* spacecraft will measure parallaxes for essentially all point sources brighter than magnitude 20 (e.g. de Bruijne, 2012), yielding distances to approximately one half of the currently known AM CVn systems. This will allow us to determine absolute magnitudes of these systems, giving us much more accurate measures of the accretion rates, and providing us with a precise test of the brightness of AM CVn systems as a function of orbital period. This will have several implications for our models of the AM CVn population, and will help us to further refine the space density. Absolute magnitudes will also allow us to place AM CVns and candidate systems in a Hertzprung-Russell diagram, which will be very useful for identification of accreting white dwarf systems from large samples. The very low resolution spectrograph aboard *Gaia* may also reveal as yet undiscovered AM CVn systems via their helium emission.

Increasing the known population of AM CVn binaries is still an important goal, especially for improving our estimates of the space density. The Large Synoptic Survey Telescope (LSST; Ivezic et al., 2008) could potentially uncover many new AM CVns via their outbursts. The PTF has already shown this approach to be successful, and since the southern hemisphere has not yet been explored to nearly as great a degree as the north, the LSST should discover many more AM CVns and ultracompact, helium-rich CVs.

The European Space Agency's upcoming *eLISA* mission should directly detect gravitational waves from many of the known AM CVn binaries (e.g. Amaro-Seoane et al., 2013; Nelemans, 2013). Whilst the longest period systems will likely be obscured by the foreground signal from the entire Galactic population of AM CVns and the more numerous double white dwarf binaries, the shortest period systems are expected to be some of the strongest sources detected (Nelemans, 2013). The exact nature of this foreground signal, and the new short period systems that will be discovered are likely to revolutionise our understanding of the AM CVn binaries, and help to resolve the questions surrounding the stability of mass transfer between white dwarfs.

Bibliography

Abazajian, K. N., et al., 2009, ApJS, 182, 543

Abbott, T. M. C., Robinson, E. L., Hill, G. J., Haswell, C. A., 1992, ApJ, 399, 680

Amaro-Seoane, P., et al., 2013, GW Notes, Vol. 6, p. 4-110, 6, 4

Anderson, S. F., et al., 2005, AJ, 130, 2230

Anderson, S. F., et al., 2008, AJ, 135, 2108

Armstrong, E., Patterson, J., Kemp, J., 2012, MNRAS, 421, 2310

Atlee, D. W., Gould, A., 2007, ApJ, 664, 53

Augusteijn, T., van Kerkwijk, M. H., van Paradijs, J., 1993, A&A, 267, L55

Augusteijn, T., van der Hooft, F., de Jong, J. A., van Paradijs, J., 1996, A&A, 311, 889

Baba, H., et al., 2002, PASJ, 54, L7

Barclay, T., Ramsay, G., Hakala, P., Napiwotzki, R., Nelemans, G., Potter, S., Todd, I., 2011, MNRAS, 413, 2696

Bergeron, P., et al., 2011, ApJ, 737, 28

Bicay, M. D., Stepanian, J. A., Chavushyan, V. H., Erastova, L. K., Ayvazyan, V. T., Seal, J., Kojoian, G., 2000, A&AS, 147, 169

Bildsten, L., Townsley, D. M., Deloye, C. J., Nelemans, G., 2006, ApJ, 640, 466

Bildsten, L., Shen, K. J., Weinberg, N. N., Nelemans, G., 2007, ApJ, 662, L95

Bradt, H., 2004, Astronomy Methods: A Physical Approach to Astronomical Observations, Cambridge Univ. Press, Cambridge

Breedt, E., Gänsicke, B. T., Marsh, T. R., Steeghs, D., Drake, A. J., Copperwheat, C. M., 2012, MNRAS, 425, 2548

Brown, W. R., Kilic, M., Allende Prieto, C., Kenyon, S. J., 2010, ApJ, 723, 1072

Brown, W. R., Kilic, M., Allende Prieto, C., Kenyon, S. J., 2011, MNRAS, 411, L31

Brown, W. R., Kilic, M., Allende Prieto, C., Kenyon, S. J., 2012, ApJ, 744, 142

Budavári, T., et al., 2009, ApJ, 694, 1281

Burbidge, E. M., Strittmatter, P. A., 1971, ApJ, 170, L39

Cardelli, J. A., Clayton, G. C., Mathis, J. S., 1989, ApJ, 345, 245

Carroll, B. W., Ostlie, D. A., 2006, An Introduction to Modern Astrophysics, Pearson Addison-Wesley, San Francisco

Carter, P. J., Steeghs, D., Marsh, T. R., Kupfer, T., Copperwheat, C. M., Groot, P. J., Nelemans, G., 2014a, MNRAS, 437, 2894

Carter, P. J., et al., 2013, MNRAS, 429, 2143

Carter, P. J., et al., 2014b, MNRAS, 439, 2848

Chandrasekhar, S., 1939, An introduction to the study of stellar structure, The University of Chicago press, Chicago

Chochol, D., et al., 2014, in The Golden Age of Cataclysmic Variables and Related Objects II, Acta Poly., in press

Copperwheat, C. M., et al., 2011, MNRAS, 410, 1113

de Bruijne, J. H. J., 2012, Ap&SS, 341, 31

Denisenko, D., 2014, vsnet-alert, 16982

Drake, A. J., et al., 2009, ApJ, 696, 870

Drake, A. J., et al., 2012, The Astronomer's Telegram, 4678, 1

Drake, A. J., et al., 2014, MNRAS, in press, (arXiv:astro-ph/1404.3732)

Dye, S., et al., 2006, MNRAS, 372, 1227

Efron, B., 1979, Ann. Statist., 7, 1

Eggleton, P. P., 1983, ApJ, 268, 368

Eisenstein, D. J., et al., 2011, AJ, 142, 72

Espaillat, C., Patterson, J., Warner, B., Woudt, P., 2005, PASP, 117, 189

Faulkner, J., 1971, ApJ, 170, L99

Faulkner, J., Flannery, B. P., Warner, B., 1972, ApJ, 175, L79+

Fitzpatrick, E. L., 1999, PASP, 111, 63

Fontaine, G., et al., 2011, ApJ, 726, 92

Frank, J., King, A., Raine, D. J., 2002, Accretion Power in Astrophysics: Third Edition, Cambridge Univ. Press, Cambridge

Gänsicke, B. T., Beuermann, K., 1996, A&A, 309, L47

Gänsicke, B. T., et al., 2009, MNRAS, 397, 2170

Garnavich, P., Littlefield, C., Marion, G. H., Irwin, J., Kirshner, R. P., Vinko, J., 2012, The Astronomer's Telegram, 4112, 1

Gehron, K., Nagel, T., Rauch, T., Werner, K., 2014, A&A, 562, A132

Girven, J., Gänsicke, B. T., Steeghs, D., Koester, D., 2011, MNRAS, 417, 1210

Greenstein, J. L., Matthews, M. S., 1957, ApJ, 126, 14

Groot, P. J., Nelemans, G., Steeghs, D., Marsh, T. R., 2001, ApJ, 558, L123

Hōshi, R., 1979, Progress of Theoretical Physics, 61, 1307

Harris, H. C., et al., 2003, AJ, 126, 1023

Harvey, D. A., Skillman, D. R., Kemp, J., Patterson, J., Vanmunster, T., Fried, R. E., Retter, A., 1998, ApJ, 493, L105

Hawley, J. F., Balbus, S. A., 1998, in Howell, S., Kuulkers, E., Woodward, C., eds., Wild Stars in the Old West, vol. 137 of *Astronomical Society of the Pacific Conference Series*, p. 273

Heber, U., 2009, ARA&A, 47, 211

Hellier, C., 2001, Cataclysmic variable stars: how and why they vary, Springer-Praxis, Chichester

Hillebrandt, W., Niemeyer, J. C., 2000, ARA&A, 38, 191

Holberg, J. B., Bergeron, P., 2006, AJ, 132, 1221

Hook, I. M., Jørgensen, I., Allington-Smith, J. R., Davies, R. L., Metcalfe, N., Murowinski, R. G., Crampton, D., 2004, PASP, 116, 425

Horne, K., 1986, PASP, 98, 609

Horne, K., Marsh, T. R., 1986, MNRAS, 218, 761

Horne, K., Wade, R. A., Szkody, P., 1986, MNRAS, 219, 791

Howell, S. B., 2000, Handbook of CCD Astronomy, Cambridge Univ. Press, Cambridge

Iben, Jr., I., 1991, ApJS, 76, 55

Iben, Jr., I., Tutukov, A. V., 1987, ApJ, 313, 727

Iben, Jr., I., Tutukov, A. V., 1991, ApJ, 370, 615

Israel, G. L., Panzera, M. R., Campana, S., Lazzati, D., Covino, S., Tagliaferri, G., Stella, L., 1999, A&A, 349, L1

Israel, G. L., et al., 2002, A&A, 386, L13

Ivanova, N., et al., 2013, A&A Rev., 21, 59

Ivezic, Z., et al., 2008, arXiv:astro-ph/0805.2366

Jordi, K., Grebel, E. K., Ammon, K., 2006, A&A, 460, 339

Kato, T., 2013a, vsnet-alert, 15652

Kato, T., 2013b, vsnet-alert, 15639

Kato, T., 2014, vsnet-alert, 17026

Kato, T., et al., 2009, PASJ, 61, 395

Kato, T., et al., 2013, PASJ, 65, 23

Kilic, M., et al., 2014, MNRAS, 438, L26

King, A. R., 1988, QJRAS, 29, 1

Kitchin, C. R., 1998, Astrophysical techniques, Institute of Physics Pub., Bristol

Knigge, C., 2006, MNRAS, 373, 484

Knigge, C., Baraffe, I., Patterson, J., 2011, ApJS, 194, 28

Koester, D., 2010, Mem. Soc. Astron. Italiana, 81, 921

Koester, D., Weidemann, V., 1980, A&A, 81, 145

Kolb, U., Baraffe, I., 1999, MNRAS, 309, 1034

Kolb, U., King, A. R., Ritter, H., 1998, MNRAS, 298, L29

Kotko, I., Lasota, J.-P., Dubus, G., Hameury, J.-M., 2012, A&A, 544, A13

Kowalski, P. M., Saumon, D., 2006, ApJ, 651, L137

Kupfer, T., Groot, P. J., Levitan, D., Steeghs, D., Marsh, T. R., Rutten, R. G. M., Nelemans, G., 2013, MNRAS, 432, 2048

Landau, L. D., Lifshitz, E. M., 1971, The classical theory of fields, Pergamon Press, Oxford

Law, N. M., et al., 2009, PASP, 121, 1395

Levitan, D., et al., 2011, ApJ, 739, 68

Levitan, D., et al., 2013, MNRAS, 430, 996

Levitan, D., et al., 2014, ApJ, 785, 114

Liebert, J., Bergeron, P., Holberg, J. B., 2005, ApJS, 156, 47

Littlefair, S. P., Dhillon, V. S., Marsh, T. R., Gänsicke, B. T., Baraffe, I., Watson, C. A., 2007, MNRAS, 381, 827

Littlefield, C., et al., 2013, AJ, 145, 145

Lomb, N. R., 1976, Ap&SS, 39, 447

Lynden-Bell, D., 1969, Nature, 223, 690

Marsh, T. R., 1989, PASP, 101, 1032

Marsh, T. R., 1999, MNRAS, 304, 443

Marsh, T. R., 2001, in Boffin, H. M. J., Steeghs, D., Cuypers, J., eds., Astrotomography, Indirect Imaging Methods in Observational Astronomy, vol. 573 of *Lecture Notes in Physics, Berlin Springer Verlag*, p. 1

Marsh, T. R., Horne, K., 1988, MNRAS, 235, 269

Marsh, T. R., Steeghs, D., 2002, MNRAS, 331, L7

Marsh, T. R., Horne, K., Rosen, S., 1991, ApJ, 366, 535

Marsh, T. R., Nelemans, G., Steeghs, D., 2004, MNRAS, 350, 113

Martin, D. C., et al., 2005, ApJ, 619, L1

Martinez, P., Klotz, A., 1998, A practical guide to CCD astronomy, Cambridge Univ. Press, Cambridge

Massey, P., Hanson, M. M., 2013, in Oswalt, T. D., Bond, H. E., eds., Planets, Stars and Stellar Systems. Volume 2: Astronomical Techniques, Software and Data, Springer Netherlands, Dordrecht, p. 35

Meyer, F., Meyer-Hofmeister, E., 1981, A&A, 104, L10

Morales-Rueda, L., Marsh, T. R., Steeghs, D., Unda-Sanzana, E., Wood, J. H., North, R. C., 2003, A&A, 405, 249

Morrissey, P., et al., 2007, ApJS, 173, 682

Nagel, T., Rauch, T., Werner, K., 2009, A&A, 499, 773

Nather, R. E., Robinson, E. L., Stover, R. J., 1981, ApJ, 244, 269

Nelemans, G., 2005, in Hameury, J.-M., Lasota, J.-P., eds., The Astrophysics of Cataclysmic Variables and Related Objects, vol. 330 of *Astronomical Society of the Pacific Conference Series*, p. 27

Nelemans, G., 2013, in Auger, G., Binétruy, P., Plagnol, E., eds., 9th LISA Symposium, vol. 467 of *Astronomical Society of the Pacific Conference Series*, p. 27

Nelemans, G., Verbunt, F., Yungelson, L. R., Portegies Zwart, S. F., 2000, A&A, 360, 1011

Nelemans, G., Portegies Zwart, S. F., Verbunt, F., Yungelson, L. R., 2001, A&A, 368, 939

Nelemans, G., Yungelson, L. R., Portegies Zwart, S. F., 2004, MNRAS, 349, 181

Nelemans, G., Yungelson, L. R., van der Sluys, M. V., Tout, C. A., 2010, MNRAS, 401, 1347

Nissanke, S., Vallisneri, M., Nelemans, G., Prince, T. A., 2012, ApJ, 758, 131

O'Donoghue, D., Menzies, J. W., Hill, P. W., 1987, MNRAS, 227, 347

O'Donoghue, D., Kilkenny, D., Chen, A., Stobie, R. S., Koen, C., Warner, B., Lawson, W. A., 1994, MNRAS, 271, 910

Osaki, Y., 1974, PASJ, 26, 429

Paczyński, B., 1967, Acta Astron., 17, 287

Paczyński, B., 1976, in Eggleton, P., Mitton, S., Whelan, J., eds., Structure and Evolution of Close Binary Systems, vol. 73 of *IAU Symposium*, p. 75

Patterson, J., et al., 2005, PASP, 117, 1204

Podsiadlowski, P., Han, Z., Rappaport, S., 2003, MNRAS, 340, 1214

Press, W. H., Rybicki, G. B., 1989, ApJ, 338, 277

Prieto, J. L., et al., 2013, The Astronomer's Telegram, 4999, 1

Pringle, J. E., 1981, ARA&A, 19, 137

Provencal, J. L., et al., 1997, ApJ, 480, 383

Ramsay, G., Hakala, P., 2005, MNRAS, 360, 314

Ramsay, G., Wu, K., Cropper, M., Schmidt, G., Sekiguchi, K., Iwamuro, F., Maihara, T., 2002, MNRAS, 333, 575

Ramsay, G., Napiwotzki, R., Hakala, P., Lehto, H., 2006, MNRAS, 371, 957

Ramsay, G., Barclay, T., Steeghs, D., Wheatley, P. J., Hakala, P., Kotko, I., Rosen, S., 2012, MNRAS, 419, 2836

Ramsay, G., et al., 2014, MNRAS, 438, 789

Rappaport, S., Joss, P. C., Webbink, R. F., 1982, ApJ, 254, 616

Rau, A., Roelofs, G. H. A., Groot, P. J., Marsh, T. R., Nelemans, G., Steeghs, D., Salvato, M., Kasliwal, M. M., 2010, ApJ, 708, 456

Rayne, M. W., Whelan, J. A. J., 1981, MNRAS, 196, 73

Richards, G. T., et al., 2009, AJ, 137, 3884

Ritter, H., Kolb, U., 2003, A&A, 404, 301

Robinson, E. L., Faulkner, J., 1975, ApJ, 200, L23

Rodríguez-Gil, P., Gänsicke, B. T., Hagen, H.-J., Marsh, T. R., Harlaftis, E. T., Kitsionas, S., Engels, D., 2005, A&A, 431, 269

Roelofs, G. H. A., 2007, The AM Canum Venaticorum Stars, Ph.D. thesis, Radboud University Nijmegen, The Netherlands

Roelofs, G. H. A., Groot, P. J., Steeghs, D., Nelemans, G., 2004, in Tovmassian, G., Sion, E., eds., Revista Mexicana de Astronomia y Astrofisica Conference Series, vol. 20 of *Revista Mexicana de Astronomia y Astrofisica Conference Series*, p. 254

Roelofs, G. H. A., Groot, P. J., Marsh, T. R., Steeghs, D., Barros, S. C. C., Nelemans, G., 2005, MNRAS, 361, 487

Roelofs, G. H. A., Groot, P. J., Marsh, T. R., Steeghs, D., Nelemans, G., 2006, MNRAS, 365, 1109

Roelofs, G. H. A., Groot, P. J., Benedict, G. F., McArthur, B. E., Steeghs, D., Morales-Rueda, L., Marsh, T. R., Nelemans, G., 2007a, ApJ, 666, 1174

Roelofs, G. H. A., Groot, P. J., Nelemans, G., Marsh, T. R., Steeghs, D., 2007b, MNRAS, 379, 176

Roelofs, G. H. A., Groot, P. J., Steeghs, D., Marsh, T. R., Nelemans, G., 2007c, MNRAS, 382, 1643

Roelofs, G. H. A., Nelemans, G., Groot, P. J., 2007, MNRAS, 382, 685

Roelofs, G. H. A., Rau, A., Marsh, T. R., Steeghs, D., Groot, P. J., Nelemans, G., 2010, ApJ, 711, L138

Roelofs, G. H. A., et al., 2009, MNRAS, 394, 367

Ruiz, M. T., Rojo, P. M., Garay, G., Maza, J., 2001, ApJ, 552, 679

Saio, H., Nomoto, K., 1985, A&A, 150, L21

Savonije, G. J., de Kool, M., van den Heuvel, E. P. J., 1986, A&A, 155, 51

Scargle, J. D., 1982, ApJ, 263, 835

Schlegel, D. J., Finkbeiner, D. P., Davis, M., 1998, ApJ, 500, 525

Schneider, D. P., Young, P., 1980, ApJ, 238, 946

Schreiber, M. R., Gänsicke, B. T., 2003, A&A, 406, 305

Schwarzenberg-Czerny, A., 1996, ApJ, 460, L107

Shafter, A. W., 1983, ApJ, 267, 222

Shakura, N. I., Sunyaev, R. A., 1973, A&A, 24, 337

Shears, J., Brady, S., Koff, R., Goff, W., Boyd, D., 2012, J. Br. Astron. Assoc., 122, 49

Shen, K. J., Bildsten, L., 2009, ApJ, 699, 1365

Shen, K. J., Bildsten, L., 2014, ApJ, in press, (arXiv:astro-ph/1305.6925)

Sienkiewicz, R., 1984, Acta Astron., 34, 325

Sion, E. M., Greenstein, J. L., Landstreet, J. D., Liebert, J., Shipman, H. L., Wegner, G. A., 1983, ApJ, 269, 253

Sion, E. M., Cheng, F. H., Szkody, P., Sparks, W., Gänsicke, B., Huang, M., Mattei, J., 1998, ApJ, 496, 449

Skumanich, A., 1972, ApJ, 171, 565

Slevinsky, R. J., Stys, D., West, S., Sion, E. M., Cheng, F. H., 1999, PASP, 111, 1292

Smak, J., 1967, Acta Astron., 17, 255

Smak, J., 1970, Acta Astron., 20, 311

Smak, J., 1975, Acta Astron., 25, 227

Smak, J., 1981, Acta Astron., 31, 395

Smak, J., 1984, PASP, 96, 5

Solheim, J., 2010, PASP, 122, 1133

Solheim, J.-E., Yungelson, L. R., 2005, in Koester, D., Moehler, S., eds., 14th European Workshop on White Dwarfs, vol. 334 of *Astronomical Society of the Pacific Conference Series*, p. 387

Steeghs, D., 2001, in Boffin, H. M. J., Steeghs, D., Cuypers, J., eds., Astrotomography, Indirect Imaging Methods in Observational Astronomy, vol. 573 of *Lecture Notes in Physics, Berlin Springer Verlag*, p. 45

Steeghs, D., 2010, in Proceedings of High Time Resolution Astrophysics - The Era of Extremely Large Telescopes (HTRA-IV). May 5 - 7, 2010. Agios Nikolaos, Crete Greece.

Stellingwerf, R. F., 1978, ApJ, 224, 953

Stoughton, C., et al., 2002, AJ, 123, 485

Szkody, P., et al., 2011, AJ, 142, 181

Thorstensen, J. R., Taylor, C. J., 2001, MNRAS, 326, 1235

Thorstensen, J. R., Fenton, W. H., Patterson, J. O., Kemp, J., Krajci, T., Baraffe, I., 2002, ApJ, 567, L49

Tokarz, S. P., Roll, J., 1997, in G. Hunt & H. Payne, ed., Astronomical Data Analysis Software and Systems VI, vol. 125 of *Astronomical Society of the Pacific Conference Series*, p. 140

Toonen, S., Nelemans, G., 2013, A&A, 557, A87

Townsley, D. M., Bildsten, L., 2003, ApJ, 596, L227

Townsley, D. M., Gänsicke, B. T., 2009, ApJ, 693, 1007

Tremblay, P.-E., Bergeron, P., Gianninas, A., 2011, ApJ, 730, 128

Tsugawa, M., Osaki, Y., 1997, PASJ, 49, 75

Tutukov, A. V., Fedorova, A. V., Ergma, E. V., Yungelson, L. R., 1985, Soviet Astronomy Letters, 11, 52

Uthas, H., Knigge, C., Long, K. S., Patterson, J., Thorstensen, J., 2011, MNRAS, 414, L85

Verbunt, F., 1982, Space Sci. Rev., 32, 379

Verbunt, F., Zwaan, C., 1981, A&A, 100, L7

Warner, B., 1972, MNRAS, 159, 315

Warner, B., 1995, Cataclysmic variable stars, Cambridge Univ. Press, Cambridge

Warner, B., Woudt, P. A., 2002, PASP, 114, 129

Weber, E. J., Davis, Jr., L., 1967, ApJ, 148, 217

Wesemael, F., Greenstein, J. L., Liebert, J., Lamontagne, R., Fontaine, G., Bergeron, P., Glaspey, J. W., 1993, PASP, 105, 761

Wheatley, J. M., Welsh, B. Y., Browne, S. E., 2008, AJ, 136, 259

Whitehurst, R., 1988, MNRAS, 232, 35

Williams, R. E., Ferguson, D. H., 1982, ApJ, 257, 672

Wils, P., Gänsicke, B. T., Drake, A. J., Southworth, J., 2010, MNRAS, 402, 436

Wood, M. A., Winget, D. E., Nather, R. E., Hessman, F. V., Liebert, J., Kurtz, D. W., Wesemael, F., Wegner, G., 1987, ApJ, 313, 757

Wood, M. A., Still, M. D., Howell, S. B., Cannizzo, J. K., Smale, A. P., 2011, ApJ, 741, 105

Woudt, P. A., Warner, B., 2001, MNRAS, 328, 159

Woudt, P. A., Warner, B., 2011, The Astronomer's Telegram, 3705, 1

Woudt, P. A., Warner, B., Pretorius, M. L., 2004, MNRAS, 351, 1015

Woudt, P. A., Warner, B., Rykoff, E., 2005, IAU Circ., 8531, 3

Woudt, P. A., Warner, B., de Budé, D., Macfarlane, S., Schurch, M. P. E., Zietsman, E., 2012, MNRAS, 421, 2414

Woudt, P. A., Warner, B., Motsoaledi, M., 2013, The Astronomer's Telegram, 4726, 1

Wright, E. L., et al., 2010, AJ, 140, 1868

Wu, X.-B., Jia, Z., 2010, MNRAS, 406, 1583

York, D. G., et al., 2000, AJ, 120, 1579

Yungelson, L. R., 2008, Astronomy Letters, 34, 620